

**“Rheological and thermal properties of structure-forming
oligosaccharides as basis of food model systems.”**

Dissertation
zur Erlangung des Grades

„Doktor der Naturwissenschaften“

im Promotionsfach Chemie

am Fachbereich Chemie, Pharmazie und Geowissenschaften
der Johannes Gutenberg-Universität
in Mainz

Steffen Beccard
geb. in Mainz

Mainz, den 11.06.2018

Dekan: Prof. Dirk Schneider

1. Berichterstatter: Prof. Thomas Vilgis

2. Berichterstatter: Prof. Angelika Kühnle

Tag der mündlichen Prüfung: 03.07.2018

Abstract

In this work, inulin particle gels, prepared with two types of long chain inulin, namely HP and HPX, were examined in terms of their structural properties and mechanical response, depending on the solvent used to prepare the gels (distilled water, water-ethanol mixtures and water-sucrose mixtures). The results are interpreted on the basis of a particle gel model, which takes into account the varying gel structure, depending on the sample preparation parameters. X-ray measurements of the inulin powders, used for the experiments, revealed HP as a mostly amorphous and HPX as a semi-crystalline powder. The inulin gels with pure water acting as solvent, were examined according to their sample preparation temperatures. The temperature profiles for the sample preparation, chosen from 25 °C to 60 °C for HP and from 25 °C to 80 °C for HPX, with constant stirring at 600 rpm, yielded viscoelastic particle gels with decreasing hardness for the HP gels and increasing hardness for the HPX gels. By application of high shear rates (7000 rpm) at the same temperature conditions, the gel hardness was increased for both types of inulin. Time resolved X-ray scattering experiments during gel formation provided information about the crystallization kinetics and examination of the inulin gels, using static light scattering, confirmed that the final gel particle size depends on the sample preparation temperature. Thus, the results show a high sensitivity of the structural and textural properties of HP and HPX gels to the variation of applied temperature and shearing during sample preparation. The inulin gels prepared with water-ethanol mixtures, were examined according to the decreasing polarity of the solvent with increasing ethanol content. The ethanol concentration in the solvent varied from 0% (w/w) up to 15% (w/w) for both types of inulin. Comparable to the inulin-water system, a constant stirring at 600 rpm during sample preparation, yielded viscoelastic particle gels with decreasing hardness at increasing ethanol concentration in the solvent for both, HP and HPX. Again, time resolved X-ray scattering experiments during gel formation provided information about the crystallization kinetics and examination of the inulin gels, using static light scattering, confirmed that the final gel particle size depends on the polarity of the solvent. The inulin gels prepared with water-sucrose mixtures, were examined according to the increasing saturation of the solvent with increasing sucrose concentration. The sucrose content in the solvent varied from 0% (w/w) up to 15% (w/w). As already mentioned for the inulin-water and the inulin-water-ethanol systems, a constant stirring at 600 rpm during sample preparation, yielded viscoelastic particle gels with decreasing

hardness at increasing sucrose concentrations for both types of inulin. As before, time resolved X-ray scattering experiments during gel formation provided information about the crystallization kinetics and examination of the inulin gels, using static light scattering, confirmed that the final gel particle size depends on the saturation of the solvent. Finally, the different systems could be linked to each other, by the determination of intersection points between the solubility curves of all three systems. Thus, the results show a high sensitivity of the structural and textural properties of HP and HPX gels to the variation of applied temperature, polarity and saturation of the solvent. Those findings allow the controlled alteration of large scale structures and thus of the textural properties in food systems containing inulin as texturizer or fat replacement.

Kurzfassung

Diese Arbeit beschäftigt sich mit Partikel-Gelen, welche mit zwei langkettigen Typen von Inulin (HP und HPX) hergestellt wurden. Diese wurden in Hinblick auf ihre strukturellen Eigenschaften und das Verhalten während der Deformation, in Abhängigkeit vom eingesetzten Lösungsmittel, untersucht. Als Lösungsmittel wurden demineralisiertes Wasser, Wasser-Ethanol Mischungen und Wasser-Saccharose Mischungen, verwendet. Die Ergebnisse wurden auf der Grundlage eines Partikel-Gel Modells interpretiert, welches die sich ändernde Gelstruktur in Abhängigkeit von den variierenden Probenvorbereitungsparametern berücksichtigt. Röntgenbeugungsmessungen der eingesetzten Inulin Pulver, identifizierten HP als größtenteils amorphes und HPX als semi-kristallines Pulver. Die Inulin-Gele, welche mit reinem Wasser als Lösungsmittel vorbereitet wurden, wurden in Abhängigkeit von einer zunehmenden Probenvorbereitungstemperatur (Temperaturprofil von 25 °C bis 60 °C für HP und von 25 °C bis 80 °C für HPX) mit einer konstanten Rührgeschwindigkeit von 600 U/min untersucht. Die auf diese Weise vorbereiteten Gele wiesen viskoelastische Eigenschaften auf, deren Gelhärte mit zunehmender Probenvorbereitungstemperatur (PV-Temp.) variierte (die Gelhärte von HP-Gelen nimmt mit zunehmender PV-Temp. ab und die Gelhärte von HPX nimmt mit zunehmender PV-Temp. zu). Durch die Anwendung erhöhter Scherraten (7000 U/min) bei identischen Temperaturbedingungen, konnte die Gelhärte für beide Inulin Typen erhöht werden. Durch zeitabhängige Röntgenbeugungsmessungen konnten Informationen über die Kristallisationskinetik der Inulin-Gele gewonnen werden. Die Partikelgrößenbestimmung der Inulin-Gele mittels statischer Lichtstreuung bestätigte, dass die endgültige Größe der Gelpartikel von der PV-Temp. abhängig ist. Somit weisen Struktur und Textur von HP und HPX Gelen, welche mit demineralisiertem Wasser als Lösungsmittel vorbereitet wurden, eine starke Abhängigkeit von der Probenvorbereitungstemperatur und der angewendeten Scherrate während der Probenvorbereitung auf. Die mit Ethanol-Wasser Mischungen präparierten Inulin-Gele, wurden in Abhängigkeit einer sinkenden Polarität, mit zunehmenden Ethanolanteil im Lösungsmittel, untersucht. Die Ethanol Konzentrationen im Lösungsmittel variierten von 0% (w/w) bis 15% (w/w) für beide Typen von Inulin. Vergleichbar zum Inulin-Wasser System, konnten durch eine konstante Scherrate von 600 U/min während der Probenvorbereitung, viskoelastische HP und HPX Gele erhalten werden, deren Gelhärte mit zunehmendem Ethanolanteil im Lösungsmittel abnahm. Wie zuvor, lieferten zeitabhängige Röntgenbeugungsexperimente Informationen

über die Kristallisationskinetik der Inulin-Gele und die Partikelgrößenbestimmung mittels statischer Lichtstreuung bestätigte eine starke Abhängigkeit der Gelpartikelgrößen von der Polarität des Lösungsmittels. Die mit Saccharose-Wasser Mischungen präparierten Inulin-Gele, wurden in Abhängigkeit einer zunehmenden Sättigung, mit zunehmenden Saccharoseanteil im Lösungsmittel, untersucht. Die Saccharose Konzentrationen im Lösungsmittel variierten von 0% (w/w) bis 15% (w/w) für beide Typen von Inulin. Vergleichbar zum Inulin-Wasser und zum Inulin-Wasser-Ethanol System, konnten durch eine konstante Scherrate von 600 U/min während der Probenvorbereitung, viskoelastische HP und HPX Gele erhalten werden, deren Gelhärte mit zunehmendem Saccharoseanteil im Lösungsmittel abnahm. Erneut lieferten zeitabhängige Röntgenbeugungsexperimente Informationen über die Kristallisationskinetik der Inulin-Gele und die Partikelgrößenbestimmung mittels statischer Lichtstreuung bestätigte eine starke Abhängigkeit der Gelpartikelgrößen von der Sättigung des Lösungsmittels. Schlussendlich konnten alle drei Systeme über Schnittpunkte der jeweiligen Löslichkeitskurven miteinander verknüpft werden. Zusammenfassend konnte festgestellt werden, dass die Gelstrukturen der HP- und HPX-Gele eine starke Abhängigkeit von der Temperatur, der Polarität und der Sättigung des Lösungsmittels aufweisen. Die Resultate dieser Arbeit ermöglichen somit die kontrollierte Beeinflussung der makroskopischen Eigenschaften von Lebensmittelsystemen, die Inulin als Texturgeber oder Fettersatzstoff enthalten.

Acknowledgements

First of all, I would like to thank Dr. Dierk Martin from Südzucker CRDS, for establishing the contact between Südzucker and the MPIP, making this project possible at all. Many thanks also to Dr. Karin Gehrich, Rudy Wouters and Dr. Jörg Bernard, also from Südzucker CRDS, for their inspiring discussions and support throughout the whole project period.

A very special thank you goes to Prof. Thomas Vilgis, for supervising me during the PhD at MPIP. Thank you for your support, advice and interesting (and most often entertaining) discussions. Without your help and guidance this work would not have been possible!

A warm thank you goes to Prof. Kurt Kremer, for accepting my PhD project in the MPIP Theory Group and providing the infrastructure necessary for the research.

A big thank you also to Prof. Angelika Kühnle, for supervising me in this project as representative from JGU Mainz and preparing the survey, necessary for the completion of my thesis. Also thank you very much to Prof. Heiner Detert and Prof. Gerald Hinze from JGU Mainz, for acting as examiner during my defense.

The author would like to thank Stefan Geiter, Michael Steiert and Prof. Markus Mezger from MPIP, for the assistance with the X-ray measurements. Many thanks go also to Dr. Kaloian Koynov, Andreas Hanewald and Andreas Best, also from MPIP, for providing the 2005 AllroundLine texture analyzer and the Olympus confocal microscope. For their invaluable help with the HPAEC measurements, I would like to express my great appreciation to Alexander Schmiega and Hans Ehlers from Südzucker CRDS.

Thank you so much, Dr. Birgitta Zielbauer from MPIP Food Group, for your always helpful and invaluable comments and advice! Also a heartily thank you to the current and former members of the Food Group (Dr. Natalie Russ, Dr. Sania Maurer, Dr. Gustav Waschatko, Dr. Trivikram Nallamilli, Hannah Hartge, Sarah Gindra, Markus Ketomäki, Martha Ghebremedin, Christine Schreiber, Anais Lavoisier and Bhagyashri Joshi) for the help and the very nice working atmosphere.

Last but not least, I would like to thank my family and especially my beloved wife Maike for the patience, the support and the backup whenever needed!

Table of contents

Abstract	3
Kurzfassung	5
Acknowledgements	7
Table of contents.....	I
List of illustrations	IV
List of tables	XI
List of abbreviations	XII
List of variables.....	XIII
1 Introduction	1
1.1 The particle gel model	2
1.2 Crystals.....	4
1.3 Classical nucleation theory and isothermal crystallization	8
1.4 Particle gels as fractal clusters [23]	12
1.5 Solute-Solvent interactions	15
1.6 Solubility measurements	20
1.7 X-ray diffraction	26
1.8 High Performance Anion Exchange Chromatography (HPAEC)	32
1.9 Texture analysis (Gel Hardness)	37
1.10 Confocal Laser Scanning Microscopy (CLSM)	41
1.11 Oscillatory rheology.....	46
1.12 Particle size determination (Light scattering)	52
2 Materials and methods.....	59
2.1 Materials.....	59
2.2 Sample preparation and analytical methods	59
2.3 Solubility in water	59

2.4	X-ray diffraction	60
2.5	High Performance Anion Exchange Chromatography	60
2.6	Texture analysis	60
2.7	Confocal Laser Scanning Microscopy	61
2.8	Oscillatory Rheology	61
2.9	Particle size determination (Light scattering)	62
3	Results and discussion	63
3.1	X-ray powder diffraction.....	63
3.2	The inulin-water system	63
3.2.1	Solubility in water.....	63
3.2.2	X-ray diffraction during gelation	66
3.2.3	High Performance Anion Exchange Chromatography	72
3.2.4	Texture analysis (Gel hardness)	76
3.2.5	Oscillatory rheology	80
3.2.6	Particle size.....	85
3.2.7	Summary	90
3.3	The inulin-water-ethanol system	92
3.3.1	Solubility in water-ethanol mixtures.....	92
3.3.2	X-ray diffraction during gelation	94
3.3.3	High Performance Anion Exchange Chromatography	101
3.3.4	Texture analysis (Gel hardness)	105
3.3.5	Oscillatory rheology	107
3.3.6	Particle size.....	111
3.3.7	Summary	116
3.4	The inulin-water-sucrose system.....	119
3.4.1	Solubility in water-sucrose mixtures.....	119

3.4.2	X-ray diffraction during gelation	121
3.4.3	High Performance Anion Exchange Chromatography	127
3.4.4	Texture analysis (Gel hardness)	132
3.4.5	Oscillatory rheology	134
3.4.6	Particle size.....	139
3.4.7	Summary	145
3.5	The inulin-water-ethanol-sucrose system.....	148
3.5.1	Solubility in different solvents.....	148
3.5.2	High Performance Anion Exchange Chromatography	154
3.5.3	Texture analysis (Gel hardness)	158
4	Conclusions	163
5	Outlook.....	165
	List of references	166
	Statutory declaration	170
	Appendix.....	171

List of illustrations

Fig. 1: Molecular structure of inulin molecule, the n at the brackets adopts at maximum 90.	1
Fig. 2: Inulin particle gel model.	3
Fig. 3: Unit cell a) and point lattice b) [18].	4
Fig. 4: Unit cell with lattice parameters [17].	4
Fig. 5: Bravais lattices [19].	5
Fig. 6: Crystal systems with lattice parameters [20].	5
Fig. 7: Indices of directions [17].	7
Fig. 8: Miller indices of planes in the cubic system. The distance d is the interplanar spacing [17].	7
Fig. 9: Solubility and metastable zone width (MSZW) [22].	9
Fig. 10: Free energy vs. nucleus size [17].	10
Fig. 11: Determination of fractal dimension D_f by oscillatory rheology	15
Fig. 12: Air/glass interface, with refracted and reflected light beams. a) Coming from air entering glass; b) coming from glass entering air [40].	22
Fig. 13: Application of Huygens' principle on a plane wave at an air/glass interface [40].	23
Fig. 14: Total reflection [40].	24
Fig. 15: Abbé refractometer [43].	25
Fig. 16: Total reflection and shadow boundary in measuring prism [44].	25
Fig. 17: Handheld digital refractometer by Bellingham and Stanley [45].	26
Fig. 18: Electromagnetic spectrum [47].	27
Fig. 19: Standard x-ray tube [47].	28
Fig. 20: Generation of x-rays [47].	28
Fig. 21: Characteristic x-ray radiation and "Bremsstrahlung" [47].	29
Fig. 22: Diffraction of x-ray wave front at lattice plane [48].	29
Fig. 23: Diffraction of x-ray radiation at lattice planes.	30
Fig. 24: a) Experimental setup and b) obtained diffractogram.	31
Fig. 25: a) Surface functionalized anion exchange substrate particle [50], b) Structural formula of Styrene-Divinylbenzene Copolymer [51].	32
Fig. 26: Conductometric detection [52].	34
Fig. 27: Chromatogram with parameters indicated [53].	35

Fig. 28: Experimental setup of the HPAEC measurements [54].....	37
Fig. 29: A typical texture analysis curve, which should be read from left to right, with peak A1 being the first chew and peak A2 the second chew [56].	38
Fig. 30: Compression of cylindrical shaped inulin gel sample.....	40
Fig. 31: A) Setup of texture analyzer for indentation measurement and B) indentation measurement of inulin gel sample.....	40
Fig. 32: Rhodamine-B structure [59].	42
Fig. 33: Fluorescence principle [58].	42
Fig. 34: A) Objective and light beam path: A point source in the focal plane is imaged and projected as bright central spot (Airy disc) with a surrounding diffraction ring pattern, B) Calculated x-y (upper images) and x-z (lower images) intensity distributions (log scale) for a point source imaged with wide-field and confocal microscopy [58].....	43
Fig. 35: Schematic diagram of an Airy disc diffraction pattern: Abbe diffraction limit, contrast, and optical resolution [58].	44
Fig. 36: Comparison of conventional light microscopy A) and CLSM B) [58].	46
Fig. 37: Two plate model [60].....	47
Fig. 38: Typical flow curves for Newtonian, shear thinning and shear thickening (dilatant) fluids: (a) shear stress vs. shear rate ,(b) viscosity vs. shear rate [61].....	48
Fig. 39: Flow curve of a thixotropic material [61].	49
Fig. 40: Parallel plate geometry [61].	51
Fig. 41: Model of equivalent sphere [63].	53
Fig. 42: Light rays interacting with a particle [64].....	54
Fig. 43: “Bull’s eye” scattering pattern [64]	55
Fig. 44: Rayleigh and Mie scattering [66].	55
Fig. 45: Optical System of the LS 13320 [65].....	56
Fig. 46: Scattering from different polarizations [65].....	58
Fig. 47: X-ray powder diffraction.....	63
Fig. 48: Solubility of HP and HPX in water at 25 °C, dependent on added amount (w/w).	64
Fig. 49: Refractive index in dependency of the mass concentration.	65
Fig. 50: Equilibrium solubility of 20% (w/w) inulin in water.	66
Fig. 51: XRD during gelation of an HP gel, prepared at 25 °C and 600 rpm shear rate.	67
Fig. 52: XRD during gelation of an HPX gel, prepared at 25 °C and 600 rpm shear rate.	68

Fig. 53: Development of the relative intensity of HP gels prepared at 25 °C, 40 °C and 60 °C.	68
Fig. 54: Development of the relative intensity of HPX gels prepared at 25 °C, 40 °C, 60 °C and 80 °C.	70
Fig. 55: Development of the relative intensity of HP/HPX gels, plotted on logarithmic scale.	70
Fig. 56: HP separated according to DP.	72
Fig. 57: HPX separated according to DP.	73
Fig. 58: Temperature dependent DP distribution of dissolved HP after 10 min stirring at preparation temperature.	74
Fig. 59: Temperature dependent DP distribution of dissolved HPX after 10 min stirring at preparation temperature.	74
Fig. 60: Temperature dependent DP distribution of dissolved HP after 24 h storage.	75
Fig. 61: Temperature dependent DP distribution of dissolved HPX after 24 h storage.	76
Fig. 62: HP gels compressed beyond fracture stress. A was prepared at 25°C, B was prepared at 60°C	77
Fig. 63: Crack pattern of strong gels [30]	77
Fig. 64: HPX gels compressed beyond fracture stress. A was prepared at 25°C, B was prepared at 80°C	77
Fig. 65: Hardness of inulin gels prepared at different temperatures	79
Fig. 66: Comparison of gel structure of HP and HPX gels, both prepared at 25 °C. Each picture was taken in a depth of 10 µm.....	79
Fig. 67: Amplitude sweep curves of HP gels, prepared at 25 °C, 40 °C and 60 °C. The device setup is indicated in the figure.....	81
Fig. 68: Shear thinning behavior of an inulin gel, under the influence of a horizontal shear force.	82
Fig. 69: Amplitude sweep curves of HPX gels, prepared at 25 °C, 40 °C, 60 °C and 80 °C. The device setup is indicated in the figure.	83
Fig. 70: Comparison amplitude sweeps of HP and HPX gels. Point of shear breakdown is indicated for each sample.	84
Fig. 71: Gel primary particle size (number average) in dependency of sample preparation temperature and shear rate.....	86
Fig. 72: Number distribution of HP gel particle size, prepared at 25 °C and 60 °C.....	86

Fig. 73: Number distribution of HPX gel particle size, prepared at 25 °C and 80 °C.....	88
Fig. 74: Volume distribution of HPX gel particle size, prepared at 25 °C and 80 °C.....	88
Fig. 75: HP particle size variation	90
Fig. 76: HPX particle size variation	91
Fig. 77: Refractive index in dependency of the mass concentration in water-ethanol mixtures.	93
Fig. 78: Equilibrium solubility of 20% (w/w) inulin in water-ethanol mixtures.	94
Fig. 79: XRD during gelation of an HP gel, prepared at 25 °C, 600 rpm shear rate and 5% Ethanol.	96
Fig. 80: XRD during gelation of an HPX gel, prepared at 25 °C, 600 rpm shear rate and 5% Ethanol.	96
Fig. 81: Development of the relative intensity of HP gels prepared at 25 °C, with 0% - 15% ethanol.	97
Fig. 82: Development of the relative intensity of HPX gels prepared at 25 °C, with 0% - 15% ethanol.	99
Fig. 83: Development of the relative intensity of HPT25E/HPXT25E gels, plotted on logarithmic scale.....	99
Fig. 84: DP distribution of dissolved HP after 10 min stirring at 25 °C, with ethanol content of 0% - 30%.	102
Fig. 85: DP distribution of dissolved HPX after 10 min stirring at 25 °C, with ethanol content of 0% - 30%.	102
Fig. 86: Polarity dependent DP distribution of dissolved HP after 24 h storage.	104
Fig. 87: Polarity dependent DP distribution of dissolved HPX after 24 h storage.	104
Fig. 88: Hardness of inulin gels prepared with different ethanol contents in the solvent	106
Fig. 89: Comparison of gel structure of HP and HPX gels, both prepared at 25 °C with different ethanol contents in the solvent. Each picture was taken in a depth of 10 µm.	106
Fig. 90: Amplitude sweep curves of HP gels, prepared at 25 °C, with ethanol contents of 0%, 5%, 10% and 15% in the solvent. The device setup is indicated in the figure.	108
Fig. 91: Amplitude sweep curves of HPX gels, prepared at 25 °C, with an ethanol content of 0%, 5%, 10% and 15% in the solvent. The device setup is indicated in the figure.	110
Fig. 92: Comparison amplitude sweeps of HPT25E and HPXT25E gels. Point of shear breakdown is indicated for each sample.....	111

Fig. 93: Gel primary particle size (number average) in dependency of ethanol content in the solvent.	112
Fig. 94: Number distribution of HP gel particle size, prepared at 25 °C with 0% and 15% ethanol in the solvent.....	113
Fig. 95: Number distribution of HPX gel particle size, prepared at 25 °C with 0% and 15% ethanol in the solvent.	114
Fig. 96: Volume distribution of HPX gel particle size, prepared at 25 °C with 0% and 15% ethanol in the solvent.	115
Fig. 97: HPT25E particle size variation	117
Fig. 98: HPXT25E particle size variation	118
Fig. 99: Refractive index in dependency of the mass concentration in water-sucrose mixtures.	120
Fig. 100: Equilibrium solubility of 20% (w/w) inulin in water-sucrose mixtures.	121
Fig. 101: XRD during gelation of an HP gel, prepared at 25 °C, 600 rpm shear rate and 5% sucrose.	122
Fig. 102: XRD during gelation of an HPX gel, prepared at 25 °C, 600 rpm shear rate and 5% sucrose.	123
Fig. 103: Development of the relative intensity of HP gels prepared at 25 °C, with 0% - 15% sucrose.	123
Fig. 104: Development of the relative intensity of HPX gels prepared at 25 °C, with 0% - 15% ethanol.	125
Fig. 105: Development of the relative intensity of HPT25Suc/HPXT25Suc gels, plotted on logarithmic scale.....	126
Fig. 106: DP distribution of dissolved HP after 10 min stirring at 25 °C, with sucrose content of 0% - 15%.	128
Fig. 107: DP distribution of dissolved HPX after 10 min stirring at 25 °C, with sucrose content of 0% - 15%.	129
Fig. 108: Saturation dependent DP distribution of dissolved HP after 24 h storage.	131
Fig. 109: Saturation dependent DP distribution of dissolved HPX after 24 h storage.	131
Fig. 110: Hardness of inulin gels prepared with different sucrose contents in the solvent ..	133
Fig. 111: Comparison of gel structure of HP and HPX gels, both prepared at 25 °C with different sucrose contents in the solvent. Each picture was taken in a depth of 10 µm.	133

Fig. 112: Amplitude sweep curves of HP gels, prepared at 25 °C, with sucrose contents of 0%, 5%, 10% and 15% in the solvent. The device setup is indicated in the figure.	135
Fig. 113: Amplitude sweep curves of HPX gels, prepared at 25 °C, with sucrose contents of 0%, 5%, 10% and 15% in the solvent. The device setup is indicated in the figure.	137
Fig. 114: Comparison amplitude sweeps of HPT25Suc and HPXT25Suc gels. Point of shear breakdown is indicated for each sample.	138
Fig. 115: Gel primary particle size (number average) in dependency of sucrose content in the solvent.	139
Fig. 116: Number distribution of HP gel particle size, prepared at 25 °C with 0% and 15% sucrose in the solvent.	140
Fig. 117: Volume distribution of HP gel particle size, prepared at 25 °C with 0% and 15% sucrose in the solvent.	140
Fig. 118: Number distribution of HPX gel particle size, prepared at 25 °C with 0% and 15% sucrose in the solvent.	143
Fig. 119: Volume distribution of HPX gel particle size, prepared at 25 °C with 0% and 15% sucrose in the solvent.	143
Fig. 120: HPT25Suc particle size variation.....	145
Fig. 121: HPXT25Suc particle size variation.....	147
Fig. 122: Comparison of the solubility of 20% (w/w) HP in different solvents	149
Fig. 123: Comparison of the solubility of 20% (w/w) HPX in different solvents	152
Fig. 124: DP distribution of dissolved HP after 10 min stirring at 25 °C, with ethanol/sucrose content of 0% - 10%.	155
Fig. 125: DP distribution of dissolved HPX after 10 min stirring at 25 °C, with ethanol/sucrose content of 0% - 10%.	155
Fig. 126: Polarity/saturation dependent DP distribution of dissolved HP after 24 h storage.	157
Fig. 127: Polarity/saturation dependent DP distribution of dissolved HPX after 24 h storage.	157
Fig. 128: Hardness of HP gels prepared with different solvents.....	158
Fig. 129: Hardness of HPX gels prepared with different solvents.....	160
Fig. 130: Hardness of HP gels, prepared at 25 °C with 0% - 10% of ethanol and sucrose in the solvent.	161

Fig. 131: Hardness of HPX gels, prepared at 25 °C with 0% - 10% of ethanol and sucrose in the solvent.	161
Fig. 132: XRD during gelation of an HP gel, prepared at 40 °C and 600 rpm shear rate.	171
Fig. 133: XRD during gelation of an HP gel, prepared at 60 °C and 600 rpm shear rate.	171
Fig. 134: XRD during gelation of an HPX gel, prepared at 40 °C and 600 rpm shear rate.	172
Fig. 135: XRD during gelation of an HPX gel, prepared at 60 °C and 600 rpm shear rate.	172
Fig. 136: XRD during gelation of an HPX gel, prepared at 60 °C and 600 rpm shear rate.	173
Fig. 137: XRD during gelation of an HP gel, prepared at 25 °C, with 10% (w/w) of ethanol in the solvent and 600 rpm shear rate.	173
Fig. 138: XRD during gelation of an HP gel, prepared at 25 °C, with 15% (w/w) of ethanol in the solvent and 600 rpm shear rate.	174
Fig. 139: XRD during gelation of an HPX gel, prepared at 25 °C, with 10% (w/w) of ethanol in the solvent and 600 rpm shear rate.	174
Fig. 140: XRD during gelation of an HPX gel, prepared at 25 °C, with 15% (w/w) of ethanol in the solvent and 600 rpm shear rate.	175
Fig. 141: XRD during gelation of an HP gel, prepared at 25 °C, with 10% (w/w) of sucrose in the solvent and 600 rpm shear rate.	175
Fig. 142: XRD during gelation of an HP gel, prepared at 25 °C, with 15% (w/w) of sucrose in the solvent and 600 rpm shear rate.	176
Fig. 143: XRD during gelation of an HPX gel, prepared at 25 °C, with 10% (w/w) of sucrose in the solvent and 600 rpm shear rate.	176
Fig. 144: XRD during gelation of an HPX gel, prepared at 25 °C, with 15% (w/w) of sucrose in the solvent and 600 rpm shear rate.	177
Fig. 145: HP separated according to DP, used as reference for the HPAEC measurements with ethanol-water mixtures acting as solvent.	177
Fig. 146: HPX separated according to DP, used as reference for the HPAEC measurements with ethanol-water mixtures acting as solvent.	178
Fig. 147: HP separated according to DP, used as reference for the HPAEC measurements with sucrose-water mixtures acting as solvent.	178
Fig. 148: HPX separated according to DP, used as reference for the HPAEC measurements with sucrose-water mixtures acting as solvent.	179

List of tables

Tab. 1: Symmetry elements.	6
Tab. 2: Values for the Avrami exponent m for different types of nucleation and growth [16].	12
Tab. 3: Average crystallization constant of HP samples.....	71
Tab. 4: Average crystallization constant of HPX samples	71
Tab. 5: HP/HPX dissolved dependent on ethanol content in solvent	98
Tab. 6: Average crystallization constant of HPT25E samples.....	100
Tab. 7: Average crystallization constant of HPXT25E samples	100
Tab. 8: HP/HPX dissolved dependent on sucrose content in solvent	124
Tab. 9: Average crystallization constant of HPT25Suc samples	126
Tab. 10: Average crystallization constant of HPXT25Suc samples.....	127

List of abbreviations

p.a. per analysis

a.u. arbitrary units

DP degree of polymerization

w/w mass ratio

HPAEC High Performance Anion Exchange Chromatography

CLSM Confocal Laser Scanning Microscopy

MSZW Metastable Zone Width

TPA Texture Profile Analysis

LVE Linear Viscoelastic Region

SAOS Small Amplitude Oscillatory Shear

LAOS Large Amplitude Oscillatory Shear

PSF Intensity Point Spread Function

List of variables

V	Volume of spherical particle [μm^3]
S	Surface of spherical particle [μm^2]
G_M	Gibbs free energy of mixture [J]
$G_{Solvent}$	Gibbs free energy of solvent [J]
G_{Solute}	Gibbs free energy of solute [J]
ΔG_M	Differential Gibbs free energy of mixture [J]
H_M	Enthalpy of mixture [J]
ΔH_M	Differential Enthalpy of mixture [J]
S_M	Entropy of mixture [J/K]
ΔS_M	Differential Entropy of mixture [J/K]
n_1, n_2	Number of moles of solvent and solute [mol]
ϕ_1, ϕ_2	Volume fraction of solvent and solute [%]
n	Degree of polymerization of solute
χ	Flory-Huggins interaction parameter
T_F	Freezing temperature at atmospheric pressure $p_{atm} = 1013 \text{ mbar}$ [$^{\circ}C$]
$a, b, c; \alpha, \beta, \gamma$	lattice parameters of point lattice
(hkl)	Miller indices
c	actual mass concentration [g/L]
c^*	mass concentration at saturation [g/L]
Δc	concentration difference between actual & saturated concentration [g/L]
S	supersaturation of solution
r	radius of nucleus/aggregate [μm]

r_c	critical radius of nucleus/aggregate [μm]
σ	solid-liquid interface tension [N/m]
V_m	molar volume of solute molecule [L/mol]
R	ideal gas constant 8,314 J/Kmol
T	temperature of solution/sample [$^{\circ}C$]
ΔG	differential Gibbs free energy [J]
ΔG_S	differential surface Gibbs free energy [J]
ΔG_V	differential volume Gibbs free energy [J]
$\Delta G_{crit.}$	differential critical Gibbs free energy [J]
$I(t)$	diffracted intensity at sample age t [$a. u.$]
I_{max}	diffracted intensity after 24 h [$a. u.$]
D_f	Fractal dimension
N	Number of “copies” of a fractal object
f	fractal scaling factor
n_r	refractive index
n_1, n_2	refractive index in medium 1/2
n_D^{20}	refractive index, measured at 20 $^{\circ}C$ with monochromatic light (sodium D – line, $\lambda = 589$ nm)
t	time interval [s]
c	speed of light in vacuum [m/s]
c_m	speed of light in medium [m/s]
ν	frequency of electromagnetic radiation [s^{-1}]
θ_1	incident angle of electromagnetic radiation [$^{\circ}$]
θ_2	refracted/diffracted angle of electromagnetic radiation [$^{\circ}$]

θ_r	reflected angle of electromagnetic radiation [°]
θ_c	critical angle of total reflection [°]
$Cu - K_\alpha$	characteristic X-ray radiation of an excited copper atom
2θ	experimental diffraction angle [°]
λ	wavelength of electromagnetic radiation [nm]
E	photon energy [J]
h	Planck's constant $6,626 \cdot 10^{-34} Js$
n	order of diffraction
d	interplanar spacing [nm]
δ	path difference between two x-ray beams [°]
K	distribution coefficient
$[X^-]_{s,m}$	concentration of sample anion in stationary/mobile phase [mol/L]
$[HCO_3^-]_{s,m}$	concentration of hydrogen carbonate anion in stationary/mobile phase [mol/L]
D	equilibrium distribution coefficient
t_R	total retention time [min]
t_0	dead time [min]
t'_R	adjusted retention time [min]
k'	capacity factor
R	resolution of chromatogram
w	peak width [cm]
$w_{1/2}$	peak width at half peak height [cm]
N	number of theoretical plates
h	peak height [cm]

$h_{1/2}$	half peak height [cm]
A	peak area [cm^2]
C	time constant of clay [$1/s$]
B	time period between begin of first chew until start of second chew
F	force [N]
d	diameter of plunger [cm]
A	area of plunger [cm^2]
$\lambda_{ex}, \lambda_{em}$	excitation/emission wavelength [nm]
$N.A.$	numerical aperture
α	half objective opening angle [$^\circ$]
d	distance between two resolvable points (resolution) [μm]
σ	shear stress [Pa]
σ_0	initial shear stress [Pa]
η	viscosity [$Pa \cdot s$]
$\dot{\gamma}$	shear rate [$1/s$]
G	shear modulus [Pa]
G^*	complex shear modulus [Pa]
G'	storage modulus [Pa]
G''	loss modulus [Pa]
γ	shear deformation/oscillation amplitude/strain [%]
γ_0	initial strain [%]
γ_c	critical strain [%]
A	area of upper plate [cm^2]
F	shear force [N]

v	speed of upper plate [m/s]
s	distance upper plate is moved by shear force [mm]
h	distance between upper and lower plate (gap size) [mm]
φ	tilt angle of sheared surface [$^\circ$]
ω	angular frequency [s^{-1}]
δ	phase shift angle [$^\circ$]
$\tan \delta$	dissipation factor
M	torque [Nm]
r	distance from center of plate [cm]
R_p	radius of plate [cm]
G'_∞	storage modulus at infinite deformation [Pa]
K	constant in Kraus equation, depending on system properties
a	deformation amplitude (equals oscillation amplitude γ) [%]
m	exponent in Kraus equation, containing fractal dimension D_f
q_x	normalized frequency distribution
Q_x	cumulative distribution
$D[1,0]$	arithmetic (number weighted) mean diameter [nm]
$D[4,3]$	volume weighted mean diameter [nm]
n_i	number of particles in size class i with mean diameter D_i
$I_{vertical}$	scattered intensity of vertical polarized light [$a. u.$]
$I_{horizontal}$	scattered intensity of horizontal polarized light [$a. u.$]

1 Introduction

Inulin is a well-known, polydisperse oligosaccharide which can be easily extracted from several economically important plants, such as chicory, onion, garlic and wheat by a production process, that is very similar to the production process of sucrose [1]. Chemically inulin belongs to the family of the fructans, built up of 2 - 90 β -(2,1) linked fructose units and, most often, a terminal glucose molecule [2]. The molecular structure of inulin is pictured in Fig. 1.

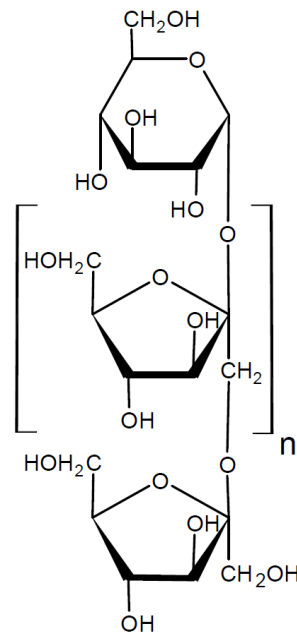


Fig. 1: Molecular structure of inulin molecule, the n at the brackets adopts at maximum 90.

Due to its many hydroxyl groups, inulin exhibits a polar character and dissolves well in polar solvents (e.g. water) and just marginally in less polar solvents (e.g. ethanol). The glycosidic bond, linking each monosaccharide to each other, is very stable, making the inulin molecule comparatively resistant against basic and acidic hydrolysis in aqueous solutions [1]. The inulin molecule's average degree of polymerization (DP) is dependent on the source it is extracted from. By ion exchange processes, the polydisperse inulin can be separated into short (average DP < 10), medium (average DP > 10) and long chain (average DP > 23) fractions (in this work the focus is placed on the long chain fractions, namely HP and HPX). Nutritionally, inulin is a dietary fiber and exhibits low calorie content, prebiotic properties and is suitable for diabetic nutrition [1, 3, 4]. Inulin/water suspensions can form particle gels with a fat like structure [5, 6]. Depending on the inulin molecule's degree of polymerization, nowadays inulin is commercially used as sugar replacement (low DP), texturizer (medium DP) and as fat replacer (high

DP) [4, 7-9]. These days consumers are becoming more and more health-conscious and emphasize a healthy nutrition [10-12]. Therefore, taking the above mentioned properties of inulin into account, inulin gels manifest as potential fat replacer in fat containing food. Regarding the summarized information, this work is focused on the basic physical properties and the development of a consistent model, explaining the gel formation of the two types of high DP inulin (HP and HPX) and providing a better understanding for its potential as fat replacer in fat containing food. Additionally the gel formation in different solvents (demineralized water, ethanol-water mixtures, sucrose-water mixtures and ethanol-sucrose water mixtures) is examined and correlated to each other.

Therefore, in section 1 the theoretical background, necessary to understand the properties of the inulin particle gels, and the analytical methods that have been used to examine the gels, are briefly summarized. In section 2, the sample preparation for each analytical method is outlined. Section 3 deals with the interpretation of the analytical results of each inulin-solvent system. The discussed results are concluded in section 4 and a brief outlook is given in section 5.

1.1 The particle gel model

In this section, the formation of an inulin particle gel is introduced. The model consist of an adaption of previous publications [13] and our personal findings.

When a certain amount of polydisperse (broad chain length distribution) long chain (average DP = 23) inulin is added to water, the dissolved amount depends on the temperature of the solvent and the chain lengths of the inulin molecules (Fig. 2). Naturally short, low molecular weight chains dissolve faster and at lower temperatures, compared to long, high molecular weight chains (this is due to the change in the Gibbs free energy of a solute/solvent mixture ΔG_M , which decreases with decreasing DP of the solute, see section 1.5). The dissolved polydisperse oligosaccharides can be approximately visualized by (semi flexible) rods of different lengths [14]. Upon cooling, the dissolved inulin molecules recrystallize selectively, driven by chain length and temperature. In addition, to start the crystallization process, crystallization nuclei are necessary. In the present case, undissolved material acts as “seeds” which enable a relative fast recrystallization process. On the contrary, if the complete amount of inulin is dissolved, e.g. at sufficiently high temperatures, a particle gel as proposed in Fig. 2 will not be formed during cooling [15]. The molecules with a larger DP recrystallize first, forming nuclei

Introduction

(due to the lower solubility in water and thermodynamic fluctuations), and the molecules with a smaller DP accumulate on the outer regions of the developing crystallites. When the crystallization process continues, the inulin crystallites form aggregates (acting as primary particles in the particle gel network). Those are characterized by very strong interactions due to their crystallization energy, when different crystallites interact via their crystalline surfaces. However, these processes happen at random places throughout the entire sample. When the gel formation continues, the primary particles form clusters of random, irregular, perhaps fractal nature, which are mainly attracted to each other by van der Waals forces [15]. Moreover, when these random clusters meet at larger scales, a particle network is formed, which defines most of the structural and mechanical properties of the macroscopic sample. The water is trapped in the meshes and interspaces of the particle gel [13]. For varying types of inulin, differing in their average DP, the particle gel network also varies in packing density and gel particle size. Those variations have a significant impact on the physical properties of the completely developed inulin gels, illustrating once more the varying texture of inulin gels prepared with different types of inulin. At the current state, it needs to be stressed, that this model is not proven in all details.

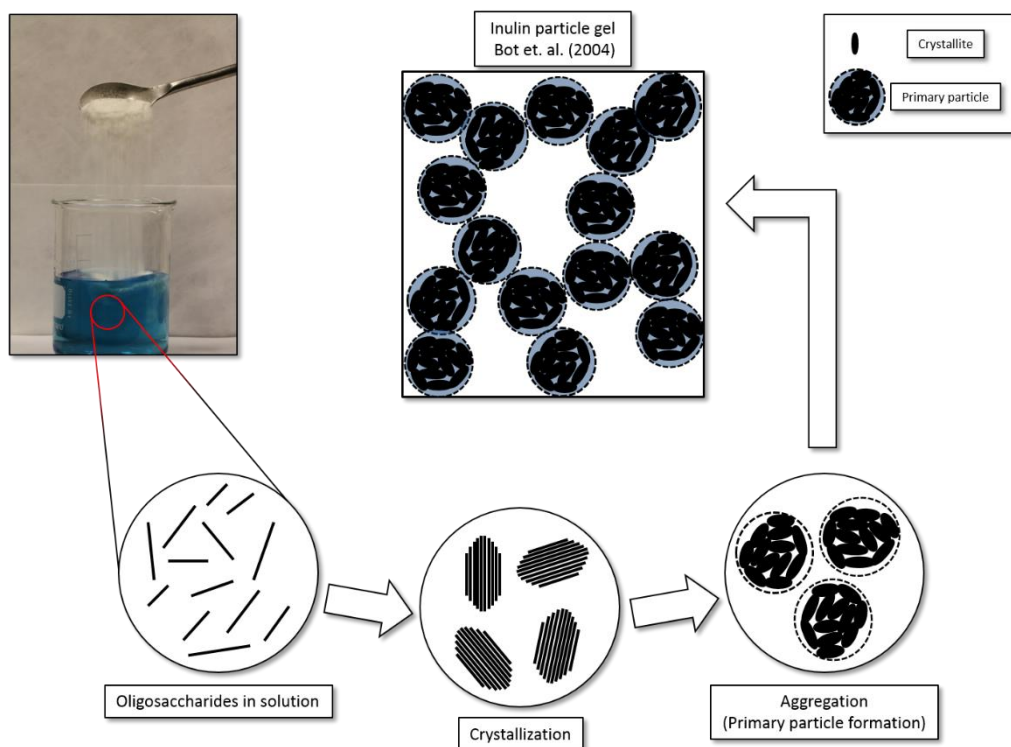


Fig. 2: Inulin particle gel model.

Introduction

1.2 Crystals

As mentioned above, the primary particles of the inulin particle gels consist of inulin crystallites. Therefore, in this section the basic knowledge about crystals is presented. The information in this section was mostly taken from [16, 17].

Crystals are solids, in which atoms/ions are arranged in three dimensional, repeating periodic structure. In a purely geometrical sense, crystals can be represented by a “point lattice” (i.e. the points represent the atoms/molecules of the crystal). A point lattice is arranged in a way, that each point has identical surroundings with three spatial dimensions (a, b and c) and three angles (α, β and γ), which are spanned by the respective axes. An example of a point lattice is pictured in Fig. 3b.

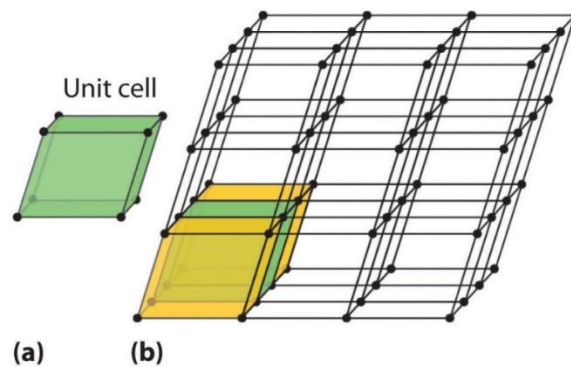


Fig. 3: Unit cell a) and point lattice b) [18].

The lattice in Fig. 3b is made up of repeating units. Those units can be characterized by the three dimensions a, b and c and the three angles α, β and γ . Choosing one of those units and making use of the spatial dimensions and angles, the lattice can be reproduced indefinitely. The mentioned lengths and angles are called “lattice parameters” and a single cell, constructed with those parameters is called a “unit cell” (see Fig. 4).

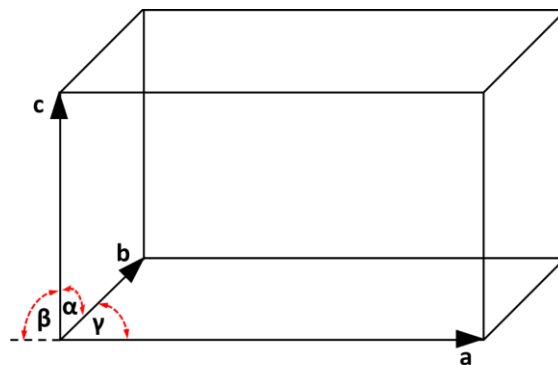


Fig. 4: Unit cell with lattice parameters [17].

Introduction

Altogether, fourteen different point lattices can be constructed (the “Bravais lattices”), which can be separated in seven categories (the seven crystal systems).

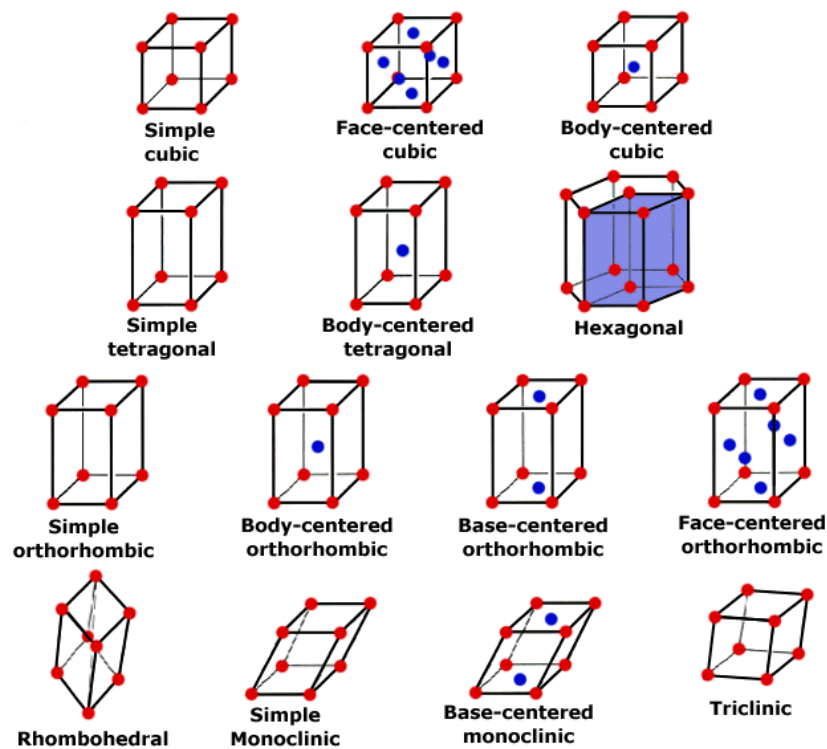


Fig. 5: Bravais lattices [19].

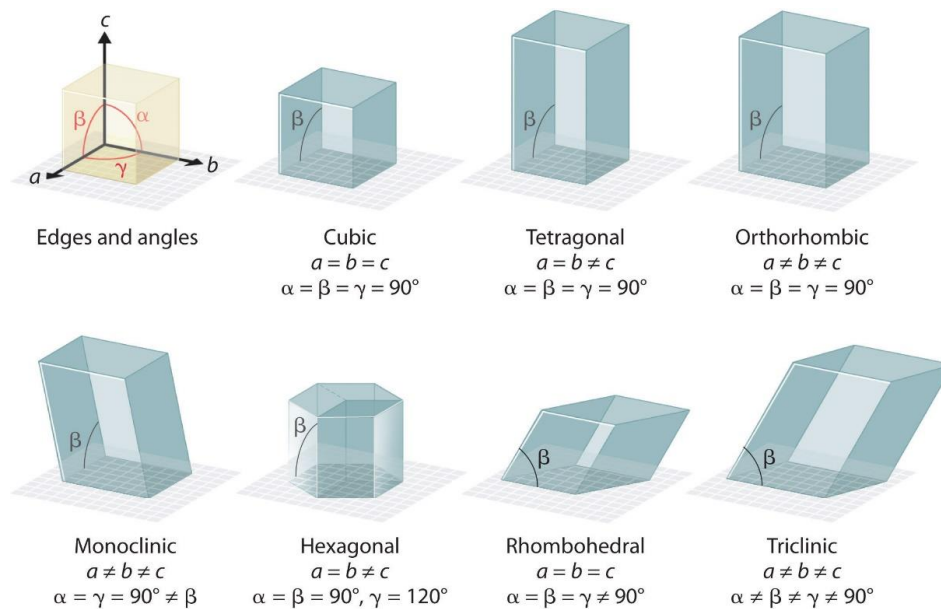


Fig. 6: Crystal systems with lattice parameters [20].

All crystal systems in Fig. 6 are explicitly defined by the lattice parameters. Additionally, each crystal system can also be defined by its symmetry, with four possible types of symmetry operations: reflection, rotation, inversion and rotation-inversion. If a lattice exhibits one of those

Introduction

types of symmetry, the lattice is superimposed on itself after the execution of the respective symmetry operation. Therefore, each lattice system can be defined by the minimum of symmetry elements, that must be present in a given crystal (a system can have more than the minimum symmetry elements, but never less (see Tab. 1)).

Tab. 1: Symmetry elements.

Crystal system	Minimum rotational symmetry
Cubic	4 threefold rotation axes
Tetragonal	1 fourfold rotation axis
Orthorhombic	3 twofold rotation axes
Rhombohedral	3 perpendicular twofold rotation axes
Hexagonal	1 sixfold rotation axis
Monoclinic	1 twofold rotation axis
Triclinic	None

If any point on the lattice is chosen and considered as origin, all vectors from the origin can be defined in terms of three coordinates. If a “cubic cell” is chosen as example, a vector going from the origin to the intersecting point with the coordinates (1,1,1), will be represented by a line going along the body diagonal in positive direction. This line will also intersect the point with the coordinates (2,2,2) and all multiples. The direction of the line can be represented in shorthand by square brackets e.g. $[1,1,1]$ (the numbers are called the “indices” of the direction). A negative number is indicated by a bar over the number e.g. $[\bar{1}, 1, 1]$. A family of directions is represented by angle brackets e.g. $\langle 1,1,1 \rangle$. The family includes all the directions using those indices, including positive and negative indices in all possible combinations. By convention, all indices are reduced to the smallest set of integers possible, either by division or by clearing fractions. In Fig. 7, a unit cell with several directions indicated, can be seen.

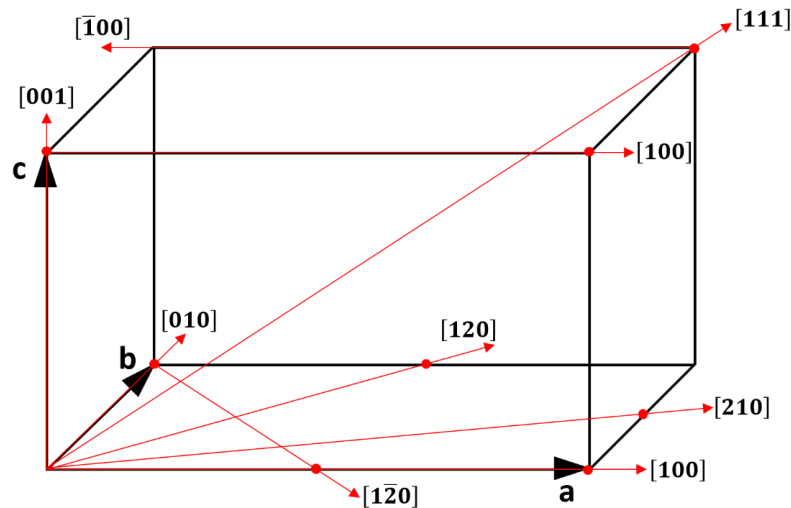


Fig. 7: Indices of directions [17].

Planes in the lattice are indicated by the “Miller indices”. In this convention, each plane is described by three parameters (hkl), which are defined as the reciprocals of the intercepts of the plane with the three crystal axes (a plane parallel to the given axis will be indicated by the index 0). Negative indices are again written with bars over the numbers. Additionally, the Miller indices refer not only to one plane, but to a whole set of planes, which are parallel to the plane specified. If all equivalent planes are specified, the indices are written in curly brackets e.g. $\{100\}$ represents all cube faces. Examples of Miller indices and the respective planes are given in Fig. 8.

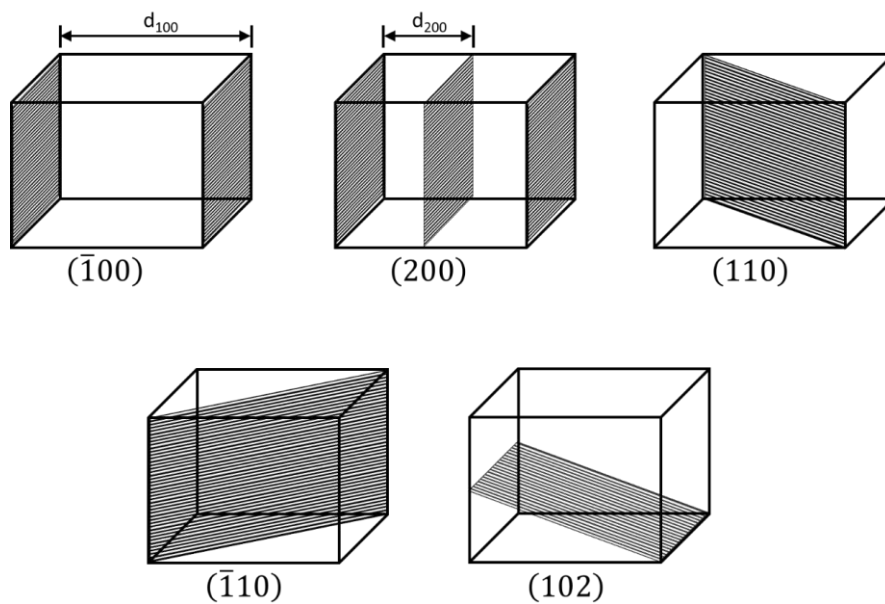


Fig. 8: Miller indices of planes in the cubic system. The distance d is the interplanar spacing [17].

1.3 Classical nucleation theory and isothermal crystallization

In this section, the basics necessary to understand the process of isothermal crystallization, are summarized. The information in this section was again mostly taken from [16, 17, 21].

Isothermal crystallization is a rate process. Thus, the time required for the crystallization, depends on a driving force. The driving force for the crystallization is the “supersaturation”. In a supersaturated solution, the solute concentration exceeds the equilibrium (or saturation) solute concentration at a given temperature. Therefore, supersaturated solutions are metastable. Supersaturation is often expressed as concentration difference between saturated (c^*) and supersaturated (c) solution and as ratio of those two different concentrations (see Eq.(1) and Eq.(2)).

$$\Delta c = c - c^* \quad (1)$$

$$S = \frac{c}{c^*} \quad (2)$$

In Eq.(2), S is the supersaturation. Supersaturated solutions can be prepared by benefiting from the temperature dependence of the solubility. For most substances, the solubility in a solvent increases with the temperature of the solvent. If a solution is saturated at a certain temperature and this solution is cooled down, with a cooling rate faster than the crystallization rate of the solute, the solution will become supersaturated until the solute crystallizes to the saturation point at the respective temperature. Depending on the system (solute, solvent, temperature, seeding nuclei etc.), the crystallization of the excessively dissolved solute occurs in different time spans. Therefore, supersaturating a solution to some amount, does not necessarily result in an immediate crystallization. A solution becomes more unstable with increasing supersaturation, resulting in faster crystallization. Every solution can just be supersaturated to a maximum amount, before becoming unstable. In Fig. 9, a solubility curve and its metastable limit are pictured.

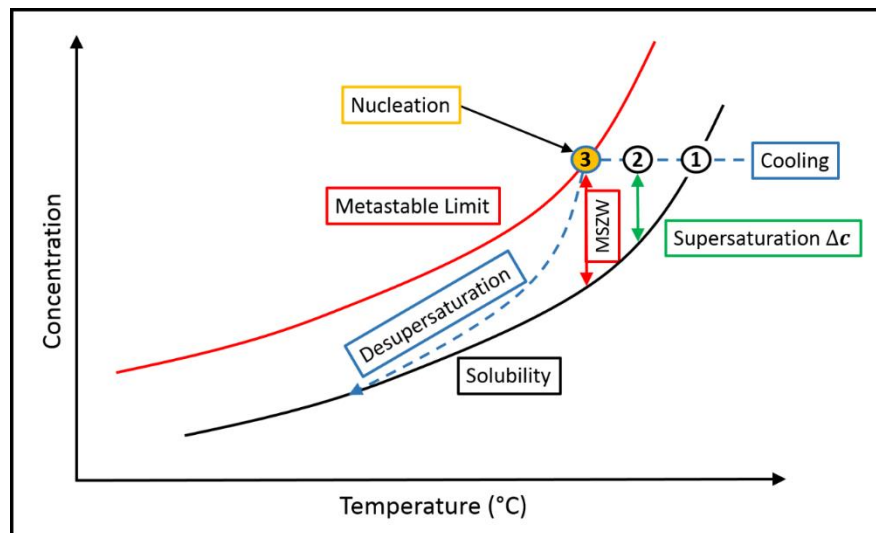


Fig. 9: Solubility and metastable zone width (MSZW) [22].

If a saturated solution (point 1 in Fig. 9) is cooled to a certain temperature, with a cooling rate faster than the respective crystallization rate, the solution becomes supersaturated (point 2 Fig. 9). At those conditions, the supersaturated solution is still in a metastable state. If the temperature is further decreased, eventually the metastable limit is reached, the supersaturated solution becomes unstable and immediate crystallization occurs (point 3 Fig. 9). If the temperature is further decreased, the solute crystallizes, following the desupersaturation curve, until equilibrium at the solubility curve is reached again. The degree of supersaturation at a given temperature, can be estimated by the concentration difference between the solubility curve and the actual concentration (see Fig. 9 Δc). The metastable zone width (MSZW) is defined as the concentration difference at a given temperature between the saturated solution and the metastable limit.

The metastability of supersaturated solutions can be explained with the “classical nucleation theory”. Nucleation is the start of the crystallization process and involves the birth of a new crystal. If the solubility of a solute in a solvent at a given temperature is exceeded, the solute molecules start to associate and form aggregates. This process is called primary nucleation. When the crystallization process continues, the already formed crystals grow by the crystallization of solute molecules on the surface of the crystallites. Since the still dissolved solute molecules are induced to crystallize by the already present crystallites (they act as seeding nuclei), this process is called secondary nucleation and involves the growth of crystals. Homogeneous nucleation (i.e. just one type of nucleation occurs) exists very rarely in practice. Therefore, most crystallization processes are a combination of primary nucleation and crystal

Introduction

growth. Before the formed crystallites can grow further, they need to exhibit a critical size r_c . Below this size the crystallites are unstable and dissolve again. The critical size of those crystallites can be determined by the “classical nucleation theory”. If the crystallites (or solute aggregates) are spherical, the Gibbs free energy change ΔG , required to form an aggregate of a given size, can be expressed by Eq.(3).

$$\Delta G = 4\pi r^2 \sigma - \left(\frac{4\pi r^3}{3V_m} \right) RT \ln(1 + S) \quad (3)$$

In Eq.(3), r is the radius of the solute aggregate, σ is the solid-liquid interface tension, V_m is the molar volume of a solute molecule, R is the ideal gas constant, T the temperature of the solution and S the supersaturation (see Eq.(2)). The left term of Eq.(3) represents the free energy change for the surface formation of the aggregates ΔG_s and the term on the right hand side describes the change of the Gibbs free energy for the volume increase of the aggregates ΔG_v . The free energy changes and their sum are shown qualitatively for a spherical nucleus in Fig. 10.

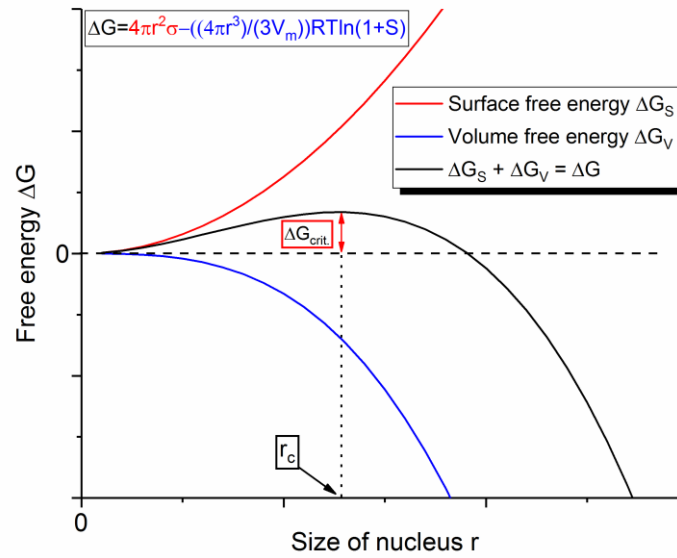


Fig. 10: Free energy vs. nucleus size [17].

For small aggregates (size below r_c see Fig. 10), the total Gibbs free energy change is positive and the unstable aggregates dissolve. If the aggregate size increases, eventually a critical aggregate size r_c is reached, above which the Gibbs free energy change decreases again, the aggregates stabilize and grow spontaneously (nucleation occurs, size above r_c in Fig. 10). The

critical size of the aggregates can be determined by setting the derivation of Eq.(3) $d\Delta G/dr = 0$ (this derivation yields $\Delta G_{crit.}$ in Fig. 10) and solving the equation for r_c .

$$r_c = \frac{2V_m\sigma}{RT\ln(1+S)} \quad (4)$$

If the supersaturation S in Eq.(4) increases, the critical size r_c of the aggregates decreases. Therefore, solutions become less stable with increasing supersaturation.

If the above mentioned critical nucleus size is exceeded or the solution still contains seeding nuclei, the Johnson – Mehl – Avrami – Kolmogorov model (JMAK) can be used to quantify the isothermal crystallization kinetics and to provide an indication of the nature of the crystal growth process. Applied to the study of inulin suspensions/gels by x-ray diffraction (see section 1.7), the Avrami equation has the following form.

$$\frac{I(t)}{I_{max}} = 1 - e^{-(k(t-t_0))^m} \quad (5)$$

$I(t)$ is the diffracted intensity at the sample age t , I_{max} is the diffracted intensity after 24 h ageing, k the crystallization constant, t the age of the sample, t_0 the begin of the phase transition and m is the geometry factor. The JMAK model describes the kinetics of liquid-solid phase transitions. It takes into account, that the crystallization occurs by primary nucleation and crystal growth (secondary nucleation). The model is based on the assumptions of isothermal transformation conditions, spatially random nucleation and linear growth kinetics, in which growth rate of the new phase depends only on the temperature and not on the time. It is also assumed, that the density of the growing bodies/particles is constant. The Avrami parameters k and m provide information of the nature of the crystallization process. The constant k is a crystallization rate constant. It is primarily a function of the crystallization temperature (it generally obeys an Arrhenius-type temperature dependency) and takes both, nucleation and crystal growth into account. In the case of the polydisperse inulin, k also depends on the degree of polymerization (DP) of the crystallizing inulin molecules. The Avrami exponent (or geometry factor) m indicates the crystal growth mechanism. This parameter is a combined function of the time dependence of nucleation and the number of dimensions, in which crystal growth takes place. Nucleation is either instantaneous, with nuclei appearing all at once at early stages in the process, or sporadic, with the number of nuclei increasing linearly

with time. Crystal growth either occurs as rods, disks or spheres in one, two or three dimensions, respectively. Tab. 2 shows values for m , expected for various types of nucleation and growth. The first number of the sum in the left hand column defines the geometry of the crystals and the second number of the sum indicates the type of nucleation.

Tab. 2: Values for the Avrami exponent m for different types of nucleation and growth [16].

m	Type of crystal growth and nucleation expected
$3 + 1 = 4$	Spherical growth from sporadic nuclei
$3 + 0 = 3$	Spherical growth from instantaneous nuclei
$2 + 1 = 3$	Plate-like growth from sporadic nuclei
$2 + 0 = 2$	Plate-like growth from instantaneous nuclei
$1 + 1 = 2$	Rod/needle/fiber-like growth from sporadic nuclei
$1 + 0 = 1$	Rod/needle/fiber-like growth from instantaneous nuclei

Although m should be an integer number, fractional values are usually obtained. This arises from the simultaneous development of two (or more) types of crystals, or similar types of crystals from different types of nuclei (sporadic vs. instantaneous). Deviations from integer values may also occur in cases, where spherical crystals arise from initially rod- or plate-like nuclei. Due to the different types of crystal geometries and/or the different types of nucleation combined, in those situations m is continually changing. This non-integer values for m also occur for the crystallization of inulin gels and can arise from the above mentioned processes (see also section 1.1). Therefore, in this work the focus of the examination of the crystallization kinetics was set on the determination of the constant k .

1.4 Particle gels as fractal clusters [23]

In this subsection the fractal nature of the networks is suggested, analogously to fat crystal networks, which are supposed to exhibit a fractal structure [24]. The nature of the crystallization process in fats and inulin have definitely many similarities, despite fats are composed of triacylglycerols. Nevertheless, the crystallization of fats is also selective, due to varying chain lengths and their saturation degree, which determines the polymorphs and crystallization defects inside the primary particles. The large scale properties look quite similar [25]. The fractal

Introduction

dimension D_f of the fat crystal network gives information about its structure and can be determined by various methods such as light microscopy (Fractal Box counting) and the determination of the solid and the liquid fraction of fats [24, 26, 27]

In this section another method is introduced, using rheological measurements of amplitude sweeps and their interpretation using a Kraus type model [24, 28, 29], where the breakdown of the structure can be related to the applied shear amplitude. This approach turns out to be more effective for (fractal) inulin particle gels.

To understand those ideas on a more quantitative basis, the basic notations, used in the following sections of this work, are summarized. The information in this section was mostly taken from references [24], [30], and [31].

The essential property of a fractal object is its “scale invariance”, meaning it is “self-similar”. Therefore, if an ideal fractal structure is subdivided into smaller structures, each subset will contain scaled down versions of the whole object. Many natural objects, such as trees, coastlines or the vascular system, exhibit fractal properties. To describe those fractal objects in a mathematical way, the Euclidian or Newtonian dimensionality, which is clearly defined in three dimensions, is not sufficient any more. Since fractal objects exhibit an irregular structure, they cannot be described by an integer, but rather a fractal dimension D_f . If an object can be subdivided into N copies of itself with scaling factor f , then its fractal dimension D_f can be determined by Eq.(6).

$$D_f = \frac{\log(N)}{\log(1/f)} \quad (6)$$

Eq.(6) applies very well for objects, which contain exact subcopies of themselves (ideal fractals). The fractal dimension of particle gels cannot be determined that easy. As already mentioned in section 1.1, the inulin particle gels consist of inulin primary particles, which aggregate under quiescent conditions. The aggregation of spherical particles at rest leads to clusters with a fractal structure [30]. The inulin particle gels consist of colloidal clusters with an average random fractal structure on certain length scales and exhibit no exact self-similarity, as known from “mathematical” fractals [32].

Nevertheless the irregular, fractal network structure is responsible for the viscoelastic response of the inulin gels [33], which can be measured by oscillation rheology. Above a certain

shear amplitude, the inulin gels show a strong and well defined shear thinning behavior [33]. This behavior suggests the comparison of the inulin particle network to a filler particle network consisting of carbon black particles, as often used in rubber compounds [29]. The rheological behavior under deformation of those network types is described by the “Payne effect”, which can be quantified by applying the “Kraus model” on amplitude sweep curves, obtained by rheological measurements [28]. The respective Equation can be seen in Eq.(7).

$$\frac{G' - G'_{\infty}}{G'_0 - G'_{\infty}} = \frac{1}{1 + K^2 a^{2m}} \quad (7)$$

In Eq.(7) G' is the storage modulus, G'_{∞} is the storage modulus at infinite deformation a , G'_0 is the storage modulus without deformation, K is a constant depending on the system properties and a the respective deformation amplitude. The exponent m contains the fractal dimension D_f as shown in Eq.(8).

$$m = \frac{1}{C - D_f + 2} \quad (8)$$

In Eq.(8) C is the connectivity of the particle network. The determination of D_f provides information about the network structure of the examined system and is therefore very important to describe the physical behavior of the sample during deformation. Fig. 11 shows the storage modulus of a typical amplitude sweep of a completely developed HP gel, prepared at 25 °C as explained in section 2.8 and measured after 24 h of ageing at room temperature. The strong decrease of the modulus corresponds to the successive break down of the particle gels for increasing amplitudes (see section 3.2.5).

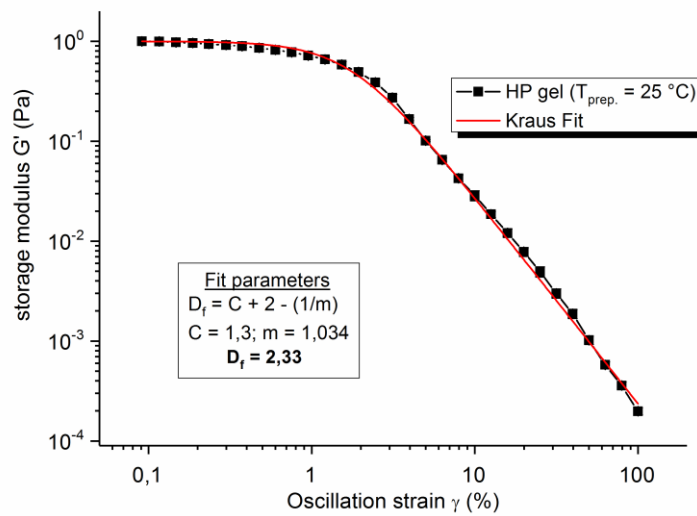


Fig. 11: Determination of fractal dimension D_f by oscillatory rheology

The inulin gel in Fig. 11 was measured with the RMS800 oscillatory rheometer by Rheometrics Inc. The sample was examined with a parallel plate geometry ($d_{\text{plate}} = 25$ mm), with an angular frequency of 10 rad/s and an oscillation strain between 0.1% and 100%. The parameters for the “Kraus” fit and the obtained fractal dimension D_f can be seen in Fig. 11. The connectivity C of the network was set to 1.3, assuming that the inulin particle network is completely percolated. The “Kraus fit” yields a formal fractal dimension of 2.3. Referring to a 3d particle gel network, the fractal dimension must adopt a value between 2 and 3. Taking into account the relatively small dry matter content of the sample (20% w/w) and the particle gel formation (see section 1.1), the sample pictured in Fig. 11 should yield a fragmentary gel structure. Therefore, the value for the fractal dimension $D_f = 2.3$ is located in the plausible range. Further independent measurements will be presented in following works.

1.5 Solute-Solvent interactions

In this work, as already mentioned in section 1, two types of long chain inulin were examined (HP: mostly amorphous powder, HPX: semi crystalline powder (see section 3.1)) in terms of their gelling properties in different solvents (water, water-ethanol mixtures and water-sucrose mixtures). The basis of the inulin gels is a particle gel network, with crystalline inulin primary particles forming the network (see section 1.1). For the formation of a completely percolated gel, the used inulin must partly dissolve in the solvent and recrystallize to form the primary

Introduction

particles, which are essential for the particle gel network. The dissolution and recrystallization of inulin in the solvent, implicates solute-solvent interactions. Those can be quantified by the “Flory-Huggins solution theory” and further solvent effects, which are the central theme of this section. The information in this section was mostly taken from [34-39].

If a solute (i.e. a polymer) is mixed with a solvent, the Gibbs free energy G_M of the mixture changes, compared to the sum of the free energies of its components G_{Solute} and $G_{Solvent}$ and can be expressed by Eq.(9).

$$\Delta G_M = G_M - (G_{Solute} + G_{Solvent}) \quad (9)$$

In Eq.(9), ΔG_M is the change in the Gibbs free energy of the mixture. Since the Gibbs free energy can be calculated by Eq.(10),

$$G_M = H_M - TS_M \quad (10)$$

with H_M as the enthalpy of the mixture, T its temperature and S_M the entropy of the mixture, the change in the Gibbs free energy can be estimated by Eq.(11).

$$\Delta G_M = \Delta H_M - T\Delta S_M \quad (11)$$

If the differential Gibbs enthalpy ΔG_M adopts negative values (exothermic), solute and solvent are miscible and form a stable mixture. In contrast, when ΔG_M adopts positive values (endothermic), solute and solvent are poorly miscible and the mixture is unstable. This instability manifests by the precipitation of solute. For ideal mixtures, solute and solvent do not interact with each other ($\Delta H_M = 0$) and ΔG_M always adopts negative values (the solute can adopt more arrangements in the solution, than in the solid state. Therefore, the change in entropy ΔS_M is always positive, what results in negative values for ΔG_M and a stable mixture). For real solute/solvent mixtures, interactions occur between solvent-solvent, solute-solute and solvent-solute. Those interactions must be considered in Eq.(11) and it results in the Flory-Huggins expression for the Gibbs free energy of mixing (Eq.(12)).

$$\Delta G_M = RT(n_1 \ln \phi_1 + n_2 \ln \phi_2 + \chi n_1 \phi_2) \quad (12)$$

In Eq.(12) n_1 and n_2 are the number of moles of solvent and solute, ϕ_1 and ϕ_2 are the volume fractions of solvent and solute, R is the ideal gas constant, T the temperature of the mixture and χ the Flory-Huggins interaction parameter. Multiplied with RT , the two terms on the left

Introduction

hand side of the bracket in Eq.(12) represent the mixing entropy ΔS_M and the term on the right hand side of the bracket represents the mixing enthalpy ΔH_M . In Eq.(12), the volume fractions ϕ_1 and ϕ_2 contain the Degree of Polymerization n as follows:

$$\phi_1 = \frac{N_1}{(N_1 + nN_2)}; \phi_2 = \frac{nN_2}{(N_1 + nN_2)} \quad (13)$$

In Eq.(13) N_1 and N_2 are the number of solvent and polymer (solute) molecules, ϕ_1 and ϕ_2 are again the volume fractions of solvent and polymer and n is the Degree of Polymerization of the polymer. Thus, for polydisperse solutes, every DP fraction exhibits its own ΔG_M , determining the solubility of this DP fraction at the given conditions in the respective solvent (e.g. if the Degree of Polymerization n increases, the left term in the bracket of Eq.(12) decreases and the two terms on the right hand side of the brackets increase. This results in an increase of ΔG_M and a decreasing solubility of this DP fraction in the solvent). The Flory-Huggins interaction parameter χ represents the sum of all pair interactions and consists of following interactions:

$$\chi = \chi_{MS} - \frac{1}{2}(\chi_{MM} + \chi_{SS}) \quad (14)$$

In Eq.(14), χ_{MS} represents the interactions between the monomers of the polymer in the mixture (solute) and the solvent, χ_{MM} are the interactions between the monomers and χ_{SS} are the interactions between the solvent molecules. For strong pair interactions, the respective parameter χ_{MS} , χ_{MM} or χ_{SS} adopts small values, for weak pair interactions the respective parameter is large. The Flory-Huggins interaction parameter χ depends on the state the system is in (temperature, pressure etc.) however, it is independent of the Degree of Polymerization (DP) of the polymer (in Eq.(14), just the interactions between the monomers and the solvent molecules contribute to the Flory-Huggins parameter. Therefore, the DP of the respective polymer does not have an impact on the solute-solvent interactions). When a polymer molecule dissolves in the solvent, for each monomer-solvent interaction established, one monomer-monomer and one solvent-solvent bond must be broken. This is represented in Eq.(14), by the factor “1/2” in front of the bracket. The Flory-Huggins interaction parameter is a very crucial quantity of Eq.(12), since it represents the interactions of the components in the mixture. If the intra-component (solvent-solvent and solute-solute) and the inter-component (solvent-

solute) interactions of a mixture are identical ($\chi_{MS} = \chi_{MM} = \chi_{SS}$), the Flory Huggins parameter adopts the value 0 (see Eq.(14)), the enthalpy term of Eq.(12) adopts the value 0 too and the mixture acts like an ideal mixture (see above). If the inter-component interactions exceed the intra-component interactions ($\chi_{MS} < \chi_{MM}, \chi_{SS}$), the Flory Huggins parameter adopts negative values and the components are miscible (stable mixture $\Delta G_M < 0$) and if the intra-component interactions exceed the inter-component interactions ($\chi_{MS} > \chi_{MM}, \chi_{SS}$), the Flory-Huggins parameter will be positive and the components are poorly miscible (unstable mixture $\Delta G_M > 0$). Thus, the Flory Huggins parameter χ influences the values of ΔG_M significantly.

If we now consider the behavior of HP and HPX in the different solvents, the observations can be explained with the Flory-Huggins theory. For the sake of clarity, we consider all three systems (inulin-water, inulin-water-ethanol and inulin-water-sucrose) during sample preparation, when the inulin powder is mixed with the solvent, at 25 °C (see section 2.2). The inulin-water system consists of the solute inulin and the solvent water. Both types of inulin exhibit a certain solubility in water at 25 °C (see Fig. 50). Since the inulin powders are polydisperse (see section 3.2.3), depending on the Degree of Polymerization of the respective inulin molecule, the solute dissolves in a larger or smaller amount. This results in a different ΔG_M for each DP of the inulin samples (see above). To simplify the discussion for the different DPs of the inulin molecules, the fractions will be referred to as short (DP < 18), medium (DP < 36) and long chain (DP ≥ 36) inulin. In section 3.2.3 the DP dependent solubility of HP and HPX during sample preparation will be examined, revealing that the short and medium chain inulin molecules (DP < 36) exhibit a significantly higher solubility in water than the long chain fractions (see Fig. 58 and Fig. 59) at 25 °C (the number of solvent molecules, that are necessary to solvate the short and medium DP inulin molecules is significantly smaller than the number of solvent molecules, that are needed for the long chain inulin. Because if this, the short and medium chain inulin dissolve much better in water than the long chain inulin). Therefore, the inter-component interactions of the short and medium chain inulin molecules (inulin-water) exceed the intra-component interactions (inulin-inulin and water-water), ΔG_M adopts negative values and the inulin molecules dissolve. For the long chain fractions, the intra-component interactions dominate, ΔG_M is positive and the long chain inulin molecules just slightly dissolve (see Eq.(12) and Eq.(13)). If we consider the DP fractions, that remain dissolved after 24 h ageing at room temperature (see Fig. 60 and Fig. 61), we can observe that only short and a small amount of medium chain inulin (DP < 36) remain dissolved. For the inulin molecules that did

not remain dissolved, the intra-component interactions dominate, resulting in $\Delta G_M > 0$ and a crystallization of those fractions (if a crystallite is formed, the lattice energy of the crystal is released and the crystal adopts a very stable state of low Gibbs free energy). If we have a look at the solubility curves of HP and HPX in water again (Fig. 50), we can see that HPX exhibits a significantly lower solubility than HP at 25 °C. This is due to the superior crystallinity of the HPX powder (see Fig. 47) and can also be explained with the Flory-Huggins theory. As mentioned before, the crystalline material in the HPX powder is in a very stable state of low Gibbs free energy G . If the inter-component interactions do not exceed the intra-component interactions of the HPX crystals (in the case of dissolution the solvation energy must exceed the lattice energy of the crystal), to transfer the crystalline HPX molecules in a state of even lower Gibbs free energy in the solution G_M , the crystals remain undissolved. This is the reason for the lower solubility of HPX compared to HP in water (as mentioned before the HP powder is mostly amorphous).

If the polarity of the solvent is decreased, by the addition of ethanol to water, the dissolution trends of HP and HPX at 25 °C remain the same as mentioned above. One significant change, compared to pure water as solvent, is very obvious. The overall solubility of HP and HPX in water-ethanol mixtures decreases (see section 3.3.1 and section 3.3.3). This is due to the change of the Flory-Huggins parameter χ . If the polarity of the solvent is decreased, the inter-component interactions of the relatively polar inulin molecules (see Fig. 1, the inulin molecule exhibits many free hydroxyl groups, giving the molecule a polar character) with the solvent, whose polarity is decreased, diminish and with it the Flory-Huggins parameter adopts larger values. This results in an increased ΔG_M and the solubility of HP and HPX in the water-ethanol mixture decreases.

If we consider the inulin-water-sucrose system, the solvent-solute interactions are not significantly different, compared to the inulin-water system. The overall solubility of HP and HPX is also decreased, compared to the solubility of HP and HPX in water. Here, this is due to a semi saturated solvent. Sucrose is also a component of the polydisperse inulin powders ($DP_{\text{Sucrose}} = 2$, see section 3.2.3). This means, if the sucrose content of the solvent is increased, the saturation degree of the solvent (by the dissolution of the well dissolving sucrose and short chain fraction of inulin) increases too. Since the polarity of the solvent does not change at all, the Flory-Huggins parameter remains the same, compared to the inulin water system. The

semi saturation of the solvent mostly affects the poorly soluble long chain fractions of HP and HPX, whose solubility is significantly decreased in comparison to the inulin-water system (see Fig. 106 and Fig. 107). Since so many solvent molecules are already “bound” by the solvation of the sucrose and the short chain inulin molecules, the number of “free” solvent molecules, which are necessary to solvate the long and medium chain inulin molecules, is significantly decreased. Therefore, the medium and long chain inulin is solvated to a much smaller extent. As mentioned before, by the solvation of molecules, the mixing entropy ΔS_M of this molecule fraction increases. Thus, the mixing entropy of the partly solvated medium and long chain fractions decreases, resulting in an increased ΔG_M for those fractions, manifesting in a decreased solubility. Despite of this overall decreased solubility of HP and HPX in water-sucrose mixtures, the solute-solvent interactions are the same, as already described for the inulin-water system.

1.6 Solubility measurements

In this section the basic principles of solubility measurements are summarized. The information in this section was mostly taken from [17, 40-42].

As mentioned above, if a solute dissolves in a solvent, the solute molecules need to be solvated completely by the solvent molecules and the lattice energy of the solute crystals needs to be overcome by the exothermic solvation energy (see section 1.5). To determine the precise solubility of a solute in a certain solvent, at a given temperature, the following requirements must be met during the solubility determination:

1. A known mass of solvent needs to be preheated to the desired temperature in a temperature controlled, sealed and preferably isolated vessel.
2. The solute must be added in excess (to ensure a saturated solution at the respective temperature) to the stirred and preheated solvent. The sample must be stirred at the desired temperature until equilibrium (normally up to 24 h. In this work, due to the sample preparation procedure of the inulin gels, the solubility was determined after 10 min of stirring at the respective sample preparation temperature).
3. The clear solution and the undissolved solute need to be separated from each other (e.g. by filtration or centrifugation) and the dissolved amount of solute in the clear solution is determined.

Introduction

The dissolved amount of solute can be measured by several physical methods. In this work, the principle of the determination of the concentration dependent refractive index, at 20 °C with monochromatic light of the wavelength $\lambda = 589 \text{ nm}$, was used.

If a ray of light hits the interface between two media with different density (e.g. an air/glass interface), one part of the light ray is reflected and the other part penetrates the second medium. After penetrating the second medium, the direction of propagation of the light ray is changed. This is called refraction. If a light ray propagates in vacuum and enters a medium with a higher density than the vacuum, the light ray is absorbed and emitted again by the atoms of the medium. This process repeats constantly, while the light ray moves through the medium. If now two light rays are compared, that were emitted from the same light source, and one of the beams propagated through vacuum and the other one through the above mentioned medium, the light ray, which propagated through the medium, arrives delayed compared to the vacuum light ray. This means, the propagation speed in the medium is smaller. Therefore, the medium exhibits a larger refractive index, than the vacuum (the refractive index of the vacuum equals 1). The refractive index n_r can be determined by Eq.(15).

$$n_r = \frac{c}{c_m} \quad (15)$$

In Eq.(15), c is the speed of the light ray in vacuum and c_m is the speed of the light beam in the medium (e.g. glass). Due to the definition of the refractive index in Eq.(15), all media exhibit a refractive index n_r larger than 1. Since the refractive index of air is just marginally larger than 1, it is approximated as 1 in practical cases. If two media are compared to each other, the medium with the larger refractive index also exhibits the larger “optical density”. As mentioned above, if a light ray travels through a medium, the light is absorbed and emitted continually by the atoms of the medium. This process does not change the frequency of the light ray, yet it changes the speed of the light ray c_m in the medium. The frequency ν of the light beam can be defined by:

$$\nu = \frac{c_m}{\lambda_m} \quad (16)$$

Therefore, with a decreasing speed of the light beam in the medium c_m , the wavelength λ_m of the light ray in the medium must also decrease, to ensure a constant frequency ν . The change of the wavelength in the medium can be estimated by Eq.(17).

$$\lambda_m = \frac{c_m}{\nu} = \frac{c/n_r}{\nu} = \frac{\lambda}{n_r} \quad (17)$$

In Eq.(17), λ is the wavelength of the light beam in vacuum. In Fig. 12, an air/glass interface is pictured.

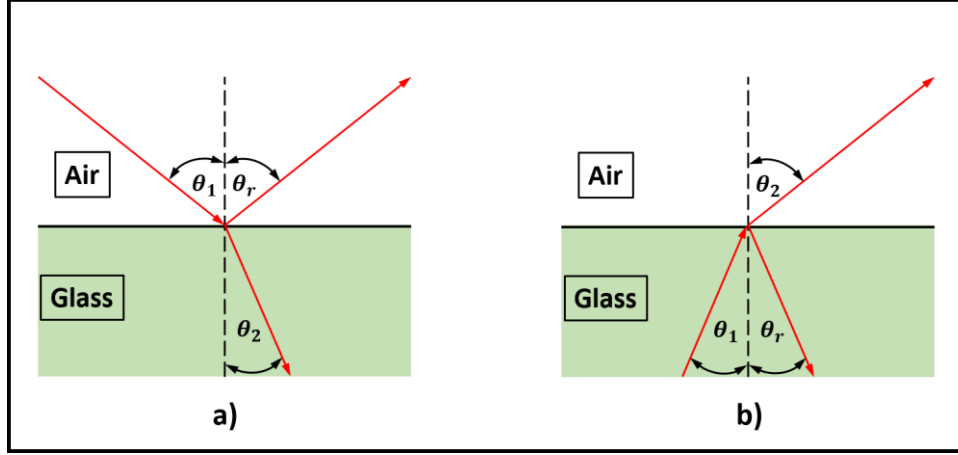


Fig. 12: Air/glass interface, with refracted and reflected light beams. a) Coming from air entering glass; b) coming from glass entering air [40].

In Fig. 12a), the light beam comes from the medium air and enters the medium glass. The incident light ray and the normal (dashed black lines in Fig. 12) span the angle θ_1 . The reflected light beam and the normal span the angle θ_r , which equals θ_1 . The light ray entering the medium glass (glass exhibits a higher optical density than air and exhibits therefore also a larger refractive index) is refracted to the normal, meaning the refractive angle θ_2 is smaller than θ_1 . In Fig. 12b), the opposite situation is pictured. The light beam comes from glass and enters the medium air (which exhibits a smaller optical density and a smaller refractive index than glass). Therefore the normal and the refracted light beam span the larger angle θ_2 (compared to θ_1). The incident angle θ_1 and the refractive angle θ_2 and the refractive indices n_1 and n_2 of the respective media, can be related to each other by “Huygens’ principle”. In Fig. 13, the refraction of a plane wave (light can also be described as wave) at an air/glass interface is pictured.

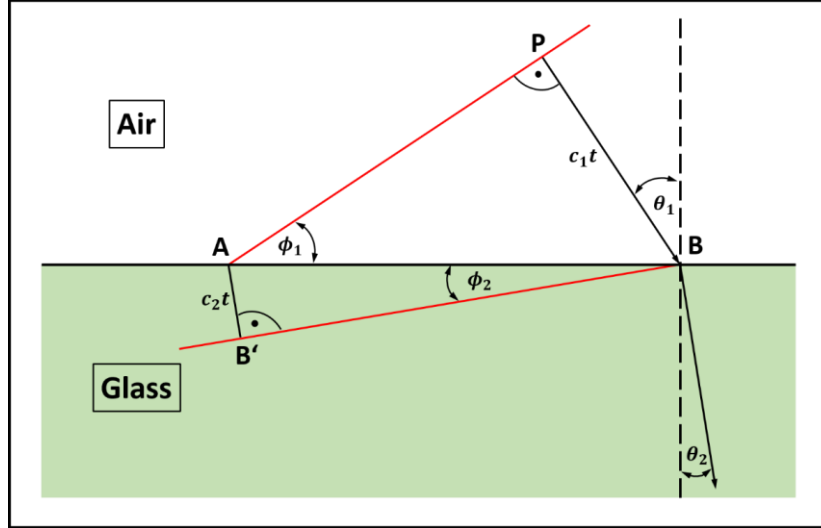


Fig. 13: Application of Huygens' principle on a plane wave at an air/glass interface [40].

In Fig. 13 the distance AP (red line in the medium air), represents a part of the incident light wave. The wave hits the air/glass interface at the angle θ_1 . The light wave originates from the point P and covers the distance $c_1 t$ in the time interval t , until arriving at point B . In the same time interval t , the wave that originates from point A and propagates in the medium glass, covers the distance $c_2 t$. Since the speed of the light wave in air c_1 and in glass c_2 is not identical, the new light wave front BB' does not propagate parallel to the light front in air AP . From the right-angled triangle BPA the distance AB can be determined via Eq.(18).

$$\overline{AB} = \frac{c_1 t}{\sin \phi_1} = \frac{c_1 t}{\sin \theta_1} \quad (18)$$

The distance AB can also be determined from the right-angled triangle $AB'B$.

$$\overline{AB} = \frac{c_2 t}{\sin \phi_2} = \frac{c_2 t}{\sin \theta_2} \quad (19)$$

By setting Eq.(18) and Eq.(19) equal, substituting $c_1 = c/n_1$ and $c_2 = c/n_2$ and the multiplication with c , Eq.(20) is obtained.

$$n_1 \sin \theta_1 = n_2 \sin \theta_2 \quad (20)$$

Eq.(20) is called "Snell's law of refraction". This law applies to all kinds of waves, which pass the interface between two different media. In Fig. 14 a punctual light source in the medium glass is pictured.

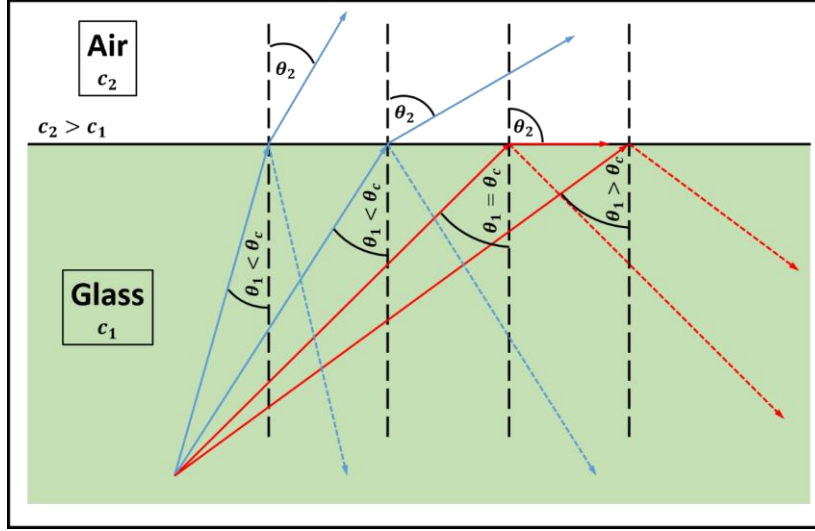


Fig. 14: Total reflection [40].

Since air exhibits a smaller optical density than glass, the refractive angle θ_2 is larger than the incident angle θ_1 . If the incident angle increases, the refractive angle increases too, until a critical incident angle θ_c is reached. A light ray, which propagates from a medium with higher optical density to a medium with lower optical density, and hits the interface of the two media at an incident angle which is larger or equal to θ_c , is reflected completely at the interface (at an incident angle which equals θ_c , the refracted light ray propagates parallel to the glass/air interface. If the incident angle exceeds θ_c , refraction does not occur anymore and the light beam is reflected completely at the interface, see Fig. 14). This phenomenon is called “total reflection”. The critical angle θ_c (with a refractive angle $\theta_2 = 90^\circ$) can be determined by Eq.(21).

$$\sin \theta_c = \frac{n_2}{n_1} \quad (21)$$

In Eq.(21), n_1 is the refractive index of the medium with the higher optical density and n_2 is the refractive index of the medium with the lower optical density ($n_1 > n_2$). The principle of the total reflection is applied for the determination of the refractive index of unknown media via Abbé refractometers. In Fig. 15, a sketch of a simple Abbé refractometer is shown. The illuminating light is emitted by the light source. The light enters the illuminating prism, is scattered by the matted surface of the illuminating prism and diffuse light enters the sample, which is contained between illuminating and measuring prism. After being refracted by the sample, the light is refracted at the sample/measuring prism interface again (according to its incident angle and the refractive indices of sample and prism). The measuring prism emits the

Introduction

refracted light, which is observed by the telescope. To determine the refractive index of the examined sample, the telescope must be focused on the shadow boundary of the total reflection (upper right hand side of Fig. 15).

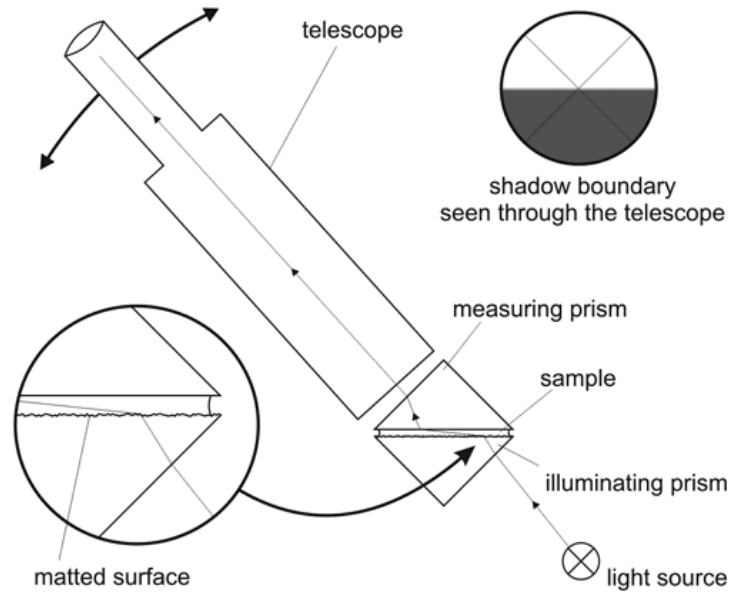


Fig. 15: Abbé refractometer [43].

Since the total reflection at the sample/measuring prism interface is the crucial part of the Abbé refractometer, in Fig. 16 the two interfaces illuminating prism/sample and sample/measuring prism are pictured more detailed.

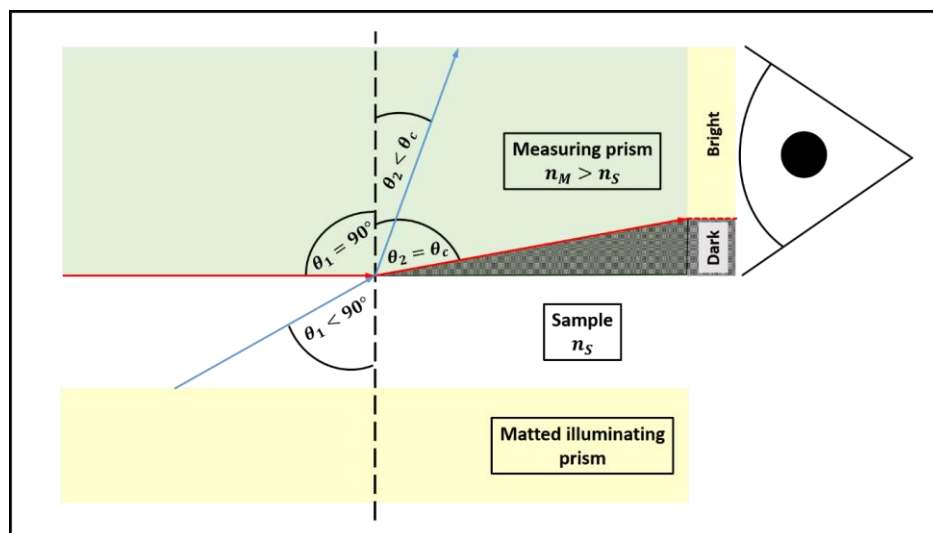


Fig. 16: Total reflection and shadow boundary in measuring prism [44].

To obtain a shadow boundary, which enables the determination of the sample's refractive index n_s , the optical density of the measuring prism must be higher than the optical density of the sample ($n_M > n_s$). Therefore, the maximum refractive index, which can be determined

Introduction

with an Abbé refractometer, is limited by the measuring prism's refractive index n_M . Every light ray, which hits the sample/measuring prism interface at an incident angle $\theta_1 < 90^\circ$, can be detected by the telescope as refracted light. The maximum possible incident angle $\theta_1 = 90^\circ$ ("grazing incidence"), results in a refractive angle θ_2 , which equals θ_c . Since no larger incident angle θ_1 is possible and the light is refracted at an angle $\theta_2 < \theta_1$ (due to the larger optical density of the measuring prism), the lower part of the measuring prism is not illuminated and appears dark (see Fig. 16). The shadow boundary represents the refractive angle of total reflection θ_c . Therefore, if the telescope is focused on the shadow boundary, the refractive index of the sample can be determined by Eq.(21). Since the refractive index of materials is dependent on the temperature of the material and the wavelength of the examination light, the refractive index is determined with monochromatic light ($\lambda = 589 \text{ nm}$) and at a temperature of $T = 20^\circ\text{C}$. Nowadays, the refractive index of samples is determined with digital refractometers, which enable a direct and very fast examination of unknown samples. In Fig. 17, an example of a handheld digital refractometer is pictured.



Fig. 17: Handheld digital refractometer by Bellingham and Stanley [45].

1.7 X-ray diffraction

Crystalline material can be examined by x-ray diffraction. As mentioned above, the inulin primary particles are crystalline (the basic information about crystals can be found in section 1.2). Therefore, in this section the basic principles of x-ray diffraction are summarized. The information in this section was mostly taken from [16, 17, 46].

Introduction

Radiation is scattered by electrons in atoms, molecules, particles and crystals. Since this scattering process is specific for each substance, this method can be used to identify and examine unknown substances. X-rays are also a type of electromagnetic radiation and therefore scattered by the electrons of substances (the scattering of x-rays depends on the electron distribution in the system). This enables the examination of samples with x-rays to obtain quantitative structural information.

As mentioned above, light (i.e. electromagnetic radiation) can be described as wave or as photon. The photon energy is given by Eq.(22).

$$E = h\nu = \frac{hc}{\lambda} \quad (22)$$

In Eq.(22), E is the photon energy, h is Planck's constant, c is the speed of light, ν is the frequency and λ is the wavelength. The different types of radiation are sorted according to their frequency and wavelength in an electromagnetic spectrum (Fig. 18).

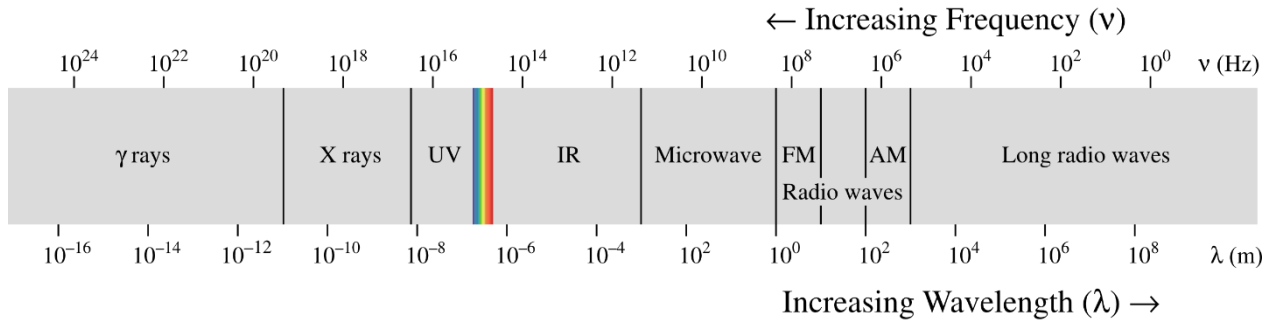


Fig. 18: Electromagnetic spectrum [47].

Light, which is visible for the human eye, exhibits a wavelength of $380 \text{ nm} - 700 \text{ nm}$ (colored region in Fig. 18). The shorter the wavelength λ and the higher the frequency ν of the radiation are, the higher is the corresponding energy (see Eq.(22)). X-rays exhibit a wavelength of approximately $\lambda = 0,01 \text{ nm} - 10 \text{ nm}$ and a frequency of $\nu = 30 \text{ PHz} - 30000 \text{ PHz}$ (10^{15}). Therefore, x-rays have a very high energy content and belong to the ionizing radiation. Conventionally, x-rays are obtained by an electron bombardment of a water cooled metal anode (often a copper target, see Fig. 19). High voltage is applied between cathode (K with corresponding voltage U_h) and anode (A with corresponding voltage U_a). Electrons are emitted by the cathode, accelerated by the high voltage and collide with the water cooled anode. Electrons of the anode material are accelerated by the collision and x-ray radiation is emitted. A sketch of an atom of the anode material can be seen in Fig. 20.

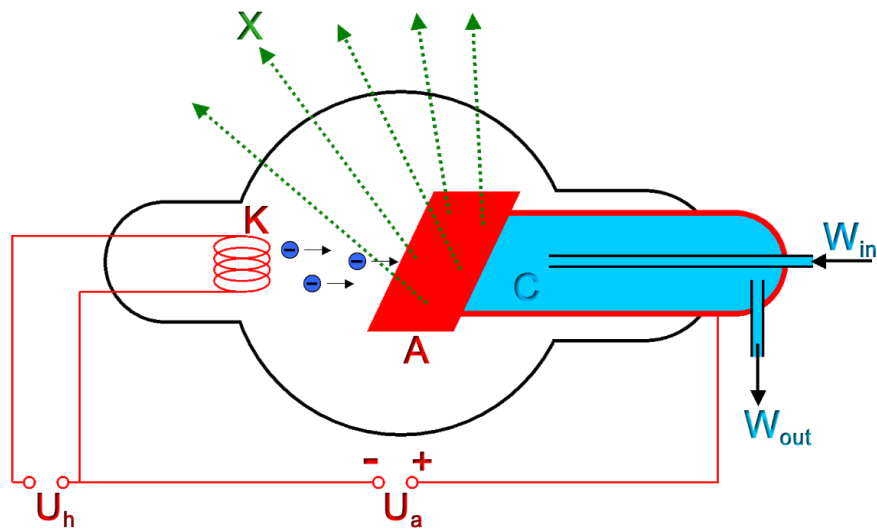


Fig. 19: Standard x-ray tube [47].

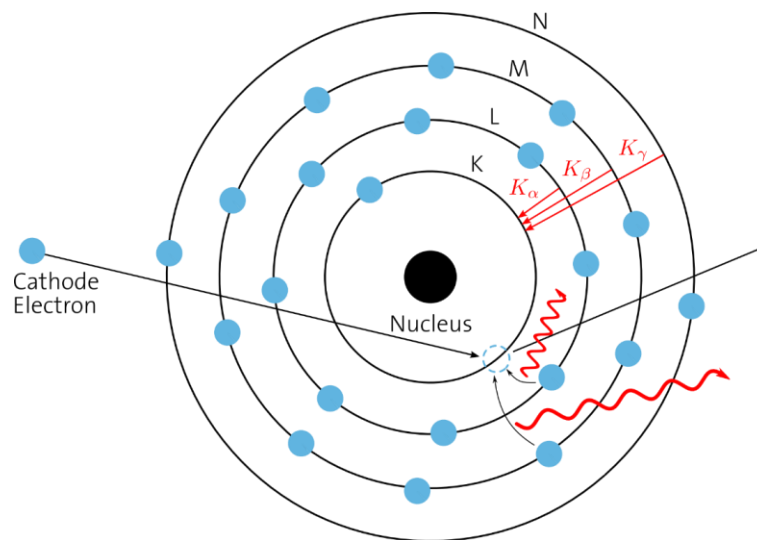


Fig. 20: Generation of x-rays [47].

If the accelerated electron hits an electron on an inner shell (in Fig. 20 the K-shell) of the anode atoms, the inner electron is knocked out of the atom and the generated hole can be refilled by an electron of an outer shell (in this case from the L, M and N shell). Depending on which shell the refilling electron originates from, the excess energy is released as characteristic x-ray radiation (e.g. for an electron transfers from L shell to K shell, the released x-ray radiation is called K_α). Additionally, when the accelerated electron enters the shell of the anode atom, the electron is deflected by the charges inside the atom and slowed down. This results in a decreasing energy of the electron. The excessive energy is released as continuous spectrum, the “Bremsstrahlung”. Both types of x-ray radiation can be seen in Fig. 21.

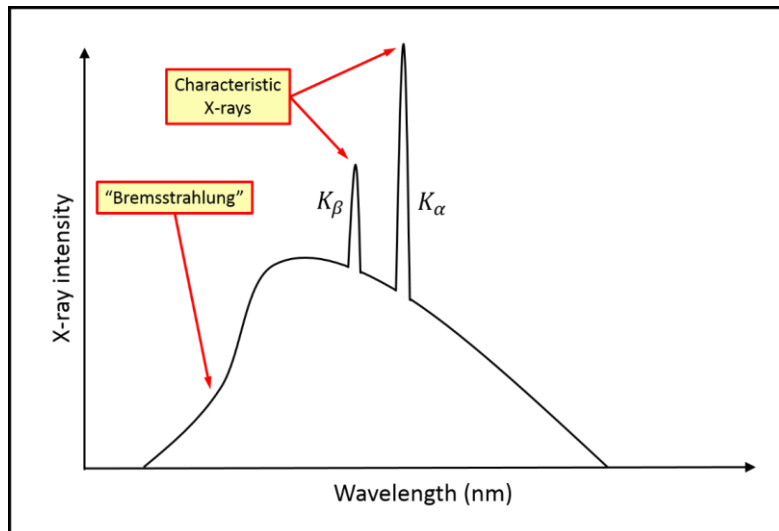


Fig. 21: Characteristic x-ray radiation and "Bremsstrahlung" [47].

Since the wavelength of this monochromatic x-ray radiation is similar to the distance of atoms in crystals, the diffraction of x-ray radiation by crystalline material can be used to obtain quantitative structural information about unknown samples. The relationship between the wavelength of x-rays and the spacing between the atoms in a crystal (the interplanar spacing is characteristic for each substance and type of crystal lattice, see "lattice parameters" section 1.2) is known as Bragg's law (Eq.(23)), which is the basis of diffraction analysis.

$$n\lambda = 2d \sin\theta \quad (23)$$

In Eq.(23), n is the order of the diffraction, λ is the wavelength of the x-ray radiation, d is the interplanar spacing in the crystal and θ the angle of the incident x-rays to the diffracting lattice plane. The diffraction of x-ray radiation by atoms of a lattice plane in a crystal can also be explained by Huygens principle (see also section 1.6). In Fig. 22, the wave front of a plane x-ray wave hits a lattice plane of a crystalline material.

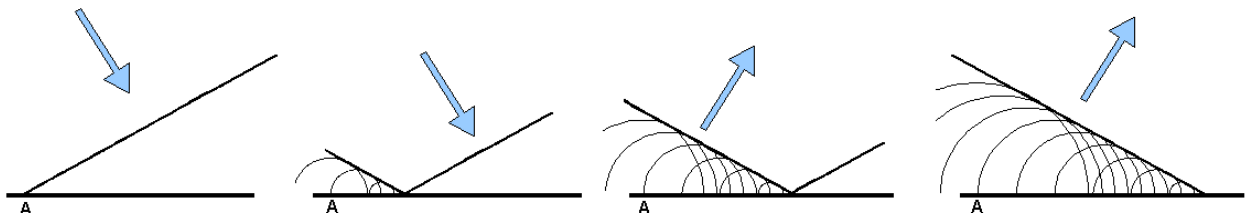


Fig. 22: Diffraction of x-ray wave front at lattice plane [48].

Introduction

The point where the wave hits the lattice plane (i.e. an atom) becomes a new center, radiating spherical waves of x-rays. Since the spherical waves propagate in all directions (i.e. the incident wave is scattered), new wave fronts of various orders are formed, if the scattered waves are in phase. In Fig. 22, only the new wave front of the first diffraction order is shown, which propagates at an angle θ_2 , which equals the incident angle of the wave front θ_1 . Since the new wave front changes its direction of propagation (compare the wave fronts on the left hand and on the right hand sides of Fig. 22), the incident x-ray wave has also been diffracted. If the incident and the diffracted angle are equal ($\theta_1 = \theta_2$) and the conditions of Bragg's law (Eq.(23)) are fulfilled, the diffracted x-ray wave front shows constructive interference and can be detected as signal with very high intensity (Bragg reflex). In Fig. 23, the diffraction of x-ray radiation at a series of lattice planes is shown.

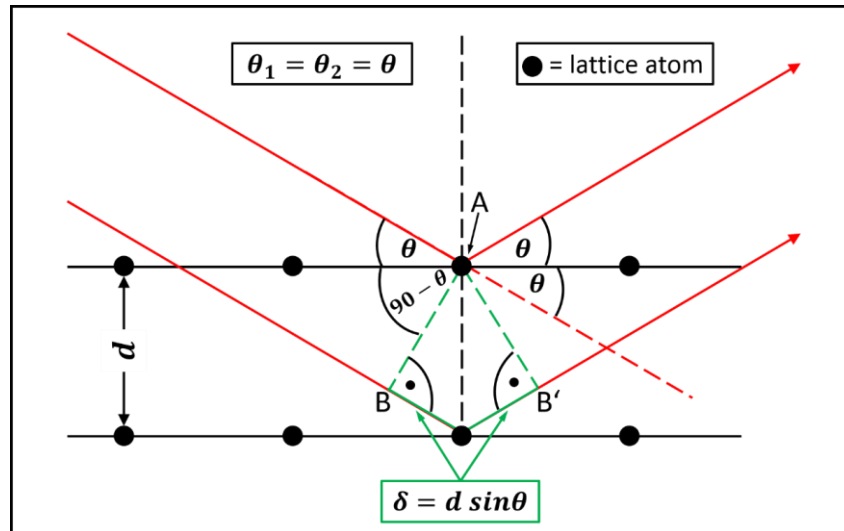


Fig. 23: Diffraction of x-ray radiation at lattice planes.

In Fig. 23, two monochromatic x-ray beams, with identical wavelength and phase, are scattered by atoms of two different lattice planes (if the x-ray radiation is described as plane wave, the incident wave front is along the left hand dashed green line AB in Fig. 23). The interplanar spacing between the two planes is given by the distance d . In Fig. 23, only the scattered beams are shown, whose scattering angle θ_2 equals the incident angle θ_1 . The lower beam traverses an extra length of $2\delta = 2d \sin\theta$ (after scattering the new wave front goes along the right hand dashed green line AB'). Since the direction of propagation has changed, the plane x-ray wave has been diffracted. See also Fig. 22). If this extra length equals an integer multiple of the wavelength of the x-ray radiation $n\lambda$, the two x-ray beams remain in phase after scattering and constructive interference occurs, resulting in very intense Bragg reflexes. Therefore,

Eq.(23) can be derived from Fig. 23. In diffraction experiments, the Bragg reflexes are detected and identified according to their diffraction angles 2θ (in diffraction experiments, the un-diffracted beam, which exhibits a diffraction order of $n = 0$, is focused on the center of the detector, see Fig. 24. Since the incident and the diffracted x-ray beam span the angle θ with the lattice planes and the un-diffracted x-ray beam also spans the angle θ with the lattice planes, the angle between un-diffracted and diffracted x-ray beam equals 2θ , see Fig. 23). In Fig. 24, the experimental setup of the used x-ray device is shown.

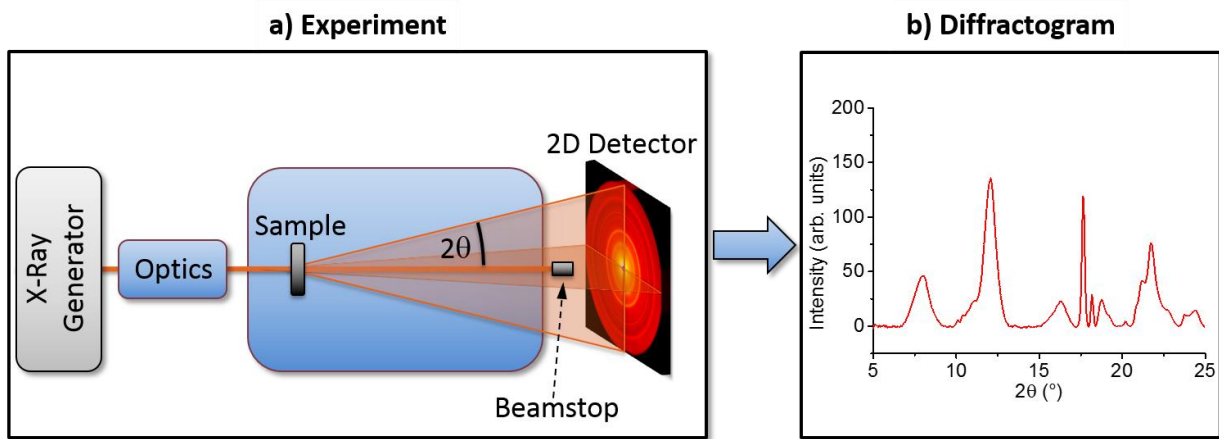


Fig. 24: a) Experimental setup and b) obtained diffractogram.

The x-rays are produced by the x-ray generator, collimated by the optics of the device (i.e. the x-rays are parallelized by a series of pinholes, which block the x-rays, that are nonparallel to the desired path of the x-ray beam) and diffracted by the sample at a diffraction angle of 2θ . In this case, the sample can be solid (powder) or liquid and is contained in glass capillaries made of quartz glass (quartz glass does not absorb $Cu-K_{\alpha}$ radiation). It is also very crucial, that the path between x-ray generator and sample is evacuated, to prevent the scattering of the x-ray beam by air, what results in a decreased intensity of the beam. After being diffracted by the sample, the x-rays are detected by a 2D detector (the un-diffracted beam is absorbed by the beamstop, to prevent the still very intense x-ray beam from damaging the detector). A radial averaging of the detected signals and a plotting of the registered intensity versus the respective diffraction angle 2θ , yields the diffractogram shown in Fig. 24b. The diffraction angles of the Bragg reflexes give information about the crystal structure of the sample and the examination of the time dependent development of the Bragg intensities can be analyzed to learn about the crystallization kinetics of the sample (see section 1.3).

1.8 High Performance Anion Exchange Chromatography (HPAEC)

As being oligo saccharides, inulin molecules can be separated and analyzed according to their degree of polymerization, by using High Performance Anion Exchange Chromatography. Therefore, in this section the basic knowledge about HPAEC is summarized. The information in this section was mostly taken from [49, 50].

HPAEC is a type of ion chromatography, making use of the high pressure of a HPLC (High Performance Liquid Chromatography) system ($10 - 50 \text{ MPa}$), resulting in a very high performance of the separation process. It belongs to the family of the physical-chemical separating processes and is based on the distribution of an anionic solute between a solid stationary phase and a liquid mobile phase.

The stationary phase consist of a polymer substrate with covalently bound cationic exchange groups (most often ammonium groups NR_3^+ , with N being nitrogen and R being the organic side chains) and an exchangeable anionic group (often hydrogen carbonate groups HCO_3^- , with H being hydrogen, C being carbon and O representing oxygen). In Fig. 25, a typical example of a surface functionalized Styrene-Divinylbenzene substrate particle can be seen, which is very often used as stationary phase for the anion exchange chromatography (especially for the separation of oligosaccharides like inulin).

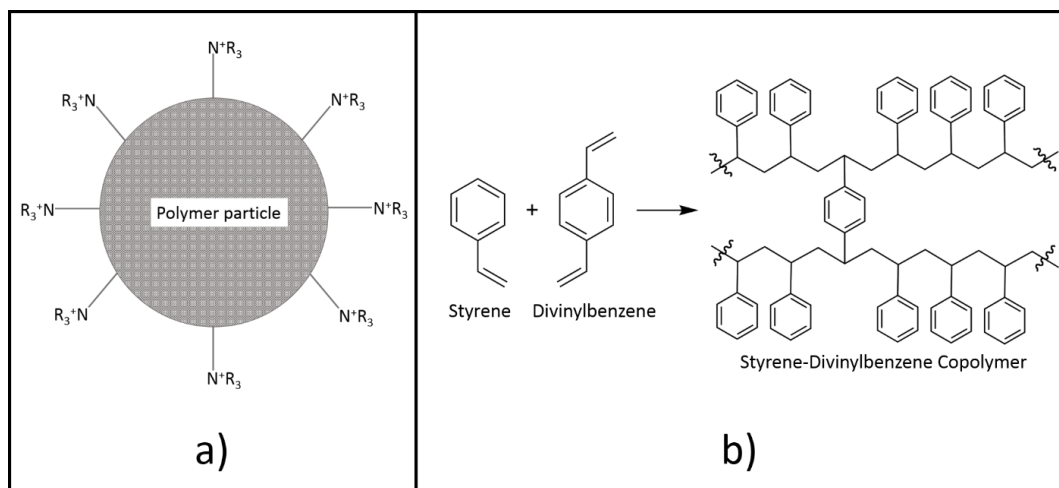


Fig. 25: a) Surface functionalized anion exchange substrate particle [50], b) Structural formula of Styrene-Divinylbenzene Copolymer [51].

Modern separation columns are packed with anion exchange granules of a diameter $d = 4 - 15 \mu\text{m}$. This type of substrate exhibits a very high stability concerning flow rate of the mobile

phase, changing ionic strength of solute and mobile phase and changing pH values (the substrate remains stable for pH values between 0 – 14). Additionally, the very small substrate particles enable a very fast mass transfer between stationary and mobile phase, what results in very efficient chromatographic separation of the different solute molecules.

If a sample containing the anions A^- and B^- is applied on the column, the anions are bound by the anion exchanger and hydrogen carbonate anions are released (see Eq.(24) and Eq.(25)).



To separate the different solute molecules from each other, the molecules must be in their anionic state. Therefore, uncharged molecules are reduced by a strong Base (for HPAEC sodium hydroxide NaOH is often used), which can be added to the eluent (i.e. the mobile phase). The separation of the anions A^- and B^- is controlled by their different affinity with the stationary phase. The equilibrium process is characterized by a distribution coefficient K .

$$K = \frac{[X^-]_s \cdot [\text{HCO}_3^-]_m}{[X^-]_m \cdot [\text{HCO}_3^-]_s} \quad (26)$$

In Eq.(26), $[X^-]_{s,m}$ is the concentration of the sample anion in the stationary respectively in the mobile phase and $[\text{HCO}_3^-]_{s,m}$ is the concentration of the hydrogen carbonate anion in the solid and the mobile phase. If a sample contains two different types of anions A^- and B^- , the anions are separated more efficiently from each other, the more their distribution coefficients K differ from each other (if an anion exhibits a very high affinity to the stationary phase, it is restrained very long by the stationary phase, resulting in large values for K . If the sample anion exhibits a very low affinity with the stationary phase, K is very small, the anion is just slightly restrained and passes the separation column very quickly). For an exchanged anion X^- , the equilibrium distribution coefficient D is defined by Eq.(27).

$$D = \frac{[X^-]_s}{[X^-]_m} \quad (27)$$

After being separated by the anion exchange column, the different anions are registered by different detection methods. In this section the focus is on the conductometric (or amperometric) detection. In Fig. 26, an amperometric flow detector can be seen. It consist of a

Introduction

working electrode (left hand electrode in Fig. 26) and a reference electrode (right hand electrode). A voltage is applied on the two electrodes (in the case of oligosaccharides $0 - 0,05\text{ V}$). If the eluent (gray spheres in Fig. 26) passes the electrodes, no current is detected. If an electroactive substance passes the measuring section between working and reference electrode, the substance is partly oxidized or reduced (in this case the anions are oxidized). A cathodic or anodic current between electrodes and sample ion is generated, which is proportional to the concentration and charge of the detected substance. Therefore, the detected current can be represented as chromatographic signal. In Fig. 26, the anion A^- has already been detected (green spheres already passed the measuring section of the electrodes and are represented as peak in the chromatogram on the upper right hand side) and anion B^- (red spheres) will be detected afterwards.

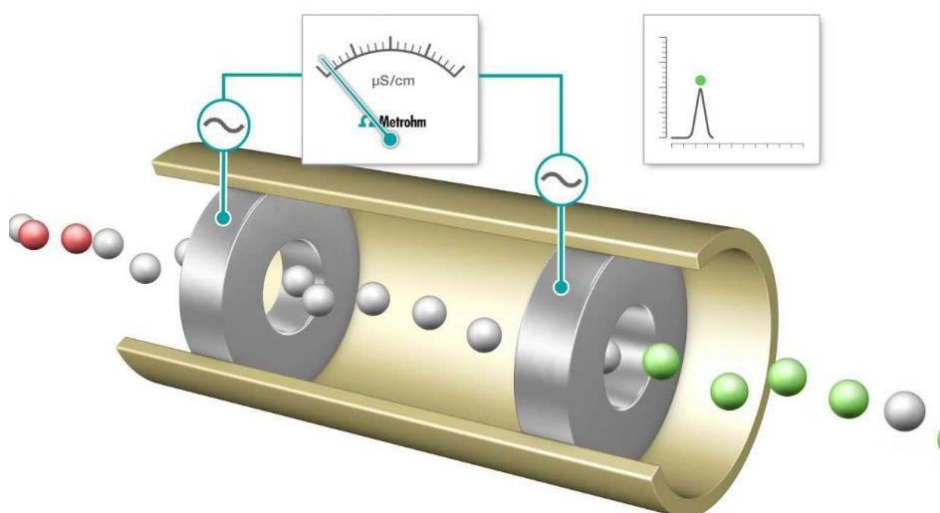


Fig. 26: Conductometric detection [52].

A very important requirement for a sensitive amperometric detection is, that no reaction products of an oxidation or reduction are deposited on the electrode surface. However, in practical experiments this is often occurs (especially if carbohydrates are detected. The deposition of substances on the electrodes is called “electrode fouling”), reducing the sensitivity of the electrodes. The electrode fouling can be reduced by application of Pulsed Amperometric Detection (PAD). This is a special type of amperometric detection, which uses very short, alternating negative and positive pulses (the duration of one pulse is approximately 60 ms), to clean the electrode surfaces. This method increases sensitivity and lifetime of working and reference electrode significantly. The amperometric detection yields a chromatogram, which

Introduction

gives information about the concentration of the different substances (area below the respective peak) contained in the analyzed sample. Since the different components of the sample have been separated according to their affinity with stationary and mobile phase, the chromatogram gives also information about the type of substance. The polydisperse inulin molecules for instance, can be separated according to their different DP. In Fig. 27, an example for a chromatogram, with the most important parameters indicated, is given.

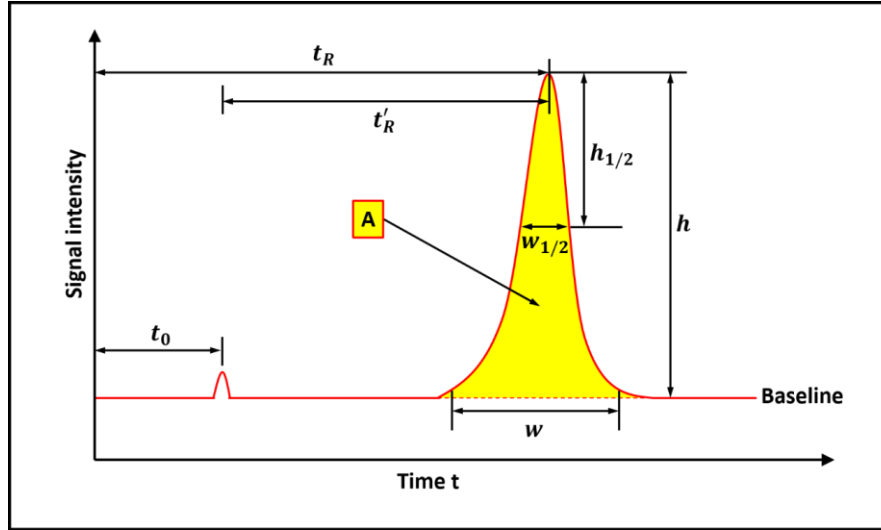


Fig. 27: Chromatogram with parameters indicated [53].

In Fig. 27, t_R is the total retention time. This is the time interval from the application of the substance until its peak maximum. Since t_R is characteristic for each substance, it gives qualitative information about the examined substance (e.g. by comparing t_R of the unknown substance to the total retention time of a known standard substance). The parameter t_0 represents the dead time. This is the time interval, from the application of a substance, which has no affinity with the stationary phase, until its detection. This is the minimum time a substance needs to travel through the separation column until being detected (in ideal cases the eluent is a substance, which has no affinity with the stationary phase). The adjusted retention time t'_R can be obtained by Eq.(28).

$$t'_R = t_R - t_0 \quad (28)$$

The adjusted retention time gives the amount of time, the substance is restrained by the stationary phase. The parameters t'_R and t_0 are also used to determine the capacity factor k' via Eq.(29).

$$k' = \frac{t_R - t_0}{t_0} = \frac{t'_R}{t_0} \quad (29)$$

The capacity factor is a measure for the velocity of migration in the chromatographic system. Additionally, it is independent of the column length and the flow rate of the eluent and therefore, in unique cases, more significant than the adjusted retention time t'_R . In Fig. 27, w and $w_{1/2}$ are the peak width and the peak width at half peak height. The parameters w and $w_{1/2}$ can be used to determine the resolution R (Eq.(30)) and the number of theoretical plates N (Eq.(31)).

$$R = \frac{2(t_{R2} - t_{R1})}{w_1 + w_2} = \frac{1,18(t_{R2} - t_{R1})}{w_{1/2,1} + w_{1/2,2}} \quad (30)$$

In Eq.(30), $t_{R1,2}$ are the total retention times of substance 1 and 2, $w_{1,2}$ are the peak widths of substance 1 and 2 and $w_{1/2,1,2}$ are the peak widths at half peak height of substance 1 and 2. The resolution R is a measure of the capability of the system, to separate substance 1 and 2 from each other. A resolution of 1,5 is sufficient to detect the two substances individually.

$$N = 16 \left(\frac{t_R}{w} \right)^2 = 5,54 \left(\frac{t_R}{w_{1/2}} \right)^2 \quad (31)$$

The number of theoretical plates N is a theoretical subdivision of the separation length of the chromatographic column in sections, which can be treated analogously to the separation steps of a bubble tray tower distillation (rectification). One theoretical plate corresponds to the length of the column, which is necessary for the distribution equilibrium to be accomplished once. The more numerous the number of theoretical plates is, the better is the resolution R of the system. In Fig. 27, h and $h_{1/2}$ are the peak height and half peak height and A is the area below the peak. The parameter $h_{1/2}$ is used to indicate the height of the peak, where $w_{1/2}$ is determined. The height of the peak h can be used to determine the area A of Gaussian-shaped peaks via Eq., to quantify the substance, which induced the analyzed peak.

$$A = h \cdot w_{1/2} \quad (32)$$

In Fig. 28, the experimental setup of the used HPAEC device is shown.

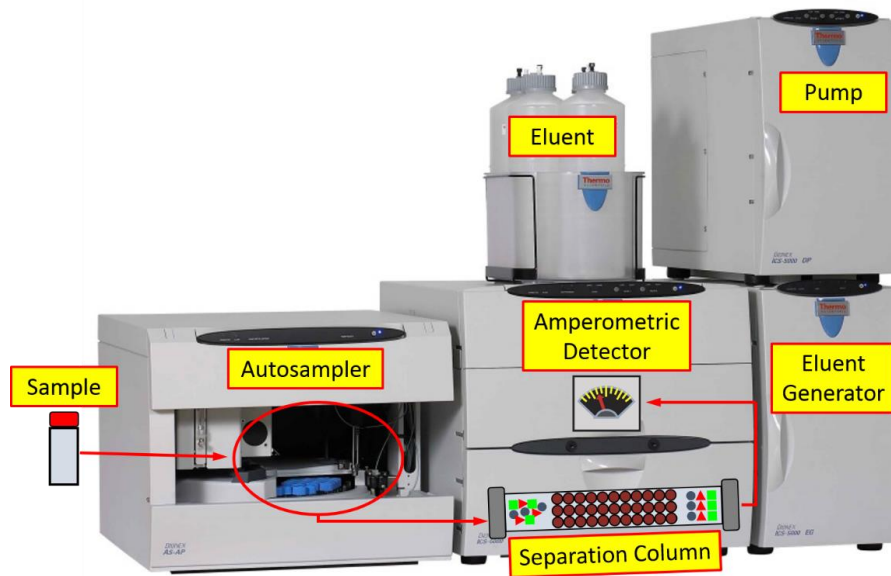


Fig. 28: Experimental setup of the HPAEC measurements [54].

The diluted sample is injected into the system by an autosampler and separated into its components by the separation column as mentioned above. The eluent, which transports the sample through the HPAEC system, can either be provided as ready for use solution or be prepared automatically by the eluent generator. After being separated from each other, the single components are detected amperometric. In the case of the polydisperse inulin samples, the molecules are reduced by the basic eluent (which contains sodium hydroxid), separated according to their different DP and oxidized again during amperometric detection.

1.9 Texture analysis (Gel Hardness)

Gels exhibit a distinctive behavior under deformation. Depending on the type of the gel and its sample preparation, the gel can be characterized by the application of a certain deformation and the measurement of the responsive force. Those results can be achieved by performing texture analysis experiments. Therefore, in this section the basic knowledge about the texture analysis of food gels is summarized. The information in this section was mostly taken from [55, 56].

The texture of food products (including edible gels), can be considered as the composite of its structural elements and the manner those elements are registered with physiological senses. The term “structural elements” refers to the microscopic and molecular structures, as well as to the macroscopic structure that can be observed visually. Textural characteristics can be grouped into three main classes: Mechanical characteristics, geometrical characteristics and

other characteristics (referring mainly to moisture and fat content of the food). “Mechanical characteristics” are determined by the examination of the reaction of food to the application of stress. Organoleptically, they are measured by pressures exerted on the teeth, tongue and the roof of the mouth during eating. “Geometrical characteristics” refer to the arrangement of the constituents of the food and are reflected mainly in the appearance of the food product. They are mostly sensed visually. In the category of “other characteristics” mouthfeel factors are included, that cannot be easily resolved on the basis of mechanical and geometrical properties. In this work, only mechanical properties were determined. Therefore, below the focus is placed on those properties.

The mechanical characteristics can be divided into five basic parameters: Hardness, cohesiveness, viscosity, elasticity (or springiness) and adhesiveness. Those parameters (except the viscosity which needs to be determined by e.g. oscillatory rheology measurements, see section 1.11) can be determined by a typical texture analysis experiment, either by compression of a sample of defined geometry (most often cylindrical shaped samples) or by penetrating a sample with a cylindrical shaped probe. The two methods will be explained in more detail below. An example of a texture analysis curve (which is plotted as force versus time), with the respective basic parameters indicated, can be seen in Fig. 29.

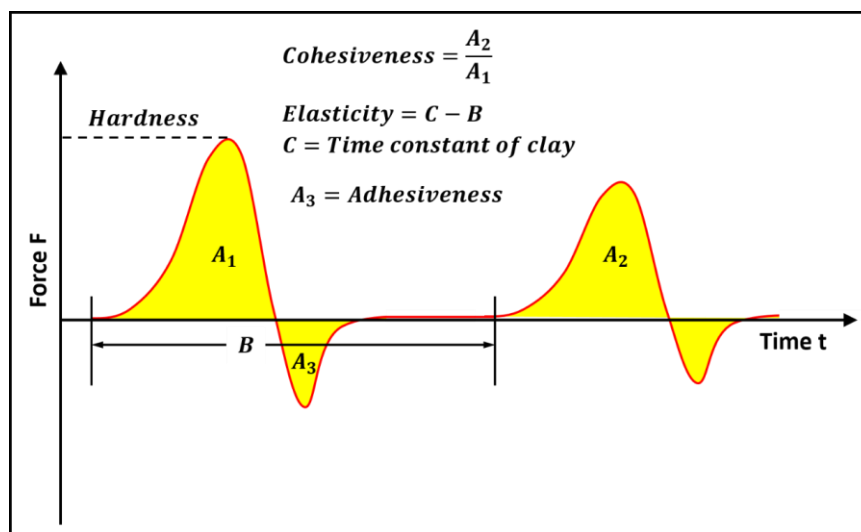


Fig. 29: A typical texture analysis curve, which should be read from left to right, with peak A_1 being the first chew and peak A_2 the second chew [56].

The “hardness” is defined as the force necessary to attain a given deformation. In Fig. 29, the hardness of the sample can be determined as the maximum of peak A_1 . The “cohesiveness” is the strength of the internal bonds, making up the body of the sample. It is defined as the

ratio of the areas of peak A_2 and peak A_1 . The “viscosity” is the rate of flow per unit force. The “elasticity” (or springiness), is represented by the rate at which a deformed material returns to its un-deformed condition, after the deforming force is removed. In Fig. 29, it can be determined as the difference between the time constant of a standard substance C (in this case clay) and the time that elapses from the begin of the first chew until the start of the second chew (the time period B in Fig. 29). “Adhesiveness” defines the work, which is necessary to overcome the attractive forces between the surface of the sample and the surface of other materials the sample comes in contact with (e.g. tongue, teeth, palate etc.). It is visible as the negative force area of peak A_3 in Fig. 29, after the first chew, when the plunger is pulled away from the food sample.

The first four characteristics are related to forces of attraction between the molecules/particles of the food sample, whereas adhesiveness is related to surface properties.

In this work, the texture profile analysis (TPA) experiments were performed with two types of stainless steel stamps. One with a diameter of $d = 7\text{ cm}$, which exceeded the diameter of the cylindrical shaped inulin samples ($d = 4\text{ cm}$) and the other stamp with a diameter of $d = 1\text{ cm}$. If the diameter of the plunger is larger than the diameter of the sample, the registered responsive force of the sample is mostly due to uniaxial compression. If the diameter of the stamp is smaller than the diameter of the sample, the registered responsive force results from puncturing of the sample, which is a combination of uniaxial compression and shear. The performance of the two different types of TPA measurements also have a very practical cause. Since the inulin gels vary in texture according to the different type of inulin employed and the sample preparation parameters used, some inulin gels exhibit a very soft texture after 24 h of ageing. Those very soft samples cannot keep the cylindrical shape of the vessel they were prepared in after being removed from it. Therefore, the determination of the gel hardness was performed as puncture/indentation experiments and the determination of the distinctive crack pattern of the samples was performed as compression experiments (see section 3.2.4). In Fig. 30 and Fig. 31, the compression and the indentation measurements of an inulin gel sample are shown. The cylindrical shaped inulin gel sample in Fig. 30 exhibits a defined geometry. All the samples are compressed for a certain distance (strain) and the responsive force is measured, which can be used to determine the gel hardness as mentioned above. Additionally, the

Introduction

inulin gels exhibit a distinctive crack pattern, after being compressed, which depends on the gels hardness (see section 3.2.4).

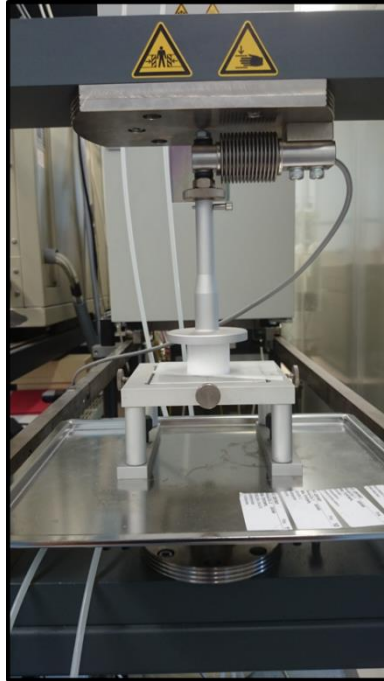


Fig. 30: Compression of cylindrical shaped inulin gel sample.

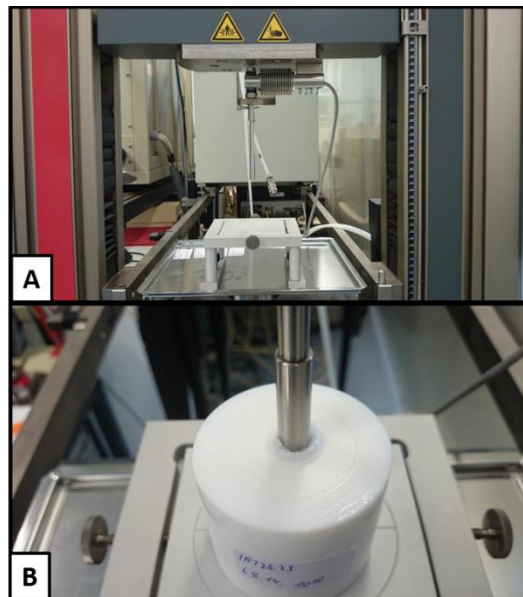


Fig. 31: A) Setup of texture analyzer for indentation measurement and B) indentation measurement of inulin gel sample.

In Fig. 31, the stainless steel plunger is pushed into the plane-parallel cylindrical shaped sample. The responsive force is measured and the gel hardness determined as mentioned above. Here it needs to be mentioned, that the measured responsive force depends on the area and with it the diameter of the used stamp (see Eq.(33)). If identical samples are examined by both

methods, the hardness trends are the same, yet the absolute hardness values are different. This must be considered, if hardness values of samples, which have been measured with different plunger diameters d , shall be compared to each other.

$$F = \sigma \cdot A = \sigma \cdot \left(\pi \frac{d}{2}\right)^2 \quad (33)$$

In Eq.(33), F is the measured responsive force, σ the stress applied on the sample, A the area of the plunger and d the diameter of the plunger. The determination of the gel hardness is very useful to learn about the texture of unknown samples. Since the compression/indentation of a gel sample also represents a stress being applied on the sample, the obtained hardness trends go along with the initial shear moduli of the respective samples, which have been examined by oscillatory rheology (see section 1.11). Therefore, the results of those two methods can be compared to each other.

1.10 Confocal Laser Scanning Microscopy (CLSM)

Inulin gel particles can be visualized by optical imaging methods such as light microscopy. Unfortunately, the primary particles of the completely developed inulin gels are very densely packed, what makes the spatial analysis of those gels with conventional light microscopy very difficult. Therefore, the inulin molecules are dyed with a fluorescent dye (Rhodamine B, see below) and visualized by Confocal Laser Scanning Microscopy (CLSM), which enables a spatial analysis of the gel samples and provides images with increased resolution, compared to conventional light microscopy. In this section, the basic knowledge about CLSM is summarized. The information in this section was mostly taken from [57, 58].

Confocal Laser Scanning Microscopy belongs to the fluorescent microscopy techniques, which are based on the excitation of fluorochromes (or fluorophores) (e.g. a dye like Rhodamine-B, which is bound to the molecule that should be examined. In the case of inulin dyeing, Rhodamine-B is bound hydrophobic to the inulin molecules, see Fig. 32) and the detection of the emitted light. Depending on the dye and the sample, those dyes can be bound to specific molecules or parts of the sample that shall be visualized.

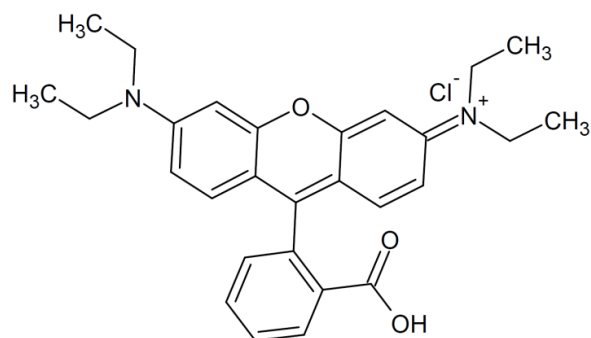


Fig. 32: Rhodamine-B structure [59].

Fluorescence belongs to the luminescent processes, in which a substance absorbs light and reemits light (photons) after a given time from an electronically excited state. The basic principle of fluorescence is pictured in Fig. 33.

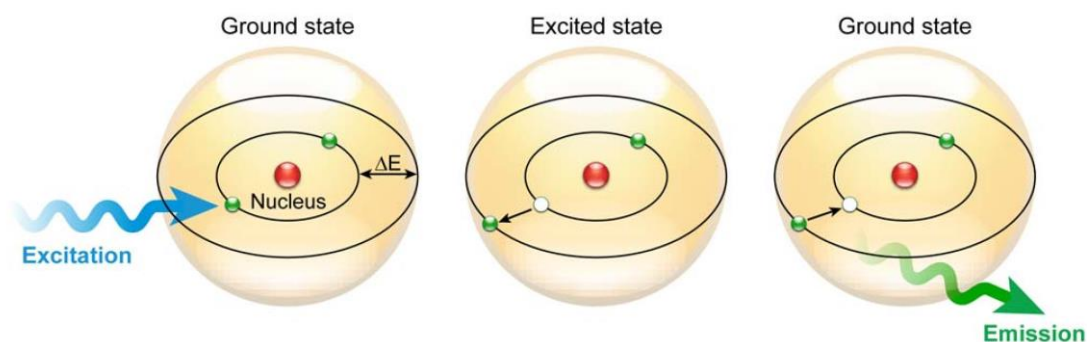


Fig. 33: Fluorescence principle [58].

In Fig. 33, a light quantum is absorbed (blue, λ_{ex}), which causes an electron to move to a higher energy orbit. After residing in this “excited state” for a particular time, the so called fluorescence lifetime, the electron falls back to its original orbit and the fluorochrome dissipates the excess energy by emitting a photon (in this case green, λ_{em}). The energy of photons involved in fluorescence and generally a quantum of light, can be expressed by Planck’s law (see Eq.(34)).

$$E = h \cdot \nu = h \cdot \frac{c}{\lambda} \quad (34)$$

In Eq.(34), E is the photon’s energy, h is Planck’s constant, ν is the frequency, λ is the wavelength of the photon and c is the speed of light.

In fluorescence microscopy (as mentioned above CLSM is also based on fluorescence microscopy), the optical resolving power determines the details observed in a specimen. If an exam-

Introduction

ined object is hit by light, the incident light is diffracted by the object. This deflection is increased with decreasing size of the object (see section 1.12). To obtain sharp microscopic images, the objective must capture as much of the diffracted light as possible. This is achieved with wide, angular openings (aperture) of the objective. The objectives light capturing capacity can be determined via its numerical aperture (N.A.).

$$N.A. = n \cdot \sin\alpha \quad (35)$$

In Eq.(35), n is the refractive index of the medium between the examined object and the objective and α is half the objective opening angle. In air, the theoretical maximum N.A. is 1. In practice, N.A. values in air above 0,95 cannot be achieved. By using immersion oils, N.A. values larger than 1 can be achieved and therefore, the use of oil immersion objectives is the only way to increase the magnification with sufficient resolution and contrast. In fluorescence microscopy, the resolution is not directly governed by the magnification. Additionally, resolution and contrast are two interrelated parameters, which are very important for fluorescence microscopy. As mentioned before, the individual objects in a specimen diffract the incident light and therefore, an illuminated point source within the examined sample is observed as bright central spot (Airy disc) with surrounding diffraction rings (Airy pattern) (see Fig. 34).

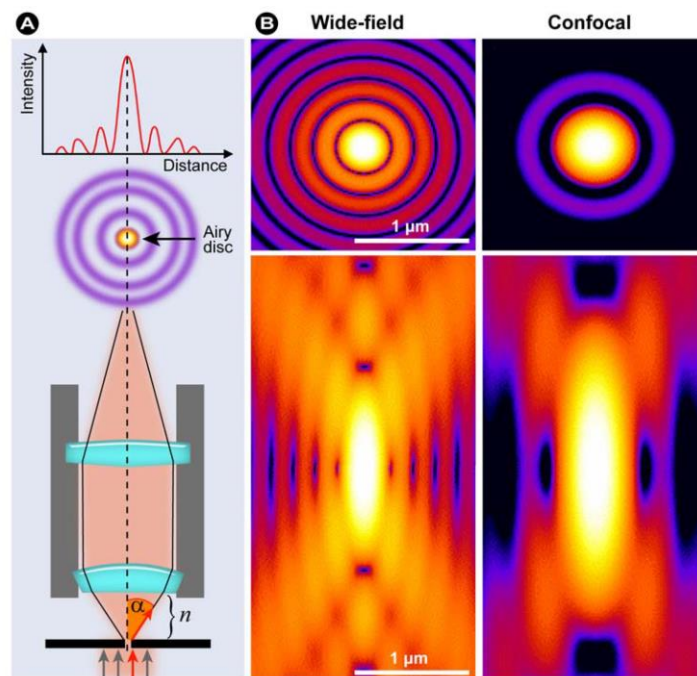


Fig. 34: A) Objective and light beam path: A point source in the focal plane is imaged and projected as bright central spot (Airy disc) with a surrounding diffraction ring pattern, B) Calculated x-y (upper images) and x-z (lower images) intensity distributions (log scale) for a point source imaged with wide-field and confocal microscopy [58].

Introduction

Optical microscopes can be assumed to be linear and shift-invariant. This means, the image of a specimen consists of the linear composition of all the specimen's single elements, resulting in the final image. This is described by the intensity point spread function (PSF). The Airy pattern is the intensity distribution of the intensity PSF in the focal plane (x-y). If the PSF in lateral (x-y) and axial (x-z) direction (see Fig. 34B) are combined, the three dimensional PSF is created, which defines the response of the entire optical system (lenses, mirrors, optical apertures and misalignments in the optical system) to the illuminated point source. Resolution can be defined as the smallest distance between two points in the specimen, that can still be discriminated as separate points at a particular contrast (see Fig. 35, diffraction limit). Therefore, the resolution can be determined via Eq.(36).

$$d = \frac{\lambda}{2N.A.} = \frac{\lambda}{2(n \cdot \sin\alpha)} \quad (36)$$

In Eq.(36), d is the distance between the two resolvable points (the resolution).

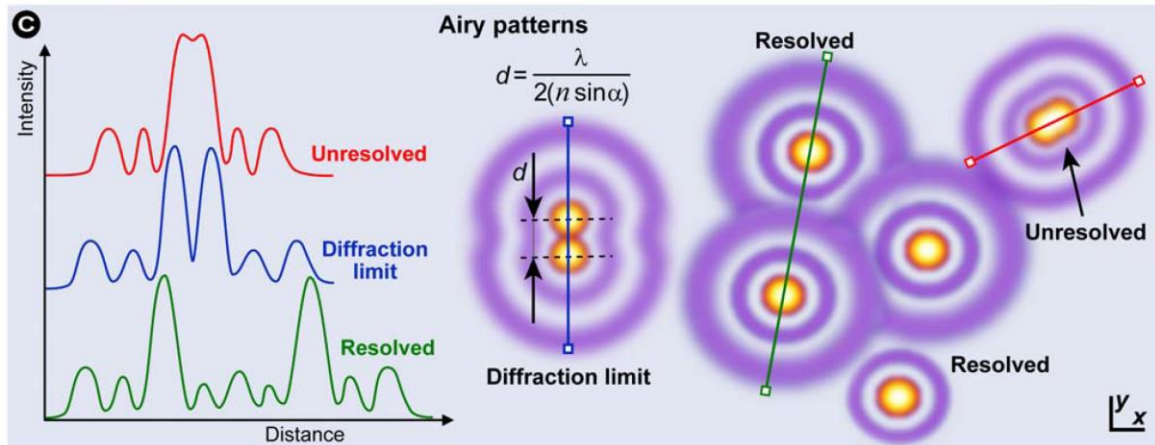


Fig. 35: Schematic diagram of an Airy disc diffraction pattern: Abbe diffraction limit, contrast, and optical resolution [58].

Contrast is defined as the difference between the maximum intensity and minimum intensity occurring in the space between two objects of equal intensity. If the two point objects are well separated, the contrast minimum between them is near zero and the objects can be discriminated (they are resolved, see green curve, Fig. 35). If the point objects approach each other and their PSFs start to overlap, the smallest distance is reached, at which the two points can still be detected separately (diffraction limit, see blue curve, Fig. 35). If the two points overlap even further, the intensity minimum between the two objects maxima disappears and the two objects are no longer resolved (see red curve, Fig. 35). Thus, the smaller the Airy patterns are, the smaller is the minimum distance between the two points and the higher is the resolution

(compare wide-field and confocal pattern in Fig. 34). For conventional light microscopes, the smallest resolvable distance between two points cannot be smaller than half the wavelength of the imaging light. Therefore, an increase in resolution can only be achieved if the wavelength of light used is as small as possible.

CLSM is based on a conventional optical microscope in which instead of a lamp, a laser beam is focused on the sample and an image is built up pixel-by-pixel by collecting the emitted photons with a photomultiplier. Therefore, CLSM combines point-by-point illumination with simultaneous point-by-point detection. A key feature of CLSM is its ability to block light, which is emitted from out of focus parts of the sample (see Fig. 36). Therefore, the resolution of CLSM is increased, compared to conventional light microscopy, and well focused images from various depth within the sample can be obtained (this process is called “optical sectioning”). In Fig. 36, the principle of conventional light microscopy (wide field) and CLSM are compared to each other. The concept of illuminating the sample with excitation light (in this case blue) and the detection of the light, which is emitted by the sample (the emitted light exhibits a longer wavelength than the excitation light, in this example green), is identical for confocal microscopy and conventional wide field fluorescence microscopy. However, there are significant differences between CLSM and wide field microscopy. Firstly, in CLSM the excitation laser light is scanned over the sample and the emitted light originates from this area (in wide field microscopy the whole sample is illuminated at once). And secondly, on the detection beam path of CLSM, a pinhole aperture in front of the detector, prevents light emitted from above or below the focal plane (dotted black lines in Fig. 36A) and B)) from reaching the detector. Since only light from the focal plane (solid black line in Fig. 36A) and B)) reaches the detector, the resolution of CLSM is increased compared to wide field microscopy. Combined with the very small focus of the excitation laser beam, this enables the collection of spatial information from defined positions within the sample. Therefore, confocal microscopy is very often used for the spatial analysis of sensitive samples, which can be damaged by the high energy of the imaging beam (e.g. as used for Transmission Electron Microscopy TEM or Scanning Electron Microscopy SEM) or by the sample preparation necessary for this imaging method (e.g. for an ordinary SEM measurement, the sample must be completely free from water. If the inulin gels are freeze dried, to sublime the contained water, the network structure is damaged by the sublimating water molecules).

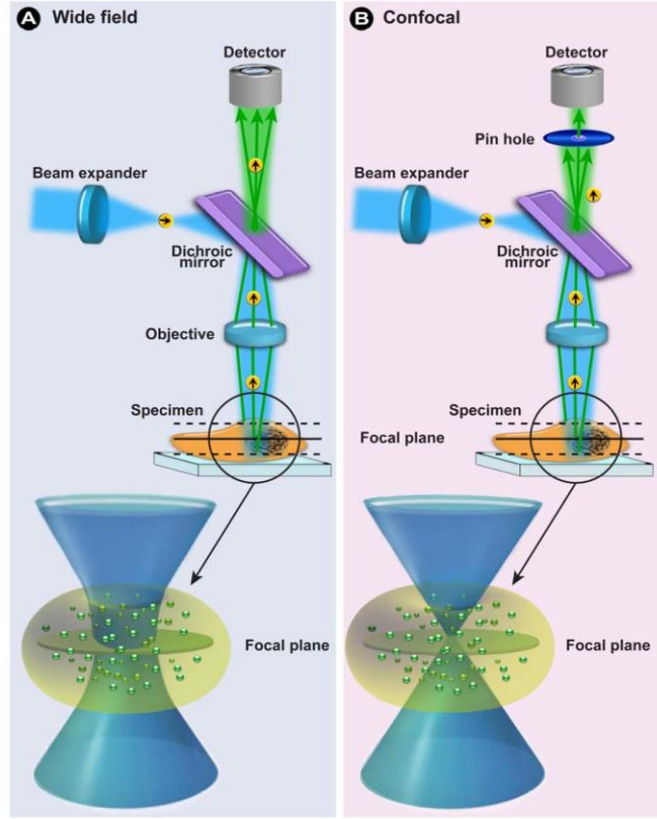


Fig. 36: Comparison of conventional light microscopy A) and CLSM B) [58].

1.11 Oscillatory rheology

Oscillatory rheology can be used to examine the viscoelastic properties of the completely developed inulin gels. Therefore, in this section the basic knowledge about oscillatory rheology is summarized. The information in this section was mostly taken from [60, 61].

Generally, the term rheology describes the deformation and the yielding of substances. The behavior of all substances under the application of a certain shear force is bordered by two extreme cases: the yielding of ideal viscous fluids and the deformation of ideal elastic solids. All real substances show properties of both extreme cases under deformation (i.e. on one hand they react like a viscous liquid and on the other hand they exhibit properties of an elastic solid) and exhibit therefore viscoelastic properties. The viscous part of the substance can be defined by Newton's law (see Eq.(37)) and the elastic part is described by Hooke's law (see Eq.(38)).

$$\sigma = \eta \dot{\gamma} \quad (37)$$

$$\sigma = G\gamma \quad (38)$$

In Eq.(37) and Eq.(38), σ is the shear stress, η is the viscosity, $\dot{\gamma}$ is the shear rate, G is the shear modulus and γ is the shear deformation (also called strain). All those basic rheological parameters can be defined via the “two plate” model (see Fig. 37).

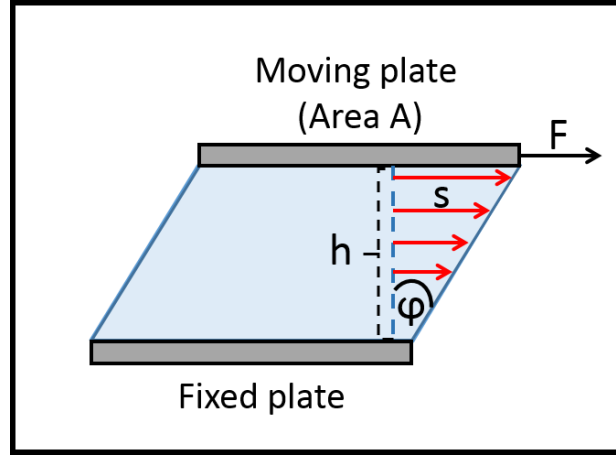


Fig. 37: Two plate model [60].

The upper plate with area A is moved by a shear force F and the resulting speed v of the upper plate is measured (the speed of the upper plate can be determined via Eq.(39)).

$$v = \frac{s}{t} \quad (39)$$

In Eq.(39), v is the resulting speed of the upper plate, s is the distance the upper plate is moved by the applied shear force and t is the time period the force is applied on the upper plate. The lower plate in Fig. 37 is fixed and does not move at all. Between the two plates with the distance h to each other, a sample is sheared. Between the surface line of the sample without deformation (dashed blue line in Fig. 37) and the resulting surface line of the sample under deformation (solid blue line on the right hand side of Fig. 37), the angle ϕ is spanned. To determine the rheological parameters precisely, the sample may not slip on the surface of the plates and only laminar flow (no turbulences) should occur in the sample. The above mentioned basic rheological parameters can be derived from Fig. 37 with following equations.

$$\sigma = \frac{F}{A} \quad (40)$$

The shear stress σ can be determined as ratio of the applied shear force F and the area of the upper plate A .

$$\dot{\gamma} = \frac{v}{h} \quad (41)$$

In Eq.(41), v is the current speed of the upper plate (v varies from its minimum to its maximum value) and h is the distance between the two plates (see Fig. 37). A fluid that obeys the linear relation of Eq.(37) is called “Newtonian” (representing the above mentioned viscous fluids), which means that its viscosity is independent of shear rate for the shear rates applied (e.g. water). A Newtonian liquid is also characterized by a constant viscosity with respect to the time of shearing, and an immediate relaxation of the shear stress if the shear force is removed. Often materials such as dispersions, emulsions and polymer solutions deviate from the Newtonian behavior and the viscosity decreases or increases with increasing shear rate, what indicates a shear thinning respectively a shear thickening (dilatant) behavior. The respective curves of shear stress versus strain and viscosity versus strain can be seen in Fig. 38.

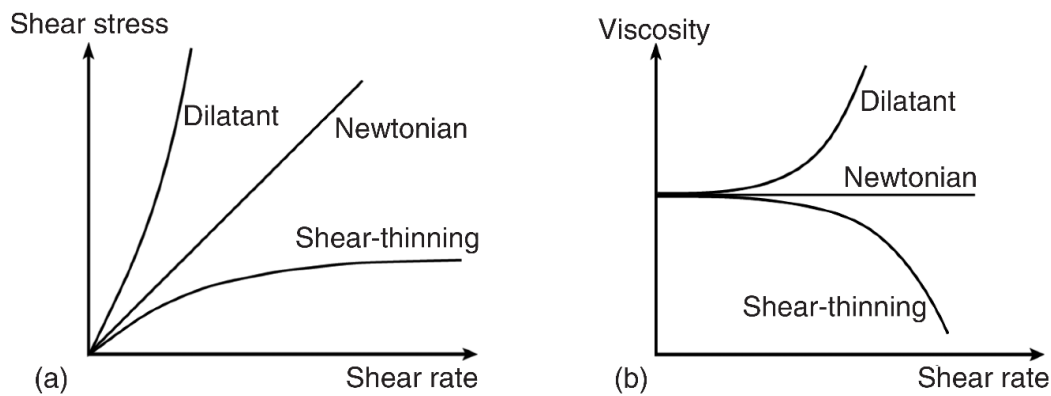


Fig. 38: Typical flow curves for Newtonian, shear thinning and shear thickening (dilatant) fluids: (a) shear stress vs. shear rate, (b) viscosity vs. shear rate [61].

For a prediction of the flow behavior of a substance, the flow history of a material needs also to be taken into account. Two important phenomena related to the time dependent flow behavior are thixotropy and rheopexy. For materials showing thixotropic behavior, the viscosity gradually decreases with time under constant shear rate or shear stress followed by a gradual structural recovery when the stress is removed. A thixotropic behavior can be determined by measuring the shear stress as a function of an increasing and decreasing shear rate. An example of a flow curve of a thixotropic fluid is pictured in Fig. 39.

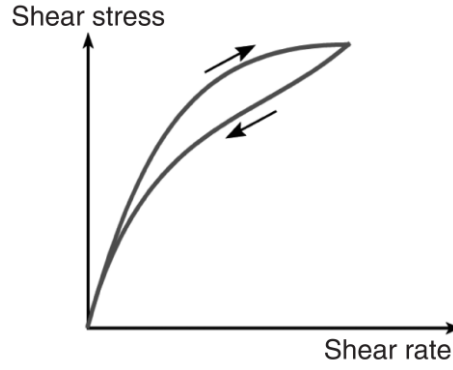


Fig. 39: Flow curve of a thixotropic material [61].

The term rheopexy is defined as shear thickening followed by a gradual structural recovery when the shearing is stopped.

As mentioned above, the other extreme response of substances to an applied shear force is the ideal elastic behavior of solids, which can be described by Eq.(38). The shear deformation γ used in Eq.(38), can also be derived from Fig. 37 by following equation.

$$\gamma = \tan\phi = \frac{s}{h} \quad (42)$$

As mentioned above, s is the distance the upper plate is moved by the applied shear force and h is the distance between upper and lower plate. The shear modulus G of an ideal elastic solid is independent of the shear stress and duration of the shear load. As soon as a deformation is applied, a responsive stress occurs instantaneously. In viscoelastic materials, stress relaxes gradually over time at constant deformation and eventually vanishes for viscoelastic liquids. In the so-called linear viscoelastic regime (LVE), the stress relaxation is proportional to the applied strain and the substance recovers its structure completely after the shear deformation is stopped. Above a critical strain, the apparent shear modulus becomes strain dependent and the structure of the substance is damaged irreversibly. This is the so-called nonlinear viscoelastic regime. To examine the linear viscoelastic properties of a substance, most often small amplitude oscillatory shear (SAOS) tests are performed. When a sinusoidal oscillatory shear strain is applied with the amplitude γ_0 and an angular frequency ω the shear deformation $\gamma(t)$ can be determined via Eq.(43).

$$\gamma(t) = \gamma_0 \sin(\omega t) \quad (43)$$

Introduction

In Eq.(43), $\gamma(t)$ is the time dependent shear deformation, γ_0 is the applied amplitude, ω is the angular frequency and t the time. The shear rate $\dot{\gamma}$ can be determined as the time derivative of the shear strain γ .

$$\dot{\gamma}(t) = \frac{d\gamma(t)}{dt} = \gamma_0 \cos(\omega t) \quad (44)$$

A linear viscoelastic substance responds with a sinusoidal course of shear stress $\sigma(t)$ with an amplitude σ_0 and an angular frequency ω , but is phase shifted by an angle δ compared to the applied strain.

$$\sigma(t) = \sigma_0 \sin(\omega t + \delta) \quad (45)$$

Depending on the substance, the phase shift angle δ can be between 0° and 90° . For ideal elastic materials the phase shift disappears, resulting in $\delta = 0^\circ$, while for ideal viscous liquids the phase shift angle equals 90° . The shear modulus G can be expressed in a complex form G^* .

$$G^*(\omega) = G'(\omega) + iG''(\omega) \quad (46)$$

In Eq.(46), G' is the storage modulus, representing the elastic behavior of the substance and G'' is the loss modulus, representing the viscous properties of the sample. The storage and the loss modulus can be expressed as sine and cosine function of the phase shift angle δ .

$$G'(\omega) = \frac{\sigma_0}{\gamma_0} \cos \delta \quad (47)$$

$$G''(\omega) = \frac{\sigma_0}{\gamma_0} \sin \delta \quad (48)$$

Therefore, the tangent of the phase shift represents the ratio of loss and storage modulus.

$$\tan \delta = \frac{G''(\omega)}{G'(\omega)} \quad (49)$$

The viscoelastic properties of a fluid can be characterized by oscillatory measurements. To characterize an unknown sample, most often amplitude sweeps (also called strain sweep) are performed (the amplitude is varied at a constant frequency). Up to a critical strain γ_c the structure of the tested fluid remains stable and G' and G'' are independent of the strain amplitude γ_0 . Those strain sweep tests have also been performed to analyze the completely developed

Introduction

inulin gels. To perform strain sweep tests, rotational rheometers are used (the materials are then characterized with an oscillatory shear flow). Three types of measuring systems are commonly used in modern rotational rheometers, namely concentric cylinder, parallel plate and cone-and-plate. The different types of measuring geometries are chosen according to the sample properties (e.g. the concentric cylinder system is especially suitable for low viscous liquids). Typical shear rates, that can be measured with rotational rheometers are in the range of 10^{-3} up to 10^3 s^{-1} . Due to the shear sensitivity of the inulin gels, in this work, a parallel plate measuring system has been used, which can be seen in Fig. 40 (the samples have been examined without being pre-sheared, see section 2.8).

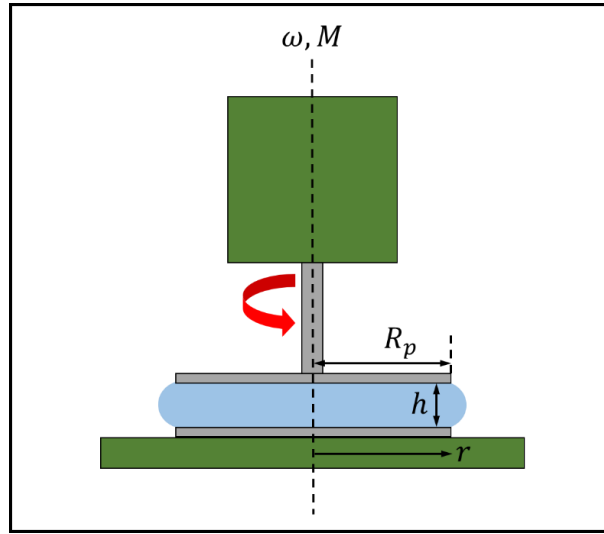


Fig. 40: Parallel plate geometry [61].

In Fig. 40, the sample within the gap of height h (also called gap size) between the two parallel plates, is sheared by the rotation/oscillation of one of the plates (most often the upper plate is the rotating/oscillating plate and the lower plate is fixed) at an angular velocity ω . The distance h between upper and lower plate is constant throughout the whole gap. The circumferential velocity v increases with increasing distance r from the center of the plate. For the distance r the following applies: $0 \leq r \leq R_p$ with $r = 0$ at the center of the plate and $r = R_p$ at the rim of the plate. The shear rate $\dot{\gamma}$ can be determined via Eq.(50).

$$\dot{\gamma} = \frac{v}{h} = \frac{(\omega r)}{h} \quad (50)$$

The shear rate at constant ω is not constant within the gap. Therefore, the calculations and analysis of rheological results in parallel plate measuring systems are typically related to the

maximum shear rate value at the rim of the plate ($r = R_p$). Thus, the shear rate can be varied over a wide range by changing the gap size h and the angular velocity ω . The shear stress σ is a function of the shear rate. Since the shear is not constant within the gap (as mentioned above), to relate the shear stress to the total torque M an expression for the $\sigma(\dot{\gamma})$ dependence is necessary. The shear stress of Newtonian liquids depends linearly on the shear rate and can be expressed by Eq.(51).

$$\sigma(R_p) = \frac{2M}{\pi R_p^3} \quad (51)$$

In Eq.(51), $\sigma(R_p)$ is called the “apparent shear stress”, M is the torque and R_p is the radius of the plate. For non-Newtonian fluids a simple approximate single point method was developed [62], to correct the shear rate data, based on the assumption that the true and apparent shear stress must be equal at some position near the rim of the plate. This actually occurs at the position where $r/R_p = 0,76$ and this holds for a wide range of liquids. The parallel plate measuring system can be used for measurements of suspensions with large particles by using large gap heights. Therefore, in this work the parallel plate geometry was chosen to analyze the shear sensitive inulin particle gels.

1.12 Particle size determination (Light scattering)

The texture of the completely developed inulin gels is significantly influenced by its primary particle size. Therefore, the determination of the average primary particle size is an essential part of the examination of the inulin gels. In this work, the average primary particle size of the completely developed inulin gels was determined by light scattering. Thus, in this section the basic knowledge about light scattering is summarized. The information was mostly taken from [63-65].

Normally, the average particle size is represented by a mean diameter. Since particles are three dimensional objects, which are not necessarily of spherical shape, they cannot be described by a diameter without further specification. Therefore, the concept of the “equivalent sphere” (see Fig. 41) is introduced, which relates a non-spherical particle to an equivalent sphere with the same properties (e.g. same weight, same surface, same volume etc.). This enables the estimation of the average particle size with the respective mean diameter.

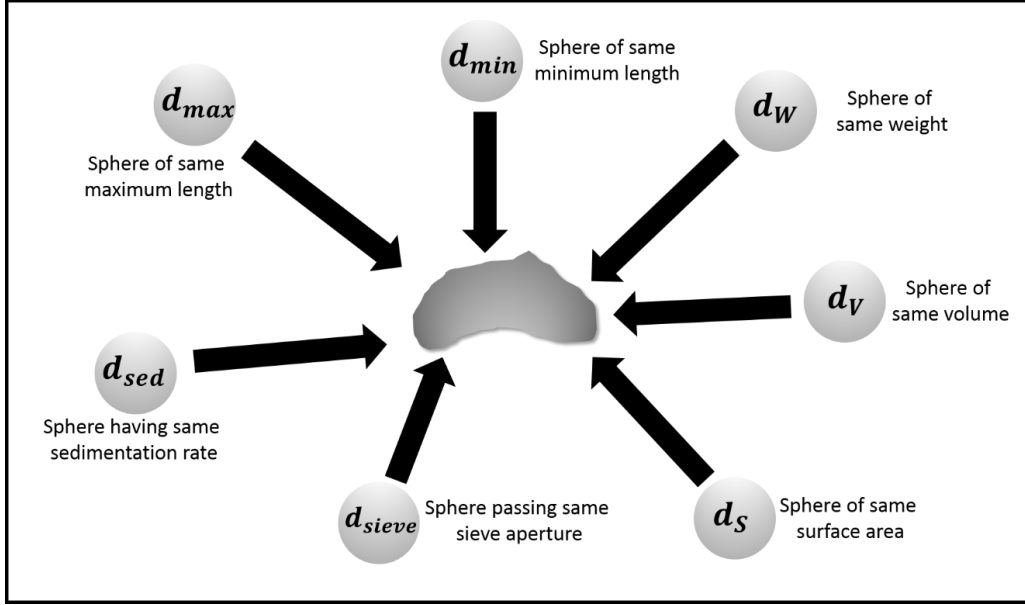


Fig. 41: Model of equivalent sphere [63].

In practice, crystallization processes often result in particles with a polydisperse particle size distribution (PSD). The particles are sorted according to their size in size classes. The narrower the classes are, the more precise is the classification of the differently sized particles. PSDs are expressed by normalized frequency distribution (q_x) and cumulative distribution (Q_x) curves. The former describes the amount of fractions within a defined interval of particle sizes. The latter indicates the quantity of particles larger or smaller than a certain size. Depending on the analysis method, PSDs can be weighted by the number of particles in a particular size class, by the volume those particles occupy or by the intensity of the detected signal (caused by the respective size fraction). For example, microscopic methods generally yield number weighted results and light scattering methods normally yield volume weighted PSDs. Normally, the results of particle size measurements are presented as weighted mean diameters. In this work, the number weighted (Eq.(52)) and the volume weighted (Eq.(53)) mean diameters were used.

$$D[1, 0] = \frac{(\sum n_i D_i)}{(\sum n_i)} \quad (52)$$

$$D[4, 3] = \frac{(\sum n_i D_i^4)}{(\sum n_i D_i^3)} \quad (53)$$

In Eq.(52) and Eq.(53), n_i is the number of particles in class i with the mean diameter D_i .

Introduction

The determination of the average particle size by light scattering techniques is based on the interaction of an incident light beam (with given wavelength λ) with particles (most often in solution). Depending on the particles physical properties, the light beam is reflected, diffracted, refracted and/or absorbed (see Fig. 42). The scattered light (including diffraction, reflection and refraction) is detected and the particle size is determined by the angular distribution of the scattered intensities. In practice, two types of light scattering are employed: static light scattering (SLS) and dynamic light scattering (DLS). In SLS experiments, the particle size is derived from the angle dependent scattered intensities. This enables the detection of particle sizes of a few hundred nanometers up to several micrometers. In DLS measurements, the particle size is determined by correlating light intensity fluctuations with hydrodynamic motions of the particles. Therefore, with DLS particles ranging from the lower nanometer region to the lower sub-micrometer region can be analyzed.

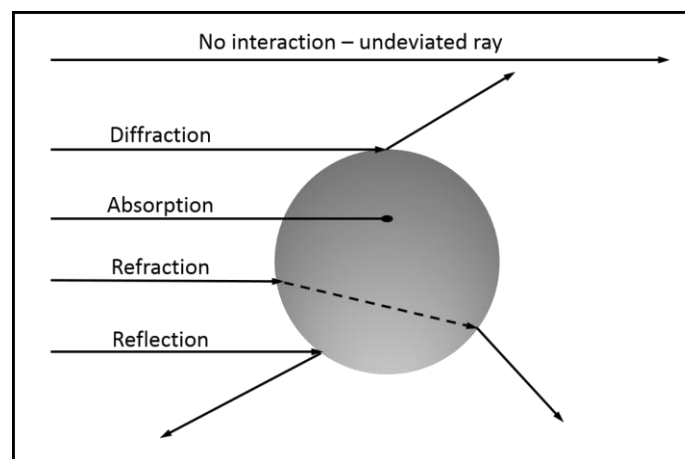


Fig. 42: Light rays interacting with a particle [64].

As already mentioned above, in this work the average primary particles sizes were determined by laser diffraction, which makes use of the principle of static light scattering. Static light scattering is based on the scattering theories of Rayleigh, Fraunhofer and Mie. Each model is valid in a particular size range of the particles and depends on the relative refractive indices between the scattering material and its surrounding medium. When a coherent laser beam hits an object, the light is scattered in all directions, resulting in characteristic scattering-angle dependent intensity patterns. As mentioned above, scattering is a combination of refraction, diffraction and reflection. The scattering pattern of spherical particles is pictured in Fig. 43 (“Bull’s eye” pattern).

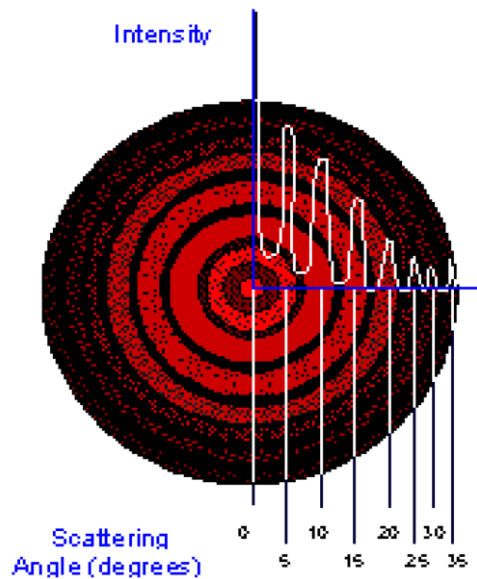


Fig. 43: "Bull's eye" scattering pattern [64]

The overlaid plot in Fig. 43 is a graphical representation of the intensity I (y-axis) versus the scattering angle θ (x-axis). This is how the scattering pattern appears to the eye if it is projected on a screen (or a 2D detector, compare section 1.7). The scattered intensity is a function of the scattering angle θ , the wavelength λ of the incident light, the particle size and the relative refractive index between scattering particles and the surrounding medium. With increasing distance from the center of the "Bull's eye" pattern, the intensity decreases and the distance between two rings becomes smaller (see Fig. 43). Simplified, small particles scatter light with low intensity at large angles (the signal is visible in the outer, dark rings of the "Bull's eye" pattern) and large particles scatter light with high intensity at small angles θ (represented by the inner rings of the "Bull's eye" pattern). In Fig. 44, the scattering patterns of differently sized spherical particles are pictured.

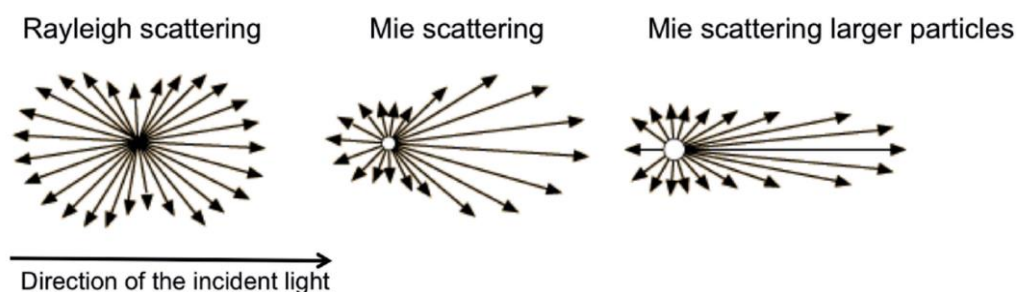


Fig. 44: Rayleigh and Mie scattering [66].

Introduction

Particles that are significantly smaller than the wavelength of the incident beam ($D < 0,1\lambda$) show Rayleigh scattering. Since the light is scattered equally in all directions in a Rayleigh scattering process, no angular information can be obtained, that could be of use for a laser diffraction experiment. Therefore, most laser particle size analyzers are based on the Fraunhofer and Mie theories. Particles with a particle size, which is similar to the wavelength of the incident light ($0,1\lambda < D < 10\lambda$), show Mie scattering (see Fig. 44). For large particles ($D > 10\lambda$) the Fraunhofer diffraction theory (the incident light is mainly diffracted at the outer boundaries of the large spherical particles) is used. It can be approximately considered as Mie scattering for very large particles (see Fig. 44, right hand side), with scattered intensities at narrow angles (for large particles the scattering intensity is concentrated in the forward direction, typically at angles smaller than 10 degrees. For this reason Fraunhofer diffraction is also known as forward scattering).

In this work, a laser particle size analyzer (LS 13320) by Beckmann Coulter was used. A schematic set-up of the device can be seen in Fig. 45.

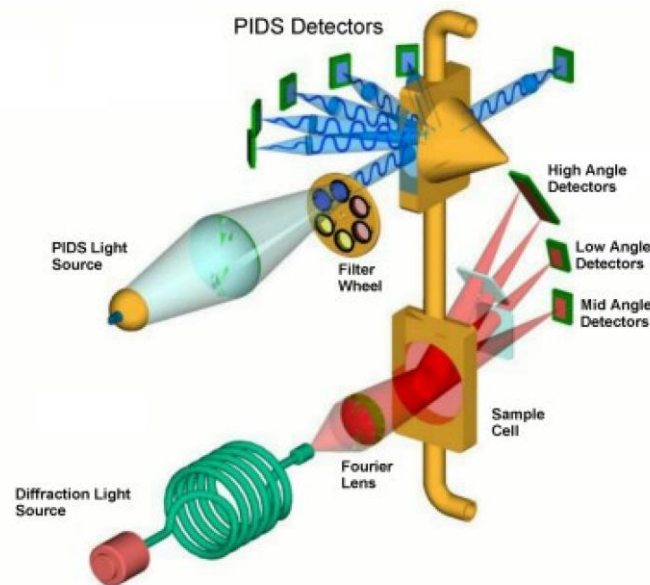


Fig. 45: Optical System of the LS 13320 [65].

The LS 13320 optical system consist of a “standard diffractometer set-up” (lower part of Fig. 45) for the detection of particles which exhibit a diameter $D > 0,4 \mu m$ and a set-up making use of the Polarization Intensity Differential Scattering (PIDS) technology (upper part of Fig. 45) for the detection of particles with a diameter of $D = 0,017 \mu m - 0,4 \mu m$. The sample

Introduction

suspension is circulated continuously through both sample cells, to ensure a homogeneous distribution of the differently sized particles in the optical system of the LS 13320. The standard set-up consist of an illumination source, the sample chamber in which the sample particles interact with the illuminating beam, a Fourier lens system used to focus the scattered light and an array of photodetectors that record the scattered light intensity patterns. The laser's radiation is converted into a beam of light by passing through a spatial filter and a projection lens. The laser beam then passes through the sample cell where particles suspended in liquid scatter the incident light in characteristic patterns according to their size. Fourier optics collect the diffracted light and focus it onto three sets of detectors, one for the low-angle scattering, the second for mid-angle scattering, and the third for large angle scattering. The PIDS assembly in the optical module uses an incandescent tungsten - halogen lamp (the PIDS light source) and three sets of vertically and horizontally polarized filters to provide polarized monochromatic light at three different wavelengths λ : 450 nm (blue), 600 nm (orange), and 900 nm (near-infrared, invisible). The light is focused through a slit and is formed into a narrow, slightly diverging beam that is projected through the PIDS sample cell. For each of the three wavelengths, the differential scattering pattern (PIDS pattern) is observed at six detectors centered at a scattering angle of about 90°. To analyze particles with a diameter $D < 0,4 \mu m$, the PIDS principle makes use of two physical light scattering effects. Firstly, the intensity of the scattered light I depends on the ratio of the particle size d of the scattering particles and the wavelength of the incident light λ (see Eq.(54)).

$$I = \frac{D}{\lambda} \quad (54)$$

Thus, the smaller the particle size D is at a constant wavelength λ , the lower is the scattered intensity I that can be detected. Therefore, the detected intensity can be significantly increased, if the wavelength of the incident light is decreased. Secondly, the scattering of light by small particles causes a so called “polarization effect”. If a small particle, much smaller than the light wavelength ($D \ll \lambda$), is located in a light beam, the oscillating electric field of the light induces an oscillating dipole moment in the particle (the electrons in the atoms of the particle move back and forth relative to the stationary particle). The induced motion of the electrons is in the direction of the oscillation of the electric field and therefore perpendicular to the direction of propagation of the light beam. Due to the transverse nature of light, the oscillating dipole radiates light in all directions except in the direction of oscillation as can be seen in Fig.

46. Thus, if a detector is facing the direction of oscillation it will receive no scattering from single dipoles. When the light beam is polarized in either the vertical or the horizontal direction, the detected scattering intensities $I_{vertical}$ and $I_{horizontal}$ at a given angle will be different. The difference between the detected intensity I and $I_{horizontal}$ ($I - I_{horizontal}$) yields the PIDS signal. Since the PIDS signal varies at different wavelengths, the measurements at several wavelengths (as mentioned above) provide additional information that can be used to further refine the size determination.

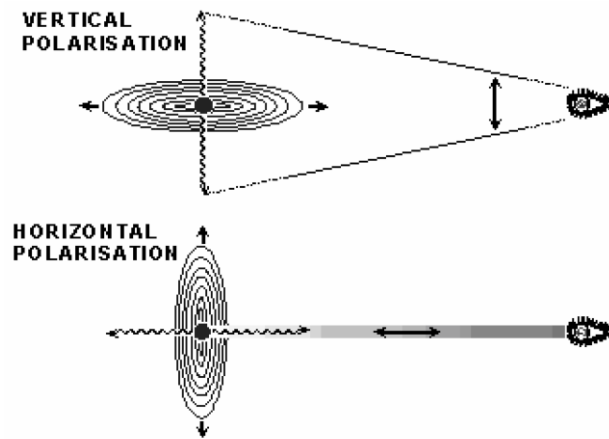


Fig. 46: Scattering from different polarizations [65].

Therefore, particles with a size ranging from the sub-micrometer region up to sizes of several micrometers, can be effectively analyzed by using the static light scattering principle of devices such as the LS 13320.

2 Materials and methods

2.1 Materials

All the samples were prepared with two types of long chain Inulin, HP and HPX (average DP = 23). They are commercially sold as spray dried, colorless powder by Beneo, Belgium.

2.2 Sample preparation and analytical methods

All samples had been prepared as inulin/solvent suspensions, containing 20% (w/w) inulin dry matter. Four different types of solvents were used: Deionized water, deionized water mixed with ethanol (VWR Chemicals, p.a., 20821.330; mass concentration of ethanol between 5 – 15 %), deionized water with a specific amount of sucrose dissolved (Sigma Aldrich, p.a., 84100-5KG; mass concentration of sucrose between 5 – 15 %) and the combination of deionized water, ethanol p.a. and sucrose p.a. (ethanol and sucrose mass concentration between 5 – 10 % respectively). The standard sample preparation was identical for all analysis methods. The suspensions were prepared by adding the inulin powder in portions under constant stirring (600 rpm) to the respective amount of solvent, which had been heated to the desired sample preparation temperatures (for deionized water as solvent 25, 40 and 60 °C, for the other solvents the samples were just prepared at 25 °C) in advance. The suspension was stirred at the desired temperature for 10 min in a sealed beaker, to minimize water loss during heating. This suspension was processed accordingly to the intended analysis method.

To learn about the impact of a higher shear rate (7000 rpm) during sample preparation, on the gel hardness and the particle size of the inulin gels, the HP and HPX gels, prepared with water acting as solvent, were also prepared as samples with a high shear rate applied during sample preparation (the suspensions were prepared as mentioned above with a shear rate of 7000 rpm instead of 600 rpm). Those suspensions were prepared for the texture analysis (section 2.6) and for the particle size determination (section 2.9). Apart from those exceptions, all the samples, no matter which solvent, were only prepared with a shear rate of 600 rpm.

2.3 Solubility in water

To determine the solubility of 20% inulin in the respective solvent (i.e. 10 g inulin in 40 g solvent), a sample was taken from the above mentioned suspension after 10 min stirring at the desired sample preparation temperature. The undissolved inulin and the solution were separated from each other by centrifugation (14800 rpm, 2 min). The refractive index of the inulin

Materials and methods

solution at 20 °C was measured, using a digital refractometer OPTI+ Brix/RI by Bellingham and Stanley (measuring range $n_D^{20} = 1,33 - 1,54$).

2.4 X-ray diffraction

The crystallinity of spray dried inulin powder and developing inulin gels, was determined by X-ray diffraction (XRD). The samples were contained in quartz mark tubes (length = 80 mm, outer diameter = 1,5 mm, wall thickness = 0,01 mm) and measured in transmission geometry for scattering angles 2θ between 5° and 25°. Measurements were done at a self-made instrument using a rotating anode x-ray generator (Rigaku MicroMax 007), multilayer optics (Osmic Confocal Max-Flux, $Cu - K_{\alpha}$, $\lambda = 1,54 \text{ \AA}$) and a 2D online image plate detector (Mar345). Diffraction patterns were obtained by radial averaging of the 2D data. To obtain the powder diffractograms, the samples were exposed for 10 minutes. For the in-situ XRD experiments during gel formation, inulin suspensions (section 2.2) were examined every 5 min over an aging time of 24 h.

2.5 High Performance Anion Exchange Chromatography

To examine how the chain length distribution of the inulin depends on the gel preparation temperature, HPAEC was performed. A sample was taken from the inulin suspension (section 2.2), after 10 minutes of stirring at the desired preparation temperature. The remainder of the suspension was decanted into disposable vessels ($d = 27 \text{ mm}$; $h = 42 \text{ mm}$), sealed airtight and another sample was taken after 24 h of quiescent storage at room temperature. For both samples, the undissolved inulin and the solution were separated from each other by centrifugation (14800 rpm, 2 min) and the overlapping solution was diluted 1:20 with deionized water. Of this dilution 10 μL were injected into the ICS – 5000+ DC by Dionex and separated on a CarboPac PA200 IC column, with a gradient of 120 – 320 mM sodium acetate in 100 mM sodium hydroxid, using a constant eluent flow of 0,5 mL/min. The separated fractions were detected by a pulsed amperometric detector (PAD).

2.6 Texture analysis

For the texture analysis of the inulin gels, two different methods were performed. To determine the distinctive crack pattern of the samples, the inulin suspension, described in section 2.2, was stored in cylindrical shaped Teflon vessels ($d = 40 \text{ mm}$; $h = 30 \text{ mm}$) and sealed airtight. After 24 h storing at room temperature, the samples were removed from the vessels and measured with the Z005 AllroundLine texture analyzer by Zwick Roell. The setup of the

Materials and methods

texture analyzer was a cylindrical shaped stainless steel stamp ($d = 7 \text{ cm}$), that compressed the sample to a maximum strain of 6 mm with a constant speed of 0,2 mm/s. To measure the gel hardness, the above mentioned inulin suspension was stored in disposable vessels as described in section 2.5 and measured after 24 h storage at room temperature with the Z005 Allround Line texture analyzer by Zwick Roell. The setup of the texture analyzer was a cylindrical shaped stainless steel stamp ($d = 1 \text{ cm}$), that penetrated the sample 6 mm deep with a constant speed of 0,2 mm/s. To determine a reproducible zero point, a trigger force of 0,1 N was set. The maximum strain of 6 mm for both types of measurements was chosen according to the inulin gels' shear sensitivity (a compression/indentation with a maximum strain of 6 mm was sufficient to exceed the point of shear breakdown for all the samples examined).

2.7 Confocal Laser Scanning Microscopy

To visualize the inulin particle gel network structure, inulin gels were analyzed with confocal laser scanning microscopy. All the HP and HPX samples were prepared as mentioned in section 2.2. The samples were dyed with Rhodamine – B by adding 4% (w/w) of a Rhodamine-B solution (0,2% (w/w) of Rhodamine^o-B by Sigma Aldrich, R6626, dissolved in distilled water) to the inulin suspension during sample preparation. After sample preparation, the suspensions were stored in sealed nunc chambers (8 wells) and analyzed after 24 h of storing at room temperature. The microscopy pictures were taken with a commercial setup consisting of an inverted microscope (IX70) and a confocal laser scanning unit (FluoView FV300, Olympus, Japan). As objective, an Olympus UPLSAPO 60xW/1,2 water immersion objective (60x magnification, N.A. = 1,2 and a working distance of 0,28 mm) was used. The Rhodamine-B dyes were excited with a helium-neon laser with an excitation wavelength of 543 nm. The images were recorded, using as emission filter a long pass filter LP565. All gel samples were examined at room temperature.

2.8 Oscillatory Rheology

To determine the viscoelastic properties of the completely developed inulin gels, oscillation rheology was performed at two different devices. All the HP samples, no matter which sample preparation temperature (between 25 °C and 60 °C) or solvent (see section 2.2) possessed a sufficient gel hardness, to be measured with the RMS 800 oscillation rheometer by Rheometrics Inc. The HP suspensions (section 2.2) were decanted into the circular opening ($d_{\text{hole}} = 25 \text{ mm}$, $h_{\text{hole}} = 10 \text{ mm}$) of rectangular plastic frames, to mold the HP gels into the

shape, necessary for the rheological measurements, without pre-shearing the shear sensitive samples. The frames were sealed airtight and after 24 h ageing at room temperature, the samples were removed from the frames and examined with a parallel plate geometry ($d_{\text{plate}} = 25 \text{ mm}$), with an angular frequency of 10 rad/s and an oscillation strain between 0,1% and 100%. To prevent the samples from slipping, p60 sandpaper was attached to the upper and the lower plate during the measurement.

All HPX gels, no matter which preparation temperature and solvent, had to be measured with a more sensitive rheometer, due to their low gel hardness. For this purpose, the Discovery HR-3 oscillation rheometer by TA Instruments was used. The HPX suspensions (section 2.2) were processed identically to the above mentioned HP samples. The samples were also measured with a parallel plate geometry ($d = 25 \text{ mm}$) and an angular frequency of 10 rad/s. Due to the very low gel hardness, the minimum oscillation strain varied between 0,001% and 0,1%. The maximum strain was set to 100% for all HPX samples. Here also p60 sandpaper was attached to upper and lower plate, to prevent the sample from slipping on the tool's surface.

2.9 Particle size determination (Light scattering)

To perform the particle size analysis, the inulin suspension was kept in disposable vessels as described in section 2.5. The inulin gel (24 h age) was diluted 1:20 with a 1:1 sucrose/water (same type of sucrose as mentioned above) solution. To disperse the gel primary particles, the diluted inulin suspension was treated with ultrasound for 1 min, with the amplitude set to 75% using the UIP1000hd ultrasonic rod ($d_{\text{(Sonotrode)}} = 22 \text{ mm}$) by Hielscher. To remove remaining aggregates, the treated sample was filtered through a filter with 4 – 7 μm pore size. The filtrate was analyzed by static light scattering using the LS13320 laser diffraction particle size analyzer by Beckmann Coulter. To determine the particle size distribution of the inulin primary particles, an optical model had to be formulated, which requires the complex refractive index as input parameter. For the real part of the refractive index 1.52 was used [67]. It is also known, that the refractive index of inulin is only marginally influenced by differences in molecular weight [13]. So the above mentioned real part of the refractive index could be used for high DP inulin and also for other types of inulin. Since the imaginary part of the complex refractive index of inulin is unknown, it was set to 0,1 according to the guidelines of Beckmann Coulter [65]. To minimize the influence of inulin aggregates, that passed the pores of the round filter or re-aggregated after filtration, the number weighted arithmetic mean diameter ($D[1,0]$) of the inulin primary particles was analyzed.

3 Results and discussion

3.1 X-ray powder diffraction

The x-ray powder diffraction was performed with the untreated HP and HPX powders provided by Beneo. The resulting patterns are represented in Fig. 47. The HP sample yields a mostly amorphous halo, without any visible Bragg reflexes for $2\theta = 5^\circ - 25^\circ$ (except one small reflex at $2\theta = 12,1^\circ$). The spectrum of HPX identifies the powder as semi-crystalline with several visible Bragg reflexes in the region of $2\theta = 5^\circ - 25^\circ$.

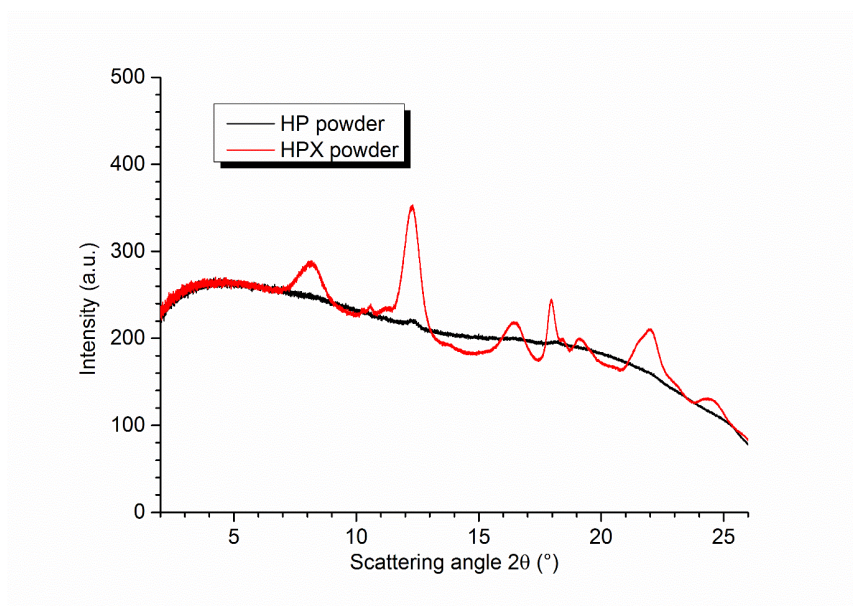


Fig. 47: X-ray powder diffraction.

The different crystallinity of the HP and HPX powders has a significant impact on the physical behavior of the analyzed samples, as will be seen later in this chapter.

3.2 The inulin-water system

In this chapter the results of the HP and HPX samples, that have been prepared with water acting as solvent, will be presented and discussed.

3.2.1 Solubility in water

Since inulin is a polydisperse oligosaccharide, the solubility does not only depend on the temperature of the used solvent (here deionized water), it also depends on the total amount of

inulin in the sample. If the total amount of inulin is increased at the same sample preparation temperature, the solubility will also increase. This is due to the broad DP distribution of the inulin powder. Because of their significantly higher solubility in water, the inulin molecules with a small DP will dissolve first and the molecules with a larger DP will follow later on, until the solution is saturated at the respective sample preparation temperature (see section 3.2.3). If the amount of added inulin at the same sample preparation temperature is increased, the amount of well dissolving small DP Inulin is also increased and the overall amount of dissolved inulin also increases. The dissolved amount of HP and HPX at 25 °C preparation temperature, dependent on the total amount added to the solvent, can be seen in Fig. 48.

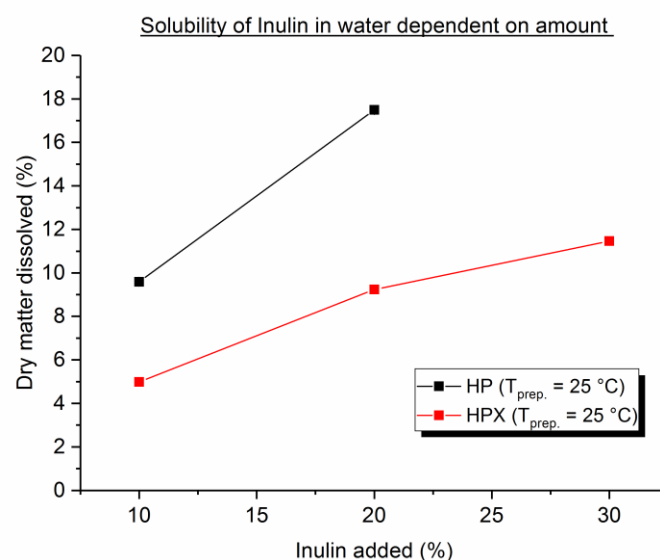


Fig. 48: Solubility of HP and HPX in water at 25 °C, dependent on added amount (w/w).

As mentioned above, with an increasing total amount of inulin added to water, the amount of dissolved HP and HPX increases too. Since the HP sample, with an added amount of 30% (w/w) of inulin, formed very hard gels, even after 10 minutes sample preparation, the dry matter and the liquid phase could not be separated properly from each other by centrifugation and no values for this concentration could be obtained. As all samples in this work were prepared with 20% dry matter of inulin, here the solubility of HP and HPX at the different sample preparation temperatures also refers to 20% dry matter in the sample. The equilibrium solubility of both types of inulin in deionized water can be seen in Fig. 50. To determine the concentration of dissolved matter, a reference curve was generated, by examination of the refractive indices at specific mass concentrations of inulin dissolved in deionized water. The measured indices were plotted against the mass concentration of inulin and fitted linearly. The data has

been fitted over the concentration range $0 \leq c \leq 0,35$ and the equation of the linear fit can be found in Fig. 49. This reference plot is the same for HP and HPX. This is why only one plot is pictured in Fig. 49.

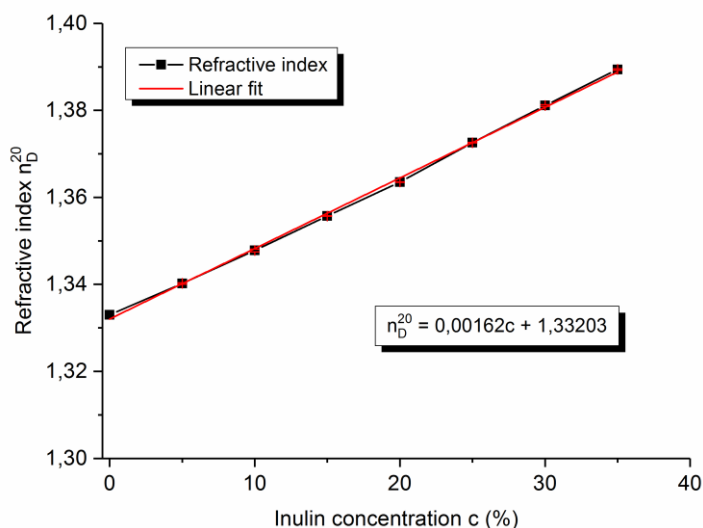


Fig. 49: Refractive index in dependency of the mass concentration.

The solubility of inulin increases with increasing sample preparation temperature. The mostly amorphous HP powder can be dissolved in a relative large amount with a comparatively small energy input. This is why almost 90% of the total amount is already dissolved at 25 °C preparation temperature. The maximum solubility of 20% of inulin dry matter is reached at temperatures slightly above 60 °C. Since the total amount of added inulin was 20%, even at increased preparation temperatures the dissolved amount will remain the same. In respect of the formation of a completely percolated gel, the maximum sample preparation temperature for HP samples was limited to 60 °C, to ensure a seeded crystallization during gel formation. The HPX powder exhibits a significantly lower solubility as HP at each sample preparation temperature employed, as can be seen in Fig. 50. The solubility trend for HPX is the same as for HP. The different solubility at each sample preparation temperature stems from the superior crystallinity of the HPX powder (see Fig. 47). During HPX production, inulin recrystallizes (see section 1), what results in crystalline inulin particles in the HPX powder. At the respective sample preparation temperature, first the amorphous parts of the HPX powder will be dissolved, starting with the short chain inulin and the longer chains follow later on. Afterwards, if still enough thermal energy is available in the solvent and the solution is not saturated yet, the inulin crystallites will start to dissolve. Because of their moderate solubility in water, the inulin molecules

with a larger DP will crystallize first during the production process. So the inulin crystallites in the HPX powder consist mainly of hardly soluble long chain inulin molecules. Additionally, to dissolve a crystalline structure, the lattice energy of the crystal network needs to be overcome by the thermal (or kinetic) energy of the solvent. Consequently, the crystalline HPX particles will remain mostly undissolved, even at increased sample preparation temperatures (at 80 °C, 10 % of the added amount of HPX are still undissolved), what results in the significantly lower solubility in water compared to the HP powder. To ensure a seeded crystallization, which leads to the formation of a completely percolated HPX gel, the sample preparation temperature of the HPX samples was limited to a maximum temperature of 80 °C.

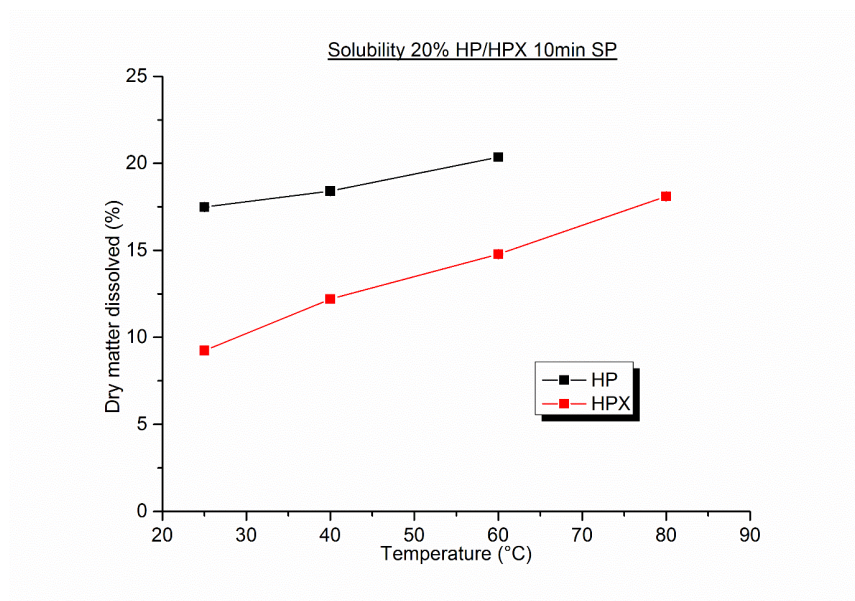


Fig. 50: Equilibrium solubility of 20% (w/w) inulin in water.

3.2.2 X-ray diffraction during gelation

The development of the particle gel network was examined by in-situ x-ray diffraction. Radial averaged diffraction patterns of an HP gel, prepared at 25 °C with a shear rate of 600 rpm and measured for 24 h during gelation, can be seen in Fig. 51. The intensity of the sample increases with increasing aging time. Since the intensity is representative for the crystallinity of the developing particle gel network [68], the crystallinity also increases with increasing sample age. Taking into account that the HP powder is mostly amorphous (Fig. 47), this result confirms that the dissolved inulin partly recrystallizes during gelation (see section 1.1). The intensities

of the Bragg reflexes at $2\theta = 12,1^\circ$ have been projected to the left hand layer, to make the gelation process more obvious.

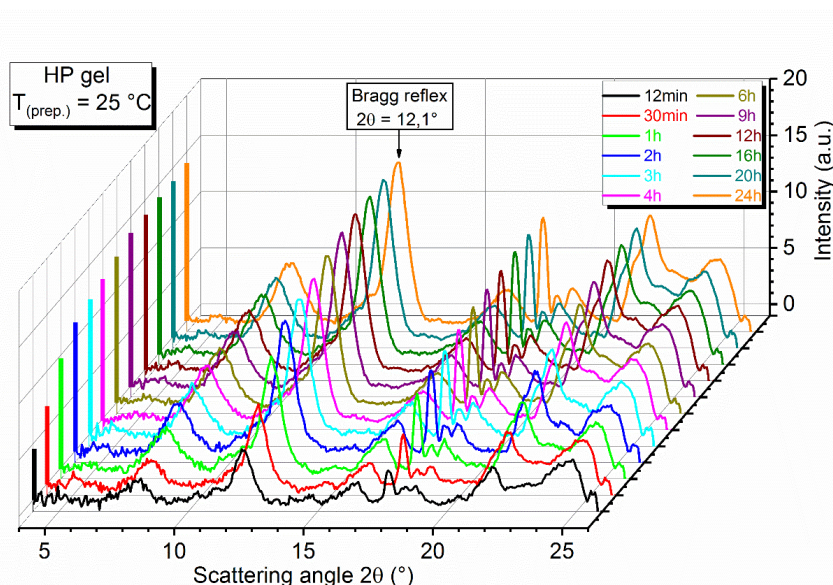


Fig. 51: XRD during gelation of an HP gel, prepared at 25°C and 600 rpm shear rate.

The diffraction patterns of an HPX gel, prepared at 25°C with a shear rate of 600 rpm and measured for 24 h during gelation, is pictured in Fig. 52. Here the same trend as for the development of the HP gel can be observed meaning, the crystallinity of the HPX sample increases with increasing aging time. This is again due to the recrystallizing inulin molecules, that had been dissolved previously during sample preparation. Again the intensities of the Bragg reflexes at $2\theta = 12,1^\circ$ have been projected to the left hand layer, to clarify the gelation process. If Fig. 51 and Fig. 52 are compared to each other, one can see, that the HPX sample exhibits a significantly higher initial intensity (black diffractogram in Fig. 52). This arises from the crystallinity of the HPX powder (see Fig. 47). The mostly amorphous HP powder dissolves almost completely even at a sample preparation temperature of 25°C . So there are very few crystalline particles present at the beginning of the gel formation, what is represented by the relatively small initial intensity of the HP sample (see Fig. 51 black diffractogram). Since the HPX powder exhibits a certain crystallinity, during sample preparation at 25°C , most of the already crystalline particles remain undissolved. So those particles are present from the beginning of the gel formation and generate a significantly higher initial intensity than compared to the respective HP sample.

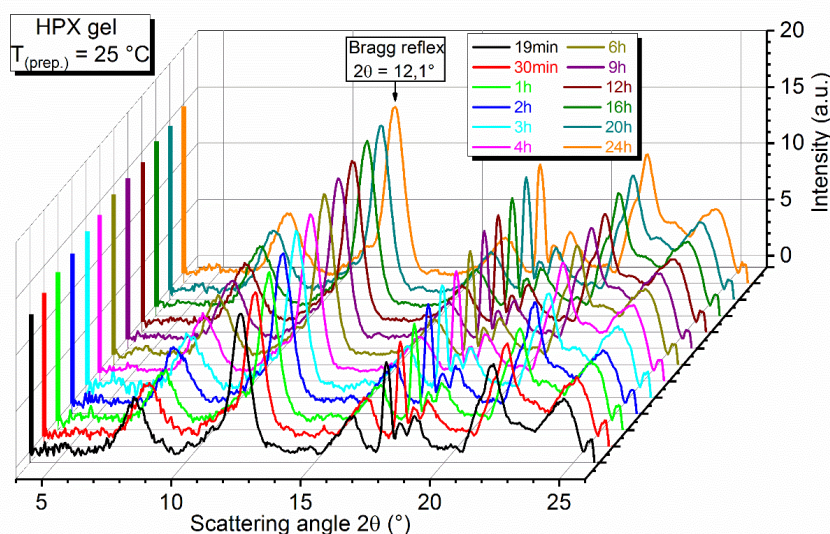


Fig. 52: XRD during gelation of an HPX gel, prepared at 25 °C and 600 rpm shear rate.

For both, HP and HPX, an increasing sample preparation temperature results in a decreased initial intensity. This finding will be explained further down in this section. Apart from that, the trends for the development of the crystallinity with increasing sample age remain the same. Because of this reason, in this section just the diffractograms for HP and HPX, prepared at 25 °C, are shown. The remaining diffractograms can be found in the Appendix section.

To examine the crystallization kinetics of the gel formation, the 12,1° reflexes were integrated and normalized to the respective maximum intensity. In Fig. 53 the relative intensities of the Bragg reflexes at $2\theta = 12,1^\circ$ of HP gels, prepared at 25 °C, 40 °C and 60 °C (shear rate 600 rpm), are compared to each other.

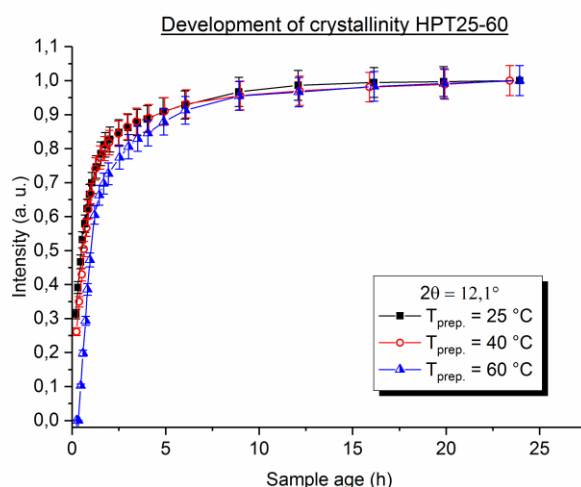


Fig. 53: Development of the relative intensity of HP gels prepared at 25 °C, 40 °C and 60 °C.

For all samples, the predominant fraction of the crystalline material forms within the first two to three hours of the gelation. In those first hours, the intensity increases to 80 – 85% of the maximum intensity. This rapid increase of the intensity is due to the crystallization process of the inulin particles. In the initial phase of the crystallization, the system exhibits a very high crystallization rate, arising from the presence of many seeds and a large amount of crystallizable material. Therefore, the crystallization will proceed very fast, distributed throughout the whole sample. In this initial phase, mostly the primary particle formation occurs. When the crystallization progresses for several hours, the system achieves a state of low Gibbs free energy, the main part of the primary particles is already formed (meaning the main part of the crystallizable material already crystallized) and the crystallization rate decreases significantly. This can be observed in Fig. 53 at sample ages above 5 h. In this stage of the crystallization process, the already formed primary particles almost reached their final size and mostly the gel network is formed by binding the primary particles to each other. In Fig. 53 it is also obvious, that the initial crystallinity of the inulin samples, represented by the values at roughly 20 min sample age, depends on the sample preparation temperature. With increasing preparation temperature, the solubility of inulin also increases, what results in decreased initial intensities. In Fig. 54 one can see, the development of the relative intensities of the $2\theta = 12,1^\circ$ Bragg reflexes of HPX gels, prepared at 25 °C, 40 °C, 60 °C and 80 °C (shear rate 600 rpm). Again the main part of the crystallization occurs in the first two to three hours (intensity increases to 85 – 90% of maximum intensity). The Increase in intensity is not as distinctively pronounced as for the HP samples (due to the crystallinity of the employed HPX powder, as explained further down in this section), still the sequence of the crystallization is the same as explained above for the HP gels. In Fig. 54 the initial crystallinity also decreases with increasing sample preparation temperature. The reason is again the increased solubility of HPX at increased sample preparation temperatures.

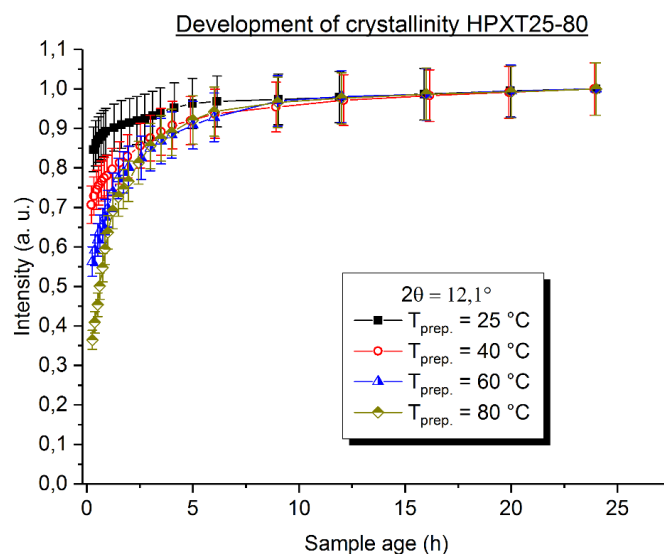


Fig. 54: Development of the relative intensity of HPX gels prepared at 25 °C, 40 °C, 60 °C and 80 °C.

To illustrate the significantly larger initial intensity of the HPX samples at the different sample preparation temperature again, the graphs of Fig. 53 and Fig. 54 have been plotted on a logarithmic scale and are illustrated simultaneously in Fig. 55.

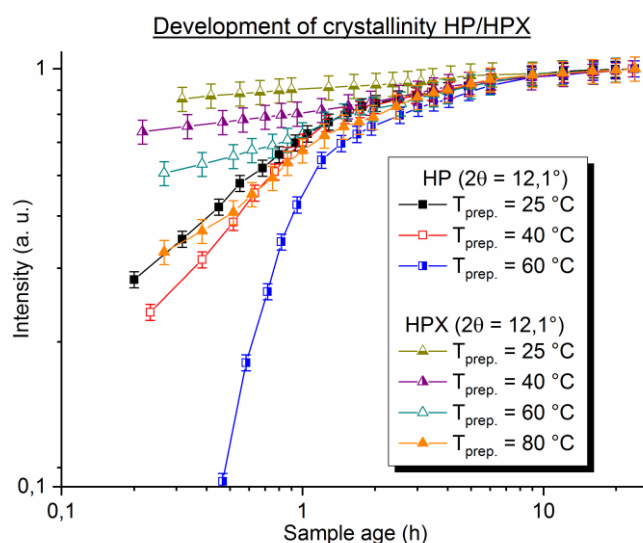


Fig. 55: Development of the relative intensity of HP/HPX gels, plotted on logarithmic scale.

In Fig. 55 it is obvious, that the initial crystallinity increases from HP prepared at 60 °C (at 60 °C, 20% (w/w) of HP are almost completely dissolved (see Fig. 50). Because of this the HP sample exhibits an initial intensity even smaller than 0,1. For the sake of clarity, the y – axis in Fig. 55 exhibits a starting value of 0,1) to HPX prepared at 25 °C (initial intensity of 0,85). This means, that the initial intensity increases with a decreasing solubility of the employed inulin. On one

hand, this depends on the applied sample preparation temperature and on the other hand on the crystallinity of the used inulin powder (see Fig. 47 and Fig. 50).

To determine the crystallization constant k of the gel formation, a Johnson – Mehl – Avrami – Kolmogorov fit (JMAK) was applied to the curves shown in Fig. 53 and Fig. 54. The JMAK model describes an isothermal phase transition [16, 69], in this case the transition from liquid to crystalline. The respective equation can be seen in Eq.(55).

$$\frac{I(t)}{I_{max}} = 1 - e^{-(k(t-t_0))^m} \quad (55)$$

$I(t)$ is the diffracted intensity at the sample age t , I_{max} is the diffracted intensity after 24 h ageing, k the crystallization constant, t the age of the sample, t_0 the begin of the phase transition and m is the geometry factor(see section 1.3). As mentioned above, in this work we just focused on the crystallization constant. In Tab. 3 and Tab. 4 the average crystallization constants for HP and HPX samples, prepared at different sample preparation temperatures and determined by applying Eq.(55) on the curves shown in Fig. 53 and Fig. 54, can be seen.

Tab. 3: Average crystallization constant of HP samples

$T_{(prep)} (^{\circ}\text{C})$	k (1/h)	Error (1/h)
25	1,34	0,04
40	1,19	0,07
60	1,00	0,44

Tab. 4: Average crystallization constant of HPX samples

$T_{(prep)} (^{\circ}\text{C})$	k (1/h)	Error (1/h)
25	2,08	0,10
40	1,26	0,03
60	1,17	0,03
80	1,02	0,04

For both types of Inulin the crystallization constant k decreases with increasing preparation temperature. As mentioned above, the solubility increases with increasing sample preparation temperature (Fig. 50) and with it the amount of nuclei, which act as seeding material, decreases. This results in a decreased crystallization rate. The decreased crystallization rate influences the average gel particle size, altering the texture of the completely developed inulin gel significantly. Those results will be explained in the following sections.

3.2.3 High Performance Anion Exchange Chromatography

To determine the chain length distribution of the initially dissolved inulin, a sample was taken from the inulin suspension (20% inulin dry matter) after 10 min stirring at the respective preparation temperature. Another one was taken from the same gel after 24 h storage at room temperature, to determine the amount of inulin remaining dissolved. Both samples were diluted with deionized water and analyzed by HPAEC. To determine the DP distribution of the samples, a reference value was prepared by completely dissolving 20% dry matter of inulin in deionized water at 85 °C. The respective chromatograms for HP and HPX can be seen in Fig. 56 and Fig. 57.

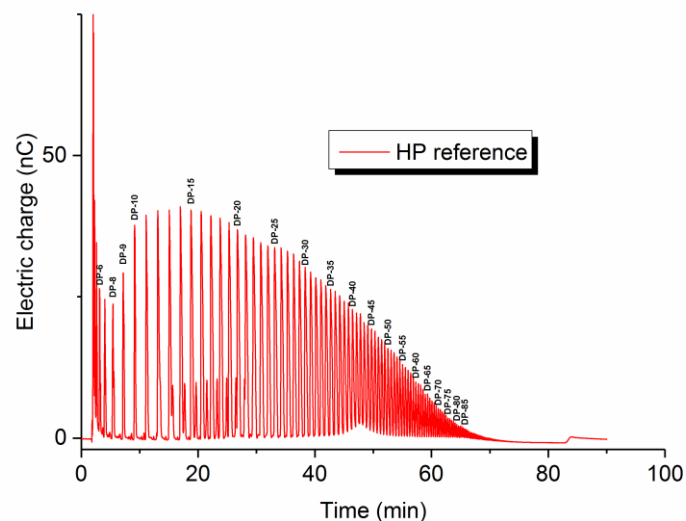


Fig. 56: HP separated according to DP.

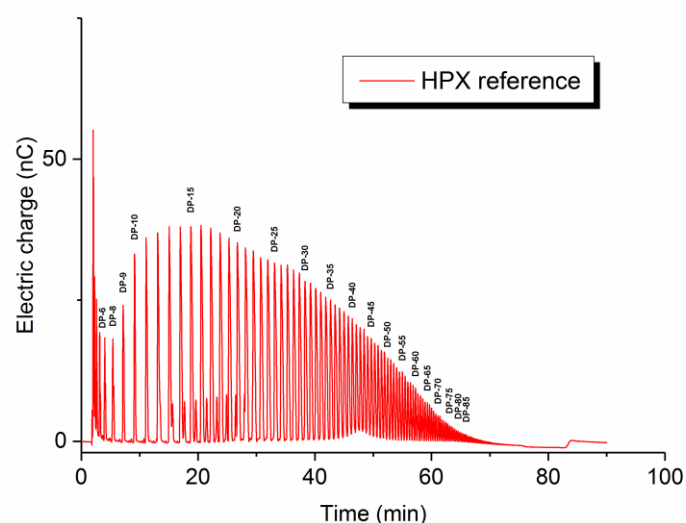


Fig. 57: HPX separated according to DP.

The retention times of the peaks are automatically compared to literature values by the chromatography software, which was used to perform the HPAEC measurements (“Chromeleon” by Thermo Fisher Scientific) and are indicated respectively in Fig. 56 and Fig. 57. The first peak identified is the DP-6 peak, meaning one glucose head group bound to a chain of five β -(2,1) linked fructose units. Molecules with a smaller DP could not be completely separated from each other, represented by the large peak at approximately 2 min retention time, originating from the application of the CarboPac PA200 column, which is mainly used for the separation of oligosaccharides. To figure out the amount of inulin of a certain DP, dissolved during sample preparation, the areas below the peaks in the chromatogram were integrated. To point out changes in the DP distribution of the dissolved inulin and to minimize concentration errors, resulting from the sample preparation, a region of ten following DPs was summed up to one fraction. The results for HP and HPX, prepared at different sample preparation temperatures and the samples taken after 10 min stirring, can be seen in Fig. 58 and Fig. 59.

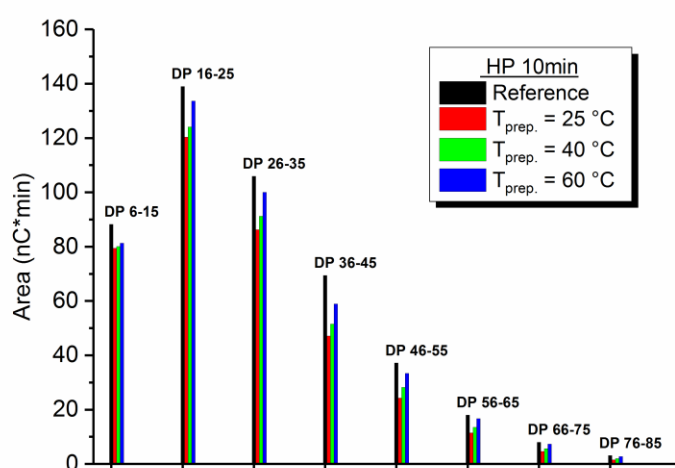


Fig. 58: Temperature dependent DP distribution of dissolved HP after 10 min stirring at preparation temperature.

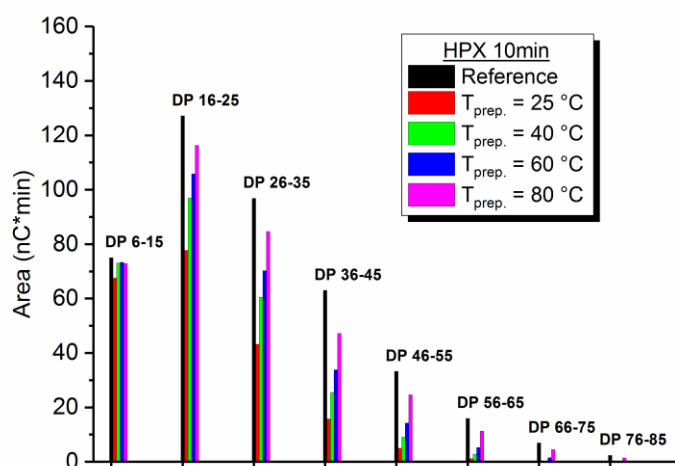


Fig. 59: Temperature dependent DP distribution of dissolved HPX after 10 min stirring at preparation temperature.

With increasing sample preparation temperature, the amount of dissolved inulin also increases. Compared to the reference values, even at 60 °C preparation temperature, for HP and at 80 °C for HPX, a small amount of inulin remains undissolved, ensuring a seeded crystallization during gel formation. As already mentioned in section 1.1, a seeded crystallization is inevitable for the formation of a completely percolated inulin gel. With increasing solubility, the amount of dissolved long chain inulin (DP 36 – 85) also significantly increases. If one compares Fig. 58 and Fig. 59, the differences between HP and HPX are clearly visible in particularly

this long chain region. For HP, even at 25 °C sample preparation temperature, a significant amount of long chain inulin is dissolved. During crystallization, the whole range of DPs is incorporated in the gel primary particles, giving a relatively homogeneous gel structure (see sections 3.2.4 - 3.2.7). Since HPX exhibits a significantly lower solubility than HP, the inulin molecules with the largest DPs (76 – 85) are just dissolved at 80 °C sample preparation temperature, in a very small amount. With decreasing sample preparation temperature, the amount of dissolved long chain inulin also decreases. Therefore, during gel formation of the HPX gels, prepared at lower temperatures (25 °C – 40 °C), almost no long chain inulin is incorporated in the crystallizing gel primary particles and a gel with an inhomogeneous gel structure forms (see sections 3.2.4 - 3.2.7).

To determine the DP distribution of the inulin, remaining dissolved after 24 h of storage at room temperature, the 24 h samples were analyzed accordingly to the 10 min samples, as already explained earlier in this section. The results are visible in Fig. 60 and Fig. 61.

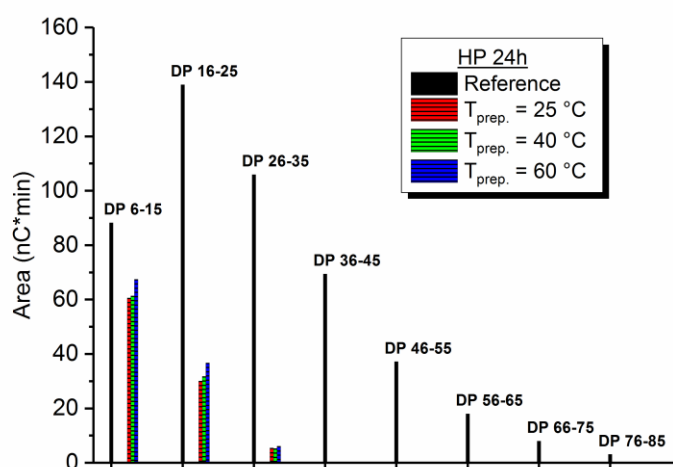


Fig. 60: Temperature dependent DP distribution of dissolved HP after 24 h storage.

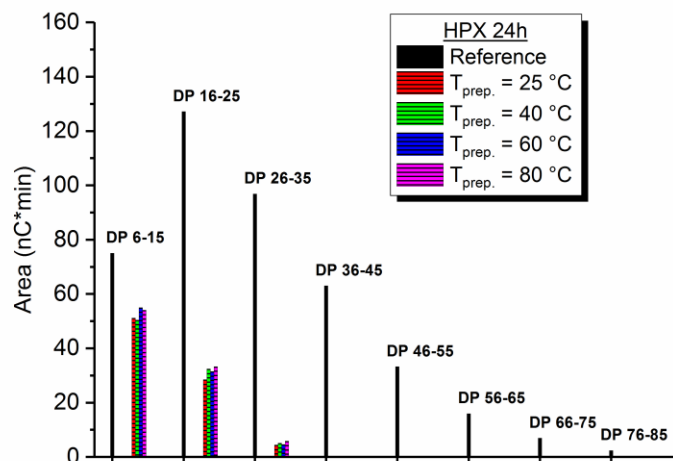


Fig. 61: Temperature dependent DP distribution of dissolved HPX after 24 h storage.

If Fig. 58 and Fig. 60 respectively Fig. 59 and Fig. 61 are compared to each other, one can clearly see, that the previously dissolved inulin almost completely recrystallizes during gel formation. Only a small amount of short and medium chain inulin, increasing with increasing preparation temperature, remains dissolved after 24 h. Above a DP of 35, for both HP and HPX, the dissolved inulin completely crystallizes. Referring to the DP distribution of the gel primary particles, which are formed during crystallization (see section 1.1), an increased sample preparation temperature leads to the incorporation of a larger amount of long chain inulin in those particles. This influences the primary particle size and the resulting texture of the completely developed inulin gel (see sections 3.2.4 and 3.2.6).

3.2.4 Texture analysis (Gel hardness)

To elucidate the fracture behavior of the completely developed inulin gels, the samples were compressed beyond their fracture stress. In Fig. 62 the reader can see two HP samples after compression, prepared at different sample preparation temperatures.

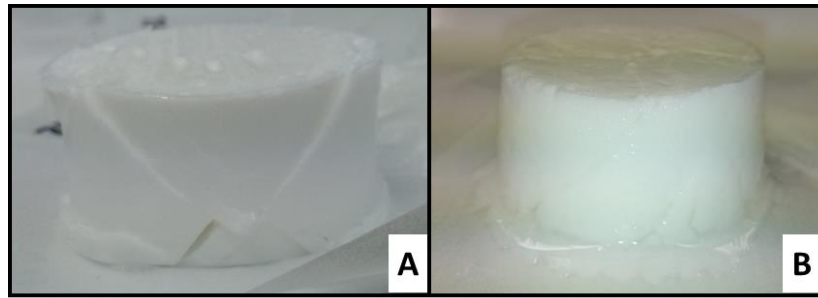


Fig. 62: HP gels compressed beyond fracture stress. A was prepared at 25°C, B was prepared at 60°C

The gel in Fig. 62 A was prepared at 25 °C. It shows a distinctive crack pattern. This is a typical behavior for a strong gel [30]. When the inulin sample is compressed uniaxial, the upper and lower parts of the sample are compressed in the direction of the applied force and the outside parts are forced sideways. This gives rise to shear forces along the diagonals, as drawn in Fig. 63. For this fracture behavior, the gel needs a certain stiffness, which arises from the binding forces between the particles in the gel.

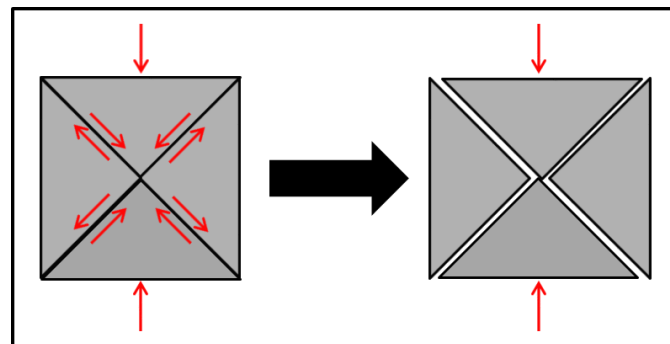


Fig. 63: Crack pattern of strong gels [30]

If the bonds between the particles of the gel get weaker, this crack pattern disappears and at larger strains the gels begin to yield and flow instead of fracturing [30]. This behavior can be observed for an HP gel, prepared at 60 °C (Fig. 62 B). In Fig. 64 one can see two HPX samples after compression, prepared at 25 °C and 80 °C.

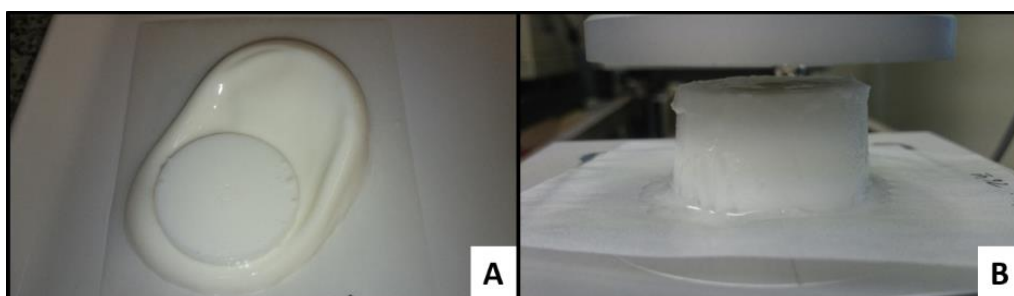


Fig. 64: HPX gels compressed beyond fracture stress. A was prepared at 25°C, B was prepared at 80°C

The HPX gel, prepared at 25 °C, is so weak, that it cannot keep the shape of the vessel it was prepared in. If the sample preparation temperature is increased to 80 °C, the hardness of the HPX gel also increases, but still not reaching the hardness of a strong gel, what is visible by the lacking crack pattern. Hence, the hardness of the HP gels decreases with increasing sample preparation temperature and the hardness of the HPX gels increases with increasing sample preparation temperature. If Fig. 62 and Fig. 64 are compared to each other, it is obvious, that HP forms harder gels than HPX at the respective preparation temperatures. So the fracture behavior of the inulin gels gives a first hint of the influence of the different sample preparation temperatures and the type of inulin that has been used, on the hardness of the gels.

To examine the hardness of the inulin gels, the samples were penetrated by a stainless steel stamp to a maximum strain of 6 mm. The responsive force was measured and the resulting gel hardness could be determined, as the first maximum of the force versus strain curve before the fracturing of the gel [56]. The results of the hardness measurements of the HP and HPX gels, prepared at different sample preparation temperatures and with low (600 rpm) and high (7000 rpm) shear rates, are pictured in Fig. 65. The hardness of the HP gels decreases with increasing sample preparation temperature. The application of a higher shear rate (7000 rpm) during sample preparation, results in increased hardness values, whereas the hardness trends for low and high shear rates remain identical throughout the whole temperature range. For the HPX samples the hardness increases with increasing sample preparation temperature. The application of a higher shear rate results also in increased hardness values and the hardness trend remains the same as for the samples, prepared with 600 rpm. The explanation for those trends will be given in the following sections.

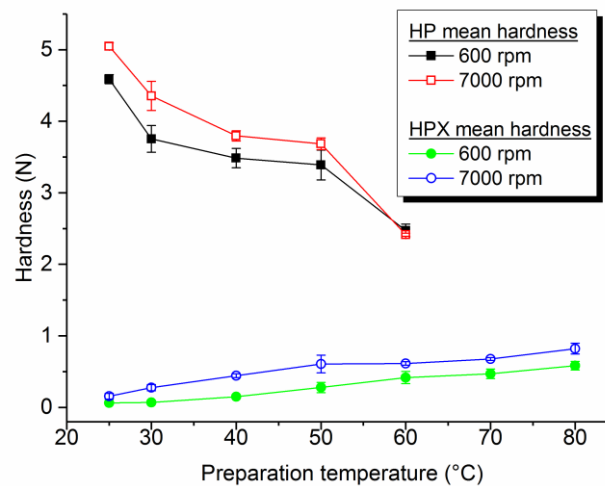


Fig. 65: Hardness of inulin gels prepared at different temperatures

For a sample preparation temperature higher than 60 °C for HP and higher than 80 °C for HPX, due to its solubility in water, no inulin gels had been prepared. Above those preparation temperatures, more than 20% of HP ($T_{prep.} > 60\text{ °C}$) respectively HPX ($T_{prep.} > 80\text{ °C}$) are dissolved, which leads to an unseeded crystallization upon cooling and results in a fragmentary gel structure. So the texture of the developing inulin gels can be influenced by the variation of shear rate and temperature during sample preparation. To illustrate the different gel structure of the HP and HPX gels once again, confocal microscopy pictures of both gels, prepared at 25 °C, are pictured in Fig. 66 and compared to the respective hardness values.

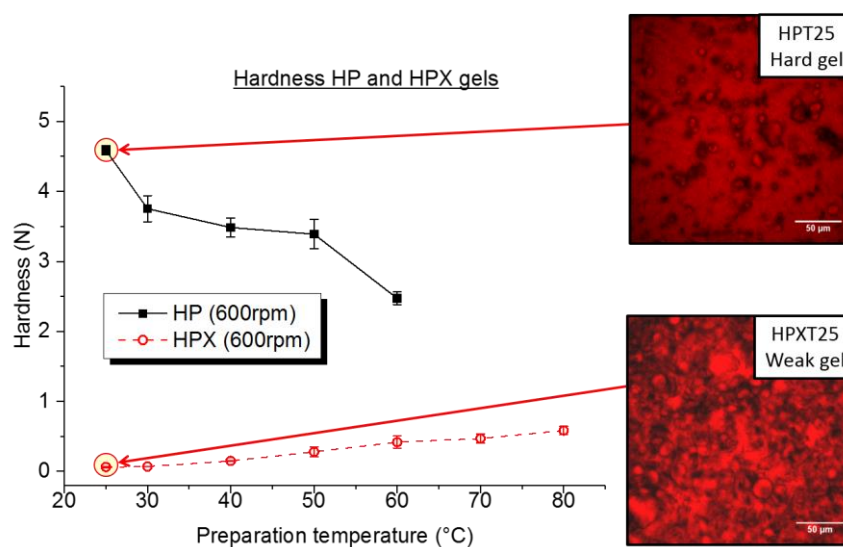


Fig. 66: Comparison of gel structure of HP and HPX gels, both prepared at 25 °C. Each picture was taken in a depth of 10 µm.

On the left hand side of Fig. 66, one can see the sample preparation temperature dependent hardness curves of HP and HPX gels, prepared with a shear rate of 600 rpm. Those curves have already been presented in Fig. 65. The CLSM pictures of an HP and an HPX gel, both prepared at 25 °C, can be seen on the right hand side of Fig. 66. Both pictures have been taken from the bulk of the samples, 10 μm above the bottom of the nunc chambers. The associated hardness values are highlighted in the diagram on the left. It is clearly visible, that HPX ($T_{\text{prep.}} = 25\text{ }^{\circ}\text{C}$) forms the weakest gel of the whole series and HP (also $T_{\text{prep.}} = 25\text{ }^{\circ}\text{C}$) yields the hardest gel. If the pictures on the right are compared to each other, significant differences in the gel structures of the HP and HPX gels are clearly visible. Since both gels are dyed with Rhodamine B, which binds hydrophobic to the inulin molecules [70], the regions where water is accumulated should appear just lightly red or almost dark in both gels. Apart from the large, lightly dyed remnants of the HP powder, that have not been dissolved during sample preparation and are dispersed throughout the whole gel, the HP gel network appears homogeneously dyed, without any obviously darker regions. This is a clear indication for a homogeneous and strong network, what can be confirmed by the associated hardness value. The HPX gel on the opposite yields an inhomogeneous gel network, interspersed with dark regions, where water is clearly accumulated. This results in a fragmentary weak gel structure, also confirmed by the respective hardness value, visible on the left hand side of Fig. 66. As already mentioned above, the formation of the different gel networks and the corresponding hardness values, will be explained in the following sections.

3.2.5 Oscillatory rheology

The viscoelastic properties of inulin gels, can be determined by oscillation rheology. Above a certain shear amplitude, the inulin gels show a shear thinning behavior [33], due to the successive breakdown of the particle gel. To determine the viscoelastic properties of the completely developed HP and HPX gels, amplitude sweeps have been performed at the unsheared samples. In Fig. 67 one can see the amplitude sweep curves of HP gels, prepared at 25 °C, 40 °C and 60 °C. The samples have been measured between 0,1% and 100% oscillation amplitude. The error bars are not indicated, due to the sake of clarity.

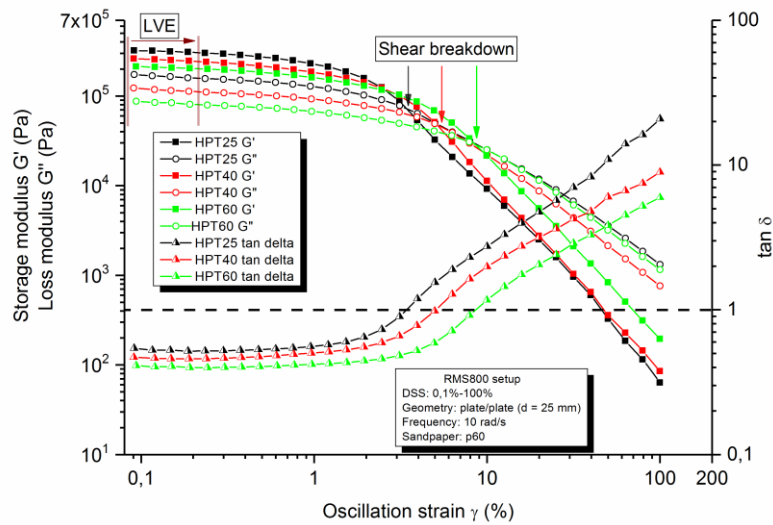


Fig. 67: Amplitude sweep curves of HP gels, prepared at 25 °C, 40 °C and 60 °C. The device setup is indicated in the figure.

In Fig. 67 one can see the storage modulus G' and the loss modulus G'' plotted against the applied oscillation strain γ . The dissipation factor $\tan \delta$ is also plotted against the oscillation strain. Since the dissipation factor is defined as the ratio of loss and storage modulus (G''/G'), it indicates very clearly, when the inulin gels start to flow (shear thinning behavior) and transform from a viscoelastic, solid gel, with dominating elastic properties ($G' > G''$), into a liquid suspension with dominating viscous properties ($G'' > G'$). In Fig. 67 the Linear Viscoelastic Region (LVE) is indicated with diagonal, brown lines. In this region, with the applied oscillation frequency and if the indicated maximum strain is not exceeded (right border of the LVE region), a deformation of the HP gels is completely reversible and the sample exhibits elastic behavior. This means, if the applied deformation does not exceed the borders of the LVE region, the sample regains the viscoelastic properties (e.g. hardness, stiffness etc.), it exhibited before the shear was applied, completely. In Fig. 67 the trend of the HP gel's shear moduli follows the trend of the respective hardness values (Fig. 65). The HP gel, prepared at 25 °C, exhibits the largest initial storage modulus, just as it exhibits the largest gel hardness. With increasing sample preparation temperature, the initial shear moduli decrease, comparable to the trend of the respective gel hardness. For all the HP samples, the initial storage modulus G' exceeds the initial loss modulus G'' . So for all the HP samples examined, the elastic properties dominate at small oscillation amplitudes, marking them as “solid” gels. If the oscillation amplitude is increased, both the moduli decrease. Because of the applied shear, the bonds between the primary particles are stressed and the gel starts to soften. If the applied strain

exceeds a certain amplitude, the gel network cannot withstand a further deformation, the primary particles are separated from each other and the gel network is destroyed. This certain point is visible for all the examined HP samples, where G' falls below G'' and is called “shear breakdown” [71]. The oscillation strain at this point, that causes the shear breakdown, is called “fracture strain” [13]. The shear breakdown of the gel is also indicated very clearly by the dissipation factor $\tan \delta$, when it adopts the value 1 (horizontal dashed line in Fig. 67). At this oscillation amplitude the gel network loses its solid character and starts behaving like a viscous fluid. To illustrate the shear thinning behavior of the inulin particle gel network, in Fig. 68 a simplified model of an inulin gel under the influence of a horizontal shear force can be seen. As already mentioned above, as long as the applied shear does not exceed the LVE region, the deformation of the gel is completely reversible (sketch in the middle of Fig. 68). When the applied strain exceeds the LVE region, the gel still exhibits dominating elastic properties, but the applied deformation is not reversible anymore. Due to the successive breakdown of the particle network, the gel shows a shear thinning behavior. As soon as the applied oscillation strain exceeds the point of shear breakdown, the particle network is completely destroyed, G' falls below G'' and the gel acts like a fluid with dominating viscous properties (right hand sketch in Fig. 68).

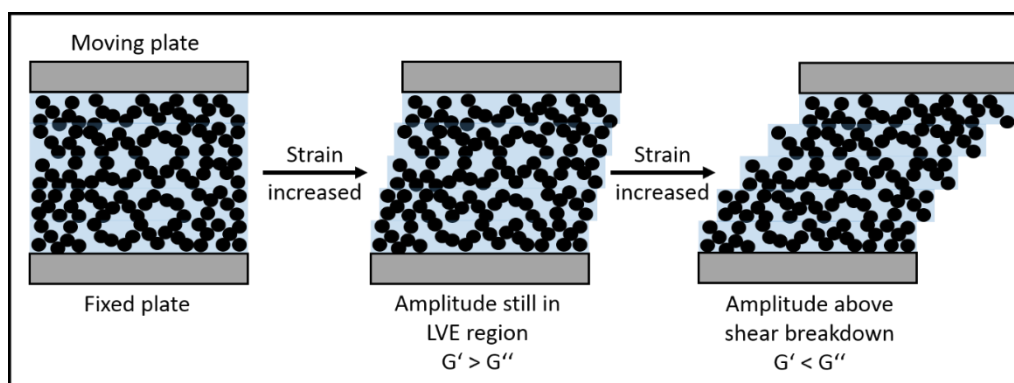


Fig. 68: Shear thinning behavior of an inulin gel, under the influence of a horizontal shear force.

What is very eye-catching, if one has a look at Fig. 67 again, is the fact that this shear breakdown is shifted to larger oscillation amplitudes, if the sample preparation temperature is increased. This means, the “softer” the HP gel is the more insensitive it reacts to deformation. So for an HP gel, prepared at increased temperatures, the primary particles in the completely developed gel are not that strong bound to each other, giving the gel a softer and more flexible structure (the primary particles can be moved to a certain extent without being separated from each other). The harder the gel is, the stiffer and more brittle the gel network becomes

(e.g. HP prepared at 25 °C). Above an oscillation amplitude of 20%, for all the gels the particle network is destroyed, the primary particles are completely separated from each other and the samples behave like viscous fluids.

In Fig. 69 one can see the amplitude sweep curves of HPX gels, prepared at 25 °C, 40 °C, 60 °C and 80 °C. Again G' , G'' and $\tan \delta$ are plotted against the oscillation strain γ . Due to their lower gel hardness, the HPX samples have been measured between 0,01% and 100% oscillation amplitude. Again the error bars are not indicated.

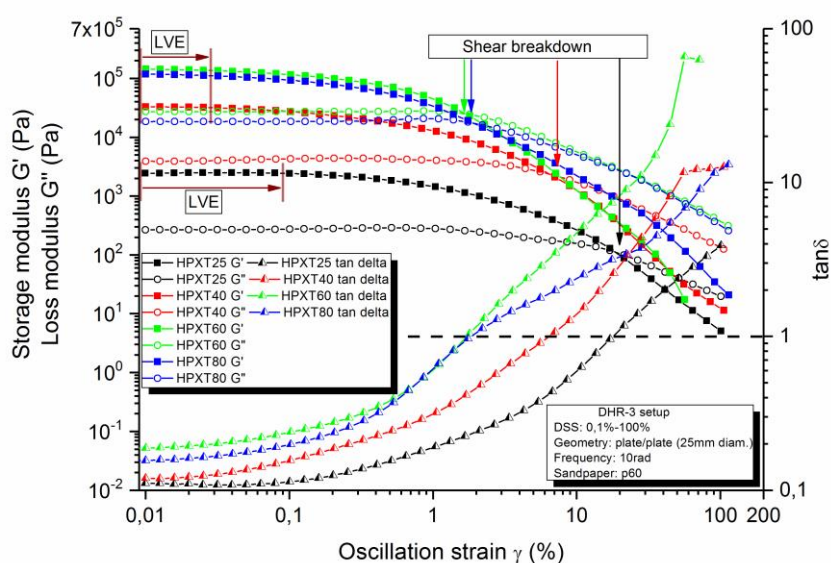


Fig. 69: Amplitude sweep curves of HPX gels, prepared at 25 °C, 40 °C, 60 °C and 80 °C. The device setup is indicated in the figure.

Again the LVE region is indicated with diagonal brown lines and the dashed horizontal line indicates again a $\tan \delta$ of 1. The points of shear breakdown are also indicated for the respective curves. Here again the shear moduli G' and G'' follow the hardness trends of the respective HPX gels (Fig. 65). If the sample preparation temperature is increased, the hardness values of the completely developed HPX gels also increase and with it the initial values of the shear moduli are increased too. Here again, as already explained above, with increasing gel hardness and increasing initial shear moduli, the gels become more shear sensitive. If one has a look at the indicated points of shear breakdown in Fig. 69, it is obvious, that the shear sensitivity increases with increasing sample preparation temperature (the HPXT25 gel shows its shear breakdown at $\gamma = 20\%$ and the HPXT80 gel at $\gamma = 1,8\%$). This behavior is also clearly visible, if the LVE regions of the gels are compared to each other. The HPX gels, prepared at 40 °C,

60 °C and 80 °C exhibit comparable LVE regions, whereas the gel prepared at 25 °C exhibits by far the largest LVE region. The reason for this behavior is again, as already explained for the HP gels, the stiffness and brittleness of hard gels and the flexibility of the primary particles in soft gels. In Fig. 70 the storage moduli of the HP and HPX gels, presented in Fig. 67 and Fig. 69, are plotted against the oscillation amplitude and compared to each other. To obtain comparable measurements, the curves are plotted between 0,1% and 100% oscillation amplitude. Again for the sake of clarity, the error bars are not indicated.

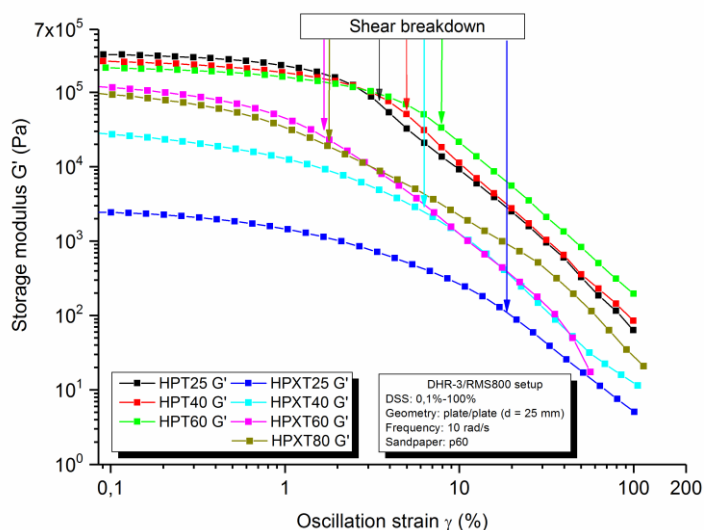


Fig. 70: Comparison amplitude sweeps of HP and HPX gels. Point of shear breakdown is indicated for each sample.

If the initial storage moduli of the HP and the HPX gels are compared to each other, again the hardness trends are followed. All the HP samples exhibit a significantly higher initial storage modulus G' . The initial storage modulus decreases from HPT25 to HPXT25. The reason for this decrease is again, as already explained for the hardness trends of the HP and HPX gels (see section 3.2.4 and Fig. 66), the change in the network structure of the gels (HPT25 homogeneous, strong network, HPXT25 fragmentary, weak network). The explanation for the changing particle network structure will be given in more detail in the following sections. In Fig. 70 the loss moduli are not plotted (for the sake of clarity). Still the points of shear breakdown are indicated. Here again the weakest gel (HPXT25), shows the point of shear breakdown at the largest oscillation amplitude. The trend of an increasing shear sensitivity with increasing initial storage moduli is still fulfilled (at least in the HP and HPX series). Except the extraordinary high shear insensitivity of the HPX gel, prepared at 25 °C, no overall trend can be seen. So the HPX

gels ($T_{\text{prep.}} > 25\text{ }^{\circ}\text{C}$) and the HP gels ($T_{\text{prep.}} = 25 - 60\text{ }^{\circ}\text{C}$) exhibit comparable stiffness and brittleness, what results in points of shear breakdown at similar oscillation amplitudes.

3.2.6 Particle size

The particle size trends of the different inulin gels provide an explanation for the above discussed hardness trends and can be observed in Fig. 71. The average size of the HP gel primary particles, prepared at low and high shear rates, increases with increasing sample preparation temperature. This is due to the increasing solubility of HP in water at higher sample preparation temperatures and the depletion of seeding material connected therewith [13]. Since all samples are cooled to room temperature for crystallization and all samples contain 20% of inulin dry matter, the amount of crystallizable material is comparable in all the samples. With increasing sample preparation temperature, the amount of seeding material, which is left in the inulin suspension, decreases, resulting in a decreasing crystallization constant k (see section 3.2.2). Additionally, a larger amount of long chain inulin is dissolved at increased preparation temperatures. As already seen in section 3.2.3, above a DP of 35, the previously dissolved inulin completely recrystallizes upon gel formation. This results in the incorporation of a larger amount of long chain inulin in the gel primary particles of the HP gels, prepared at higher temperatures. Therefore, the decreasing crystallization constant and the incorporation of a larger amount of long chain inulin at increased preparation temperatures, cause the formation of larger and less numerous crystalline gel primary particles. Those larger gel particles are also responsible for the decreased hardness of the inulin gels [15] at increased sample preparation temperatures (see Fig. 65). The gel primary particles are approximately spherical shaped. Since the surface S of a sphere increases with the radius r squared ($S = 4\pi r^2$) and the volume V with the radius r cubed ($V = \frac{4}{3}\pi r^3$), compared to smaller spherical particles, the surface to volume ratio of larger spherical particles is smaller. Thus, the larger particles can form fewer bonds between each other and the HP gel hardness decreases with increasing sample preparation temperature.

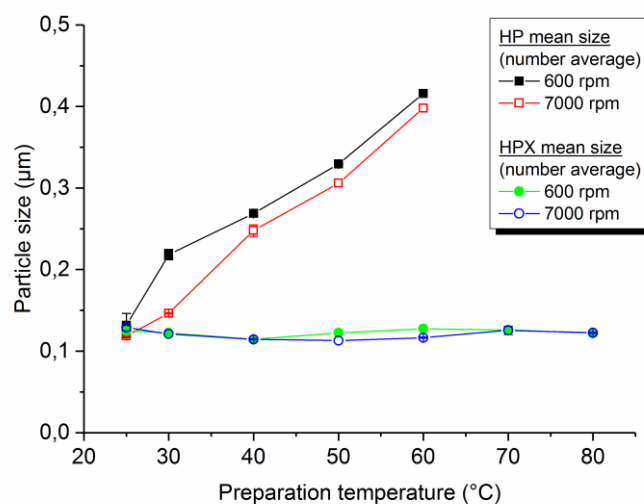


Fig. 71: Gel primary particle size (number average) in dependency of sample preparation temperature and shear rate.

To illustrate the increasing particle size of the HP primary particles once again, the number distribution of the HP gel particle size, prepared at 25 °C and 60 °C and examined by static light scattering, are pictured in Fig. 72. If one compares the particle size distribution of the sample prepared at 25 °C and the one prepared at 60 °C, it is obvious, that the curve of the 60 °C sample is shifted to larger particle sizes. The mean primary particle size (number average) is written next to the respective curve in Fig. 72.

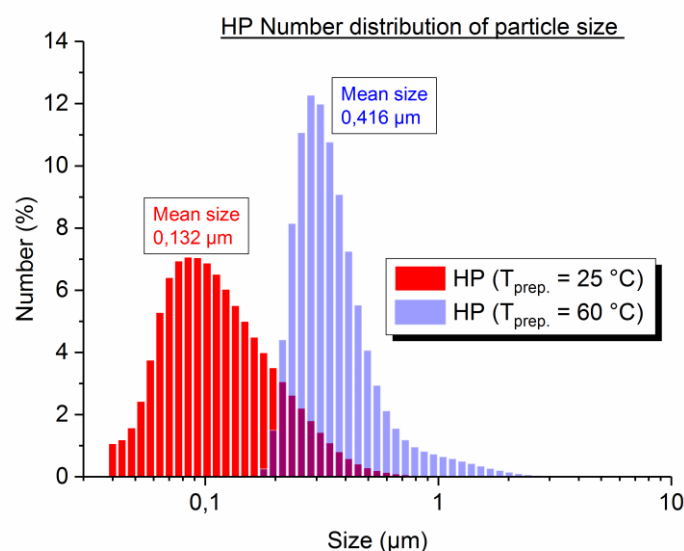


Fig. 72: Number distribution of HP gel particle size, prepared at 25 °C and 60 °C.

The average primary particle size of HPX gels, prepared at different sample preparation temperatures, behaves considerably different as the respective HP primary particle size. For the

HPX gels, prepared at low and high shear rates, the average primary particle size remains constant even at increased sample preparation temperatures. This arises from the semi-crystallinity of the used HPX powder. When the sample preparation temperature is increased, the solubility of the HPX powder in water also increases. Since the HPX powder already contains a certain amount of crystalline particles, its solubility in water is significantly smaller than the respective solubility of HP. Even at a sample preparation temperature of 80 °C, 10% of the added amount of HPX is still undissolved (see Fig. 50). The inferior solubility of HPX at the particular sample preparation temperatures results in increased crystallization constants k (due to the existence of a sufficient amount of seeds at each preparation temperature), compared to the respective crystallization constants of HP. Apart from the average particle size of the samples prepared at 25 °C, the average primary particle sizes of the HPX gels are significantly smaller than the respective HP gel particles (see Fig. 71). Taking into account the surface to volume ratio of small particles compared to large ones (see above), the HPX gels should exhibit a considerably higher gel hardness than the comparable HP gels. If we have a look at Fig. 65, we can see, that the gel hardness of the HPX gels increases with increasing sample preparation temperature, yet it remains clearly below the hardness value of even the weakest HP gel. To understand the hardness and particle size trends of the HPX gels, we need to consider the primary particle size distribution of the HPX samples. In Fig. 73 the number distribution of the primary particle size of HPX gels, one prepared at 25 °C and one at 80 °C, are pictured. The particle size distributions of both gels look almost identical. For the preparation of the number distribution of the primary particle size, each particle, no matter which size, is weighted equally. Therefore, changes in the outer regions of the number distribution, where the less numerous small and large particles are represented, are just slightly visible in Fig. 73. To point out changes in the particle sizes of the less numerous particles (the ones in the outer regions of the number distribution), one needs to examine the volume distribution of the HPX gel particle size. For the volume distribution, the particles are weighted according to their volume. This means that very few, very large particles, exhibit a comparable volume as a large number of very small particles. The volume distribution of the HPX gels pictured in Fig. 73, can be seen in Fig. 74.

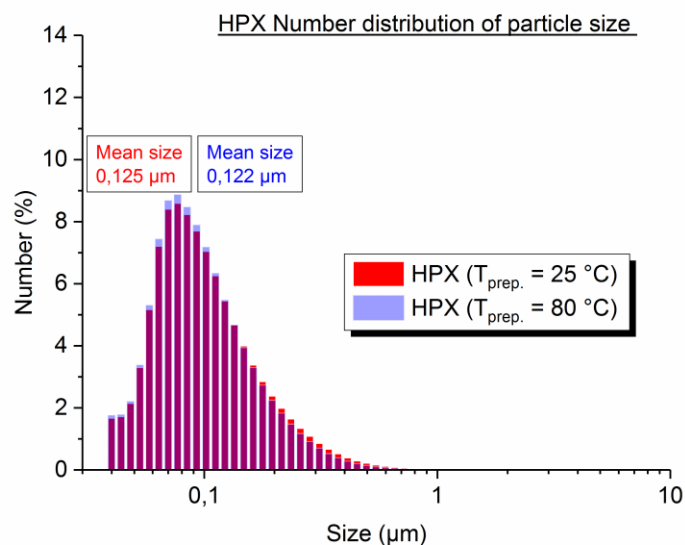


Fig. 73: Number distribution of HPX gel particle size, prepared at 25 °C and 80 °C.

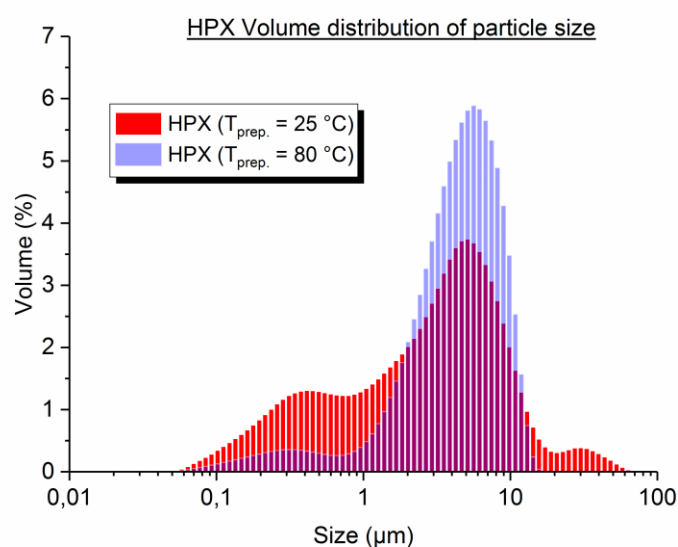


Fig. 74: Volume distribution of HPX gel particle size, prepared at 25 °C and 80 °C.

In Fig. 74 the changes in the particle sizes are clearly visible. At 25 °C preparation temperature, HPX exhibits a moderate solubility (Fig. 50). If one looks at Fig. 59, it is obvious, that almost no long chain HPX ($\text{DP} > 35$) is dissolved at 25 °C. Since the crystalline particles, which are already present in the HPX powder, exhibit a very low solubility in water and remain mostly undissolved at 25 °C, those particles consist of mainly long chain inulin. This means, those crystalline particles are present in the HPX gel after 24 h of ageing as very large primary particles, visible on the right hand side of the volume distribution in Fig. 74. Since mostly HPX with a $\text{DP} < 35$ is

dissolved at 25 °C sample preparation temperature, the primary particles that crystallize during gel formation, consist mainly of short and medium chain length inulin. Therefore, the crystallizing primary particles are mainly visible as very small particles on the left hand side of the volume distribution in Fig. 74. The volume average primary particle size of the HPX gel, prepared at 25 °C, can be roughly determined at the maximum in the center of the volume distribution. Since the particle sizes in Fig. 74 are volume weighted, aggregates that passed the pores of the filter or re-aggregated after filtration during sample preparation, have a significant impact on the volume average of the primary particle size. Because of this the volume average differs significantly from the number average of the primary particle size. If the sample preparation temperature is increased to 80 °C, the solubility of HPX also increases and a significant amount of long chain HPX is dissolved during sample preparation (see Fig. 59). This means, that the crystalline particles, which are already present in the HPX powder, are partially dissolved and decrease in size. On the other hand, the additionally dissolved long chain inulin is incorporated in the crystallizing primary particles upon gel formation, which increase in size. This development is clearly visible if the volume distributions in Fig. 74 are compared to each other. The significant amount of very small and very large particles, present in the 25 °C sample (maxima on the right and on the left of the 25 °C volume distribution), decreases and with it the amount of medium sized primary particles increases (maximum in the center of the 80 °C volume distribution). If one compares the maxima in the centers of the volume distributions of the 25 °C and the 80 °C samples to each other, it is obvious that the average primary particle size of the HPX gels remains constant (the maxima in the middle of the 25 °C and the 80 °C sample are in the same particle size region), even at increased sample preparation temperatures (see Fig. 71). The maximum in the center of the 80 °C sample is much more intense, whereas the two maxima in the outer regions almost vanish. This means that the HPX gels, prepared at increased preparation temperatures, exhibit a narrower primary particle size distribution. This results in gels with a more densely packed particle network with an increased gel hardness. As already mentioned above, in Fig. 71 the development of the number average was examined, to minimize the undesired impact of aggregates in the samples on the average primary particle size.

Another obvious trend is the smaller particle size for both, HP and HPX gels, prepared with high shear rates (7000 rpm). The inulin powder, depending on the amount of inulin and the temperature, partly dissolves in water. The undissolved material, as already mentioned, acts

as seeding material upon cooling. If the shear rate during sample preparation is significantly increased (comparing 600 rpm and 7000 rpm), the undissolved material is much better dispersed and eventually numerous seeds are broken apart and therefore reduced in size [72]. This results in smaller and more numerous gel primary particles. Those smaller particles yield gels with increased hardness (see Fig. 65) [73]. The reason for this is again the larger surface to volume ratio of smaller spherical particles and the additional bonds, which can be established between those primary particles. The impact of a higher shear rate on the HPX primary particle size is not as distinctive as for the HP primary particle size. This is due to the superior crystallinity of the used HPX powder. The undissolved crystallites in the HPX samples, which act as crystallization seeds, are much more robust than the mostly amorphous crystallization seeds in the HP samples. Nevertheless, the crystalline seeds in the HPX samples are also reduced in size and yield gels with increased hardness (Fig. 65). The reason for this effect is again the increased surface to volume ratio of smaller particles, as already explained above. So the inulin gel properties depend delicately on the gel primary particle size.

3.2.7 Summary

Taking the above discussed results into account, the preparation temperature dependent hardness variation of the completely developed inulin gels can be summarized by a simple model. The models are pictured in Fig. 75 and Fig. 76.

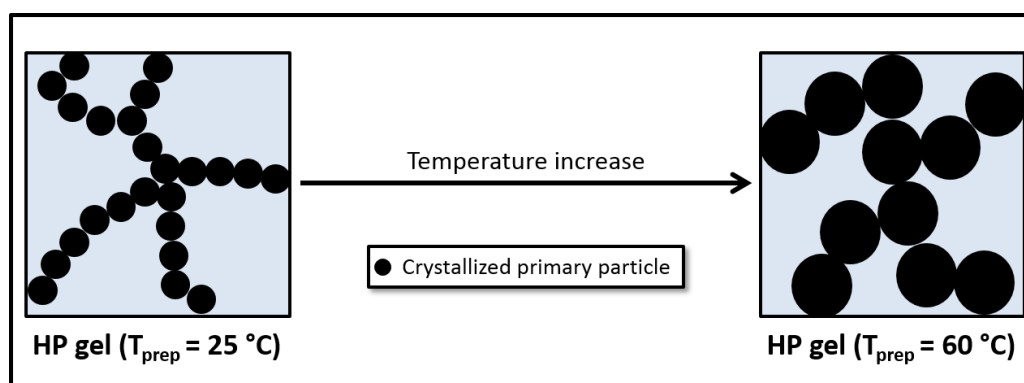


Fig. 75: HP particle size variation

In Fig. 75 one can see the particle gel structures of two completely developed HP gels, one prepared at $25\text{ }^{\circ}\text{C}$ and one prepared at $60\text{ }^{\circ}\text{C}$. Since the model in Fig. 75 is simplified and intended to illustrate the temperature dependent particle size variation, the pictured dimensions are randomly chosen. For the gel prepared at $25\text{ }^{\circ}\text{C}$, a sufficient amount of inulin remains

undissolved during sample preparation and acts as crystallization nuclei, ensuring a seeded crystallization. After 24 h of crystallization, the resulting HP gel consists of small primary particles and exhibits a hard texture. If the preparation temperature is increased to 60 °C, the solubility of HP in water also significantly increases and with it the amount of undissolved nuclei decreases. This causes a considerable decrease in crystallization velocity. Additionally, a larger amount of long chain inulin is incorporated in the crystallizing gel primary particles. The resulting gel consists of fewer but larger particles and exhibits a remarkably decreased hardness (Fig. 65 and Fig. 71).

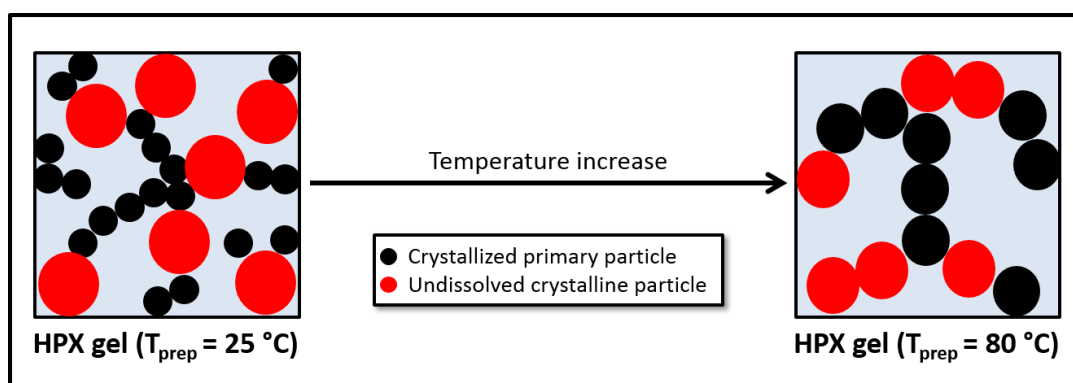


Fig. 76: HPX particle size variation

In Fig. 76 the particle gel structures of two completely developed HPX gels, one prepared at 25 °C and one prepared at 80 °C, are pictured. Again this is a very simplified model to illustrate the particle size variation. At 25 °C, HPX exhibits a moderate solubility in water (Fig. 50) and mostly short and medium chain inulin is dissolved during sample preparation. Additionally, the HPX powder already contains a significant amount of crystalline particles, which can act as seeding material during crystallization. For the HPX gel, prepared at 25 °C, this results in a fragmentary gel structure (see Fig. 66 and Fig. 76), consisting of small, during gel formation crystallized primary particles (black particles in Fig. 76, that mainly consist of short and medium chain inulin) and large, undissolved crystalline primary particles, that were already present in the HPX powder (red particles in Fig. 76, which mainly consist of long chain inulin, see also Fig. 74). Because of this fragmentary, not very densely packed gel structure, the 25 °C HPX gel exhibits a very low gel hardness. If the sample preparation temperature is increased to 80 °C, the solubility of HPX also increases and the crystalline powder particles are partly dissolved and decrease in size. The dissolved long chain inulin is incorporated in the crystallizing particles, which increase in size. So the particle size of the crystalline powder particles and the

crystallizing primary particles equalizes. The gel structure of the completely developed gel becomes more homogeneous and more densely packed and the gel hardness increases (Fig. 65).

3.3 The inulin-water-ethanol system

In this chapter the results of the HP and HPX samples, that have been prepared with water-ethanol mixtures acting as solvent, will be presented and discussed. For all the measurements in this section the results for HP and HPX, prepared at 25 °C in water, were used as reference values. This means, the sample preparation temperature was set to 25 °C for all the samples and the ethanol concentration in the solvent adjusted to 0% (reference values of HP and HPX at 25°C in water), 5%, 10% and 15% (w/w). Due to the significant change in polarity of the solvent (with increasing ethanol content the polarity of the solvent decreases) and the increasing disequilibrium of the system connected therewith, the maximum concentration of ethanol was limited to 15% (w/w). In the following sections the processes, that give rise to the disequilibrium, will be explained in more detail. For further information concerning the solute-solvent interactions see also section 1.5.

3.3.1 Solubility in water-ethanol mixtures

In section 3.2.1 the solubility of 20% dry matter of inulin at different sample preparation temperatures in water, was discussed. In this section, we consider water-ethanol-mixtures, with different mass concentrations of ethanol, as solvent. As mentioned above, the preparation temperature was set to 25 °C and the ethanol concentration (w/w) of the solvent increased from 0% to 15%. As already noted in section 3.2.1, all samples in this work were prepared with 20% dry matter of inulin, so here the solubility of HP and HPX in the varying solvent also refers to 20% dry matter in the sample. The equilibrium solubility of both types of inulin in deionized water with increasing ethanol content can be seen in Fig. 78. Again, the concentration of the dissolved inulin was determined by measuring the refractive indices of the samples and comparison to reference values, obtained at specified mass concentrations of dissolved inulin. Since the refractive index of the pure solvent changes with differing ethanol content, a reference curve had to be generated, as described in section 3.2.1, for each ethanol content used for the experiments. For the determination of the concentration of dissolved inulin in water (ethanol content 0%), the reference curve from section 3.2.1 was used (Fig. 49). For the ethanol-water mixtures with an ethanol content $\geq 5\%$, the data has been fitted over the concentration range $0 \leq c \leq 0,075$ and the equations of the linear fits can be found in Fig. 77. The

reference curve for an ethanol content of 0%, was fitted as mentioned in section 3.2.1. The reference plots are again the same for HP and HPX. This is why only one series of plots is pictured in Fig. 77. The reference plot for pure deionized water can be found in Fig. 49.

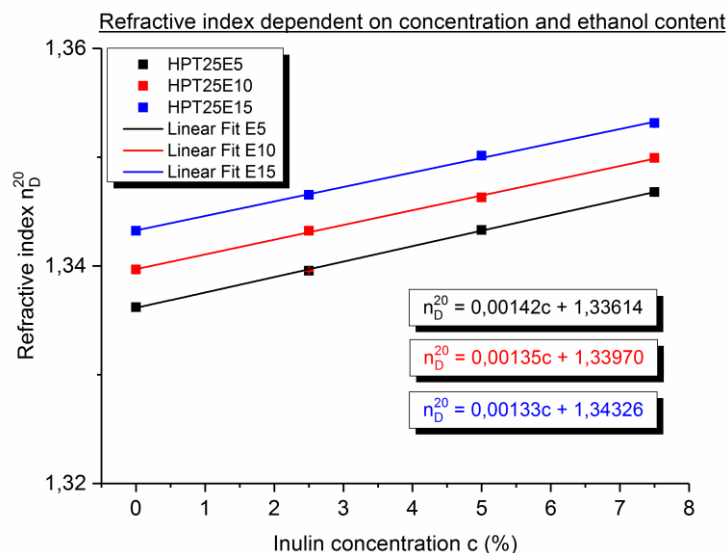


Fig. 77: Refractive index in dependency of the mass concentration in water-ethanol mixtures.

The solubility of inulin decreases with increasing ethanol content in the solvent (Fig. 78). Since ethanol exhibits a lower relative polarity than water [37], with increasing ethanol content, the polarity of the solvent decreases. Due to the free hydroxyl groups of the fructose and glucose units of the inulin chain (see Fig. 1), the inulin molecules exhibit a semi-polar character. This enables the inulin molecules to dissolve to a certain amount in the polar solvent water (depending on the chain length of the inulin molecule and the temperature of the water). If the polarity of the solvent is decreased (e.g. ethanol addition), the solubility of inulin in this solvent also decreases (see also section 1.5 and section 3.3.3). From Fig. 78, it is also obvious, that HPX exhibits a significantly lower solubility than HP at each ethanol content examined. The reason for this is again, as already discussed in section 3.2.1, the superior crystallinity of the employed HPX powder. Apart from this overall decreased solubility of HPX, the solubility trend of both types of inulin in the water-ethanol mixtures is comparable. If one compares the increase of the preparation temperature to the decrease of the solvent polarity, the change in polarity has a significantly higher impact on the system. If the preparation temperature of water is increased, the solubility of HP and HPX increases too. Since all the samples are cooled to room temperature after heating (see section 2.2), the previously dissolved inulin recrystallizes (depending on its DP) and contributes to the gel formation process. If the polarity of the solvent

is decreased by the addition of ethanol to water, depending on their chain length (or DP), the inulin molecules are precipitated (see section 3.3.3). This means, the precipitated molecules are insoluble in the solvent, are removed from the system and do not take part in the gel formation process anymore. By changing the polarity of the solvent, the whole inulin-solvent system is changed. Because of this, the ethanol mass concentration in the solvent was minimized to 15%. The DP dependent solubility of HP and HPX in water-ethanol mixtures will be discussed more detailed in section 3.3.3.

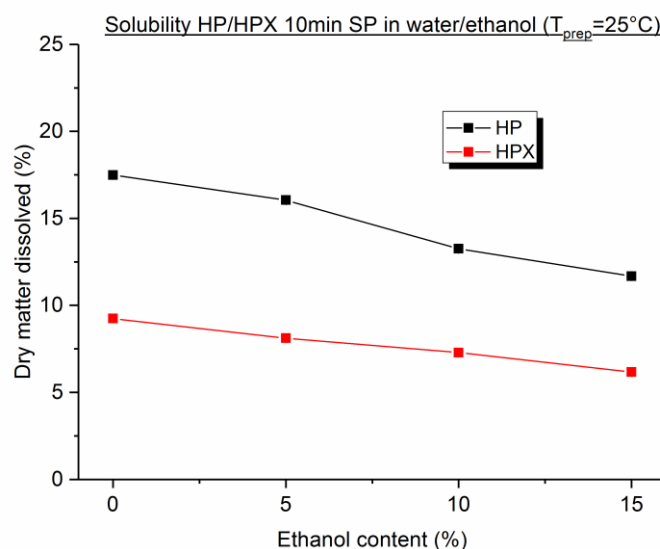


Fig. 78: Equilibrium solubility of 20% (w/w) inulin in water-ethanol mixtures.

3.3.2 X-ray diffraction during gelation

The development of the particle gel network, with water-ethanol mixtures acting as solvent, was examined by in-situ x-ray diffraction too. The radial averaged diffraction patterns of the HP and HPX gels, prepared at 25 °C, with an ethanol mass concentration of 5% and measured for 24 h during gelation, can be seen in Fig. 79 and Fig. 80. The intensities of the Bragg reflexes at $2\theta = 12,1^\circ$ have been projected to the left hand layer, to make the gelation process more obvious. Again, as already seen in section 3.2.2 (see Fig. 51 and Fig. 52), the intensity of the HP and HPX samples increases with increasing aging time. This increasing intensity confirms, that HP and HPX in a water-ethanol milieu, with 20% (w/w) of inulin in the sample, crystallize during gelation. The process is the same as described in section 3.2.2. If one compares Fig. 79 and Fig. 80 to each other, the HPX sample exhibits a significantly higher initial intensity. The

reason for this is the same as for the inulin-water system, namely the superior crystallinity of the employed HPX powder (see Fig. 47 and section 3.2.2). If the absolute intensities of Fig. 79 and Fig. 80 are compared to Fig. 51 and Fig. 52, it is obvious, that the diffraction spectra of the HP and HPX samples, prepared with 5% ethanol in the solvent, exhibit a remarkably lower intensity than the respective samples prepared with pure water. This could arise from three reasons. Firstly, the intensity of the incident x-ray beam, emitted from the x-ray source, fluctuates (due to the setup of the x-ray diffractometer and the configuration of the x-ray source). If the intensity of the incident beam decreases, the diffracted intensities also decrease, what results in x-ray spectra with decreased absolute intensities. Secondly, the used mark tubes exhibit a diameter variability of approximately 20%. Due to the setup of the x-ray device, only a small part of the sample in the mark tube (roughly 1 mm in height, depending on the beam-width of the incident beam) actually diffracts the x-ray beam. If the diameter of the irradiated part of the mark tube varies, the volume of the irradiated part of the sample varies too. Since the intensity of the diffracted radiation is proportional to the amount of diffracting material, the diffracted intensity also varies with the diameter of the used mark tubes. And thirdly, the amount of inulin in the sample. All the samples were prepared as inulin/solvent suspensions, containing 20% (w/w) of inulin. As already mentioned in section 3.3.1, a decreasing polarity of the solvent by addition of ethanol, results in the precipitation of inulin. The precipitated material does not take part in the gelation process anymore (this also influences the gel structure of the completely developed gels significantly, as will be explained in the following sections). If the suspension is pipetted into the mark tubes, the precipitated material accumulates on the bottom of the mark tubes. During the diffraction experiment, this material is not in the beam path of the incident beam (due to the setup of the device) and does not contribute to the diffracted intensity, also resulting in diffraction spectra with decreased absolute intensities. The first two reasons for the decreased diffracted intensities are exclusively of experimental nature (setup of the device and mark tubes, that were used to contain the samples). Reason three is of physical nature and arises from the polarity decrease of the solvent. The fluctuations in the absolute intensities could not be investigated systematically. So all the samples, belonging to the same series of experiments (e.g. the samples prepared in pure water), were measured in the shortest time interval possible, to minimize the influence of a fluctuating incident x-ray intensity. Additionally, as already mentioned in section 3.2.2, all the intensities of the $2\theta = 12,1^\circ$ reflexes of one sample were normalized to the respective maximum

intensity (i.e. the measured intensity after 24 h of ageing), to further minimize the influence of a fluctuating incident intensity. Apart from the above mentioned difference in initial intensity, the development of the diffraction patterns of the HP and HPX gels, prepared with 5% - 15% ethanol in the solvent, look very similar. Because of this, in this section just the diffractograms for HP and HPX, prepared at 25 °C with an ethanol content of 5%, are shown. The remaining diffractograms can again be found in the Appendix section.

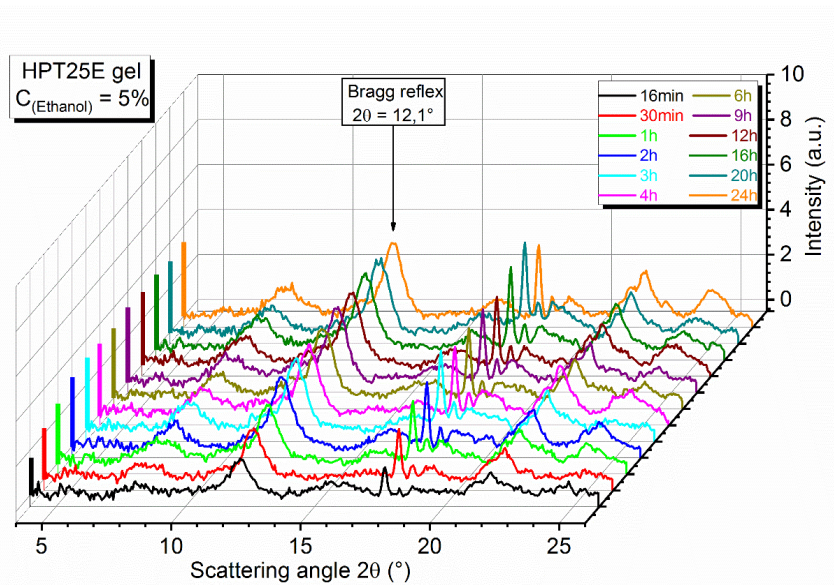


Fig. 79: XRD during gelation of an HP gel, prepared at 25 °C, 600 rpm shear rate and 5% Ethanol.

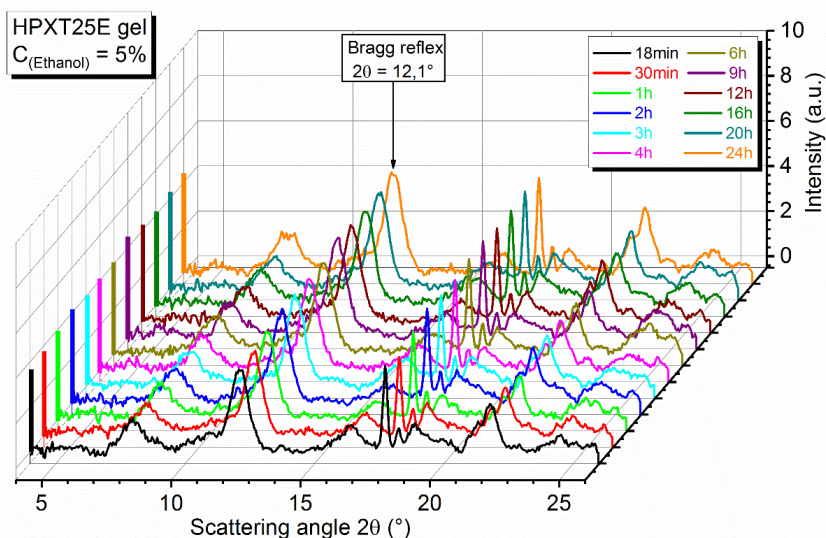


Fig. 80: XRD during gelation of an HPX gel, prepared at 25 °C, 600 rpm shear rate and 5% Ethanol.

To examine the crystallization kinetics of the gel formation, the $12,1^\circ$ reflexes were integrated and normalized to the respective maximum intensity. In Fig. 81 the relative intensities of the

Results and discussion

Bragg reflexes at $2\theta = 12,1^\circ$ of HP gels, prepared at 25°C , with an ethanol concentration of 0%, 5%, 10% and 15%, are compared to each other.

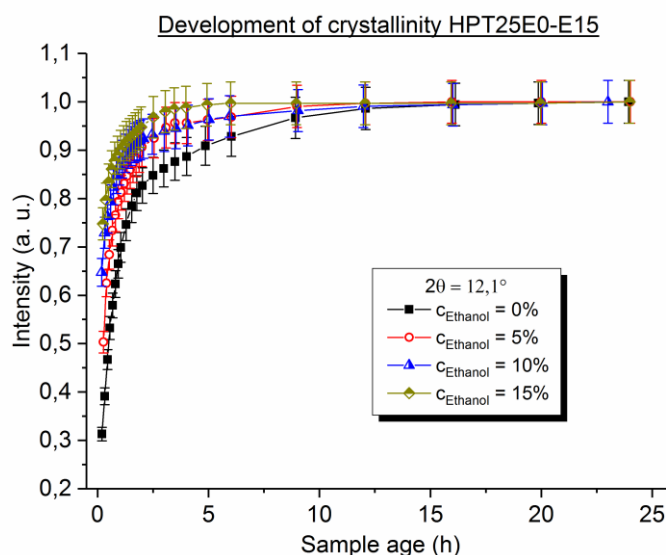


Fig. 81: Development of the relative intensity of HP gels prepared at 25°C , with 0% - 15% ethanol.

For all the samples, the main part of the crystallization takes place in the first two to three hours of the gelation. In those first hours, the intensity increases to 85 – 95% of the maximum intensity. This rapid increase of the intensity is again due to the crystallization process of the inulin particles, as already explained in section 3.2.2 (first primary particle formation, followed by aggregation and particle gel network formation). In Fig. 81 it is also obvious, that the initial crystallinity of the inulin samples, represented by the values at roughly 20 min sample age, depends on the amount of ethanol in the solvent. With increasing ethanol content, the solubility of HP decreases (Fig. 78), what results in increased initial intensities. In Fig. 82 one can see, the development of the relative intensities of the $2\theta = 12,1^\circ$ Bragg reflexes of HPX gels, prepared at 25°C , with an ethanol content of 0%, 5%, 10% and 15% in the solvent. The error bars are not indicated for the sake of clarity. Again the main part of the crystallization occurs in the first two to three hours (intensity increases to 90 – 95% of maximum intensity) and again this is due to the crystallization process and the particle gel formation. The increase in intensity is not as distinctively pronounced as for the HP samples (due to the crystallinity of the employed HPX powder, already mentioned in section 3.2.2). The curves in Fig. 82 look

almost identical and no obvious trend concerning the ethanol concentration can be determined. If the reader has a look at Fig. 78, it is obvious, that the already moderate solubility of HPX at 25 °C in water, is not influenced as much as the solubility of HP, by an increasing ethanol content in the solvent (see Tab. 5).

Tab. 5: HP/HPX dissolved dependent on ethanol content in solvent

Sample	Ethanol conc. (%)	Inulin diss. (%)
HPT25E0	0	17,49
HPT25E5	5	16,05
HPT25E10	10	13,26
HPT25E15	15	11,68
HPXT25E0	0	9,24
HPXT25E5	5	8,12
HPXT25E10	10	7,28
HPXT25E15	15	6,17

Since only a very small amount of long chain, hardly soluble HPX (DP > 45) is dissolved at 25 °C in water (see Fig. 59), the solubility of HPX at 25 °C is not influenced very much by a decreasing polarity of the solvent (HPX solubility decreases from 9,24% at 0% ethanol content to 6,17% at 15% ethanol content) and a significant part of the medium and short chain inulin (DP < 46) gets dissolved, even at an ethanol content of 15% (see Fig. 85). So the initial intensity of HPX is just slightly influenced by an increasing ethanol content and no obvious trend is visible. For HP, a significant amount of long chain inulin is already dissolved at 25 °C in water (see Fig. 58). The dissolved amount of long chain HP, which is just slightly soluble in pure water at 25 °C, reacts very sensitive to a decreasing polarity of the solvent. This is visible in Tab. 5, at the severe decrease of dissolved HP at increased ethanol contents.

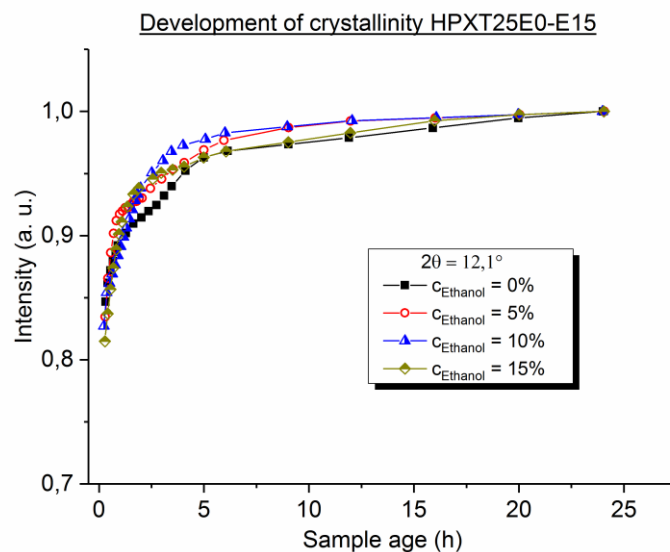


Fig. 82: Development of the relative intensity of HPX gels prepared at 25 °C, with 0% - 15% ethanol.

If Fig. 81 and Fig. 82 are compared to each other, it is obvious, that the HPX samples exhibit a significantly larger initial intensity. This is again, as already explained in section 3.2.2, due to the superior crystallinity of the HPX powder. To illustrate the significantly larger initial intensity of the HPX samples at the different ethanol contents again, the graphs of Fig. 81 and Fig. 82 have been plotted on a logarithmic scale and are illustrated simultaneously in Fig. 83. Again the error bars are not indicated for the sake of clarity.

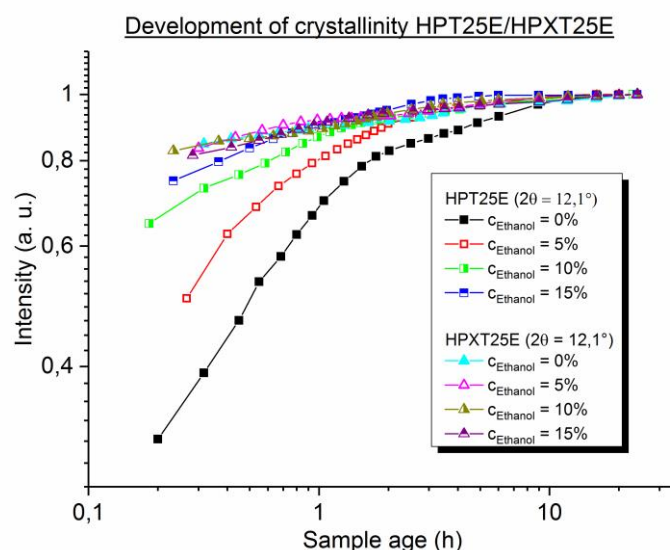


Fig. 83: Development of the relative intensity of HPT25E/HPXT25E gels, plotted on logarithmic scale.

In Fig. 83 it is obvious, that the initial crystallinity increases from HP, with an ethanol content of 0% to HP with an ethanol content of 15%. As mentioned above, the reason for this is the

decreasing solubility of HP with decreasing polarity of the solvent. Here it is also visible again, that the HPX samples exhibit no obvious trend, concerning the ethanol concentration, as already explained above.

To determine the crystallization constant k of the gel formation, a Johnson – Mehl – Avrami – Kolmogorov fit (JMAK) was applied to the curves shown in Fig. 81 and Fig. 82 (see section 3.2.2 and Eq.(55)). Again we just focused on the crystallization constant k . In Tab. 6 and Tab. 7 the average crystallization constants for HP and HPX samples, prepared with different ethanol concentrations in the solvent and determined by applying Eq.(55) on the curves shown in Fig. 81 and Fig. 82, can be seen.

Tab. 6: Average crystallization constant of HPT25E samples

$C_{(Ethanol)} (\%)$	$k (1/h)$	Error (1/h)
0	1,34	0,04
5	2,75	0,05
10	3,16	0,13
15	4,05	0,09

Tab. 7: Average crystallization constant of HPXT25E samples

$C_{(Ethanol)} (\%)$	$k (1/h)$	Error (1/h)
0	2,08	0,10
5	3,29	0,29
10	3,73	0,10
15	4,07	0,33

For both types of Inulin the crystallization constant k increases with increasing ethanol content in the solvent. As mentioned above, the solubility decreases with increasing ethanol concentration (Fig. 78) and with it the amount of nuclei, which act as seeding material, increases (The material, that is not precipitated, but remains undissolved during sample preparation,

acts as seeding material. Additionally, as mentioned in section 1.5, the polar inulin molecules and the solvent with a decreased polarity, form an unstable mixture. Therefore, the Gibbs free energy G_M of the mixture can be decreased, by the crystallization of inulin molecules, that can also act as seeding nuclei for further inulin molecules to crystallize on.). This results in an increased crystallization rate. The increased crystallization rate, as mentioned in section 3.2.2, influences the average gel particle size, altering the texture of the completely developed inulin gel significantly. Those results will again be explained in the following sections. If Tab. 6 and Tab. 7 are compared to each other, one can see, that the crystallization constant of the HP samples increases much more rapid, than it does for the HPX samples. This confirms the statement from above once more, that HP is influenced more by a decreasing polarity of the solvent at 25 °C sample preparation temperature, than HPX at the same conditions.

3.3.3 High Performance Anion Exchange Chromatography

To determine the chain length distribution of the inulin, dissolved during sample preparation and remaining dissolved after 24 h of ageing, one sample was taken from the inulin suspension (20% inulin dry matter, ethanol concentration 0% - 30%, $T_{\text{prep.}} = 25\text{ °C}$) after 10 min stirring and one was taken from the same gel after 24 h of ageing at room temperature. The samples were processed as described in section 2.5. To determine the DP distribution of the samples, a reference value was prepared, as described in section 3.2.3. The chromatograms are identically to the ones used for the inulin-water HPAEC experiments and can be seen in Fig. 56 and Fig. 57. To figure out the amount of inulin of a certain DP, dissolved during sample preparation, the areas below the peaks in the chromatogram were integrated, as mentioned in section 3.2.3. Again, the changes in the DP distribution of the dissolved inulin were pointed out and the concentration errors were minimized, by summing up a region of ten following DPs to one fraction. The results for HP and HPX, prepared at 25 °C with different ethanol contents in the solvent and the samples taken after 10 min sample preparation, can be seen in Fig. 84 and Fig. 85.

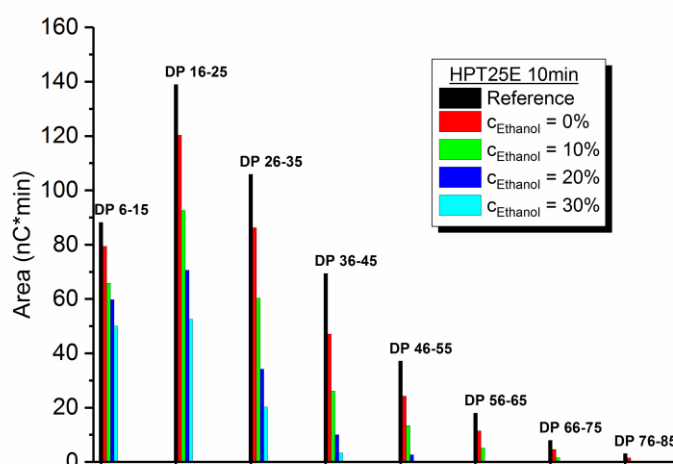


Fig. 84: DP distribution of dissolved HP after 10 min stirring at 25 °C, with ethanol content of 0% - 30%.

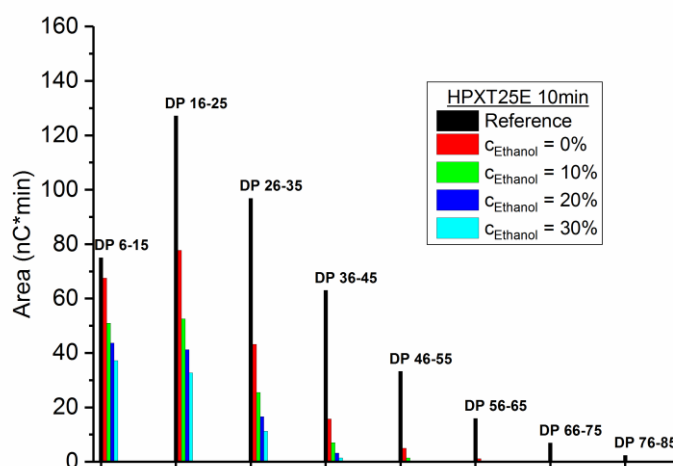


Fig. 85: DP distribution of dissolved HPX after 10 min stirring at 25 °C, with ethanol content of 0% - 30%.

With increasing ethanol content, the amount of dissolved inulin decreases. If the HP and HPX samples with increasing ethanol content in the solvent, are compared to the respective samples prepared in pure water, it is obvious, that the solubility is significantly decreased by a decreasing polarity of the solvent. Since the long chain inulin exhibits a very low solubility in water, the most crucial change in the DP distribution of the dissolved inulin is visible in this DP region (DP > 36 – 45). At ethanol contents of 20%, for both HP and HPX, practically no long

chain inulin is dissolved during sample preparation. Since the previously dissolved inulin partially crystallizes during gel formation, a considerable change in the DP distribution of the dissolved inulin changes the properties of the completely developed particle gel too. Because of this, as already mentioned in section 3.3.1, the ethanol concentration in the solvent was limited to 15% (w/w) for all the other experiments. With a decreasing solubility, the amount of undissolved material, that could act as seeding nuclei, also increases. Here it is important to consider, that undissolved material is also precipitated and removed from the system, that forms the particle gel network. So not all the undissolved material contributes to the gel formation. Due to the nature of the inulin suspensions during sample preparation, a selective separation of undissolved, not precipitated and undissolved, precipitated material was not possible. So here no information about the ratio of undissolved inulin and undissolved precipitated inulin can be given. Yet, the amount of undissolved HP and HPX, that acts as nuclei during crystallization, increases with increasing ethanol content in the sample (see section 3.3.2, increasing crystallization constant k for HP and HPX with increasing ethanol content). Still the gel hardness of the HP and HPX gels decreases with increasing ethanol content, what will be explained in section 3.3.4. If one compares Fig. 84 and Fig. 85, the significantly lower solubility of HPX is once again clearly visible (superior crystallinity of HPX powder, see section 3.3.1). Due to the lower solubility of HPX, even at an ethanol concentration of 0% in the solvent (pure water), almost no long chain inulin is dissolved. At an ethanol content of 10%, no long chain inulin ($DP > 36 - 45$) is dissolved anymore. So a further decreasing polarity by increasing the ethanol concentration, only affects the well dissolving medium and short chain HPX ($DP < 46$). For HP the decreasing polarity of the solvent has a more fiercely impact on the solubility. If one has a look at Fig. 84, even at 25 °C sample preparation in pure water (red columns), a significant amount of long chain inulin is dissolved. If the ethanol content is increased, all the DP fractions of HP are affected by a decreasing polarity and with it the precipitation of dissolved material. So the overall decrease in solubility of HP with an increasing ethanol content is much more pronounced, than for HPX (see section 3.3.1). Thus, with an increasing ethanol content in the solvent, the amount of dissolved HP and HPX is decreased and also the overall amount of inulin, that is incorporated in the crystallizing primary particles, is decreased (e.g. the slightly soluble long chain inulin is precipitated even at low ethanol contents and partly removed from the system).

Results and discussion

To determine the DP distribution of the inulin, remaining dissolved after 24 h of storage at room temperature, the 24 h samples were analyzed accordingly to the 10 min samples, as already explained earlier in this section. The results are visible in Fig. 86 and Fig. 87.

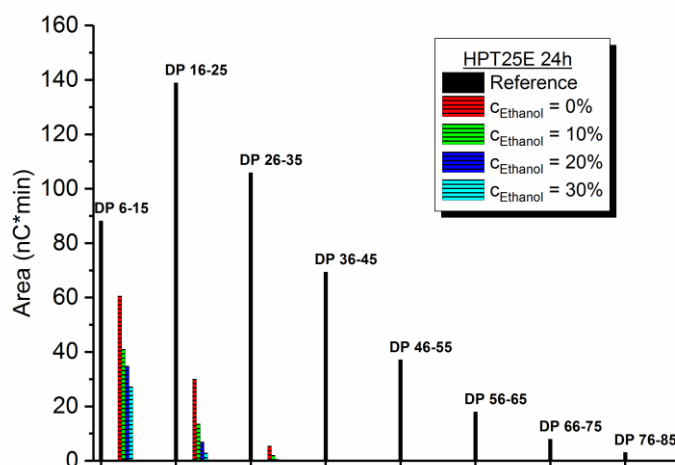


Fig. 86: Polarity dependent DP distribution of dissolved HP after 24 h storage.

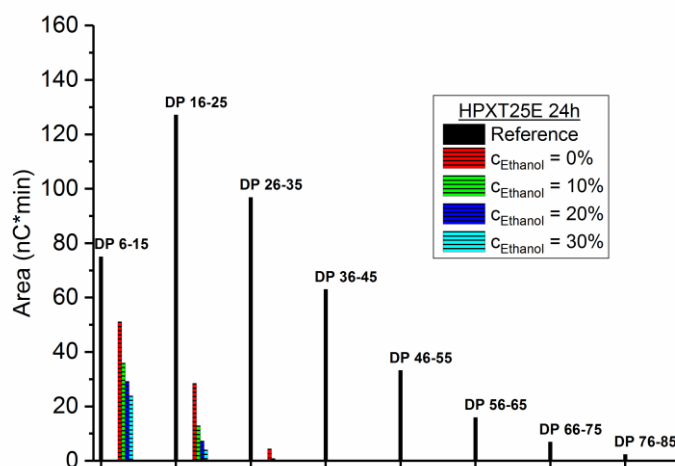


Fig. 87: Polarity dependent DP distribution of dissolved HPX after 24 h storage.

If Fig. 84 and Fig. 86 respectively Fig. 85 and Fig. 87 are compared to each other, one can clearly see, that the previously dissolved inulin almost completely recrystallizes during gel formation. Only a small amount of short and medium chain inulin, decreasing with increasing ethanol content, remains dissolved after 24 h. Above a DP of 35, for both HP and HPX, the

dissolved inulin completely crystallizes. Referring to the DP distribution of the gel primary particles, which are formed during crystallization (see section 1.1), an increased ethanol concentration in the solvent leads to the incorporation of a smaller overall amount of inulin, but an increased amount of long chain inulin in those primary particles. Since the solubility of long chain inulin is affected more fiercely by a decreasing polarity of the solvent, than the short and medium chain inulin, a significant amount of long chain inulin already remains undissolved at small ethanol contents. With increasing ethanol content in the solvent, the undissolved amount increases too. This undissolved long chain inulin is only partly precipitated during sample preparation. So the undissolved, not precipitated amount can act as seeding nuclei and is incorporated in the gel primary particles during crystallization. This influences the primary particle size and with it the texture of the completely developed inulin gel (see sections 3.3.4 and 3.3.6).

3.3.4 Texture analysis (Gel hardness)

In section 3.2.4, the completely developed inulin gels were compressed beyond their fracture stress, to learn about their fracture behavior. This type of experiment was not possible for the HP and HPX gels, prepared with ethanol in the solvent, due to the decreasing hardness of the gels. At increasing ethanol contents, even the HP gels became too soft to keep the cylindrical shape of the vessel, after being removed from it. In consequence, no compression experiments were performed for the water-ethanol system.

To examine the hardness of the inulin gels, the samples were penetrated by a stainless steel stamp to a maximum strain of 6 mm and the resulting gel hardness was determined as described in section 3.2.4. The results of the hardness measurements of the HP and HPX gels, prepared at 25 °C with different ethanol concentrations in the solvent (shear rate 600 rpm), are pictured in Fig. 88. One can observe the hardness of the HP and HPX gels decrease with increasing ethanol content. The explanation for those trends is on one hand, as already mentioned in section 3.3.1 and 3.3.3, the decreased solubility of HP and HPX and the precipitation of material connected therewith, that is not incorporated in the gel formation. This results in fragmentary, soft gels and the gel hardness decreases. On the other hand, the incorporation of more long chain HP and HPX in the gel primary particles and the increasing crystallization constant k with increasing ethanol content, result in a changing primary particle size. This will be explained more detailed in section 3.3.6.

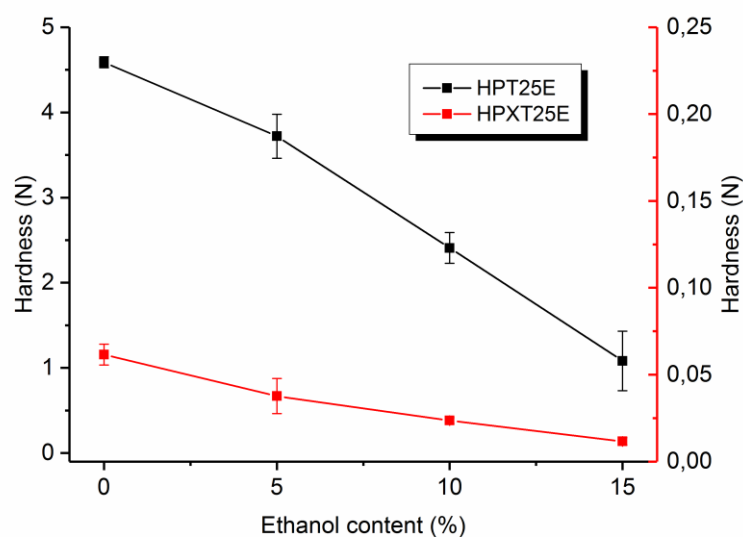


Fig. 88: Hardness of inulin gels prepared with different ethanol contents in the solvent

Therefore, the texture of the developing inulin gels can be influenced by the variation of the polarity of the used solvent. To illustrate the different gel structure of the HPT25E and HPXT25E gels, in Fig. 89 confocal microscopy pictures of an HP gel, prepared at 25 °C with an ethanol content of 0% and an HPX gel, prepared at 25 °C with an ethanol concentration of 15% in the solvent, are presented and compared to the respective hardness values.

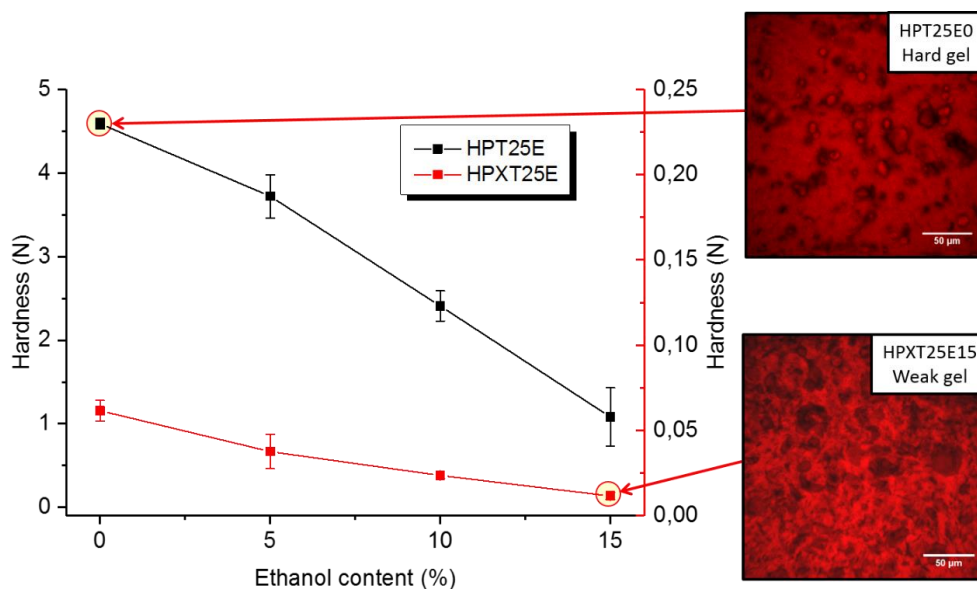


Fig. 89: Comparison of gel structure of HP and HPX gels, both prepared at 25 °C with different ethanol contents in the solvent. Each picture was taken in a depth of 10 μm .

On the left hand side of Fig. 89, one can see the polarity dependent hardness curves of HP and HPX gels, prepared with a shear rate of 600 rpm. Those curves have already been presented

in Fig. 88. The CLSM pictures of an HPT25E0 ($T_{prep.} = 25\text{ }^{\circ}\text{C}$, $c_{Eth} = 0\%$) and an HPXT25E15 gel ($T_{prep.} = 25\text{ }^{\circ}\text{C}$, $c_{Eth} = 15\%$), can be seen on the right hand side of Fig. 89. Again, both pictures have been taken from the bulk of the samples, 10 μm above the bottom of the nunc chambers. The associated hardness values are highlighted in the diagram on the left. It is clearly visible, that HPXT25E15 forms the weakest gel of the whole series and HPT25E0 yields the hardest gel. If the pictures on the right are compared to each other, significant differences in the gel structures of the HP and HPX gels are clearly visible. As already mentioned in section 3.2.4, both gels are dyed with Rhodamine B. Therefore, the regions where water is accumulated, again appear just lightly red or almost dark in both gels. Apart from the large, lightly dyed remnants of the HP powder, that have not been dissolved during sample preparation and are dispersed throughout the whole gel, the HPT25E0 gel network appears homogeneously dyed, without any obviously darker regions. As before, this is a clear indication for a homogeneous and strong network, what can be confirmed by the associated hardness value. The HPXT25E15 gel on the opposite yields an inhomogeneous gel network, interspersed with dark regions, where water is clearly accumulated. Comparable to the HPX gel, prepared at 25 $^{\circ}\text{C}$ in pure water (Fig. 66), this results in a fragmentary weak gel structure, also confirmed by the respective hardness value, visible in Fig. 89. Due to the precipitation of inulin, that does not take part in the particle gel network formation, the HPXT25E15 is even weaker, than the respective HPX gel, prepared in pure water (hardness value at 0% of ethanol in Fig. 89). As already seen for the HP and HPX gels, prepared with pure water, the hardness values of the HPXT25E gels remain way below the respective HPT25E hardness values, what is due to the fragmentary gel structure of the HPX gels. As already mentioned above, the formation of the different gel networks and the corresponding hardness values, will be explained in the following sections. Since the confocal microscopy pictures of the HP and HPX gels, prepared with different ethanol contents in the solvent, did not show any obvious change in structure, that could be referred to the respective ethanol concentration, in this section just the two microscopy pictures pictured in Fig. 89, are presented (the remaining pictures can be found in the Appendix section).

3.3.5 Oscillatory rheology

As already presented for the inulin-water samples, the viscoelastic properties of the completely developed HP and HPX gels, prepared at 25 $^{\circ}\text{C}$ and with an increasing ethanol content

Results and discussion

in the solvent, were also determined by performing amplitude sweeps at the unsheared samples. In Fig. 90 one can see the amplitude sweep curves of HP gels, prepared at 25 °C and with ethanol concentrations of 0%, 5%, 10% and 15% in the solvent. The samples have been measured between 0,1% and 100% oscillation amplitude. The error bars are not indicated, due to the sake of clarity.

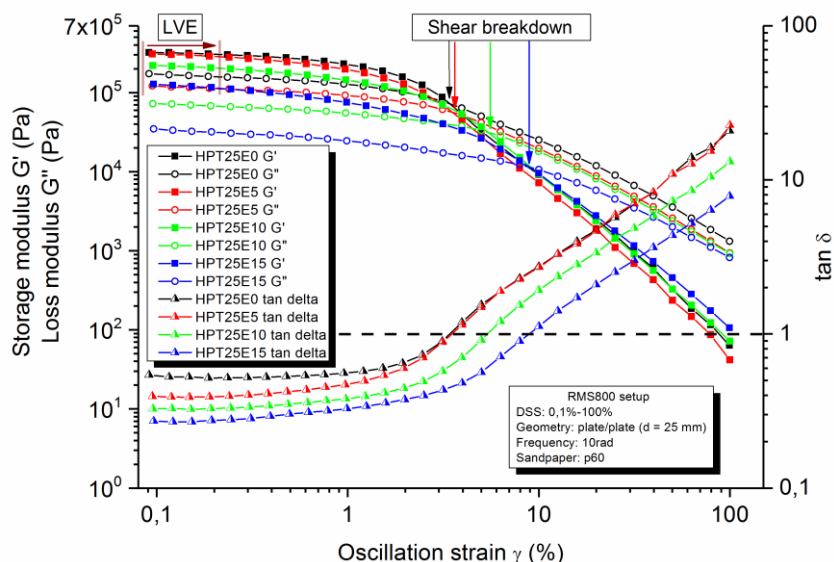


Fig. 90: Amplitude sweep curves of HP gels, prepared at 25 °C, with ethanol contents of 0%, 5%, 10% and 15% in the solvent. The device setup is indicated in the figure.

Again, the storage modulus G' and the loss modulus G'' are plotted against the applied oscillation strain γ . The dissipation factor $\tan \delta$ is also plotted against the oscillation strain. In Fig. 90 the Linear Viscoelastic Region (LVE) is again indicated with diagonal, brown lines. The LVE regions of all the HP gels span comparable strain regions and do not show any obvious change, that could be traced back to the different ethanol contents. The trend of the HP gel's shear moduli follows the trend of the respective hardness values (Fig. 88). The HP gel, prepared at 25 °C with an ethanol content of 0% in the solvent, exhibits the largest initial storage modulus, just as it exhibits the largest gel hardness. With increasing ethanol concentration, the initial shear moduli decrease, comparable to the trend of the respective gel hardness. For all the HP samples, the initial storage modulus G' exceeds the initial loss modulus G'' . Therefore, the elastic properties of all the HP samples dominate at small oscillation amplitudes, marking them as “solid” gels. If the oscillation amplitude is increased, both the moduli decrease. This

shear thinning behavior is again due to the weakening of the bonds between the primary particles, which are stressed by the increased shear forces (see section 3.2.5). If the applied strain exceeds the “fracture strain”, the particle gel network is destroyed, what is again visible in the point of shear breakdown. The shear breakdown for each gel is indicated in Fig. 90 and a dissipation factor $\tan \delta$ of the value 1, can be recognized again by a horizontal dashed line. Comparable to the HP gels, prepared at different sample preparation temperatures (Fig. 67), the shear breakdown is shifted to larger oscillation amplitudes, if the ethanol concentration in the solvent is increased. This means, the “softer” the HP gel is the more insensitive it reacts to deformation. Therefore, for an HP gel, prepared with increased ethanol concentration in the solvent, the primary particles in the completely developed gel are not that strong bound to each other, giving the gel a softer and more flexible structure. This is on one hand due to the change of the primary particle size with a changing polarity of the solvent (see section 3.3.6) and on the other hand, as already mentioned in section 3.3.1 and 3.3.4, to the precipitation of inulin at increased ethanol concentrations and the weakening of the network structure connected therewith. Above an oscillation amplitude of 10%, for all the gels the particle network is destroyed, the primary particles are completely separated from each other and the samples behave like viscous fluids. If Fig. 67 and Fig. 90 are compared to each other, it is obvious, that an increasing sample preparation temperature and a decreasing polarity of the solvent, have a similar impact on the viscoelastic properties of the HP gels and result in a weakening of the particle gel network.

In Fig. 91 one can see the amplitude sweep curves of HPX gels, prepared at 25 °C, with an ethanol content of 0%, 5%, 10% and 15% in the solvent. Again G' , G'' and $\tan \delta$ are plotted against the oscillation strain γ and the samples have been measured between 0,1% and 100% oscillation amplitude. Again, the error bars are not indicated.

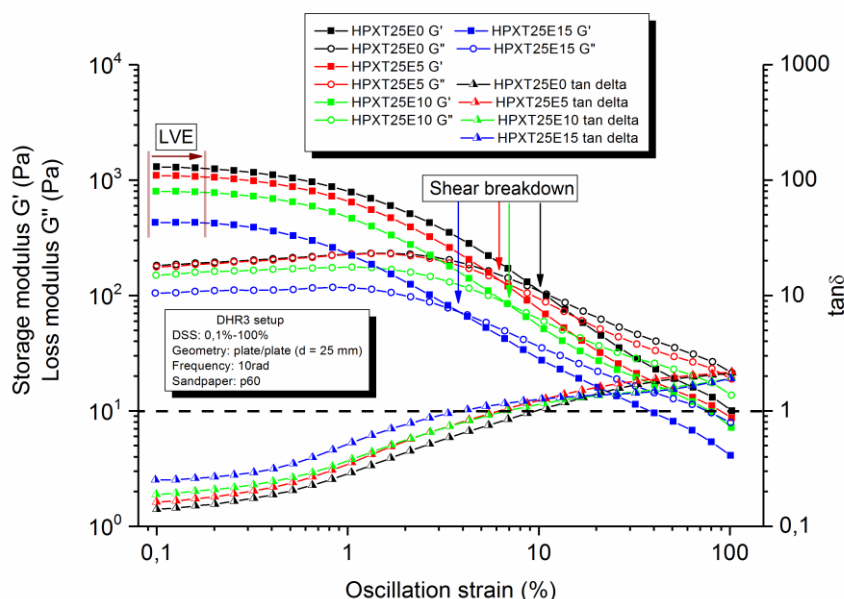


Fig. 91: Amplitude sweep curves of HPX gels, prepared at 25 °C, with an ethanol content of 0%, 5%, 10% and 15% in the solvent. The device setup is indicated in the figure.

As before, the LVE region is indicated with diagonal brown lines and the dashed horizontal line indicates a $\tan \delta$ of 1. The points of shear breakdown are also indicated for the respective curves. Here again the shear moduli G' and G'' follow the hardness trends of the respective HPX gels (Fig. 88). If the ethanol concentration is increased, the hardness values of the completely developed HPX gels decrease and with it the initial values of the shear moduli decrease too. As already mentioned above, with decreasing gel hardness and decreasing initial shear moduli, the gels become more shear insensitive. If one considers the indicated points of shear breakdown in Fig. 91, it is obvious, that the HPX gels with different ethanol concentrations, show no obvious trend concerning the shear sensitivity. This is due to the very soft structure of the HPX gels. If the initial shear moduli are compared to the initial shear moduli of the respective HP gels (Fig. 92), one can see, that the shear moduli of the HPX gels are at least to orders of magnitude smaller than the respective HP values. So even the “stiffest” HPX gel, namely the HPX gel with pure water acting as solvent, is already very soft and shear insensitive. Therefore, the HPXTE gels are relatively indifferent to increased ethanol concentrations, concerning the shear breakdown. In Fig. 92 the storage moduli of the HPT25E and HPXT25E gels, presented in Fig. 90 and Fig. 91, are plotted against the oscillation amplitude and compared to each other. The curves are plotted between 0,1% and 100% oscillation amplitude and the error bars are not indicated.

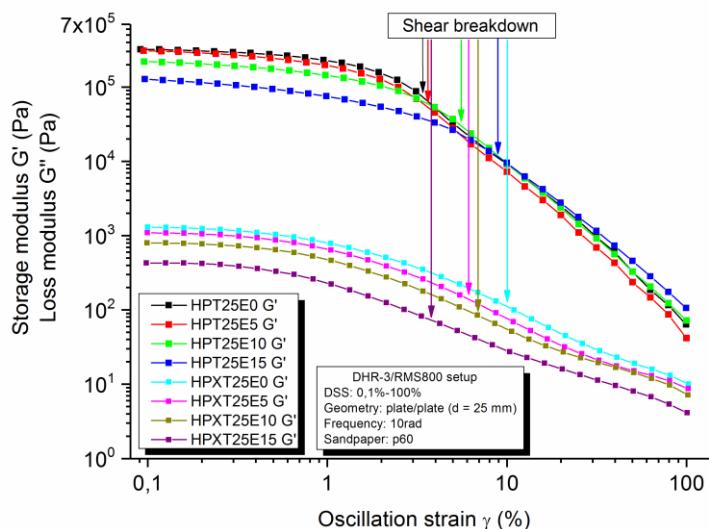


Fig. 92: Comparison amplitude sweeps of HPT25E and HPXT25E gels. Point of shear breakdown is indicated for each sample.

If the initial storage moduli of the HP and the HPX gels are compared to each other, again the hardness trends are followed. All the HP samples exhibit a significantly higher initial storage modulus G' . The initial storage modulus decreases from HPT25E0 to HPXT25E15. The reason for this decrease is again, as already explained for the hardness trends of the HPT25E and HPXT25E gels (see section 3.3.4), the change in the network structure of the gels (HPT25E0 homogeneous, strong network, HPXT25E0 - E15 fragmentary, weak network). The explanation for the changing particle network structure will be given in more detail in the following sections. In Fig. 92 the loss moduli are not plotted (for the sake of clarity). Again, the points of shear breakdown are indicated. The trend of an increasing shear sensitivity with increasing initial storage moduli is still fulfilled (at least in the HP series). As mentioned above, due to their soft gel structure, for HPX no overall trend can be seen. The HPX gels ($c_{\text{Ethanol}} = 0\% - 15\%$) and the “soft” HP gels ($c_{\text{Ethanol}} \geq 10\%$) exhibit comparable stiffness and brittleness, what results in points of shear breakdown at similar oscillation amplitudes.

3.3.6 Particle size

The particle size trends of the HP and HPX gels, prepared at 25 °C and with an ethanol content of 0%, 5%, 10% and 15% in the solvent, provide an explanation for the above discussed hardness trends and can be observed in Fig. 93. The average size of the HP gel primary particles, increases with increasing ethanol content in the solvent. As already shown in section 3.3.2 (Tab. 6), the crystallization constant k of the HP samples prepared at 25 °C, increases with

increasing ethanol content in the solvent. Typically, the average particle size decreases with increasing crystallization speed (see section 3.2.6). Thus, the average particle size of the HP samples with increasing ethanol content, acts inversely as expected concerning the respective crystallization constants. This is due to the decreasing solubility of HP with decreasing polarity of the solvent (see Fig. 78) and the incorporation of a larger amount of long chain inulin in the crystallizing gel primary particles connected therewith (see section 3.3.3), which overcompensates the increasing crystallization speed. Those larger gel particles and the precipitation of inulin, that is not incorporated in the primary particles (see section 3.3.4), are responsible for the decreased hardness of the inulin gels at increased ethanol concentrations (see Fig. 88). As mentioned before, the surface to volume ratio of larger spherical particles is smaller. Thus, the larger particles can form fewer bonds between each other. Additionally, the smaller overall amount of inulin, that is incorporated in the primary particles, results in a fragmentary and weak particle gel network. Therefore, the HP gel hardness decreases with increasing ethanol content in the solvent, as already expected from the polarity considerations and the development of the crystallinity.

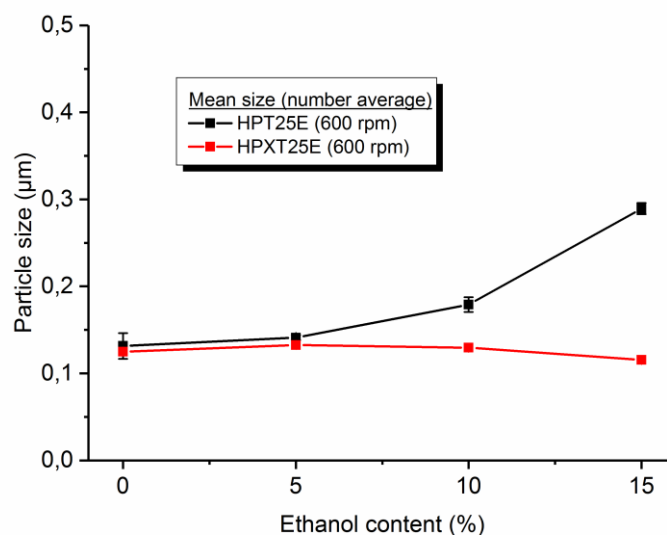


Fig. 93: Gel primary particle size (number average) in dependency of ethanol content in the solvent.

To illustrate the increasing particle size of the HP primary particles once again, the number distributions of the HP gel particle size, prepared at 25 °C with an ethanol content of 0% and 15% in the solvent and examined by static light scattering, are pictured in Fig. 94. If one compares the particle size distribution of the sample prepared with 0% of ethanol and the one

prepared with 15% of ethanol, it is obvious, that the curve of the 15% sample is shifted to larger particle sizes. The mean primary particle size (number average) is indicated next to the respective curve in Fig. 94.

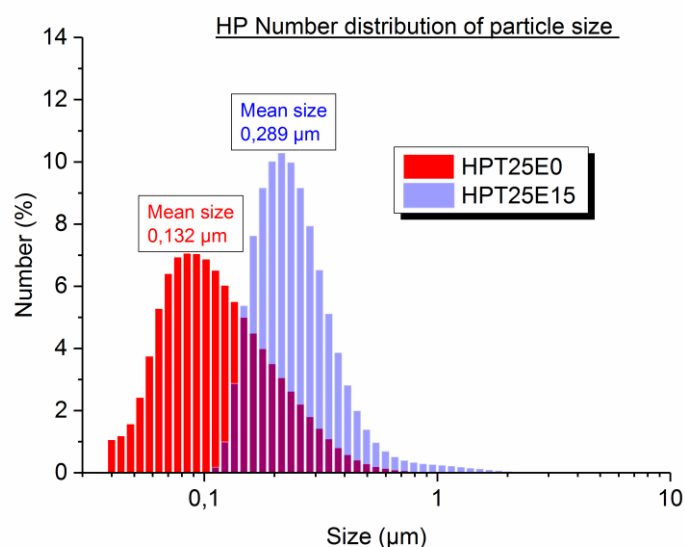


Fig. 94: Number distribution of HP gel particle size, prepared at 25 °C with 0% and 15% ethanol in the solvent.

The average primary particle size of the HPX gels, prepared with different ethanol contents in the sample, behaves considerably different as the respective HP primary particle size. For the HPX gels the average primary particle size remains constant even at increased ethanol concentrations. This arises from the semi-crystallinity of the used HPX powder. The decreasing polarity of the solvent, with increasing ethanol concentration, affects the HPX powder just as the HP powder and the solubility of HPX decreases too, with increasing ethanol content. As mentioned before, due to its semi-crystalline character, the HPX powder exhibits a significantly lower solubility in the solvent than HP. If we recall the DP distribution of the dissolved HPX with increasing ethanol content (Fig. 85), we recognize, that even at 25 °C with an ethanol content of 0% in the solvent, only a very small amount of long chain inulin is dissolved, that can be incorporated in the primary particles during gelation. Therefore, at increased ethanol contents almost no long chain inulin is dissolved during sample preparation, that can be “forced” to crystallize by the decreasing polarity and inversely to the HP samples at increased ethanol contents, the amount of long chain HPX, that is incorporated in the primary particles during crystallization, decreases with increasing ethanol content. This should result in a decreasing average particle size, yet the average particle size remains constant. Additionally, due to the decreased solubility and with it an increased amount of undissolved material, that can

act as crystallization nuclei, the crystallization constant k of the HPX samples increases with increasing ethanol content (see Tab. 7). This should also result in gels with decreased primary particle sizes and connected therewith, increased hardness values at increased ethanol concentrations. Yet the HPX gel hardness decreases with increasing ethanol content and remains way below the gel hardness of the respective HP gels (see Fig. 88). To understand this, we need to consider the distribution of the HPX primary particle sizes. In Fig. 95 the number distribution of the primary particle size of HPX gels, prepared at 25 °C with 0% and 15% ethanol in the solvent, are pictured. The particle size distributions of both gels look almost identical. As already mentioned in section 3.2.6, changes in the outer regions of the number distribution, where the less numerous small and large particles are represented, are just slightly visible in Fig. 95. Still we can see, that the amount of very small primary particles (on the left hand side of the curve) increases with increasing ethanol content and the amount of very large primary particles (on the right hand side) decreases with increasing ethanol content in the solvent. Again, as already mentioned in section 3.2.6, to point out changes in the particle sizes of the less numerous particles (the ones in the outer regions of the number distribution), one needs to examine the volume distribution of the HPX gel particle size. The volume distribution of the HPX gels pictured in Fig. 95 is visible in Fig. 96.

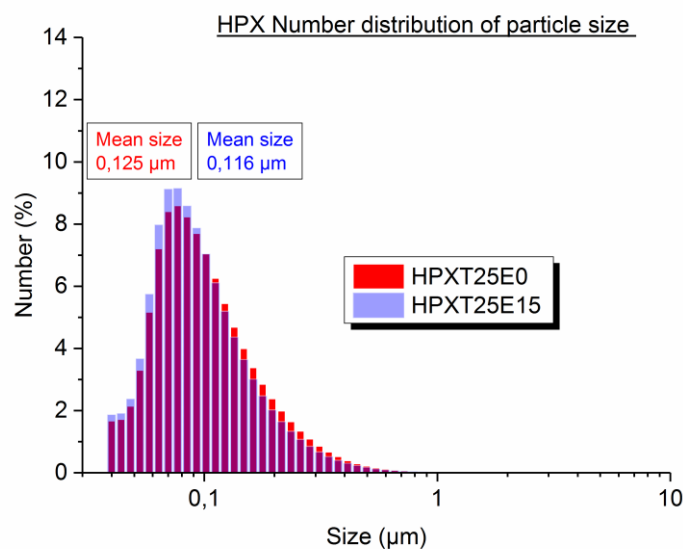


Fig. 95: Number distribution of HPX gel particle size, prepared at 25 °C with 0% and 15% ethanol in the solvent.

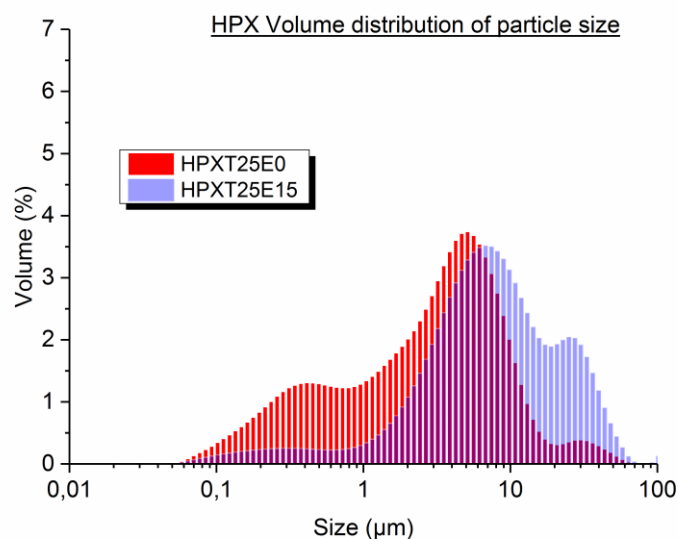


Fig. 96: Volume distribution of HPX gel particle size, prepared at 25 °C with 0% and 15% ethanol in the solvent.

In Fig. 96 the changes in the particle sizes are clearly visible. If one compares the curves of the 0% ethanol and the 15% ethanol sample to each other, it is obvious, that the volume the very small particles take up decreases and the volume the very large particles occupy increases with increasing ethanol content. The average primary particle size (approximately represented by the maximum in the middle) remains relatively constant. To interpret the development of the primary particle sizes correctly, we need to take the number and the volume distribution into account. As already mentioned above, the number of very small particles increases with increasing ethanol content (Fig. 95 left hand side). The increased number of very small particles at an ethanol content of 15% in the solvent, occupy a smaller volume than the less numerous small particles at 0% ethanol in the sample (Fig. 96 left hand side). This means, the very small primary particles decrease in size with increasing ethanol content. If we have a look on the right hand side of the number and the volume distributions, we can see, that the number of very large particles decreases with increasing ethanol content (Fig. 95 right hand side). Those less numerous very large primary particles occupy a larger volume at an increased ethanol concentration (Fig. 96 right hand side). This means, the very large primary particles increase in size with increasing ethanol content in the solvent. As already mentioned, with a decreasing polarity the solubility of HPX in the solvent decreases too. Normally, with increasing solubility, the crystalline particles, which consist of mainly long chain inulin and are already present in the HPX powder, are partly dissolved and decrease in size. Since the solubility decreases, the crystalline particles are just poorly dissolved and exhibit a larger size, compared

to the crystalline, undissolved particles at lower ethanol concentrations. The long chain inulin, that is contained in the undissolved crystalline particles, is unavailable for the crystallizing primary particles. Therefore, a smaller amount of long chain inulin is incorporated in the newly crystallizing primary particles and they decrease in size, compared to the crystallizing particles at decreased ethanol contents in the solvent. This means, with increasing ethanol content, the newly crystallizing primary particles decrease in size and the already crystalline, undissolved primary particles increase in size. Those two processes roughly compensate each other and the average primary particle size of the HPX gels remains constant, even at an increased ethanol concentration. The decreased solubility of HPX (resulting in an increased amount of undissolved material, that can act as crystallization nuclei) and the decreasing particle size of the newly crystallizing primary particles at increased ethanol contents, go along with an increased crystallization constant k (see Tab. 7). Still, as already mentioned above, the hardness decreases with decreasing polarity of the solvent (inversely to the expectation of an increasing gel hardness with decreased primary particle size or a constant hardness with constant average particle size). This is due, as mentioned in section 3.3.4, to the precipitation of inulin at increased ethanol concentrations and with it the overall decreased amount of inulin, that is incorporated in the primary particle network during gel formation. Here it should be mentioned again, that inulin primary particle clusters, which passed the pores of the filter or re-aggregated after filtration during sample preparation, have a significant impact on the volume average of the primary particle size. Because of this, the volume average differs significantly from the number average of the primary particle size. Therefore, as already done in section 3.2.6, in Fig. 93 the number weighted average primary particle sizes of the HP and HPX gels have been evaluated, to minimize the undesired impact of particle clusters in the samples on the average primary particle size.

3.3.7 Summary

Taking the above discussed results into account, the polarity dependent hardness variation of the completely developed inulin gels can be summarized by a simple model. The models are pictured in Fig. 97 and Fig. 98.

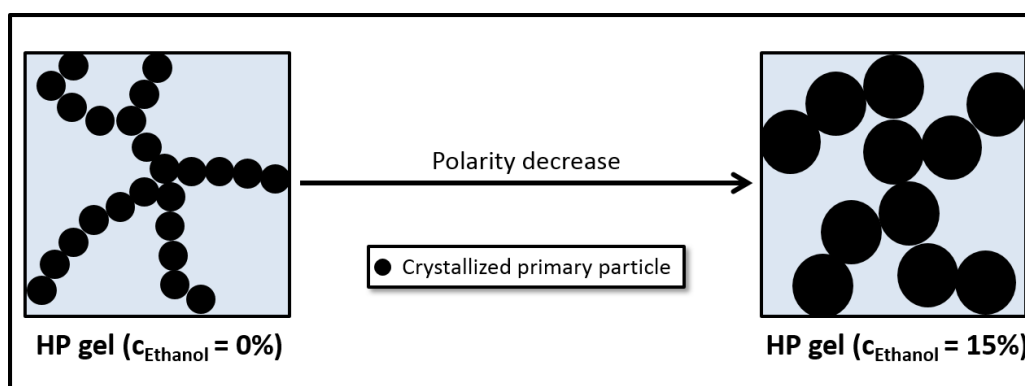


Fig. 97: HPT25E particle size variation

Fig. 97 illustrates the particle gel structures of two completely developed HP gels, one prepared at 25 °C with 0% ethanol in the solvent and one prepared at 25 °C with an ethanol concentration of 15%. Since the model in Fig. 97 is simplified and intended to illustrate the polarity dependent particle size variation, the pictured dimensions are randomly chosen. For the gel prepared with an ethanol concentration of 0%, a sufficient amount of inulin remains undissolved during sample preparation and acts as crystallization nuclei, ensuring a seeded crystallization. After 24 h of crystallization, the resulting HP gel consists of small primary particles and exhibits a hard texture. If the polarity is decreased by the addition of ethanol to water, the solubility of HP in this solvent significantly decreases and with it the amount of undissolved nuclei increases. This causes a considerable increase in crystallization velocity. Inversely to the expectations, the average primary particle size increases (Fig. 93). At increased ethanol concentrations, a significant amount of long chain HP remains undissolved during sample preparation, acting as crystallization nuclei (Fig. 84). The increased amount of undissolved long chain inulin is partly incorporated in the crystallizing primary particles during gel formation, but also partially precipitated. This results in HP gels with an increased average primary particle size (due to the increased amount of long chain inulin in the primary particles) and a decreased gel hardness (due to the decreased overall amount of inulin incorporated in the particle gel network) at an increased ethanol content in the solvent (Fig. 88).

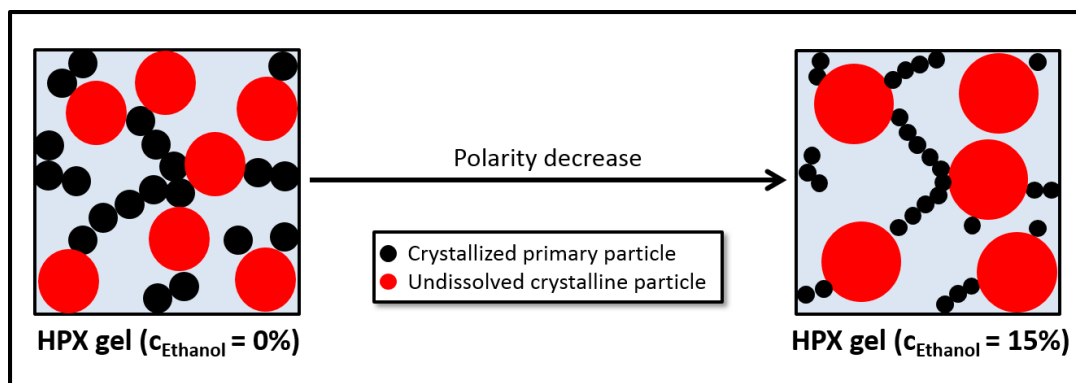


Fig. 98: HPXT25E particle size variation

In Fig. 98 the particle gel structures of two completely developed HPX gels, one prepared at 25 °C with 0% ethanol in the solvent and one prepared at 25 °C with an ethanol concentration of 15%, are pictured. Again, this is a very simplified model to illustrate the particle size variation. At 25 °C and 0% ethanol content, HPX exhibits a moderate solubility in the solvent (Fig. 78) and mostly short and medium chain inulin is dissolved during sample preparation. Additionally, the HPX powder already contains a significant amount of crystalline particles, which can act as seeding material during crystallization. For the HPX gel, prepared with an ethanol concentration of 0%, this results in a fragmentary gel structure (see Fig. 66 and Fig. 98), that consists of small, during gel formation crystallized primary particles (black particles in Fig. 98, that mainly consist of short and medium chain inulin) and large, undissolved crystalline primary particles, that were already present in the HPX powder (red particles in Fig. 98, which mainly consist of long chain inulin). As already mentioned in section 3.2.7, this fragmentary, not very densely packed gel structure of the 0% ethanol content HPX gel results in a very low hardness. If the ethanol concentration is increased to 15%, the solubility of HPX decreases. At 25 °C sample preparation temperature with an ethanol content of 0% (solvent is pure water), the crystalline powder particles are poorly dissolved and therefore just slightly decreased in size. If the solubility of HPX decreases at increased ethanol concentrations, the crystalline powder particles are even less dissolved and therefore their size is increased compared to the crystalline powder particles at 0% of ethanol in the solvent (see section 3.3.6). Since the undissolved crystalline particles consist of mainly long chain HPX, this undissolved amount of long chain inulin is unavailable for the newly crystallizing particles during gel formation (black particles in Fig. 98), a smaller amount of long chain HPX is incorporated in those crystallizing particles and they decrease in size, compared to the crystallizing particles at 0% of ethanol in the solvent. Additionally, due to the decreased polarity at increased ethanol concentrations,

part of the undissolved HPX (mainly medium and long chain inulin) is precipitated. Therefore, the amount of long chain inulin, that can be incorporated in the crystallizing particles, is even further decreased, also adding to the decreased size of the crystallizing particles. Furthermore, by the precipitation of HPX, the overall amount of inulin, that is incorporated in the particle gel network during gel formation, decreases, weakening the gel network even more. This means, at increased ethanol contents, HPX still forms a fragmentary network, that is even weaker than the HPX gel prepared with an ethanol concentration of 0% in the solvent (Fig. 88).

3.4 The inulin-water-sucrose system

In this chapter the results of the HP and HPX samples, that have been prepared with water-sucrose mixtures acting as solvent, will be presented and discussed. For all the measurements in this section the results for HP and HPX, prepared at 25 °C in water, were used as reference values. This means, the sample preparation temperature was set to 25 °C for all the samples and the sucrose concentration in the solvent adjusted to 0% (reference values of HP and HPX at 25°C in water), 5%, 10% and 15% (w/w) (the sucrose mass concentrations were also chosen, to operate at similar additive concentrations in the solvent as used for the inulin-ethanol system).

3.4.1 Solubility in water-sucrose mixtures

In section 3.2.1 the solubility of 20% dry matter of inulin at different sample preparation temperatures in water, was discussed. In this section water-sucrose mixtures act as solvent. As mentioned above, the preparation temperature was set to 25 °C and the sucrose concentration (w/w) of the solvent increased from 0% to 15%. As already mentioned in section 3.2.1, all samples in this work were prepared with 20% dry matter of inulin, so here the solubility of HP and HPX in the varying solvent also refers to 20% dry matter in the sample. The equilibrium solubility of both types of inulin in deionized water with increasing sucrose content is shown in Fig. 100. Again, the concentration of the dissolved inulin was determined by measuring the refractive indices of the samples and comparison to reference values, obtained at specified mass concentrations of dissolved inulin. Since the refractive index of the pure solvent changes with differing sucrose content, a reference curve had to be generated, as described in section 3.2.1, for each sucrose content used for the experiments. For the determination of the concentration of dissolved inulin in water (sucrose content 0%), the reference curve from section

3.2.1 was used (Fig. 49). For the sucrose-water mixtures with a sucrose content $\geq 5\%$, the data has been fitted over the concentration range $0 \leq c \leq 0,075$ and the equations of the linear fits can be found in Fig. 99. The reference curve for a sucrose content of 0%, was fitted as mentioned in section 3.2.1. The reference plots are again the same for HP and HPX. This is why only one series of plots is pictured in Fig. 99. The reference plot for pure deionized water can be found in Fig. 49.

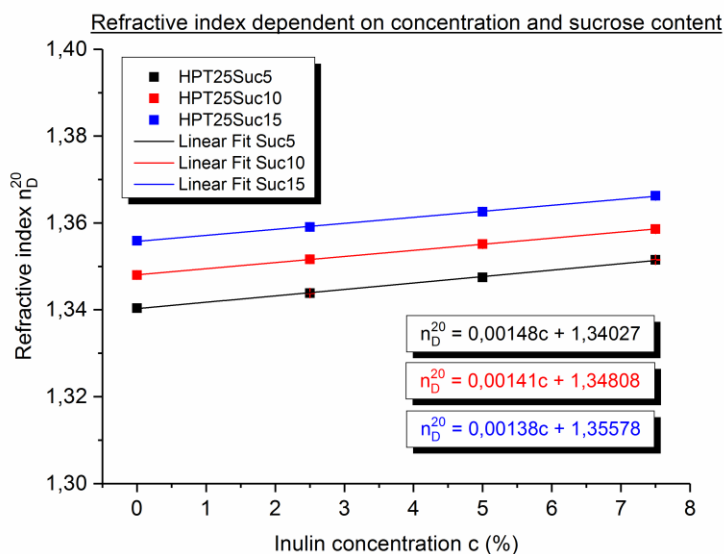


Fig. 99: Refractive index in dependency of the mass concentration in water-sucrose mixtures.

The solubility of inulin decreases with increasing sucrose content in the solvent (Fig. 100). Sucrose is a disaccharide ($DP_{\text{sucrose}} = 2$) and therefore very well soluble in water, even at 25 °C (compared to the inulin molecules with a $DP > 3$, the small and polar sucrose molecule can be very easy hydrated by the water molecules.). Thus, the amount of sucrose, added to the solvent, is preferably dissolved. The higher the sucrose content in the solvent, the higher is also its degree of saturation. Therefore, the amount of inulin that can be still dissolved in the solvent at 25 °C, decreases with increasing sucrose concentration (the long chain fractions of HP and HPX will again be affected the most by the increasing saturation of the solvent, see section 3.4.3). If one has a look at Fig. 100, it is also obvious, that HPX exhibits a significantly lower solubility than HP at each sucrose content examined. The reason for this is again, as already discussed in section 3.2.1, the superior crystallinity of the employed HPX powder. Apart from this overall decreased solubility of HPX, the solubility trend of both types of inulin in the water-ethanol mixtures is comparable.

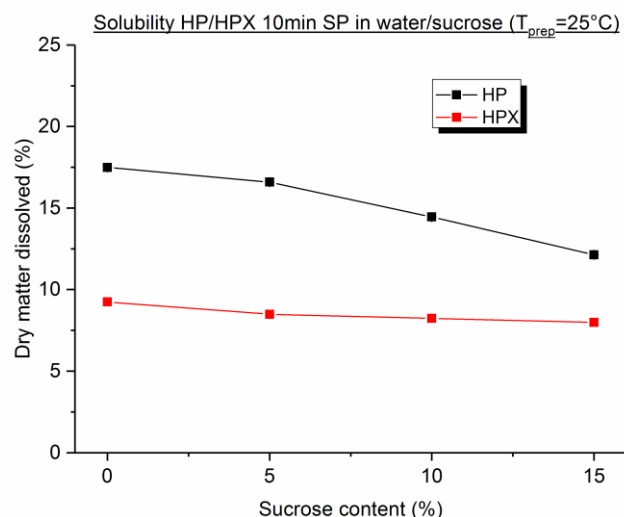


Fig. 100: Equilibrium solubility of 20% (w/w) inulin in water-sucrose mixtures.

3.4.2 X-ray diffraction during gelation

The development of the particle gel network, with water-sucrose mixtures acting as solvent, was examined by in-situ x-ray diffraction too. The radial averaged diffraction patterns of the HP and HPX gels, prepared at 25 °C, with a sucrose mass concentration of 5% and measured for 24 h during gelation, can be seen in Fig. 101 and Fig. 102. The intensities of the Bragg reflexes at $2\theta = 12,1^\circ$ have been projected to the left hand layer, to make the gelation process more obvious. Again, as already seen in section 3.2.2 (see Fig. 51 and Fig. 52), the intensity of the HP and HPX samples increases with increasing aging time. This increasing intensity confirms, that HP and HPX in a water-sucrose milieu, with 20% (w/w) of inulin in the sample, crystallize during gelation. The process is similar as already described in section 3.2.2. If one compares Fig. 101 and Fig. 102 to each other, the HPX sample exhibits a significantly higher initial intensity. The reason for this is the same as for the two other inulin-solvent systems, namely the superior crystallinity of the employed HPX powder (see Fig. 47 and section 3.2.2). If the absolute intensities of Fig. 101 and Fig. 102 are compared to Fig. 51 and Fig. 52, it is obvious, that the diffraction spectra of the HP and HPX samples, prepared with 5% sucrose in the solvent, exhibit a remarkably lower intensity than the respective samples prepared with pure water. Again, this could arise from the three reasons, already discussed in section 3.3.2. Since an increased sucrose content in the solvent does not change the polarity of the same and no inulin is precipitated during sample preparation, the decreased diffracted intensity of the sucrose samples is exclusively of experimental nature. If one compares the absolute intensities of the HP and HPX samples, prepared with 5% sucrose in the solvent (Fig. 101 and

Fig. 102), to the respective absolute intensities of the samples, prepared with 5% ethanol in the solvent (Fig. 79 and Fig. 80), the decreased intensities of the samples prepared in the water-ethanol mixture, attract the observers attention. As the water-ethanol and the water-sucrose samples have been examined in immediate succession, the intensity fluctuations, which arise from the experimental setup, were minimized and have just a minor impact on the decreased diffracted intensity values. Therefore, the decreased absolute intensities of the water-ethanol samples are of physical nature, namely the decreasing polarity of the solvent with increasing ethanol content and the precipitation of inulin connected therewith (see section 3.3.2). Again, the fluctuations in the absolute intensities could not be investigated systematically. So all the samples, belonging to the same series of experiments (e.g. the samples prepared in water-sucrose mixtures), were measured in the shortest time interval possible, to minimize the influence of a fluctuating incident x-ray intensity. Additionally, as already mentioned in section 3.2.2, all the intensities of the $2\theta = 12,1^\circ$ reflexes of one sample were normalized to the respective maximum intensity (i.e. the measured intensity after 24 h of ageing), to further minimize the influence of a fluctuating incident intensity. Apart from the above mentioned difference in initial intensity, the development of the diffraction patterns of the HP and HPX gels, prepared with 5% - 15% sucrose in the solvent, look very similar. Because of this, in this section just the diffractograms for HP and HPX, prepared at 25 °C with a sucrose content of 5%, are shown. The remaining diffractograms can again be found in the Appendix.

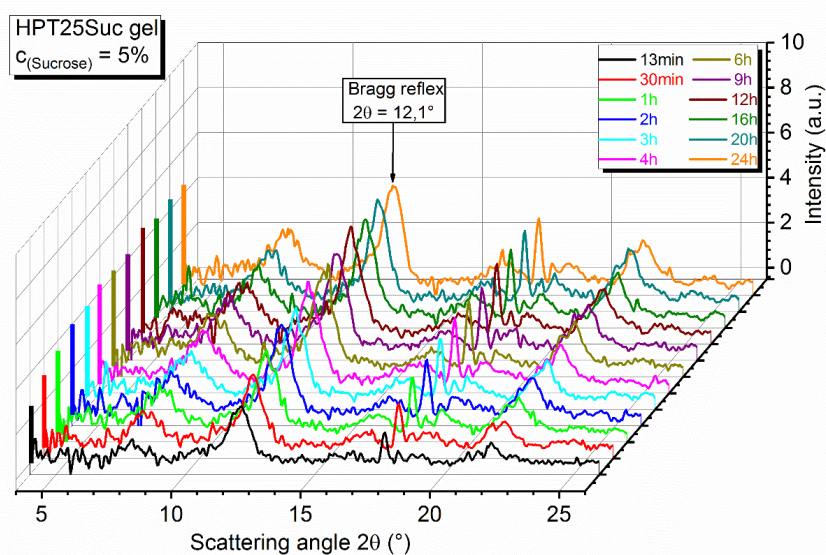


Fig. 101: XRD during gelation of an HP gel, prepared at 25 °C, 600 rpm shear rate and 5% sucrose.

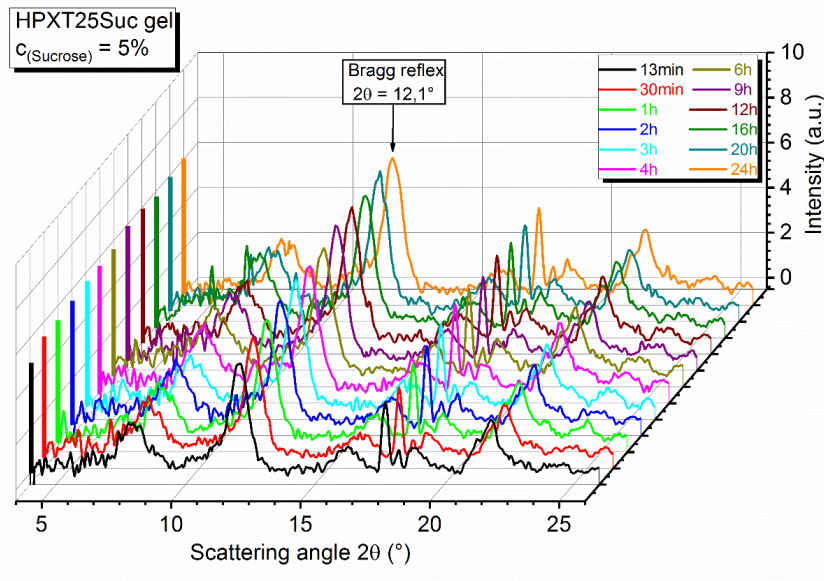


Fig. 102: XRD during gelation of an HPX gel, prepared at 25 °C, 600 rpm shear rate and 5% sucrose.

Again, the crystallization kinetics of the gel formation were examined, by the integration and normalization of the $12,1^\circ$ reflexes. In Fig. 103 the normalized intensities of the Bragg reflexes at $2\theta = 12,1^\circ$ of HP gels, prepared at 25 °C, with a sucrose concentration of 0%, 5%, 10% and 15%, are compared to each other.

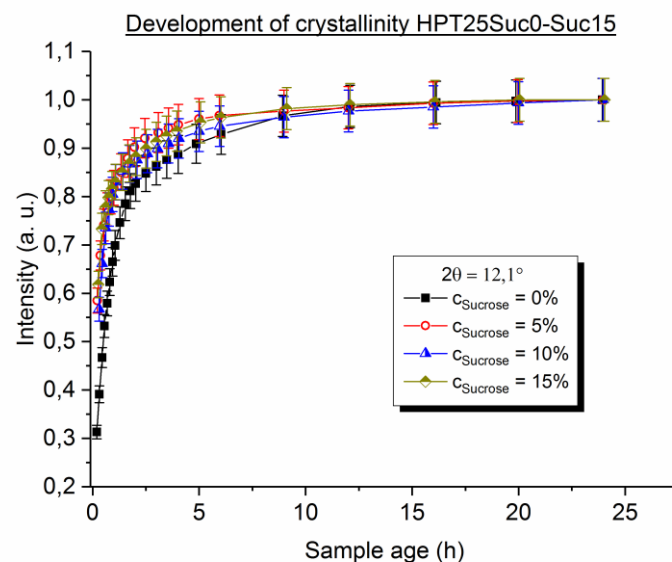


Fig. 103: Development of the relative intensity of HP gels prepared at 25 °C, with 0% - 15% sucrose.

For all the samples, the main part of the crystallization takes place in the first two to three hours of the gelation. In those first hours, the intensity increases to 85 – 90% of the maximum

intensity. This rapid increase of the intensity is again due to the crystallization process of the inulin particles, as already explained in section 3.2.2 (first primary particle formation, followed by aggregation and particle gel network formation). In Fig. 103 it is also obvious, that the initial crystallinity of the inulin samples, represented by the values at roughly 20 min sample age, depends on the amount of sucrose in the solvent. With increasing sucrose content, the solubility of HP decreases (Fig. 100), what results in increased initial intensities. The minor deviations of the initial intensities from the predicted trend (i.e. increasing initial intensity with increasing sucrose concentration), are again of experimental nature (fluctuating intensity of the incident x-ray beam and varying diameter of the used mark tubes). In Fig. 104 one can see the development of the relative intensities of the $2\theta = 12,1^\circ$ Bragg reflexes of HPX gels, prepared at 25 °C, with a sucrose content of 0%, 5%, 10% and 15% in the solvent. The error bars are not indicated for the sake of clarity. Again the main part of the crystallization occurs in the first two to three hours (intensity increases to 90 – 95% of maximum intensity) and again this is due to the crystallization process and the particle gel formation. Comparable to the observations in section 3.3.2, the increase in intensity is not as distinctively pronounced as for the HP samples (due to the crystallinity of the employed HPX powder, already mentioned in section 3.2.2). Again, the curves in Fig. 104 look almost identical and no obvious trend concerning the sucrose concentration can be determined. If the reader has a look at Fig. 100, it is obvious, that the already moderate solubility of HPX at 25 °C in water, is not influenced as much as the solubility of HP, by an increasing sucrose content in the solvent (see Tab. 8).

Tab. 8: HP/HPX dissolved dependent on sucrose content in solvent

Sample	Sucrose conc. (%)	Inulin diss. (%)
HPT25Suc0	0	17,49
HPT25Suc5	5	16,60
HPT25Suc10	10	14,46
HPT25Suc15	15	12,14
HPXT25Suc0	0	9,24
HPXT25Suc5	5	8,49
HPXT25Suc10	10	8,24
HPXT25Suc15	15	7,99

The reason for the different solubility behavior of HP and HPX in water-sucrose mixtures and the different crystallization characteristics connected therewith, is the same as already discussed for the water-ethanol mixtures (section 3.3.2). In short, almost no long chain HPX (DP > 45) is dissolved in pure water at 25 °C, that can be affected by an increasing saturation of the solvent (i.e. increasing sucrose concentration). Therefore, the solubility of HPX remains relatively constant just as the initial intensity of the gels with increasing sucrose content. The good solubility of HP and with it the dissolution of a significant amount of long chain inulin at 25 °C in pure water, result in a relevantly decreased solubility at increased sucrose contents and a non negligible amount of undissolved long chain HP connected therewith. Therefore, the initial intensity of the HP samples increases with an increasing sucrose concentration in the solvent.

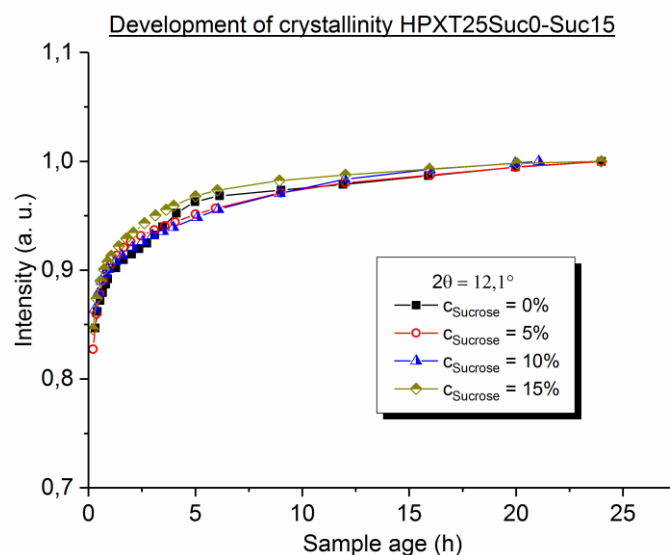


Fig. 104: Development of the relative intensity of HPX gels prepared at 25 °C, with 0% - 15% ethanol.

If Fig. 103 and Fig. 104 are compared to each other, it is obvious, that the HPX samples exhibit a significantly larger initial intensity. This is again, as already explained in section 3.2.2, due to the superior crystallinity of the HPX powder. To illustrate the significantly larger initial intensity of the HPX samples at the different sucrose contents again, the graphs of Fig. 103 and Fig. 104 have been plotted on a logarithmic scale and are illustrated simultaneously in Fig. 105. Again the error bars are not indicated for the sake of clarity.

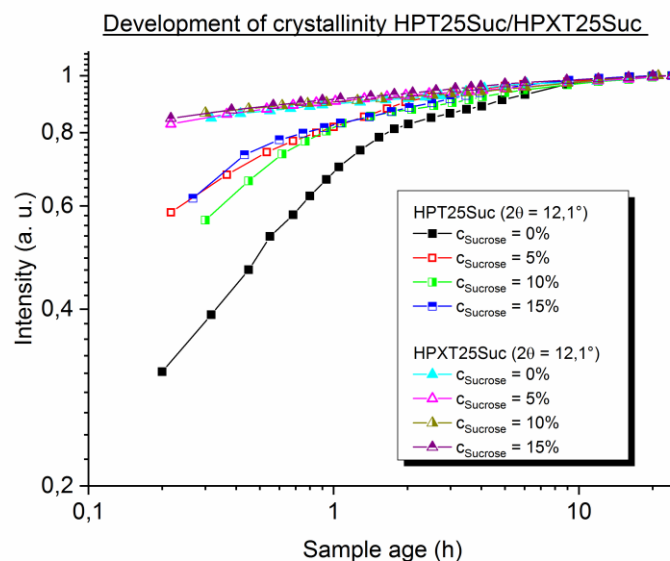


Fig. 105: Development of the relative intensity of HPT25Suc/HPXT25Suc gels, plotted on logarithmic scale.

In Fig. 105 it is obvious, that the initial crystallinity increases from HP, with a sucrose content of 0% to HP with a sucrose content of 15%. As mentioned above, the reason for this is the decreasing solubility of HP with increasing saturation degree of the solvent. Here it is again visible, that the HPX samples exhibit no obvious trend, concerning the sucrose concentration, as already explained above.

To determine the crystallization constant k of the gel formation, a Johnson – Mehl – Avrami – Kolmogorov fit (JMAK) was applied to the curves shown in Fig. 103 and Fig. 104 (see section 3.2.2 and Eq.(55)). Again we just focused on the crystallization constant k . In Tab. 9 and Tab. 10 the average crystallization constants for HP and HPX samples, prepared with different sucrose concentrations in the solvent and determined by applying Eq.(55) on the curves shown in Fig. 103 and Fig. 104, can be seen.

Tab. 9: Average crystallization constant of HPT25Suc samples

$C_{\text{(Sucrose)}}$ (%)	k (1/h)	Error (1/h)
0	1,34	0,04
5	2,85	0,10
10	3,28	0,21
15	4,04	0,23

Tab. 10: Average crystallization constant of HPXT25Suc samples

$C_{\text{(Sucrose)}} (\%)$	$k (1/h)$	Error (1/h)
0	2,08	0,10
5	3,00	0,30
10	3,53	0,22
15	4,00	0,23

For both types of Inulin the crystallization constant k increases with increasing sucrose content in the solvent. As mentioned above, the solubility decreases with increasing sucrose concentration (Fig. 100) and with it the amount of nuclei, which act as seeding material, increases. This results in an increased crystallization rate. The increased crystallization rate, as mentioned in section 3.2.2, influences the average gel particle size, altering the texture of the completely developed inulin gel significantly. Those results will again be explained in the following sections. If Tab. 9 and Tab. 10 are compared to each other, it can be seen, that the crystallization constant of the HP samples increases much more rapid, than it does for the HPX samples. This again confirms the statement from above, that HP is influenced more by an increasing saturation of the solvent at 25 °C sample preparation temperature, than HPX at the same conditions. Compared to the X-ray diffraction experiments of the samples prepared in water-ethanol mixtures (section 3.3.2), an increased sucrose concentration in the solvent results in the same trends as observed for the water-ethanol system, for both types of inulin.

3.4.3 High Performance Anion Exchange Chromatography

To determine the chain length distribution of the inulin, dissolved during sample preparation and remaining dissolved after 24 h of ageing, one sample was taken from the inulin suspension (20% inulin dry matter, sucrose concentration 0% - 15%, $T_{\text{prep.}} = 25\text{ °C}$) after 10 min stirring and one was taken from the same gel after 24 h of ageing at room temperature. The samples were processed as described in section 2.5. To determine the DP distribution of the samples, a reference value was prepared, as described in section 3.2.3. Apart from the overall decreased intensity of the amperometric signal, the chromatograms are identically to the ones used for the inulin-water HPAEC experiments and can be seen in Fig. 56 and Fig. 57 (see also

Appendix). This decreased overall intensity, compared to the respective intensities of the HPAEC measurements in water and water-ethanol mixtures, is visible for all the measurements, presented in this section. This arises from the operating hours of the used gold electrode. The longer the electrode is in use, the more organic material is precipitated permanently on the electrode (normally the electrode can be cleaned by a short electric shock, called “cleaning pulse”, but after certain hours of operating time, even this pulse cannot remove the contaminations from the electrode anymore. This process is called “electrode fouling”, see section 1.8). Therefore, the sensitivity of the electrode is decreased and the detected signals decrease in intensity. Apart from this decrease in intensity, the retention times of the individual DP fractions remain the same. Thus, for each solvent series a reference value was measured, to make a qualitative and quantitative interpretation of the achieved chromatograms possible. To figure out the amount of inulin of a certain DP, dissolved during sample preparation, the areas below the peaks in the chromatogram were integrated, as mentioned in section 3.2.3. Again, the changes in the DP distribution of the dissolved inulin were pointed out and the concentration errors were minimized, by summing up a region of ten following DPs to one fraction. The results for HP and HPX, prepared at 25 °C with different sucrose contents in the solvent and the samples taken after 10 min sample preparation, can be seen in Fig. 106 and Fig. 107.

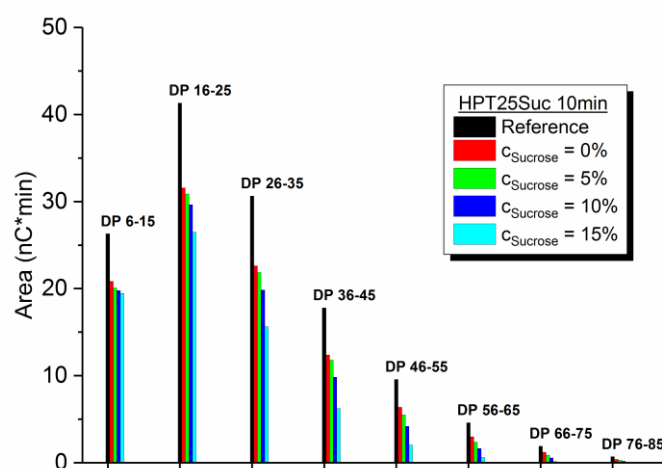


Fig. 106: DP distribution of dissolved HP after 10 min stirring at 25 °C, with sucrose content of 0% - 15%.

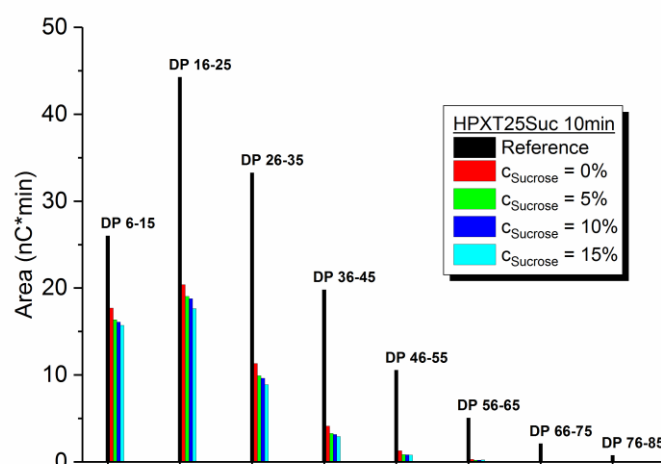


Fig. 107: DP distribution of dissolved HPX after 10 min stirring at 25 °C, with sucrose content of 0% - 15%.

With increasing sucrose content, the amount of dissolved inulin decreases. If the HP and HPX samples with increasing sucrose content in the solvent, are compared to the respective samples prepared in pure water, it is obvious, that the solubility is significantly decreased by an increasing saturation degree of the solvent. Since the long chain inulin exhibits a very low solubility in water, the most crucial change in the DP distribution of the dissolved inulin is visible in this DP region (DP > 36 – 45). At sucrose contents of 15%, for both HP and HPX, practically no long chain inulin is dissolved during sample preparation. Since the previously dissolved inulin partially crystallizes during gel formation, a considerable change in the DP distribution of the dissolved inulin changes the properties of the completely developed particle gel too. With a decreasing solubility, the amount of undissolved material, that can act as seeding nuclei, also increases (see section 3.4.2, increasing crystallization constant k for HP and HPX with increasing sucrose content). Yet, the gel hardness of the HP and HPX gels decreases with increasing sucrose content, what will be explained in section 3.4.4. If one compares Fig. 106 and Fig. 107, the significantly lower solubility of HPX is once again clearly visible (superior crystallinity of HPX powder, see section 3.4.1). Due to the lower solubility of HPX, even at a sucrose concentration of 0% in the solvent (pure water), almost no long chain inulin is dissolved. Thus, a further increasing saturation by increasing the sucrose concentration, only affects the well dissolving medium and short chain HPX (DP < 46). For HP the increasing saturation of the solvent has a more fiercely impact on the solubility. Fig. 106 indicates, that even at 25 °C sample

preparation in pure water (red columns), a significant amount of long chain inulin is dissolved. If the sucrose content is increased, all the DP fractions of HP are affected by an increasing saturation. So the overall decrease in solubility of HP with an increasing sucrose content is much more pronounced, than for HPX (see section 3.4.1).

In contrast to a decreased polarity with increasing ethanol content (see section 3.3.3), an increasing degree of saturation with increasing sucrose content in the solvent, does not have a significant impact on the solubility of HPX (if one compares Tab. 5 and Tab. 8, the dissolved amount of HPX decreases from 9,24% of dissolved HPX at 0% ethanol to 6,17% dissolved HPX at 15% ethanol. For sucrose the dissolved amount of HPX decreases from 9,24% to 7,99% at 15% of sucrose in the solvent). Therefore, at increased sucrose concentrations the DP distribution of HPX, even for the long chain fractions, is just slightly influenced (if Fig. 85 and Fig. 107 are compared to each other, one can see, that almost no HPX with $DP > 45$ is dissolved at an ethanol concentration of 10%. The dissolved amount of HPX with $DP > 45$ at a sucrose concentration of 10% is also very small, yet larger than for the respective water-ethanol sample and not significantly decreased compared to the reference value in pure water.). This is due to the change of ΔG_M of the respective solvent-solute mixture (see section 1.5). If the polarity of the solvent is decreased, the Flory-Huggins parameter χ changes with it. Since the miscibility of inulin and the water-ethanol mixtures is getting worse with increasing ethanol content, the Flory-Huggins parameter adopts positive values and ΔG_M adopts positive values too (see Eq.(12)). This results in unstable mixtures, a significantly decreased solubility of inulin in this solvent and the precipitation of material. If the sucrose content of the solvent is increased, the Flory-Huggins parameter does not change at all. As already mentioned in section 1.5, the differential Gibbs free energy ΔG_M of the inulin-water-sucrose mixture adopts positive values, due to a decreasing differential mixing entropy ΔS_M , arising from the decreased degree of solvation of the medium and long chain inulin fractions at increased sucrose concentrations in the solvent. However, this is due to an increasing degree of saturation and not to a changing polarity. Therefore, the miscibility of inulin and the water-sucrose mixtures is not influenced (as mentioned above, the Flory-Huggins parameter χ remains constant with increasing sucrose content), ΔG_M just slightly increases and just a minor decrease of the solubility (compared to the respective samples in the water-ethanol mixtures) can be observed.

Results and discussion

To determine the DP distribution of the inulin, remaining dissolved after 24 h of storage at room temperature, the 24 h samples were analyzed accordingly to the 10 min samples, as already explained earlier in this section. The results are visible in Fig. 108 and Fig. 109.

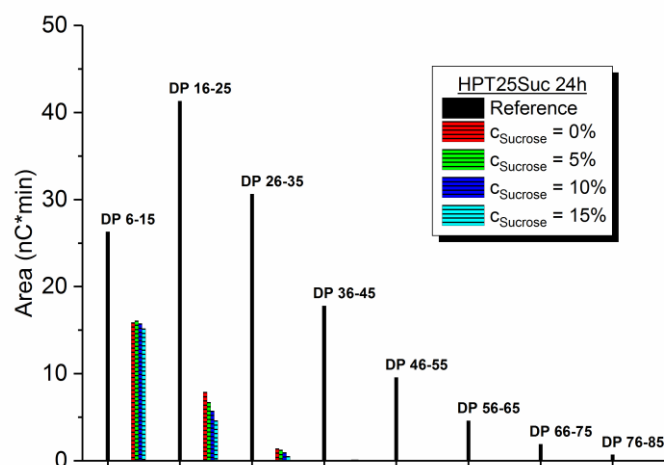


Fig. 108: Saturation dependent DP distribution of dissolved HP after 24 h storage.

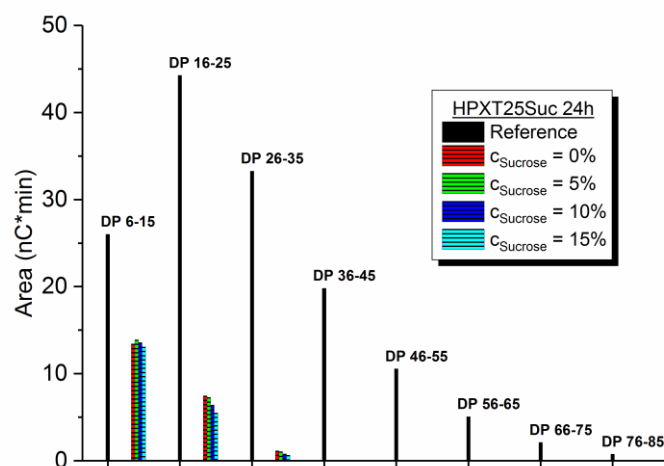


Fig. 109: Saturation dependent DP distribution of dissolved HPX after 24 h storage.

If Fig. 106 and Fig. 108 respectively Fig. 107 and Fig. 109 are compared to each other, one can clearly see, that the previously dissolved inulin almost completely recrystallizes during gel formation. Only a small amount of short and medium chain inulin, decreasing with increasing sucrose content, remains dissolved after 24 h. Above a DP of 35, for both HP and HPX, the

dissolved inulin completely crystallizes. Referring to the DP distribution of the gel primary particles, which are formed during crystallization (see section 1.1), an increased sucrose concentration in the solvent leads to the incorporation of an increased amount of long chain inulin in those primary particles. Since the solubility of long chain inulin is affected more fiercely by an increasing saturation of the solvent, than the short and medium chain inulin, a significant amount of long chain inulin already remains undissolved at small sucrose contents. With increasing sucrose concentration in the solvent, the undissolved amount increases too. This undissolved long chain inulin is not precipitated during sample preparation. Therefore, the undissolved amount can act as seeding nuclei and is incorporated in the gel primary particles during crystallization. This influences the primary particle size and with it the texture of the completely developed inulin gel (see sections 3.4.4 and 3.4.6).

3.4.4 Texture analysis (Gel hardness)

In section 3.2.4, the completely developed inulin gels were compressed beyond their fracture stress, to learn about their fracture behavior. This type of experiment was not possible for the HP and HPX gels, prepared with sucrose in the solvent, due to the decreasing hardness of the gels. At increasing sucrose contents, even the HP gels became too soft to keep the cylindrical shape of the vessel, after being removed from it. In consequence, no compression experiments were performed for the water-sucrose system.

To examine the hardness of the inulin gels, the samples were penetrated by a stainless steel stamp to a maximum strain of 6 mm and the resulting gel hardness was determined as described in section 3.2.4. The results of the hardness measurements of the HP and HPX gels, prepared at 25 °C with different sucrose concentrations in the solvent (shear rate 600 rpm), are pictured in Fig. 110. One can observe the hardness of the HP and HPX gels decrease with increasing sucrose content. As already mentioned in section 3.4.2 and 3.4.3, the increasing degree of saturation with increasing sucrose content results on one hand in increasing crystallization constants k and on the other hand in the incorporation of a larger amount of long chain inulin in the crystallizing primary particles. The primary particle size distribution of the HP and HPX gels changes and fragmentary, soft gels with a decreased gel hardness are formed. This will be explained more detailed in section 3.4.6.

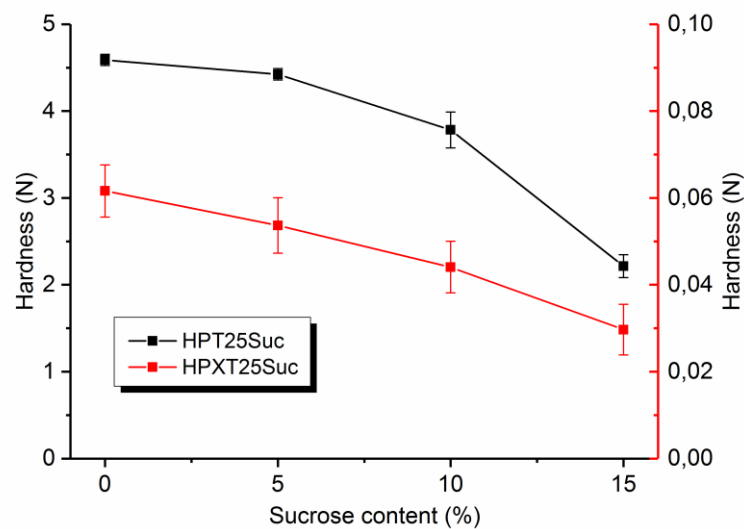


Fig. 110: Hardness of inulin gels prepared with different sucrose contents in the solvent

Therefore, the texture of the developing inulin gels can be influenced by the variation of the degree of saturation of the used solvent. To illustrate the different gel structure of the HPT25Suc and HPXT25Suc gels, in Fig. 111 confocal microscopy pictures of an HP gel, prepared at 25 °C with a sucrose content of 0% and an HPX gel, prepared at 25 °C with a sucrose concentration of 15% in the solvent, are presented and compared to the respective hardness values.

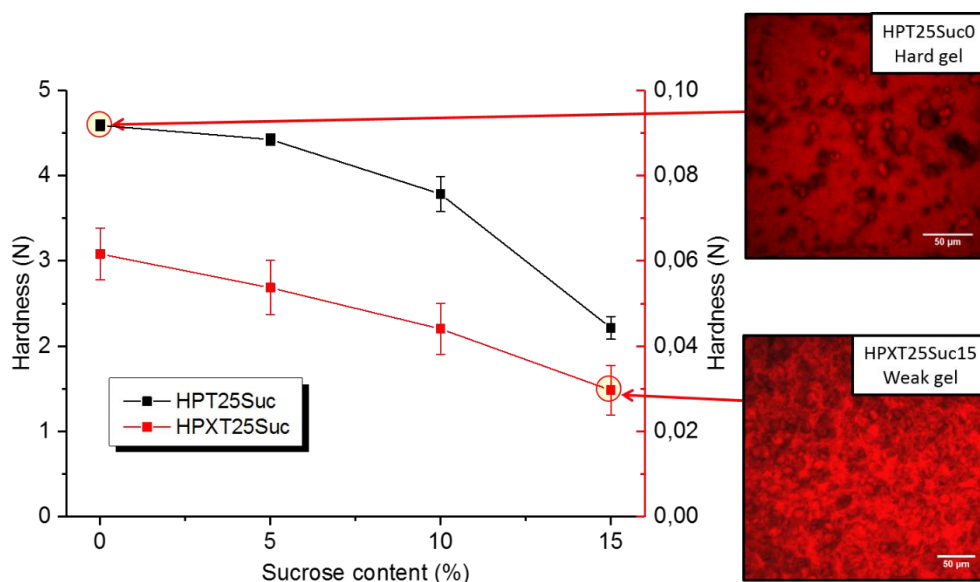


Fig. 111: Comparison of gel structure of HP and HPX gels, both prepared at 25 °C with different sucrose contents in the solvent. Each picture was taken in a depth of 10 μ m.

On the left hand side of Fig. 111, one can see the saturation dependent hardness curves of HP and HPX gels, prepared with a shear rate of 600 rpm. Those curves have already been presented in Fig. 110. The CLSM pictures of an HPT25Suc0 ($T_{prep.} = 25\text{ }^{\circ}\text{C}$, $c_{Suc} = 0\%$) and an HPXT25Suc15 gel ($T_{prep.} = 25\text{ }^{\circ}\text{C}$, $c_{Suc} = 15\%$), can be seen on the right hand side of Fig. 111. Again, both pictures have been taken from the bulk of the samples, 10 μm above the bottom of the nunc chambers. The associated hardness values are highlighted in the diagram on the left. It is clearly visible, that HPXT25Suc15 forms the weakest gel of the whole series and HPT25Suc0 yields the hardest gel. If the pictures on the right are compared to each other, significant differences in the gel structures of the HP and HPX gels are clearly visible. As already mentioned in section 3.2.4, both gels are dyed with Rhodamine B. Therefore, the regions where water is accumulated, again appear just lightly red or almost dark in both gels. Apart from the large, lightly dyed remnants of the HP powder, that have not been dissolved during sample preparation and are dispersed throughout the whole gel, the HPT25Suc0 gel network appears homogeneously dyed, without any obviously darker regions. As before, this is a clear indication for a homogeneous and strong network, what can be confirmed by the associated hardness value. The HPXT25Suc15 gel on the opposite yields an inhomogeneous gel network, interspersed with dark regions, where water is clearly accumulated. Comparable to the HPX gel, prepared at 25 $^{\circ}\text{C}$ in pure water (Fig. 66), this results in a fragmentary weak gel structure, also confirmed by the respective hardness value, visible in Fig. 111. As already seen for the HP and HPX gels, prepared with pure water, the hardness values of the HPXT25Suc gels remain way below the respective HPT25Suc hardness values, what is due to the fragmentary gel structure of the HPX gels. As already mentioned above, the formation of the different gel networks and the corresponding hardness values, will be explained in the following sections. Since the confocal microscopy pictures of the HP and HPX gels, prepared with different sucrose contents in the solvent, did not show any obvious change in structure, that could be referred to the respective sucrose concentration, in this section just the two microscopy pictures, visible in Fig. 111, are presented (the remaining pictures can be found in the Appendix section).

3.4.5 Oscillatory rheology

As already presented for the inulin-water samples, the viscoelastic properties of the completely developed HP and HPX gels, prepared at 25 $^{\circ}\text{C}$ and with an increasing sucrose content in the solvent, were also determined by performing amplitude sweeps at the unsheared samples. In Fig. 112 one can see the amplitude sweep curves of HP gels, prepared at 25 $^{\circ}\text{C}$ and

Results and discussion

with sucrose concentrations of 0%, 5%, 10% and 15% in the solvent. The samples have been measured between 0,1% and 100% oscillation amplitude. The error bars are not indicated, due to the sake of clarity.

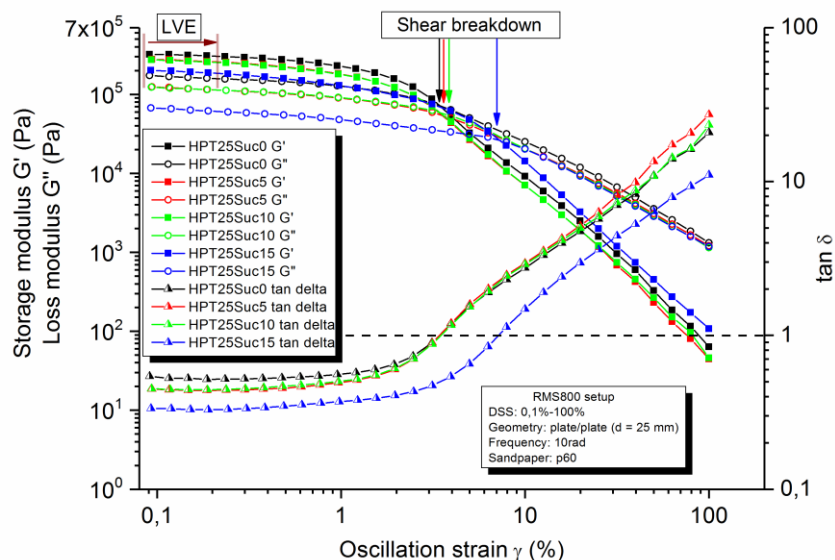


Fig. 112: Amplitude sweep curves of HP gels, prepared at 25 °C, with sucrose contents of 0%, 5%, 10% and 15% in the solvent. The device setup is indicated in the figure.

Again, the storage modulus G' and the loss modulus G'' are plotted against the applied oscillation strain γ . The dissipation factor $\tan \delta$ is also plotted against the oscillation strain. In Fig. 112 the Linear Viscoelastic Region (LVE) is again indicated with diagonal, brown lines. The LVE regions of all the HP gels span comparable strain regions and do not show any obvious change, that could be traced back to the different sucrose contents. The trend of the HP gel's shear moduli follows the trend of the respective hardness values (Fig. 110). The HP gel, prepared at 25 °C with a sucrose content of 0% in the solvent, exhibits the largest initial storage modulus, just as it exhibits the largest gel hardness. With increasing sucrose concentration, the initial shear moduli decrease, comparable to the trend of the respective gel hardness. For all the HP samples, the initial storage modulus G' exceeds the initial loss modulus G'' . Therefore, the elastic properties of all the HP samples dominate at small oscillation amplitudes, marking them as “solid” gels. If the oscillation amplitude is increased, both the moduli decrease. This shear thinning behavior is again due to the weakening of the bonds between the primary particles, which are stressed by the increased shear forces (see section 3.2.5). If the applied strain exceeds the “fracture strain”, the particle gel network is destroyed, what is again visible in the

point of shear breakdown. The shear breakdown for each gel is indicated in Fig. 112 and a dissipation factor $\tan \delta$ of the value 1, can be recognized again by a horizontal dashed line. Comparable to the HP gels, prepared at different sample preparation temperatures (Fig. 67), the shear breakdown is shifted to larger oscillation amplitudes, if the sucrose concentration in the solvent is increased. This means, the “softer” the HP gel is the more insensitive it reacts to deformation (in contrast to the inulin-water and the inulin-water-ethanol system, in Fig. 112 a significant shift to larger shear amplitudes of the shear breakdown is only noticeable for the HPT25Suc15 gel. This again confirms the larger impact of an increased sample preparation temperature and a decreased polarity on the viscoelastic properties of the HP gels). Therefore, for an HP gel, prepared with increased sucrose concentration in the solvent, the primary particles in the completely developed gel are not that strong bound to each other, giving the gel a softer and more flexible structure. As already mentioned in section 3.4.4, this is due to the change of the primary particle size with a changing degree of saturation of the solvent (see section 3.4.6). Above an oscillation amplitude of 10%, for all the gels the particle network is destroyed, the primary particles are completely separated from each other and the samples behave like viscous fluids. By comparing Fig. 67, Fig. 90 and Fig. 112 to each other, it is obvious, that an increasing sample preparation temperature, a decreasing polarity and an increased degree of saturation of the solvent, have a similar impact on the viscoelastic properties of the HP gels and result in a weakening of the particle gel network (yet the impact of the increasing sample preparation temperature and the decreasing polarity on the viscoelastic properties is more pronounced).

In Fig. 113 one can see the amplitude sweep curves of HPX gels, prepared at 25 °C, with a sucrose content of 0%, 5%, 10% and 15% in the solvent. Again G' , G'' and $\tan \delta$ are plotted against the oscillation strain γ and the samples have been measured between 0,1% and 100% oscillation amplitude. Again, the error bars are not indicated.

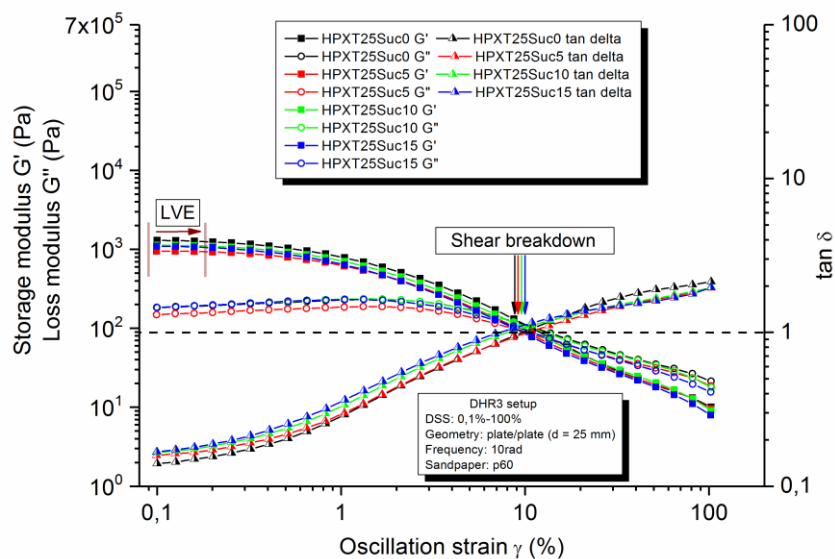


Fig. 113: Amplitude sweep curves of HPX gels, prepared at 25 °C, with sucrose contents of 0%, 5%, 10% and 15% in the solvent. The device setup is indicated in the figure.

As before, the LVE region is indicated with diagonal brown lines and the dashed horizontal line indicates a $\tan \delta$ of 1. The points of shear breakdown are also indicated for the respective curves. The shear moduli G' and G'' of the HPX gels show no obvious trend concerning the sucrose content and the respective hardness values (Fig. 110). If the sucrose concentration is increased, the hardness values of the completely developed HPX gels decrease. Since the HPX gel, prepared at 25 °C with pure water, already exhibits a very soft, flexible gel structure and the solubility of HPX is only slightly affected by an increased sucrose concentration (see section 3.4.1 and 3.4.2), the viscoelastic properties of the HPX gels are also just slightly affected by an increased saturation of the solvent, what results in almost identical curve progressions of the HPXT25Suc gels' shear moduli. As already mentioned above, with decreasing gel hardness and decreasing initial shear moduli, the gels become more shear insensitive. If one considers the indicated points of shear breakdown in Fig. 113, it is obvious, that the HPX gels with different sucrose concentrations, show no obvious trend concerning the shear sensitivity. This is due to the very soft structure of the HPX gels. If the initial shear moduli are compared to the initial shear moduli of the respective HP gels (Fig. 112), one can see, that the shear moduli of the HPX gels are at least to orders of magnitude smaller than the respective HP values. So even the "stiffest" HPX gel, namely the HPX gel with pure water acting as solvent, is already very soft and shear insensitive. Therefore, the HPXT25Suc gels are relatively indifferent to increased sucrose concentrations, concerning the shear breakdown. In Fig. 114 the storage

moduli of the HPT25Suc and HPXT25Suc gels, presented in Fig. 112 and Fig. 113, are plotted against the oscillation amplitude and compared to each other. The curves are plotted between 0,1% and 100% oscillation amplitude and the error bars are not indicated.

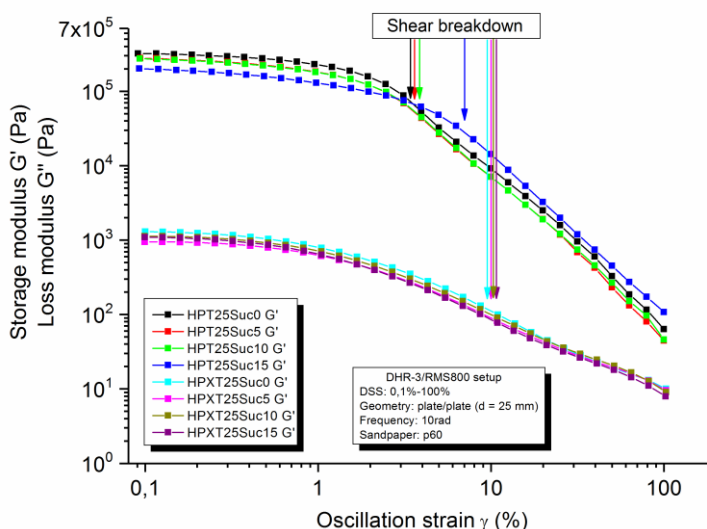


Fig. 114: Comparison amplitude sweeps of HPT25Suc and HPXT25Suc gels. Point of shear breakdown is indicated for each sample.

If the initial storage moduli of the HP and the HPX gels are compared to each other, as mentioned before, the hardness trends are followed by the HP gels and the HPX gels show no obvious trend. All the HP samples exhibit a significantly higher initial storage modulus G' . The initial storage modulus decreases from HPT25Suc0 to HPXT25Suc0-15. The reason for this decrease is again, as already explained for the hardness trends of the HPT25Suc and HPXT25Suc gels (see section 3.4.4), the change in the network structure of the gels (HPT25Suc0 homogeneous, strong network, HPXT25Suc0 - Suc15 fragmentary, weak network). The explanation for the changing particle network structure will be given in more detail in the following sections. In Fig. 114 the loss moduli are not plotted (for the sake of clarity). Again, the points of shear breakdown are indicated. The trend of an increasing shear sensitivity with increasing initial storage moduli is still followed (at least in the HP series). As mentioned above, due to their soft gel structure, for HPX no overall trend can be seen. The HPX gels ($C_{\text{Sucrose}} = 0\% - 15\%$) and the “soft” HP gels ($C_{\text{Sucrose}} \geq 15\%$) exhibit comparable stiffness and brittleness, what results in points of shear breakdown at similar oscillation amplitudes.

3.4.6 Particle size

The particle size trends of the HP and HPX gels, prepared at 25 °C and with a sucrose content of 0%, 5%, 10% and 15% in the solvent, provide an explanation for the above discussed hardness trends and can be observed in Fig. 115.

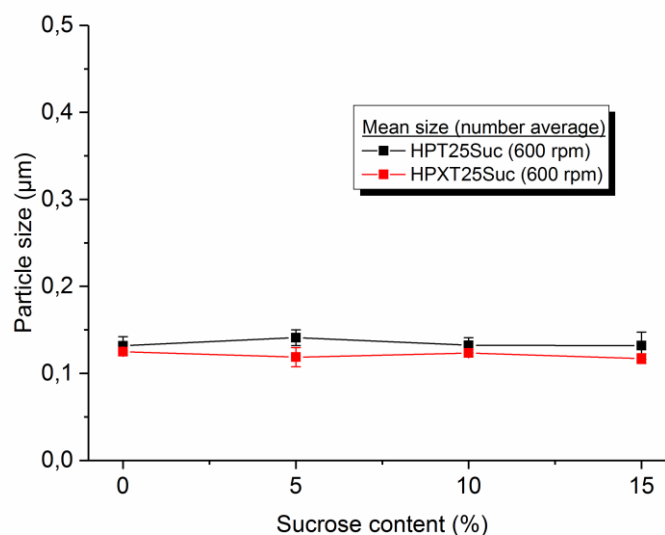


Fig. 115: Gel primary particle size (number average) in dependency of sucrose content in the solvent.

The average size of the HP gel primary particles, remains constant with increasing sucrose content in the solvent. As already shown in section 3.4.2 (Tab. 9), the crystallization constant k of the HP samples prepared at 25 °C, increases with increasing sucrose content. Typically, the average particle size decreases with increasing crystallization speed (see section 3.2.6). Thus, the average particle size of the HP samples with increasing sucrose content, acts divergently as expected concerning the respective crystallization constants. This is due to the decreasing solubility of HP with increasing saturation of the solvent (see Fig. 100) and the incorporation of a larger amount of long chain inulin in the crystallizing gel primary particles connected therewith (see section 3.4.3). Therefore, the average primary particle size of the HP gels should increase with increasing sucrose content, yet it remains constant. To understand this, we need to consider the primary particle size distributions of the completely developed gels, with different sucrose concentrations in the solvent. In Fig. 116, the number distributions of the HP gel particle size, prepared at 25 °C with a sucrose content of 0% and 15% in the solvent and examined by static light scattering, are pictured. As before, the mean primary

Results and discussion

particle size (number average) is indicated next to the respective curve in Fig. 116. If one compares the particle size distribution of the sample prepared with 0% of sucrose and the one prepared with 15% of sucrose, the curves look almost identically. The particle size distribution of the sample with 15% of sucrose in the solvent, appears to be slightly shifted to larger particle sizes, still the average particle size remains constant. As mentioned before, to illustrate changes in the outer regions of the particle size distribution more obvious, one needs to consider the volume distribution of the samples too. The volume distributions of the HP gels pictured in Fig. 116 are pictured in Fig. 117.

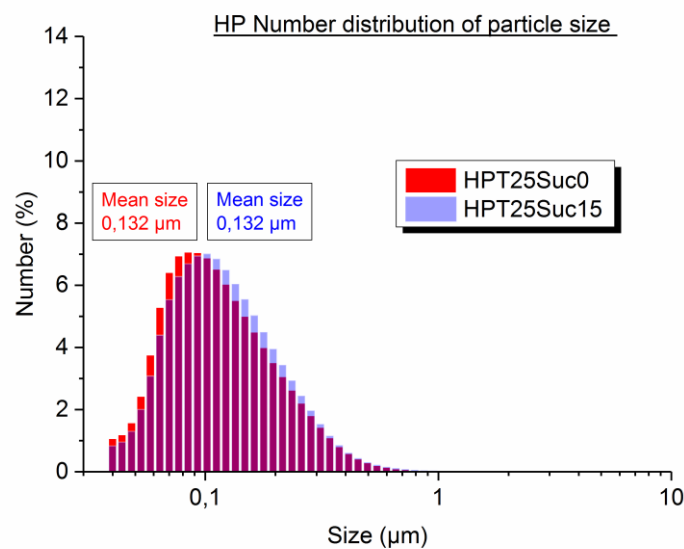


Fig. 116: Number distribution of HP gel particle size, prepared at 25 °C with 0% and 15% sucrose in the solvent.

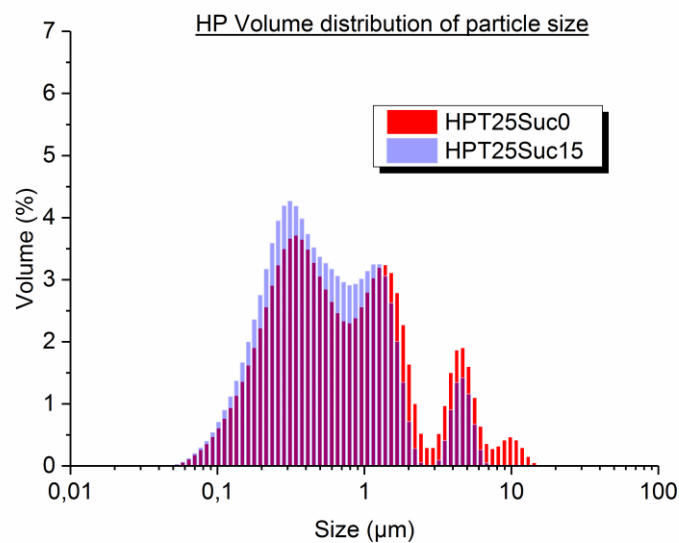


Fig. 117: Volume distribution of HP gel particle size, prepared at 25 °C with 0% and 15% sucrose in the solvent.

If the volume distributions of the 0% sucrose and the 15% sucrose samples are compared to each other, it gets obvious, that the curve of the HPT25Suc15 gel is not shifted to increased particle sizes (here it should be mentioned, that the peaks above a particle size of 3 μm arise from primary particle clusters, that passed the pores of the filter during sample preparation or re-aggregated after filtration. Those clusters have just a minor impact on the number average of the primary particle size. Therefore, for both HP samples pictured in Fig. 117, those peaks are neglected concerning the interpretation of the particle size distribution). However, the volume, that is occupied by small particles (particle size $\leq 0,4 \mu\text{m}$) and by large particles (particle size $\geq 0,5 \mu\text{m}$), is significantly increased, compared to the HPT25Suc0 curve. This means, the number of small and large primary particles increases, with increasing sucrose content in the solvent. This is, as already mentioned before, due to the decreased solubility of HP at increased sucrose contents. If the degree of saturation of the solvent increases, the amount of undissolved HP increases too (most significantly the amount of undissolved long chain HP increases, see section 3.4.3). The undissolved long chain inulin acts as seeding nuclei, is incorporated in the crystallizing primary particles during gel formation and those primary particles increase in size, compared to the ones of the HP gels, prepared with lower sucrose contents in the solvent. Additionally, the increasing degree of saturation with increasing sucrose concentration, results in an increased nucleation rate (see section 1.3). This means, new nuclei are formed faster than compared to lower sucrose concentrations in the solvent. Since only a very small amount of long chain HP is still dissolved at a concentration of 15% sucrose in the solvent, the newly formed nuclei mainly consist of medium and short chain inulin. This process also contributes to the increasing crystallization constant k (see section 3.4.2) and with it the formation of smaller HP primary particles, as compared to the primary particles at lower sucrose contents. Therefore, the developing HP primary particles at increased sucrose contents can be roughly separated into two types. Firstly, the ones, that originate from the crystal growth of seeding nuclei, consisting of mainly undissolved long chain inulin. Those primary particles exhibit a larger particle size, compared to the respective particles at decreased sucrose concentrations. And secondly, the particles that develop out of newly formed seeds consisting of mainly medium and short chain inulin, arising from the increased nucleation rate at increased sucrose contents. Those primary particles exhibit a smaller particle size, compared to the respective primary particles at decreased sucrose concentrations. Those two pro-

cesses result in an increased number of large and small primary particles and the average primary particle size remains constant at increasing sucrose concentrations in the solvent. Due to this, the primary particle size distribution becomes more unbalanced (see Fig. 117, the two maxima increase in size, retaining the bimodal character of the volume distribution) and comparable to the HPX gel, prepared at 25 °C in pure water (see Fig. 66), the HP gels at increased sucrose contents develop a weaker gel structure with an increasing fragmentary character. Therefore, the gel hardness of the HP gels decreases with increasing sucrose content in the solvent.

The average primary particle size of the HPX gels, prepared with different sucrose contents in the sample, behaves similar as the respective HP primary particle size. For the HPX gels, the average primary particle size also remains constant at increased sucrose concentrations. In this case, this mainly arises from the semi-crystallinity of the used HPX powder. The increasing saturation of the solvent, with increasing sucrose concentration, affects the HPX powder just as the HP powder and the solubility of HPX decreases too, with increasing sucrose content. As remarked before, due to its semi-crystalline character, the HPX powder exhibits a significantly lower solubility in the solvent than HP. If we recall the DP distribution of the dissolved HPX with increasing sucrose content (Fig. 107), we recognize, that even at 25 °C with a sucrose content of 0% in the solvent, only a very small amount of long chain inulin is dissolved, that can be incorporated in the primary particles during gelation. Therefore, at increased sucrose contents almost no long chain inulin is dissolved during sample preparation, that can be incorporated in the newly crystallizing primary particles and inversely to the HP samples at increased sucrose contents, the amount of long chain HPX, that is incorporated in the primary particles during crystallization, decreases with increasing ethanol content. This should result in a decreasing average particle size, yet the average particle size remains constant. Additionally, due to the decreased solubility at an increased degree of saturation of the solvent, the nucleation rate and the amount of undissolved material, that can act as crystallization nuclei, increase and the crystallization constant k of the HPX samples increases with increasing sucrose content (see Tab. 10). This should also result in gels with decreased primary particle sizes and connected therewith, increased hardness values at increased sucrose concentrations. Yet the HPX gel hardness decreases with increasing ethanol content and remains way below the gel hardness of the respective HP gels (see Fig. 110). To understand this, we need

to consider the distribution of the HPX primary particle sizes. In Fig. 118 the number distribution of the primary particle size of HPX gels, prepared at 25 °C with 0% and 15% sucrose in the solvent, are pictured. The particle size distributions of both gels seem to be almost identical, yet it is noticeable, that the number of small primary particles slightly increases with increasing sucrose content. Again, as already mentioned in section 3.2.6, to point out changes in the particle sizes of the less numerous particles (the ones in the outer regions of the number distribution), one needs to examine the volume distribution of the HPX gel particle size. The volume distribution of the HPX gels pictured in Fig. 118 is visible in Fig. 119.

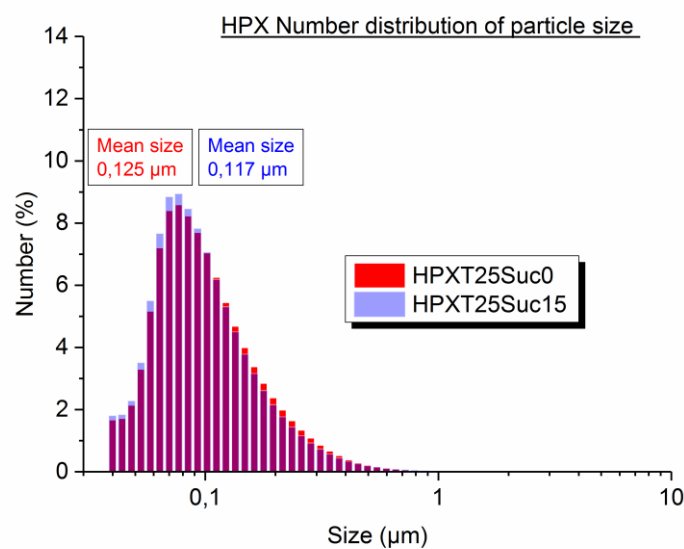


Fig. 118: Number distribution of HPX gel particle size, prepared at 25 °C with 0% and 15% sucrose in the solvent.

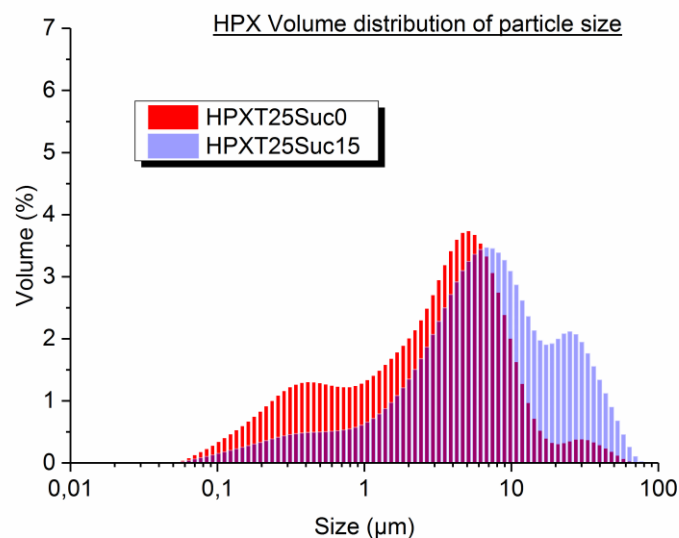


Fig. 119: Volume distribution of HPX gel particle size, prepared at 25 °C with 0% and 15% sucrose in the solvent.

In Fig. 119 the changes in the particle sizes are clearly visible. If one compares the curves of the 0% sucrose and the 15% sucrose sample to each other, it is obvious, that the volume the very small particles take up decreases and the volume the very large particles occupy increases with increasing sucrose content. The average primary particle size (approximately represented by the maximum in the middle) remains relatively constant. To interpret the development of the primary particle sizes correctly, we need to take the number and the volume distribution into account. As already mentioned above, the number of very small particles increases with increasing sucrose content (Fig. 118 left hand side). The increased number of very small particles at a sucrose content of 15% in the solvent, occupy a smaller volume than the less numerous small particles at 0% sucrose in the sample (Fig. 119 left hand side). This means, the very small primary particles decrease in size with increasing sucrose content. As already described for the HPT25Suc gels at increased sucrose contents, this arises from the increased nucleation and crystallization rates at increased sucrose contents and the formation of newly crystallizing, small primary particles, that mainly consist of short and medium chain HPX (due to the almost non existent dissolution of long chain inulin, that cannot be incorporated in the primary particles during crystallization, see Fig. 107). If we have a look on the right hand side of the number and the volume distributions, we can see, that the number of very large particles decreases with increasing sucrose content (Fig. 118 right hand side). Those less numerous very large primary particles occupy a larger volume at an increased sucrose concentration (Fig. 119 right hand side). This means, the very large primary particles increase in size with increasing sucrose content in the solvent. As already mentioned, with an increasing saturation the solubility of HPX in the solvent decreases too. Normally, with increasing solubility, the crystalline particles, which consist of mainly long chain inulin and are already present in the HPX powder, are partly dissolved and decrease in size. Since the solubility decreases, the crystalline particles are just poorly dissolved and exhibit a larger size, compared to the crystalline, undissolved particles at lower sucrose concentrations. The long chain inulin, that is contained in the undissolved crystalline particles, is unavailable for the crystallizing primary particles. Therefore, a smaller amount of long chain inulin is incorporated in the newly crystallizing primary particles and they decrease in size, compared to the crystallizing particles at decreased sucrose contents in the solvent. This means, with increasing sucrose content, the newly crystallizing primary particles decrease in size and the already crystalline, undissolved primary particles increase in size. Those two processes roughly compensate each other and the average

primary particle size of the HPX gels remains constant, even at an increased sucrose concentration. The decreased solubility of HPX (resulting in an increased amount of undissolved material, that can act as crystallization nuclei) and the decreasing particle size of the newly crystallizing primary particles at increased sucrose contents, are in agreement with an increased crystallization constant k (see Tab. 10). Still, as already mentioned above, the hardness decreases with increasing saturation of the solvent (inversely to the expectation of an increasing gel hardness with decreased primary particle size or a constant hardness with constant average particle size). This is due, as already mentioned above for the HPT25Suc gels, to an increasing unbalance of the HPX primary particle size distribution and the HPX gels at increased sucrose contents develop a weaker gel structure with an increasing fragmentary character. Therefore, the HPX gel hardness decreases with increasing sucrose content in the solvent. Here it should be mentioned again, that inulin primary particle clusters, which passed the pores of the filter or re-aggregated after filtration during sample preparation, have a significant impact on the volume average of the primary particle size. Because of this, the volume average differs significantly from the number average of the primary particle size. Therefore, as already done in section 3.2.6, in Fig. 115 the number weighted average primary particle sizes of the HP and HPX gels have been evaluated, to minimize the undesired impact of particle clusters in the samples on the average primary particle size.

3.4.7 Summary

Taking the above discussed results into account, the saturation dependent hardness variation of the completely developed inulin gels can be summarized by a simple model. The models are pictured in Fig. 120 and Fig. 121.

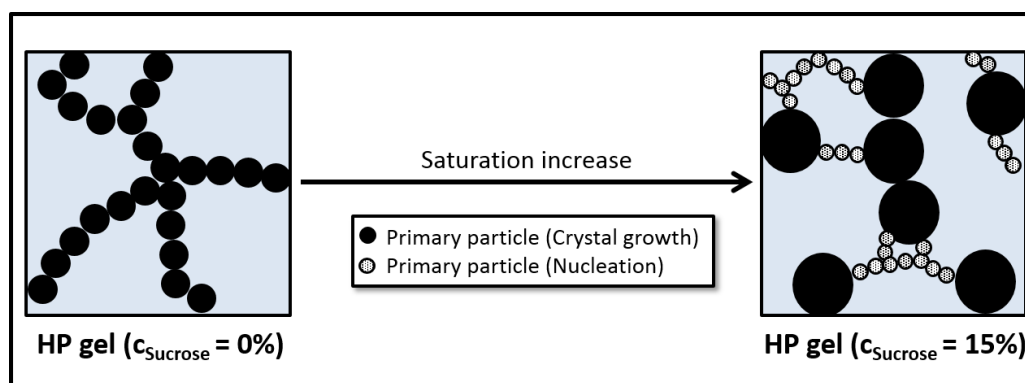


Fig. 120: HPT25Suc particle size variation

Fig. 120 illustrates the particle gel structures of two completely developed HP gels, one prepared at 25 °C with 0% sucrose in the solvent and one prepared at 25 °C with a sucrose concentration of 15%. Since the model in Fig. 120 is simplified and intended to illustrate the saturation dependent particle size variation, the pictured dimensions are randomly chosen. For the gel prepared with a sucrose concentration of 0%, a sufficient amount of inulin remains undissolved during sample preparation and acts as crystallization nuclei, ensuring a seeded crystallization. After 24 h of crystallization, the resulting HP gel consists of small primary particles and exhibits a hard texture. If the degree of saturation is increased by the addition of sucrose to water, the solubility of HP in this solvent significantly decreases and with it, the amount of undissolved nuclei increases. This causes a considerable increase in crystallization velocity. Divergently to the expectations, the average primary particle size remains constant (Fig. 115). At increased sucrose concentrations, a significant amount of long chain HP remains undissolved during sample preparation, acting as crystallization nuclei (Fig. 106). Due to the increased amount of long chain HP, that is incorporated in the growing primary particles, they increase in size, compared to the respective particles at decreased sucrose concentrations in the solvent (black particles in Fig. 120. Those larger particles are mainly formed by crystal growth of the nuclei, mainly consisting of long chain inulin, see section 3.4.6). Additionally, the increased degree of saturation results in an increased nucleation rate. The newly formed nuclei mainly consist of short and medium chain HP (since almost no long chain HP is dissolved at increased sucrose concentrations, that can be incorporated in the newly formed nuclei), the crystallization constant k increases too (see Tab. 9) and those primary particles decrease in size, compared to the respective particles at decreased sucrose concentrations (shaded particles in Fig. 120). Those two processes compensate each other and the average primary particle size remains constant at increasing sucrose concentrations. Due to the increasing unbalance of the primary particle size distribution, the gel network weakens, the fragmentary character of the particle network increases and the gel hardness of the HP gels decreases with increasing sucrose content in the solvent (Fig. 110).

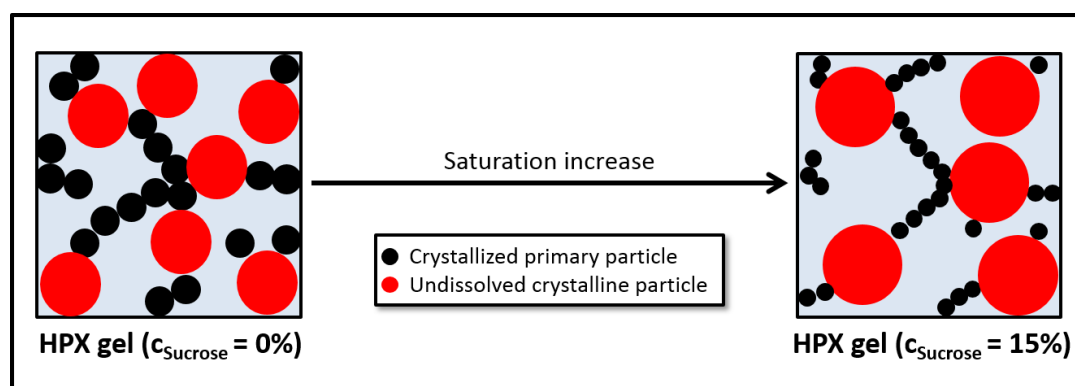


Fig. 121: HPXT25Suc particle size variation

In Fig. 121 the particle gel structures of two completely developed HPX gels, one prepared at 25 °C with 0% sucrose in the solvent and one prepared at 25 °C with a sucrose concentration of 15%, are pictured. Again, this is a very simplified model to illustrate the particle size variation. At 25 °C and 0% sucrose content, HPX exhibits a moderate solubility in the solvent (Fig. 78) and mostly short and medium chain inulin is dissolved during sample preparation. Additionally, the HPX powder already contains a significant amount of crystalline particles, which can act as seeding nuclei during crystallization. For the HPX gel, prepared with a sucrose concentration of 0%, this results in a fragmentary gel structure (see Fig. 66 and Fig. 119), that consists of small, during gel formation crystallized primary particles (black particles in Fig. 121, that mainly consist of short and medium chain inulin) and large, undissolved crystalline primary particles, that were already present in the HPX powder (red particles in Fig. 121, which mainly consist of long chain inulin). As already mentioned in section 3.2.7, this fragmentary, not very densely packed gel structure of the 0% sucrose content HPX gel results in a very low hardness. If the sucrose concentration is increased to 15%, the solubility of HPX decreases. At 25 °C sample preparation temperature with a sucrose content of 0% (solvent is pure water), the crystalline powder particles are poorly dissolved and therefore just slightly decreased in size. If the solubility of HPX decreases at increased sucrose concentrations, the crystalline powder particles are even less dissolved and therefore their size is increased compared to the crystalline powder particles at 0% of sucrose in the solvent (see section 3.4.6). Since the undissolved crystalline particles consist of mainly long chain HPX, this undissolved amount of long chain inulin is unavailable for the newly crystallizing particles during gel formation (black particles in Fig. 121), a smaller amount of long chain HPX is incorporated in those crystallizing particles and they decrease in size, compared to the crystallizing particles at 0% of sucrose in

the solvent. Additionally, due to the increased degree of saturation at increased sucrose concentrations, the nucleation and crystallization rate are increased, also resulting in a decreased size of the crystallizing particles. Due to the increasing unbalance of the primary particle size distribution at increased sucrose concentrations, the fragmentary character of the HPX gels increases even further, yielding soft gels with a weakened particle network and the gel hardness of the HPX gels decreases with increasing sucrose content in the solvent (Fig. 110).

3.5 The inulin-water-ethanol-sucrose system

In this chapter the results of the HP and HPX samples, that have been prepared with water-ethanol-sucrose mixtures acting as solvent, will be presented and discussed. As before, for all the measurements in this section the results for HP and HPX, prepared at 25 °C in water, were used as reference values. This means, the sample preparation temperature was set to 25 °C for all the samples and the ethanol, respectively the sucrose concentration in the solvent adjusted to 0% (reference values of HP and HPX at 25°C in water), 5% and 10% (w/w). Thus, the minimum concentration of additives in the solvent was set to 0% (pure water) and the maximum concentration was set to 20% (10% of ethanol and 10% of sucrose in the solvent). As already seen in section 3.3 and 3.4, the addition of ethanol and sucrose to the solvent result in similar trends concerning the macroscopic gel structure (an increasing concentration of ethanol and sucrose in the solvent yields softer HP and HPX gels after 24 h of ageing at room temperature). Therefore, this section focusses on the analysis methods, which clearly show the different impact of ethanol and sucrose on the macroscopic gel structure of the HP and HPX gels (i.e. solubility, HPAEC and texture analysis).

3.5.1 Solubility in different solvents

In this section the solubility trends of the three examined systems, namely inulin-water, inulin-water-ethanol and inulin-water-sucrose, are compared to each other in terms of the solubility of 20% (w/w) HP and HPX in those systems. The identification of intersection points, concerning the solubility in the different solvents, allows the establishment of a relationship between temperature, polarity and saturation of the solvent. In Fig. 122 and Fig. 123 the solubility of 20% (w/w) of HP and HPX in water ($T_{prep.} = 25 - 60$ °C for HP and $T_{prep.} = 25 - 80$ °C for HPX, representing the temperature dependent solubility), water-ethanol mixtures ($T_{prep.} = 25$ °C, $C_{Ethanol} = 0 - 15\%$, representing the polarity dependent solubility) and water-sucrose mixtures

Results and discussion

($T_{prep.} = 25\text{ }^{\circ}\text{C}$, $c_{Sucrose} = 0 - 15\%$, representing the saturation dependent solubility) are pictured. The curves have been fitted with a linear fit (slopes m visible next to the respective fit), to identify intersection points between the different systems. The sample preparation temperature and respectively the ethanol and sucrose concentration of the solvent can be read off on the x-axis. All three solubility curves have one intersection point in common. This reference point “ y_0 ” is indicated in Fig. 122 and Fig. 123 with the amount of HP and HPX dissolved at the respective conditions. This intersection arises from the reference system, namely the solubility of HP respectively HPX at $25\text{ }^{\circ}\text{C}$ in pure water, used for all three systems. To adjust the x-coordinates of the reference point for all three systems to “ $x_0 = 0$ ”, the sample preparation temperature dependent solubility curves for HP and HPX in pure water, were shifted for “ $-25\text{ }^{\circ}\text{C}$ ”. Therefore, the sample preparation temperature can be read off on the x-axis, by adding $25\text{ }^{\circ}\text{C}$ to the respective value. Due to the freezing point of pure water at atmospheric pressure ($T_{F,water} = 0\text{ }^{\circ}\text{C}$; 1013 mbar), the x-axis shows as smallest value “ $-25\text{ }^{\circ}\text{C}$ ” (due to the shift of the x-axis, as already mentioned above, $0\text{ }^{\circ}\text{C} - 25\text{ }^{\circ}\text{C}$). At sample preparation temperatures significantly below room temperature, the kinetic processes in the system become very slow and render a proper particle gel formation almost impossible. Therefore, this lower limit of the x-axis was chosen.

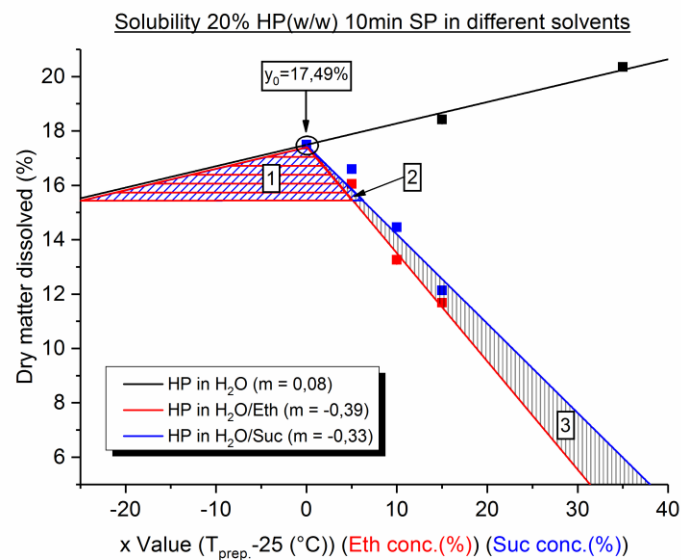


Fig. 122: Comparison of the solubility of 20% (w/w) HP in different solvents

The solubility of HP at $25\text{ }^{\circ}\text{C}$ decreases with increasing ethanol and sucrose content in the solvent (resulting in linear fits with negative slope, red and blue lines in Fig. 122). The solubility of HP in pure water increases with increasing temperature (linear fit with positive slope, black

fit in Fig. 122). Therefore, an intersection point of the three solubility curves, except the reference point, is not possible. The areas below the solubility curves, which are bordered by two different systems, have been indicated in Fig. 122. The red region connects the inulin-water and the inulin-water-ethanol system, the inulin-water and the inulin-water-sucrose system are connected by the blue region and the grey shaded region connects the inulin-water-ethanol and the inulin-water-sucrose systems. Any horizontal line, that is drawn in one of those regions and intersects the solubility curves of the two bordering systems, indicates the conditions in each system, at which the dissolved amount of HP during sample preparation in those different solvents is identical. Thus, the HP gels, which are prepared at those conditions (e.g. for the inulin-water and the inulin-water-sucrose systems a sucrose concentration of 3,4% and a sample preparation temperature in pure water of 11,6 °C, result in the dissolution of the same amount of HP, namely 16,4%, and with it also the similar DP distribution of the dissolved inulin molecules. For the inulin-water and the inulin-water-ethanol systems, 16,4% of HP are dissolved at a temperature of 11,6 °C in pure water and an ethanol concentration of 2,7%), result in the formation of very similar gel structures with comparable macroscopic properties. This is due to the similar DP distribution of the dissolved and undissolved amount of inulin, which are available for the formation of the particle gel network. Here it needs to be mentioned, that the practical implementation of those similar samples, prepared in different solvents, proves to be very problematic. If the HP gel, prepared at 25 °C with a concentration of 3,4% sucrose in the solvent, should be prepared in pure water, the sample preparation temperature needs to be adjusted to 11,6 °C, to achieve the same amount of dissolved HP during sample preparation. The resulting particle gel structure is influenced by many parameters, e.g. the crystallization constant k and the nucleation rate, which delicately depend on the temperature of the system. Therefore, the temperature of the HP sample must be adjusted to 25 °C again, directly after dissolving the respective amount of inulin at 11,6 °C, to provide the same crystallization conditions as the 3,4% sucrose sample. Due to the increased solubility of HP in pure water at 25 °C, compared to the solubility at 11,6 °C, previously undissolved HP molecules dissolve during gel formation. The DP distribution of the dissolved and undissolved amount of inulin changes and the resulting gel structure differs from the HP gel, prepared at 25 °C with a sucrose content of 3,4% in the solvent. Therefore, at the current state of this work, the established relationships between temperature, saturation and polarity are of

mostly hypothetical nature. Additionally, in Fig. 122 the regions have been marked with numbers, where two of the previously mentioned bordering regions overlap. In region number 1, the intersecting region of the inulin-water and the inulin-water-ethanol systems (red region) overlaps with the intersecting region of the inulin-water and the inulin-water-sucrose systems (blue region). In region number 2, the intersecting region of the inulin-water and the inulin-water-sucrose systems (blue region) overlaps with the intersecting region of the inulin-water-ethanol and the inulin-water-sucrose systems (grey region). Region number 3 is just an intersecting region of the inulin-water-ethanol and the inulin-water-sucrose solubility curves. Therefore, every horizontal line, which is drawn in regions number 1 and number 2, and intersects the solubility curves of all three bordering systems, indicates the conditions in all three systems, at which the dissolved amount of HP in those different solvents is identical. Thus, the inulin-water, the inulin-water-ethanol and the inulin-water-sucrose system are connected to each other by region number 1 and region number 2 (e.g. 16,4% of HP dissolve at 11,6 °C in pure water, at 25 °C with 2,7% of ethanol in the solvent and at 25 °C with 3,4% of sucrose in the solvent).

The slightly steeper negative slope of the water-ethanol solubility curve in Fig. 122, compared to the slope of the water-sucrose solubility curve (slightly decreased solubility of HP in water-ethanol mixtures compared to the respective water-sucrose mixtures) confirms again, as already mentioned in section 3.3 and 3.4, the larger impact of a decreasing polarity, than the impact of an increasing saturation of the solvent, on the solubility of HP. This will become apparent once again in section 3.5.3, when the hardness values of the gels, prepared in all three solvents, are compared to each other.

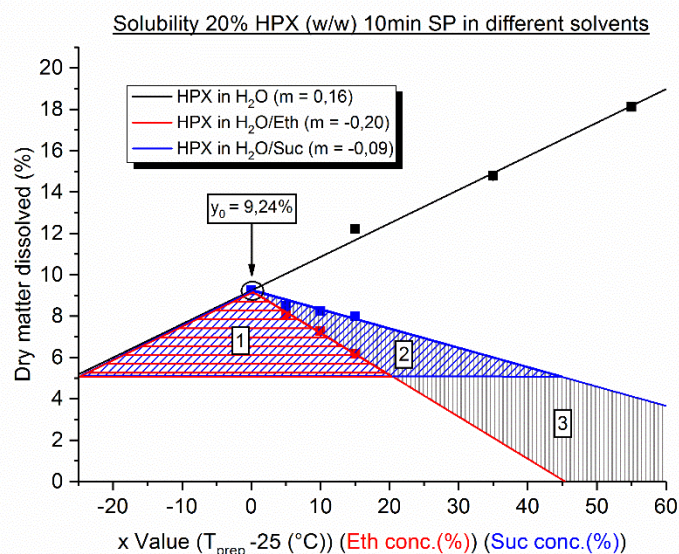


Fig. 123: Comparison of the solubility of 20% (w/w) HPX in different solvents

In Fig. 123, the trends of the solubility of HPX in the three different systems are similar to the solubility trends of HP. The solubility of HPX in water increases with increasing temperature and decreases in water-ethanol and water-sucrose mixtures at 25 °C, with increasing ethanol/sucrose content in the solvent. Again, the solubility of HPX in water-ethanol mixtures is decreased, compared to the respective water-sucrose mixtures (slope of the water-ethanol solubility curve is steeper than the slope of the water-sucrose curve). This illustrates the larger impact of a decreased polarity of the solvent on the solubility of HPX once again. The areas below the solubility curves, which are bordered by two different systems, have again been indicated in Fig. 123 (red region: connects inulin-water and inulin-water-ethanol systems, blue region: connects inulin-water and inulin-water-sucrose systems, grey region: connects inulin-water-ethanol and inulin-water-sucrose systems). As already mentioned above, any horizontal line, that is drawn in one of those regions and intersects the solubility curves of the two bordering systems, indicates the conditions in each system, at which the dissolved amount of HPX in those different solvents is identical. Again, the gels prepared at the determined conditions in the different solvents exhibit a comparable gel structure after 24 h of ageing at room temperature. As before, due to the complicated practical implementation of those gels, the established relationships of temperature, polarity and saturation are mostly hypothetical. In Fig. 123, the regions, that connect all three systems to each other, have been indicated with the numbers 1 and 2 again (in region number 1, again the intersecting region of the inulin-water and the inulin-water-ethanol systems (red region) overlaps with the intersecting region of the

inulin-water and the inulin-water-sucrose systems (blue region). In region number 2, the intersecting region of the inulin-water and the inulin-water-sucrose systems (blue region) overlaps with the intersecting region of the inulin-water-ethanol and the inulin-water-sucrose systems (grey region). Region number 3 is again just an intersecting region of the inulin-water-ethanol and the inulin-water-sucrose solubility curves). As before, every horizontal line, which is drawn in regions number 1 and number 2, and intersects the solubility curves of all three bordering systems, indicates the conditions in all three systems, at which the dissolved amount of HPX in those different solvents is identical. Thus, the inulin-water, the inulin-water-ethanol and the inulin-water-sucrose system are again connected to each other by region number 1 and region number 2 (e.g. 7,9% of HPX dissolve at 16,6 °C in pure water, at 25 °C with 6,5% of ethanol in the solvent and at 25 °C with 14,6% of sucrose in the solvent).

If Fig. 122 and Fig. 123 are compared to each other, the overall decreased solubility of HPX in all three systems stands out again. As mentioned before, this is due to the superior crystallinity of the used HPX powder (Fig. 47). Considering the slopes of the solubility curves of HP and HPX in all three solvents (Fig. 122 and Fig. 123), the following can be observed: The slope of the solubility curve of HPX in water exceeds the slope of the respective curve of HP. This is due to the added amount of inulin to the solvent. As mentioned in section 2.2, the total amount of inulin in every sample is 20% (w/w). For HP, 20% of inulin are dissolved at 60 °C in pure water. Since 17,49% of HP are already dissolved at 25 °C, the solubility curve exhibits a small slope until the maximum solubility is reached at 60 °C. Due to the lower solubility of HPX at 25 °C (9,24% of HPX are dissolved at 25 °C in pure water), the undissolved amount of HPX is significantly larger as compared to the respective HP samples and the solubility curve exhibits a very steep slope, until the maximum solubility of 20% (w/w) is reached at 80 °C. The solubility curves of HP in water-ethanol and water-sucrose mixtures exhibit a significantly steeper negative slope, than the respective HPX curves. This is due to the DP distribution of the dissolved HP and HPX in the water-ethanol and water-sucrose mixtures (see section 3.3.2 and 3.4.2). The HP solubility curves in water-ethanol/sucrose mixtures exhibit very similar, steep slopes. Since a large amount of long chain HP is already dissolved at 25 °C in water (see section 3.2.3), the increasing ethanol and sucrose contents in the solvent have a very similar impact on the solubility of the moderately soluble long chain inulin. Thus, the decreasing solubility at increased ethanol and sucrose concentrations in the solvent is mostly caused by the undissolved long chain HP (see section 3.3.3 and 3.4.3). For HPX at 25 °C in water, mostly short chain inulin

is dissolved (section 3.2.3). This well dissolving short chain HPX is only marginally affected by an increasing ethanol and sucrose content, the solubility of HPX at increased ethanol and sucrose contents is only slightly decreased and the slopes of the HPX solubility curves are smoother than the slopes of the respective HP curves. What is also very eye catching, is the larger difference of the slopes of the HPX water-ethanol/sucrose solubility curves compared to the corresponding HP curves. Therefore, the solubility of HP is similarly influenced by a decreasing polarity and an increasing saturation of the solvent (due to the significant amount of poorly soluble long chain inulin). The solubility of HPX reacts more sensitive to a decreased polarity compared to an increased saturation of the solvent (due to the almost exclusively dissolved short and medium chain inulin). The different impact of polarity and saturation on the solubility of HP and HPX will be visible again in section 3.5.3, by the varying decrease in gel hardness of the HP and HPX gels.

3.5.2 High Performance Anion Exchange Chromatography

To determine the chain length distribution of the inulin, dissolved during sample preparation and remaining dissolved after 24 h of ageing, one sample was taken from the inulin suspension (20% inulin dry matter, ethanol and sucrose concentration 0% - 10%, $T_{\text{prep.}} = 25\text{ }^{\circ}\text{C}$) after 10 min stirring and one was taken from the same gel after 24 h of ageing at room temperature. The samples were processed as described in section 2.5. To determine the DP distribution of the samples, a reference value was prepared, as described in section 3.2.3. Apart from the overall decreased intensity of the amperometric signal, the chromatograms are identically to the ones used for the inulin-water HPAEC experiments and can be seen in Fig. 56 and Fig. 57 (see also Appendix section). As already mentioned in section 3.4.3, the decreased overall intensity, compared to the respective intensities of the HPAEC measurements in water and water-ethanol mixtures, arises from “electrode fouling”. Apart from this decrease in intensity, the retention times of the individual DP fractions remain the same. Thus, for each solvent series a reference value was measured, to make a qualitative and quantitative interpretation of the achieved chromatograms possible. To figure out the amount of inulin of a certain DP, dissolved during sample preparation, the areas below the peaks in the chromatogram were integrated, as mentioned in section 3.2.3. Again, the changes in the DP distribution of the dissolved inulin were pointed out and the concentration errors were minimized, by summing up a region of ten following DPs to one fraction. The results for HP and HPX, prepared at $25\text{ }^{\circ}\text{C}$

Results and discussion

with different ethanol and sucrose contents in the solvent and the samples taken after 10 min sample preparation, are shown in Fig. 124 and Fig. 125.

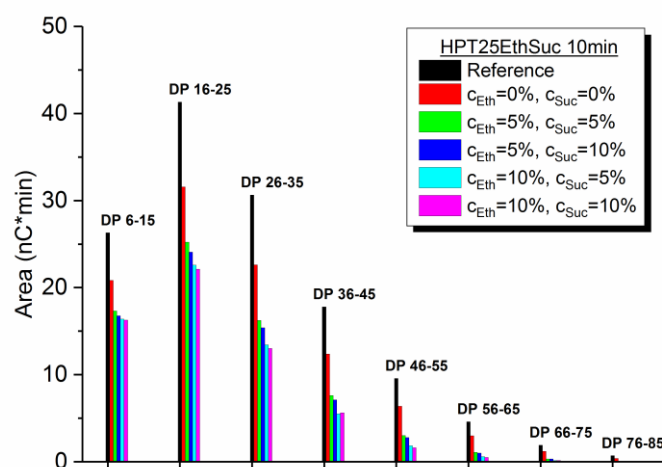


Fig. 124: DP distribution of dissolved HP after 10 min stirring at 25 °C, with ethanol/sucrose content of 0% - 10%.

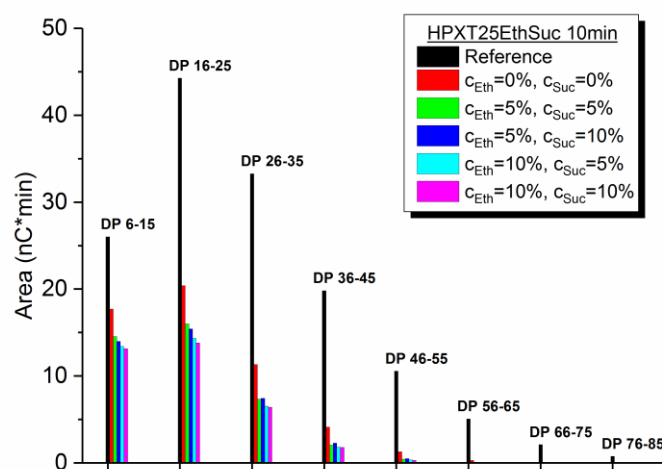


Fig. 125: DP distribution of dissolved HPX after 10 min stirring at 25 °C, with ethanol/sucrose content of 0% - 10%.

With increasing additives content (i.e. ethanol and sucrose) in the solvent, the amount of dissolved inulin decreases. If the HP and HPX samples with increasing ethanol and sucrose content in the solvent, are compared to the respective samples prepared in pure water, it is obvious, that the solubility is significantly decreased by a decreasing polarity and an increasing

saturation degree of the solvent. Since the long chain inulin exhibits a very low solubility in water, the most crucial change in the DP distribution of the dissolved inulin is visible in this DP region ($DP > 36 - 45$). Thus, both additives combined show the expected impact on the solubility of HP and HPX. The decreasing polarity and the increasing saturation add to each other and based on the respective ethanol and sucrose content in the solvent, the decreased solubility of HP and HPX is just a combination of the two systems, water-ethanol and water-sucrose. At ethanol and sucrose contents of 10% (i.e. 20% of additives in the solvent), for both HP and HPX, practically no long chain inulin is dissolved during sample preparation. Since the previously dissolved inulin partially crystallizes during gel formation, a considerable change in the DP distribution of the dissolved inulin changes the properties of the completely developed particle gel too. The processes, that give rise to the change of the gel properties of the HP and HPX gels with decreasing polarity and increasing saturation, have already been discussed in section 3.3 and 3.4 (e.g. particle size distribution, precipitation of inulin etc.), and as already mentioned above, are combined according to the respective ethanol and sucrose content in the solvent. The impact of the respective additives on the gel hardness is illustrated again in section 3.5.3. In Fig. 124 and Fig. 125, the larger impact of a decreasing polarity on the solubility of HP and HPX is clearly visible once again. If only the total amount of additives in the solvent is taken into account, the samples with ethanol and sucrose contents of 5% and 10% (dark blue columns in Fig. 124 and Fig. 125) and the ones with ethanol and sucrose concentrations of 10% and 5% (cyan columns in Fig. 124 and Fig. 125), equal each other. Yet the dissolved amount of HP and HPX is significantly decreased for the samples with an ethanol content of 10%. This again confirms the larger impact of a decreased polarity compared to an increased saturation on the solubility of HP and HPX. If one compares Fig. 124 and Fig. 125, the significantly lower solubility of HPX is once again clearly visible. This is again due to the superior crystallinity of the HPX powder. The resulting impact on the solubility and the particle gel structure is, as mentioned before, a combination of the water-ethanol and water-sucrose systems, and was already discussed in section 3.3 and 3.4.

To determine the DP distribution of the inulin, remaining dissolved after 24 h of storage at room temperature, the 24 h samples were analyzed accordingly to the 10 min samples, as already explained earlier in this section. The results are visible in Fig. 126 and Fig. 127.

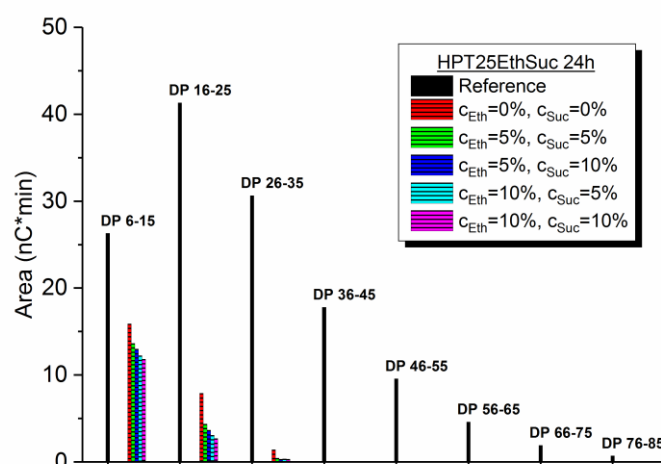


Fig. 126: Polarity/saturation dependent DP distribution of dissolved HP after 24 h storage.

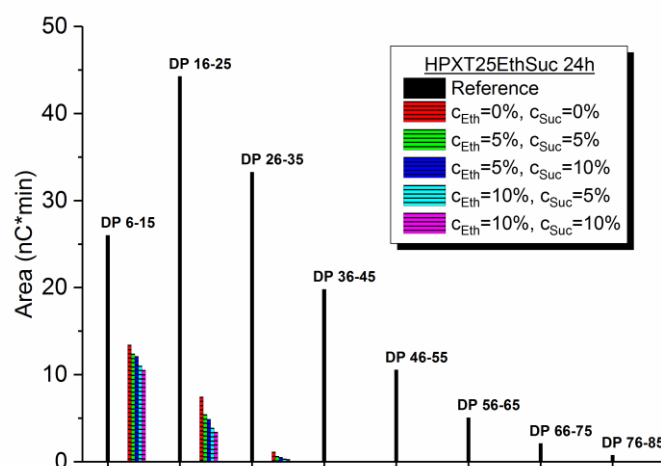


Fig. 127: Polarity/saturation dependent DP distribution of dissolved HPX after 24 h storage.

If Fig. 124 and Fig. 126 respectively Fig. 125 and Fig. 127 are compared to each other, one can clearly see, that the previously dissolved inulin almost completely recrystallizes during gel formation. Only a small amount of short and medium chain inulin, decreasing with increasing ethanol and sucrose content, remains dissolved after 24 h. Above a DP of 35, for both HP and HPX, the dissolved inulin completely crystallizes. Again, the trends for HP and HPX behave as expected and represent a combination of the water-ethanol and water-sucrose systems. The larger impact of a decreased polarity on the solubility of HP and HPX is visible anew, by the

comparison of the 5% ethanol and 10% sucrose samples with the 10% ethanol and 5% sucrose samples.

3.5.3 Texture analysis (Gel hardness)

In section 3.2.4, the completely developed inulin gels were compressed beyond their fracture stress, to learn about their fracture behavior. This type of experiment was not possible for the HP and HPX gels, prepared with ethanol and sucrose in the solvent, due to the decreasing hardness of the gels. At increasing ethanol/sucrose contents, even the HP gels became too soft to keep the cylindrical shape of the vessel, after being removed from it. In consequence, no compression experiments were performed for the water-ethanol-sucrose system.

To examine the hardness of the inulin gels, the samples were penetrated by a stainless steel stamp to a maximum strain of 6 mm and the resulting gel hardness was determined as described in section 3.2.4. The results of the hardness measurements of the HP and HPX gels, prepared at 25 °C with all three solvents (i.e. water, water-ethanol and water-sucrose mixtures) and a stirring rate of 600 rpm, are pictured in Fig. 128 and Fig. 129.

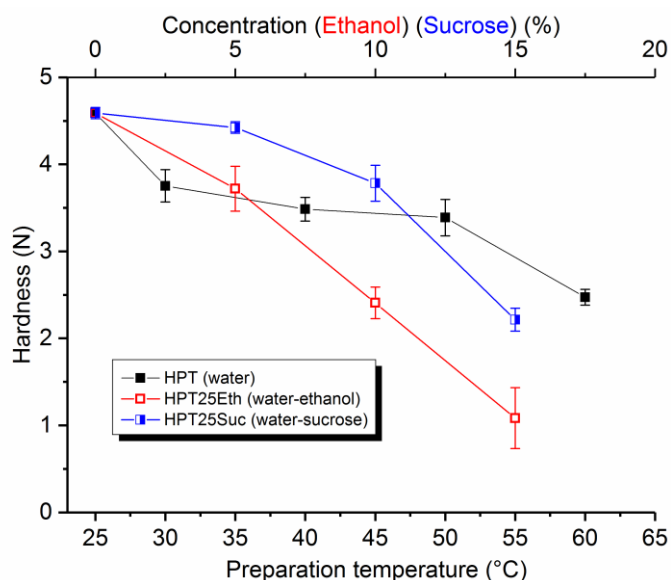


Fig. 128: Hardness of HP gels prepared with different solvents

As already observed in the previous sections, the hardness of the HP gels decreases with increasing sample preparation temperature, increasing ethanol content and increasing sucrose concentration in the solvent. The processes, that give rise to the hardness trends of the HP gels in the different solvents, have already been presented in sections 3.2, 3.3 and 3.4 (HPT: increasing sample preparation temperature results in an increasing average primary particle

size and the formation of softer gels. HPT25E: precipitation of inulin at decreased polarity of the solvent yields softer gels. HPT25Suc: increasing saturation of the solvent causes increasing unbalance of the primary particle size and the formation of softer gels). Therefore, the focus in Fig. 128 is set on the comparison of those hardness trends. Again, all three hardness curves exhibit the same initial value. As mentioned before, this is due to the reference value, that all three systems have in common, namely the hardness value of the HP gel, prepared at 25 °C in pure water. If we focus on the intersection points of the different curves, we can observe two obvious crossovers, one between the water ($T_{prep.} \approx 35\text{ °C}$) and the water-ethanol curve ($c_{Ethanol} \approx 5\%$) at approximately 3,6 N gel hardness and one between the water ($T_{prep.} \approx 50\text{ °C}$) and the water-sucrose ($c_{Sucrose} \approx 12\%$) curve at roughly 3,4 N gel hardness. The water-ethanol and the water-sucrose curves do not show a common intersection point. At the intersection points, the HP gels, prepared in different solvent, exhibit the same hardness values (the gels, prepared with all three solvents, exhibit many intersection points with each other, at the crossover points of a horizontal line with the hardness curves, drawn at a certain gel hardness in Fig. 128. Here, the two above mentioned intersection points were chosen, because those two points illustrate the different impact of ethanol and sucrose on the gel hardness very clearly). Yet those same hardness values do not arise from similar particle gel structures, due to the different DP distribution of dissolved and undissolved inulin. If the dissolved amount of HP for the respective systems is determined (Fig. 122), at the conditions of the intersection points of the corresponding hardness curves (for the water and the water-ethanol systems the dissolved amounts of HP at the intersection points of the hardness curves are 18,2% and 15,9%, for the water and the water-sucrose systems the dissolved amounts are 19,5% and 12,7%), one can see, that the dissolved amounts and with it the DP distribution of dissolved and undissolved HP, are not similar. Therefore, those same hardness values arise from gels with different gel structures (e.g. different primary particle size distributions). The similar hardness values of the gels just occur, because of the different processes, that alter the particle gel structure of the respective system and decrease the gel hardness at those conditions to the same extent (e.g. for the intersection point of the hardness curves of the water and the water-ethanol system, the hardness of the gel, prepared at 35 °C in pure water, decreases because of the increasing average particle size. The hardness of the gel, prepared at 25 °C with 5% of ethanol, decreases due to the precipitation of inulin at a decreasing polarity of the solvent). If the hardness curves of the water-ethanol and the water-sucrose system

in Fig. 128 are compared to each other, the larger impact of a decreased polarity of the solvent on the gel hardness becomes obvious again (the hardness of the water-ethanol HP gels remains below the hardness of the respective water-sucrose gels throughout the whole concentration range). The different impacts of ethanol and sucrose on the solubility of HP, have already been explained in section 1.5 and 3.4.3.

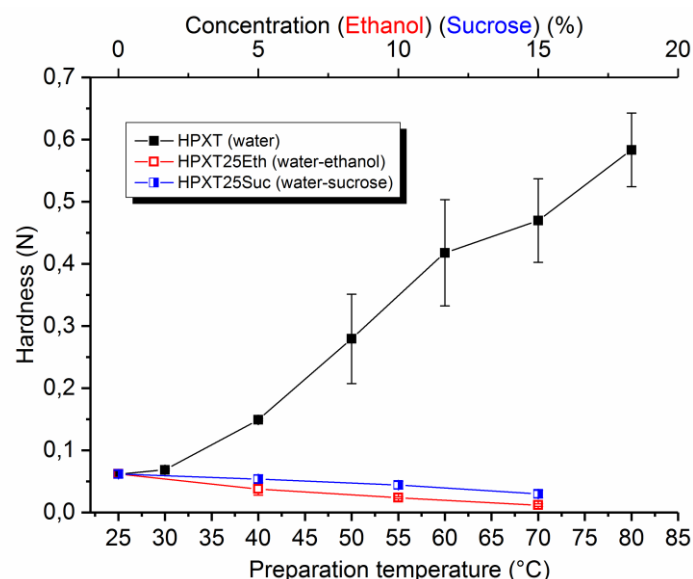


Fig. 129: Hardness of HPX gels prepared with different solvents

In Fig. 129, the hardness curves of all three systems also follow the trends observed in the previous sections. As before, the processes giving rise to the hardness trends have already been explained sections 3.2, 3.3 and 3.4 (HPXT: increasing sample preparation temperature induces the formation of gels with equalizing primary particle sizes and increasing gel hardness. HPXT25E: precipitation of inulin at decreased polarity of the solvent results in softer gels. HPXT25Suc: increasing saturation of the solvent causes an increasing unbalance of the primary particle sizes, yielding softer gels). Similar to the HP gels, the HPX gels exhibit the same initial hardness value, due to the same reference value. The increasing sample preparation temperature for the water system and the increasing ethanol and sucrose concentrations in the solvent for the other two systems, have a contrary impact on the gel hardness (gel hardness increases with increasing sample preparation temperature and the gel hardness decreases with increasing ethanol and sucrose contents in the solvent). Thus, no intersection points of the water hardness curve with the water-ethanol and water-sucrose curves can be determined. Again, the larger impact of a decreasing polarity on the gel hardness is obvious in Fig.

Results and discussion

129 and the hardness values of the water-ethanol system remain below the hardness values of the water-sucrose system, throughout the whole concentration range.

To examine the combined impact of ethanol and sucrose on the gel hardness, HP and HPX gels have been prepared at 25 °C, with ethanol and sucrose contents of 0% - 10% in the solvent. The results of the hardness measurements of the HP and HPX gels, can be seen in Fig. 130 and Fig. 131.

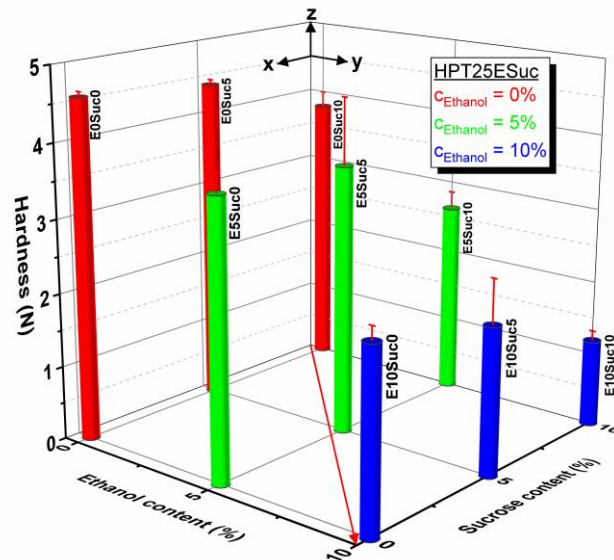


Fig. 130: Hardness of HP gels, prepared at 25 °C with 0% - 10% of ethanol and sucrose in the solvent.

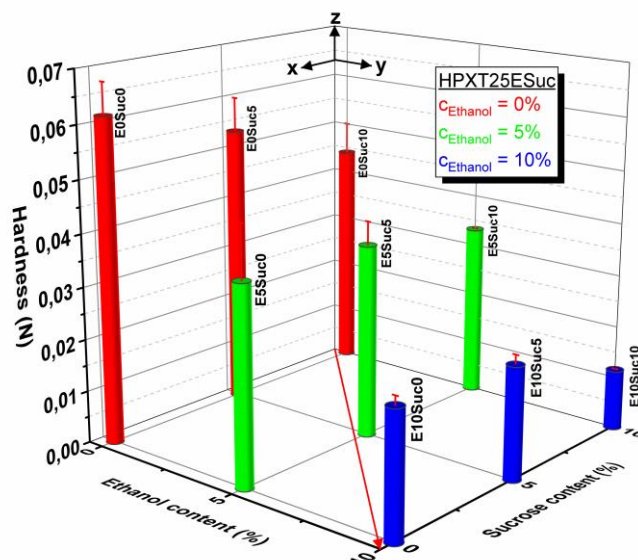


Fig. 131: Hardness of HPX gels, prepared at 25 °C with 0% - 10% of ethanol and sucrose in the solvent.

In Fig. 130 and Fig. 131, the sucrose content is plotted on the x-axis, the ethanol content on the y-axis and the gel hardness on the z-axis. Again, the trends in both figures confirm the decreasing hardness of the HP and HPX gels with increasing ethanol and sucrose content in the solvent. Additionally, no antagonistic (meaning an increasing ethanol and an increasing sucrose content in the solvent, neutralize each other's impact on the gel hardness) and no synergistic (an increasing ethanol and an increasing sucrose content in the solvent, potentiate each other's impact on the gel hardness) effects can be observed. The impact of ethanol and sucrose on the gel hardness just add up, related to their respective content in the solvent. The larger impact of an increased ethanol content on the gel hardness is again visible in Fig. 130 and Fig. 131. This is visible very clearly, if a diagonal line in the xy-plane is traced in the direction of the red arrow from the back to the front. For all the samples, located on the same diagonal line, the overall amount of additives in the solvent is the same. The sucrose content in the solvent decreases and the ethanol content increases from the back to the front. For both types of inulin, HP and HPX, the samples with the highest ethanol content located on those diagonals, exhibit the lowest gel hardness. This larger impact of a decreasing polarity on the gel hardness is again due, as mentioned in the previous sections (see section 1.5), to the increase of the Flory-Huggins parameter χ with increasing ethanol content in the solvent. This is also clearly visible at the blue columns in Fig. 130 and Fig. 131. Those samples have been prepared with the highest ethanol content in the solvent ($C_{Ethanol} = 10\%$) and exhibit the lowest gel hardness of all the gels pictured in Fig. 130 and Fig. 131.

4 Conclusions

In this work, the gel formation process of HP and HPX has been examined according to the sample preparation temperature (in the solvent water), the polarity of the solvent (ethanol-water mixtures) and the saturation of the solvent (sucrose-water mixtures). To learn about the crystallinity of the used inulin powders, HP and HPX were successfully examined by x-ray powder diffraction and identified HP as mostly amorphous and HPX as semi-crystalline powder. X-ray diffraction during gelling confirmed the crystallization of the gel primary particles, as postulated by Bot et al. [13] and provided information about the crystallization kinetics of the gel formation process of both inulin types. For HP, the results indicated a decreasing crystallization constant k with increasing sample preparation temperature, an increasing constant k with increasing ethanol content (and therefore a decreasing polarity) and an increasing crystallization constant k with increasing sucrose content (meaning an increasing saturation of the solvent). Similar to the crystallization constant of the HP samples in the different solvents, the constant k of the HPX samples decreased with increasing sample preparation temperature and increased with decreasing polarity and increasing saturation of the solvent. By the application of HPAEC, the preparation temperature dependent, the polarity dependent and the saturation dependent chain length distribution of the initially and the after 24 h still dissolved HP and HPX was successfully determined. The results showed a significant increase in solubility of the large DP molecules at increased preparation temperatures and a significant decrease in solubility of the large DP molecules with increasing ethanol and sucrose content, for both types of inulin. Hardness measurements of the completely developed gels revealed a distinct dependency of the texture on the variation of shear rate, temperature, polarity and saturation during sample preparation for the HP and the HPX gels. An increase in shear rate from 600 rpm to 7000 rpm resulted in an increased hardness for both types of inulin gels. The reason for this increase could be successfully identified as a decrease in the primary particle size of the gel network. An increase in temperature during sample preparation resulted in HP gels with decreased hardness, arising from the increase in primary particle size and an increased gel hardness for HPX, resulting from the equalizing primary particle size and connected therewith a more homogeneous gel network formation. An increasing ethanol content in the solvent (decreasing polarity), yielded HP and HPX gels with decreasing gel hardness. For both types of inulin, the decreasing hardness arose from the precipitation of inulin with decreasing polarity. The decreasing polarity also resulted in an increasing average primary particle size for HP and

Conclusions

an increasing inhomogeneity in the gel particle size for HPX, decreasing the gel hardness even further. An increasing sucrose concentration in the solvent (increasing saturation), also resulted in HP and HPX gels with decreasing gel hardness. For both types of inulin, the decreasing hardness arose from the increasing inhomogeneity of the gel primary particle size and connected therewith an increasing fragmentary character of the completely developed inulin gels. The above mentioned hardness trends of the inulin gels, prepared with the three different solvents, could be confirmed by the determination of the gel particle size by static light scattering. Eventually, the preparation temperature dependent, the polarity dependent and the saturation dependent variations of the gel primary particle size could be summarized by a simple model. Finally, the different systems could be linked to each other, by the determination of intersection points between the solubility curves of all three systems. All told, the achieved results mark inulin gels as suitable fat replacer or texturizer in food applications, which offer the user a large variation in applicability due to the excellent controllability of the resulting texture of the gels, by the variation of the temperature, the polarity or the saturation of the solvent.

5 Outlook

In this study, the gel structures of HP and HPX gels, prepared with solvents of different temperature, polarity and saturation, were examined. The results were also interpreted on the basis of a fractal structure of the inulin gels (see section 1.4). As already mentioned in this section, the fractal dimension D_f of a substance gives significant information about its network structure and therefore also its textural properties. In section 1.4, an example is given for the determination of the fractal dimension of an HP gel, by the application of the Kraus model on an amplitude sweep curve, obtained by oscillatory rheology. Due to time limitations, this method was just performed experimentally for the HP sample mentioned in section 1.4. Since the application of the Kraus model on the inulin gels yielded promising results, it is worth to extend the determination of the fractal dimension by oscillatory rheology on the whole inulin sample spectrum, presented in this work. Additionally, the fractal dimension obtained by the rheological measurements could be certified with other methods such as 3D box counting [74]. For this purpose, confocal microscopy images of completely developed inulin gels could be examined to analyze the fractal dimension. Furthermore, D_f can be determined by Small Angle X-ray Scattering (SAXS) [75]. Therefore, the examination of inulin gels by SAXS could yield another independent value for the fractal dimension. If the values for the fractal dimensions of the inulin gels, examined with the above mentioned methods, are compared to each other, relatively reliable data could be obtained about the spatial structure of the completely developed inulin gels. This information could be the basis for further experiments, concerning the structure of inulin gels prepared with different types of inulin or even different solvents, not yet employed in this work.

List of references

1. Meyer, D., Blaauwhoed, J. P., *Inulin*, in *Handbook of Hydrocolloids*, G.O. Phillips, Williams, P. A., Editor. 2009, Woodhead Publishing. p. 829-845.
2. Franck, A. and B. Leveck, *Inulin*, in *Ullmann's Encyclopedia of Industrial Chemistry*. 2000, Wiley-VCH Verlag GmbH & Co. KGaA.
3. P. Diederich Meyer, J.D.W., Peter Olivier, *Inulin und Fructooligosaccharide*, in *Handbuch Süßungsmittel*, U.N. K. Rosenplenter, Editor. 2007, Behr's Verlag. p. 155 - 193.
4. Kaur, N. and A. Gupta, *Applications of inulin and oligofructose in health and nutrition*. Journal of Biosciences, 2002. **27**(7): p. 703-714.
5. Bot, A., Flöter, E., Lammers, J. G. & Pelan, E. G., *Controlling the texture of spreads*, in *Texture in Food, Volume 1 - Semi-Solid Foods*, B.M. McKenna, Editor. 2003, Woodhead Publishing. p. 350-372.
6. de Bruijne, D.W., Bot, A. , *Fabricated fat-based foods*, in *Food texture : measurement and perception*. 1999, Aspen Publishers: Gaithersburg [Maryland]. p. 185-227.
7. Tárrega, A. and E. Costell, *Effect of inulin addition on rheological and sensory properties of fat-free starch-based dairy desserts*. International Dairy Journal, 2006. **16**(9): p. 1104-1112.
8. Meyer, D., et al., *Inulin as texture modifier in dairy products*. Food Hydrocolloids, 2011. **25**(8): p. 1881-1890.
9. Hennelly, P.J., et al., *Textural, rheological and microstructural properties of imitation cheese containing inulin*. Journal of Food Engineering, 2006. **75**(3): p. 388-395.
10. Story, M., et al., *Creating healthy food and eating environments: Policy and environmental approaches*, in *Annual Review of Public Health*. 2008, Annual Reviews: Palo Alto. p. 253-+.
11. Glanz, K., et al., *Stages of Change in Adopting Healthy Diets: Fat, Fiber, and Correlates of Nutrient Intake*. Health Education & Behavior, 1994. **21**(4): p. 499-519.
12. Mason, J.O. and J.M. McGinnis, *"Healthy People 2000": an overview of the national health promotion and disease prevention objectives*. Public Health Reports, 1990. **105**(5): p. 441-446.
13. Bot, A., et al., *Influence of crystallisation conditions on the large deformation rheology of inulin gels*. Food Hydrocolloids, 2004. **18**(4): p. 547-556.
14. Harding, S.E., *Conformation zones*, in *An introduction to polysaccharide biotechnology*. 2017, CRC Press: Boca Raton.
15. Kim, Y., M.N. Faqih, and S.S. Wang, *Factors affecting gel formation of inulin*. Carbohydrate Polymers, 2001. **46**(2): p. 135-145.
16. Marangoni, A.G. and L.H. Wesdorp, *Structure and properties of fat crystal networks*. 2013, Boca Raton: CRC Press.
17. Myerson, A.S., *Handbook of industrial crystallization*. 2002, Boston: Butterworth-Heinemann.
18. "Point-lattice-and-unit-cell".Available-from:
<https://2012books.lardbucket.org/books/principles-of-general-chemistry-v1.0/s16-02-the-arrangement-of-atoms-in-cr.html>.
19. "Bravais-lattices".Available-from:
<https://epionelynx.wordpress.com/2013/02/14/the-bravais-lattices-song/>.

List of references

20. "Crystal-systems-with-lattice-parameters". Available from: <https://2012books.lardbucket.org/books/principles-of-general-chemistry-v1.0/s16-02-the-arrangement-of-atoms-in-cr.html>.
21. Sharples, A., *Introduction to polymer crystallization*. 1966, London: Edward Arnold.
22. O'Grady, D., *Crystallization and Precipitation*. 2014, Mettler Toledo. p. 16.
23. Beccard, S., Vilgis, T. A., Bernard, J., Gehrich, K., Wouters, R., Zielbauer, B., Mezger, M., *Alteration of the structural properties of inulin gels "manuscript submitted for publication"*. Food Hydrocolloids, 2018.
24. Narine, S.S. and Marangoni, A.G., *Fractal nature of fat crystal networks*. Physical Review E, 1999. **59**(2): p. 1908-1920.
25. Vilgis, T.A., Joshi, B., Beccard, S., *Fractals in crystallizing food systems "manuscript submitted for publication"*. Current Opinion in Food Science, 2018.
26. Marangoni, A.G. and D. Rousseau, *Is plastic fat rheology governed by the fractal nature of the fat crystal network?* Journal of the American Oil Chemists' Society, 1996. **73**(8): p. 991-994.
27. Narine, S.S. and A.G. Marangoni, *Relating structure of fat crystal networks to mechanical properties: a review*. Food Research International, 1999. **32**(4): p. 227-248.
28. Huber, G., Vilgis, T.A., *Universal properties of filled rubbers : Mechanisms for reinforcement on different length scales*. Kautschuk Gummi Kunststoffe, 1999. **52**(2): p. 102-107.
29. Huber, G., Vilgis, T. A.; Heinrich, G., *Universal properties in the dynamical deformation of filled rubbers*. Journal of Physics: Condensed Matter, 1996. **8**(29): p. L409.
30. Vliet, T.v., *Rheology and Fracture Mechanics of Food*. 2013: CRC Press.
31. Crilly, A.J., R. Earnshaw, and H. Jones, *Fractals and chaos*. 2012: Springer Science & Business Media.
32. Mandelbrot, B.B., *The fractal geometry of nature*. 1983, New York: Freeman.
33. Glibowski, P. and A. Wasko, *Effect of thermochemical treatment on the structure of inulin and its gelling properties*. International Journal of Food Science & Technology, 2008. **43**(11): p. 2075-2082.
34. Burchard, W., *Solution Thermodynamics of Non-Ionic Water-Soluble Polymers*, in *Chemistry and Technology of Water-Soluble Polymers*, C.A. Finch, Editor. 1983, Springer US: Boston, MA. p. 125-142.
35. Franks, F. and Ives, D.J.G., *The structural properties of alcohol-water mixtures*. Quarterly Reviews, Chemical Society, 1966. **20**(1): p. 1-44.
36. Franks, F., *Water Solubility and Sensitivity - Hydration Effects*, in *Chemistry and Technology of Water-Soluble Polymers*, C.A. Finch, Editor. 1983, Springer US: Boston, MA. p. 157-178.
37. Reichardt, C. and T. Welton, *Solvents and Solvent Effects in Organic Chemistry*. 2011.
38. Tieke, B., *Makromolekulare Chemie eine Einführung*. 2005, Weinheim: Wiley-VCH.
39. Gennes, P.-G.d., *Scaling concepts in polymer physics*. 2005, Ithaca, NY: Cornell Univ. Press.
40. Tipler, P.A. and J.S. Walker, *Physik Arbeitsbuch, Arbeitsbuch*. 1994, Heidelberg: Spektrum Akad. Verl.
41. Atkins, P.W. and J. De Paula, *Physikalische Chemie [Hauptbd.] / Peter W. Atkins ; Julio de Paula [Hauptbd.] / Peter W. Atkins ; Julio de Paula*. 2013, Weinheim ~[u.a.]: Wiley-VCH.
42. *Abbé Refractometer*. 2011; Available from: <http://www.refractometer.pl>.
43. "Abbé-refractometer". 2011.

List of references

44. "Total-reflection-and-shadow-boundary-in-measuring-prism". Available from: <http://www-ekp.physik.uni-karlsruhe.de/~simonis/praktikum/p-nebenfach/versuchsanleitungen/v49-Refraktometer.pdf>.
45. "Handheld-digital-refractometer-by-Bellingham-and-Stanley".2018; Available-from: https://www.bellinghamandstanley.com/general_pdfs/literature_page/HHO-EN-2018.pdf.
46. Jeu, W.H.d., *Basic X-Ray scattering for soft matter*. Vol. 1. 2016: Oxford.
47. Cattin , P. 2016; Available from: <https://miac.unibas.ch/PMI/01-BasicsOfXray.html>.
48. Weidner , H. *Diffraction-of-wave-at-lattice-plane*. 2009; Available from: https://de.wikipedia.org/wiki/Huygenssches_Prinzip.
49. Dionex Corporation, *Analysis of Carbohydrates by High-Performance Anion-Exchange Chromatography with pulsed Amperometric Detection (HPAE-PAD)*. 2004: p. 13.
50. Eith , C., Kolb , M. , Seubert , A. , Viehweger , K. , *Praktikum-der-Ionenchromatographie*. Methrom AG.
51. Macks,D.,*Styrol-Divinylbenzol-Copolymer*.Available-from: <https://de.wikipedia.org/wiki/Styrol-Divinylbenzol-Copolymer>.
52. Methrom-AG,*Conductometric-Detection*. 2013; Available from: https://www.youtube.com/watch?v=fA4p8_Icyaw.
53. *Chromatogram*.Available-from: http://www.chemgapedia.de/vsengine/vlu/vsc/de/ch/3/anc/croma/chromatographie_grundlagen.vlu/Page/vsc/de/ch/3/anc/croma/basics/saulen_chr/chromatogramm/chromatogrammm65ht1100.vscml.html.
54. Thermo-Fisher-Scientific;Available-from: <http://www.thermofisher.com/de/de/home/industrial/chromatography.html>.
55. Szczesniak, A.S., *Classification of Textural Characteristics*. Journal of Food Science, 1963. **28**(4): p. 385-389.
56. Pons, M. and S.M. Fiszman, *INSTRUMENTAL TEXTURE PROFILE ANALYSIS WITH PARTICULAR REFERENCE TO GELLED SYSTEMS*. Journal of Texture Studies, 1996. **27**(6): p. 597-624.
57. Wilhelm , S., Gröbler , B. , Gluch , M. , Heinz , H. , *Confocal Laser Scanning Microscopy*. Carl Zeiss.
58. Ishikawa-Ankerhold, H.C., Ankerhold, R. and Drummen, G.P.C., *Advanced Fluorescence Microscopy Techniques—FRAP, FLIP, FLAP, FRET and FLIM*. Molecules, 2012. **17**(4): p. 4047.
59. *Rhodamine-B_structure*.Available-from: https://de.wikipedia.org/wiki/Rhodamin_B.
60. Thomas, G.M., *Das Rheologie Handbuch*. [Place of publication not identified]: Vincentz Network.
61. Willenbacher, N., Georgieva, K., *Rheology of Disperse Systems*, in *Product Design and Engineering*. p. 7 - 49.
62. Giesekus, H. and Langer, G., *Die Bestimmung der wahren Fließkurven nicht-newtonscher Flüssigkeiten und plastischer Stoffe mit der Methode der repräsentativen Viskosität*. Rheologica Acta, 1977. **16**(1): p. 1-22.
63. Rawle, A., *The Basic Principles of Particle Size Analysis*. Vol. 86. 2003. 58-65.
64. Webb, P.A., *A Primer on Particle Sizing by Static Laser Light Scattering*. 2000: p. 82.
65. Beckmann Coulter Inc., *LS 13320 Laser Diffraction Particle Size Analyzer*, in *Optical Models - Refractive Index*. 2011, Beckmann Coulter Inc. p. C-1-C-2.
66. Goure, J.P., *Optics in Instruments : Applications in Biology and Medicine*. 2013.

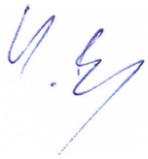
List of references

67. Munoz, C.R., *Colored suspensions of inulin*. Anales de Fisica y Quimica, 1944. **40**: p. 646-59.
68. Lee, T.H., Boey, F.Y.C. and Khor, K.A., *X-ray diffraction analysis technique for determining the polymer crystallinity in a polyphenylene sulfide composite*. Polymer Composites, 1995. **16**(6): p. 481-488.
69. Humphreys, F.J. and Hatherly, M., *Chapter 7 - Recrystallization of Single-Phase Alloys*, in *Recrystallization and Related Annealing Phenomena (Second Edition)*. 2004, Elsevier: Oxford. p. 215-IV.
70. Silva, A., et al., *Rhodamine B as ligand for affinity chromatography. Fixation studies onto cellulose by a curing method*. European Polymer Journal, 2006. **42**(10): p. 2270-2282.
71. Pirro, D.M., Wessol, A.A. and Wills, J.G., *Lubrication fundamentals*. 2001.
72. Sánchez-Valdes, S., Ramos-De Valle, L.F. and Manero, O., *Polymer Blends*, in *Handbook of Polymer Synthesis, Characterization, and Processing*. 2013, John Wiley & Sons, Inc. p. 505-517.
73. Ronkart, S.N., et al., *Development of gelling properties of inulin by microfluidization*. Food Hydrocolloids, 2010. **24**(4): p. 318-324.
74. Suzuki, M., *A three dimensional box counting method for measuring fractal dimensions of 3D models*. 2007.
75. Johansen, D., Trewella, J. and Goldenberg, D.P., *Fractal dimension of an intrinsically disordered protein: Small-angle X-ray scattering and computational study of the bacteriophage λ N protein*. Protein Science : A Publication of the Protein Society, 2011. **20**(12): p. 1955-1970.

Statutory declaration

I declare that I have developed and written the enclosed PhD thesis completely by myself, and have not used sources or means without declaration in the text. Any thoughts from others or literal quotations are clearly marked. The PhD thesis was not used in the same or in a similar version to achieve an academic grading or is being published elsewhere.

Mainz, 11.06.2018

A handwritten signature in blue ink, appearing to read 'U. Beccard', with a stylized flourish at the end.

Steffen Beccard

Appendix

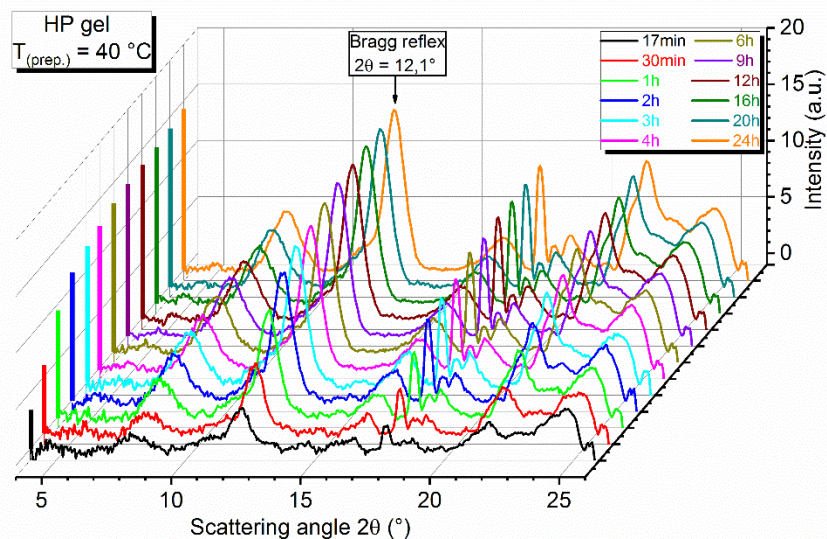


Fig. 132: XRD during gelation of an HP gel, prepared at 40 °C and 600 rpm shear rate.

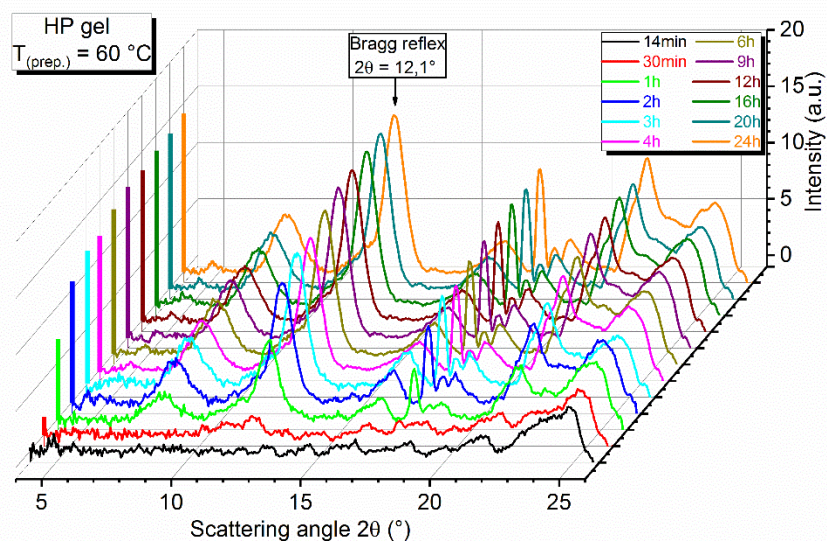


Fig. 133: XRD during gelation of an HP gel, prepared at 60 °C and 600 rpm shear rate.

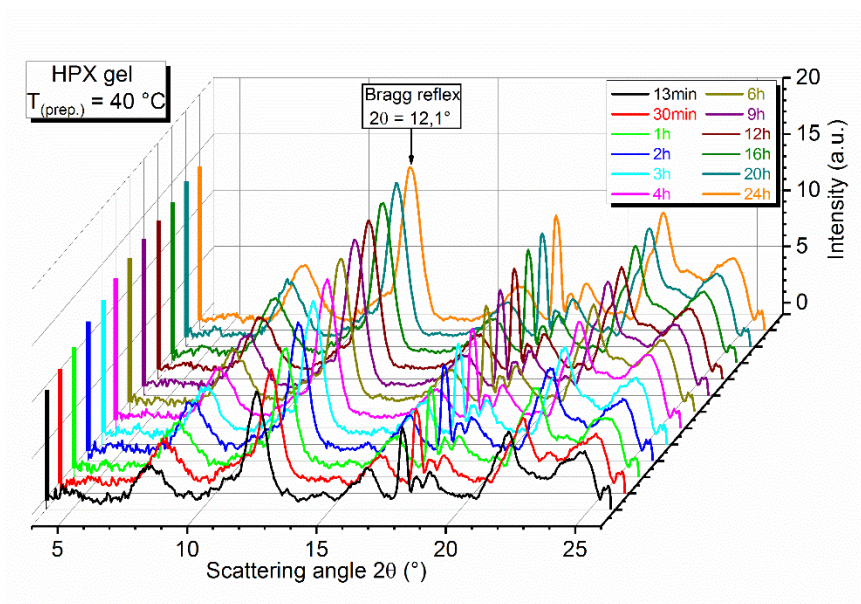


Fig. 134: XRD during gelation of an HPX gel, prepared at 40 °C and 600 rpm shear rate.

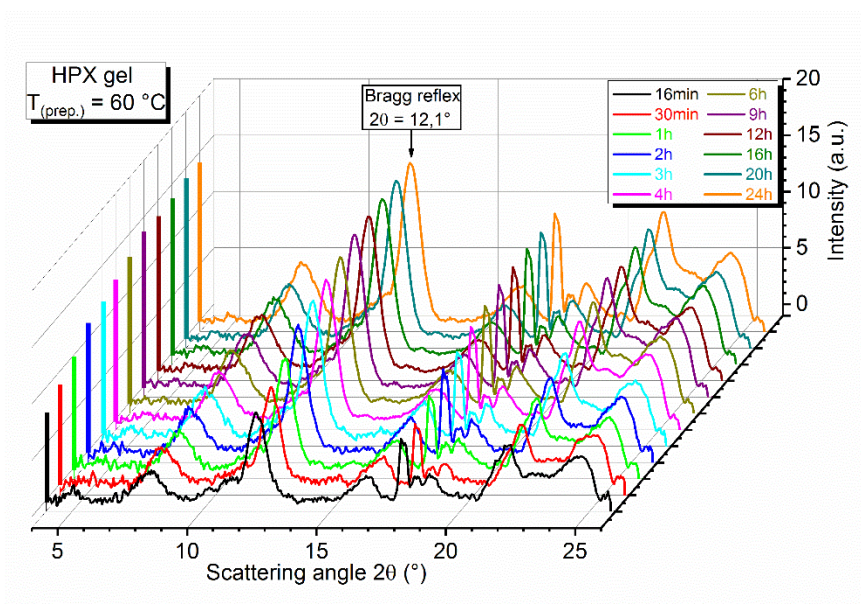


Fig. 135: XRD during gelation of an HPX gel, prepared at 60 °C and 600 rpm shear rate.

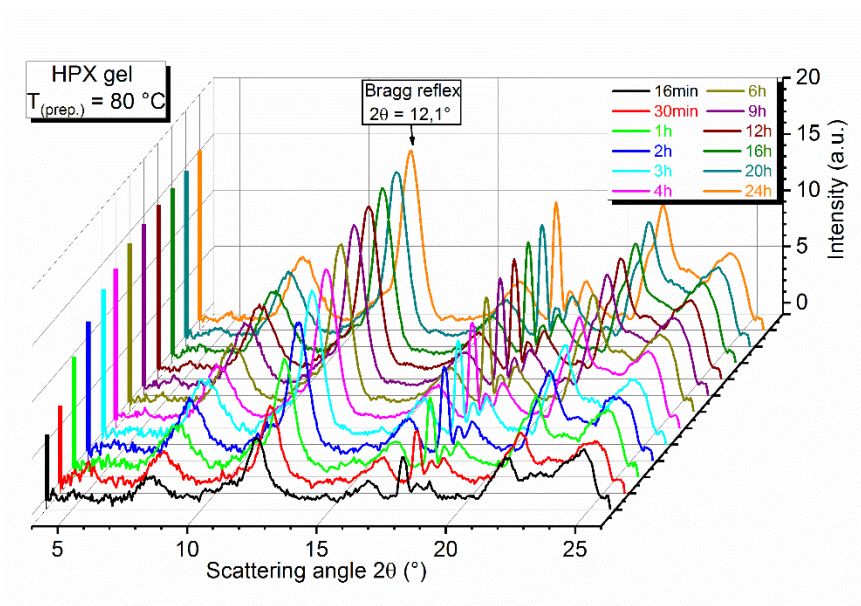


Fig. 136: XRD during gelation of an HPX gel, prepared at 60 °C and 600 rpm shear rate.

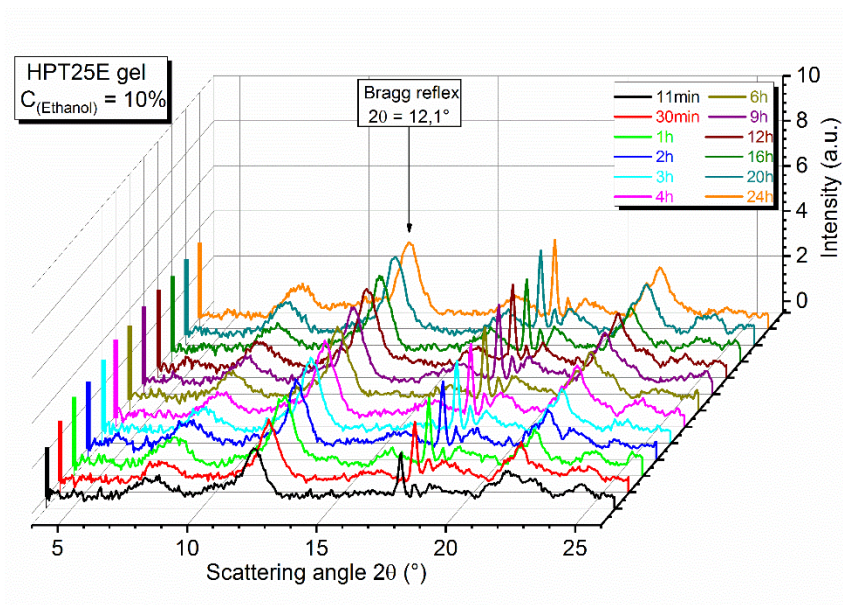


Fig. 137: XRD during gelation of an HP gel, prepared at 25 °C, with 10% (w/w) of ethanol in the solvent and 600 rpm shear rate.

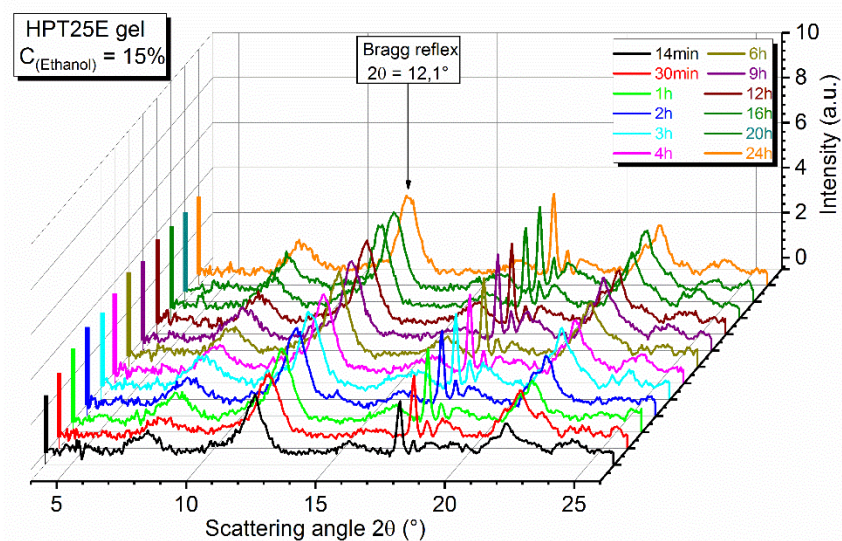


Fig. 138: XRD during gelation of an HP gel, prepared at 25 °C, with 15% (w/w) of ethanol in the solvent and 600 rpm shear rate.

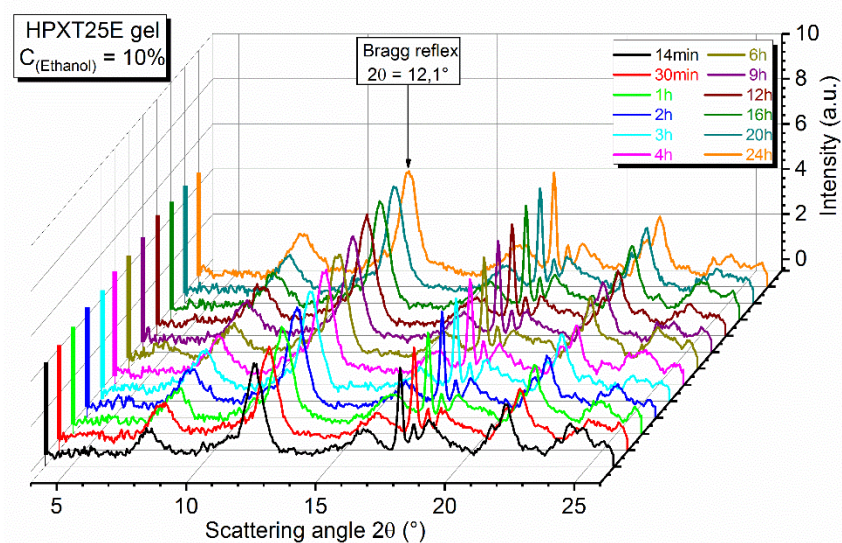


Fig. 139: XRD during gelation of an HPX gel, prepared at 25 °C, with 10% (w/w) of ethanol in the solvent and 600 rpm shear rate.

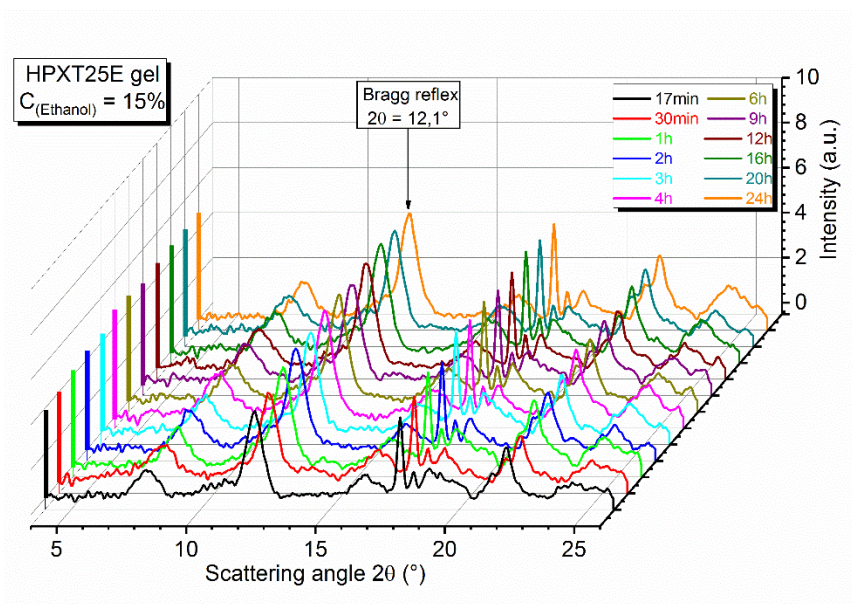


Fig. 140: XRD during gelation of an HPX gel, prepared at 25 °C, with 15% (w/w) of ethanol in the solvent and 600 rpm shear rate.

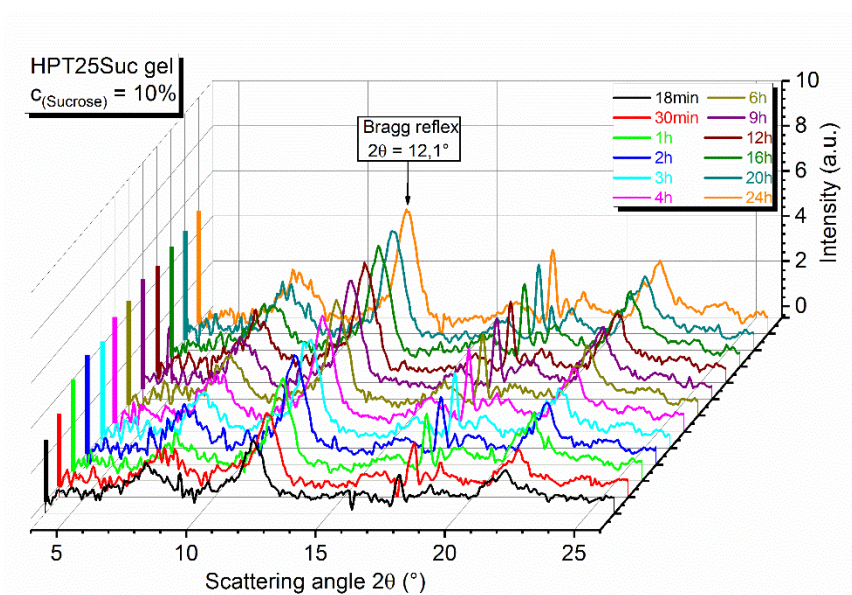


Fig. 141: XRD during gelation of an HP gel, prepared at 25 °C, with 10% (w/w) of sucrose in the solvent and 600 rpm shear rate.

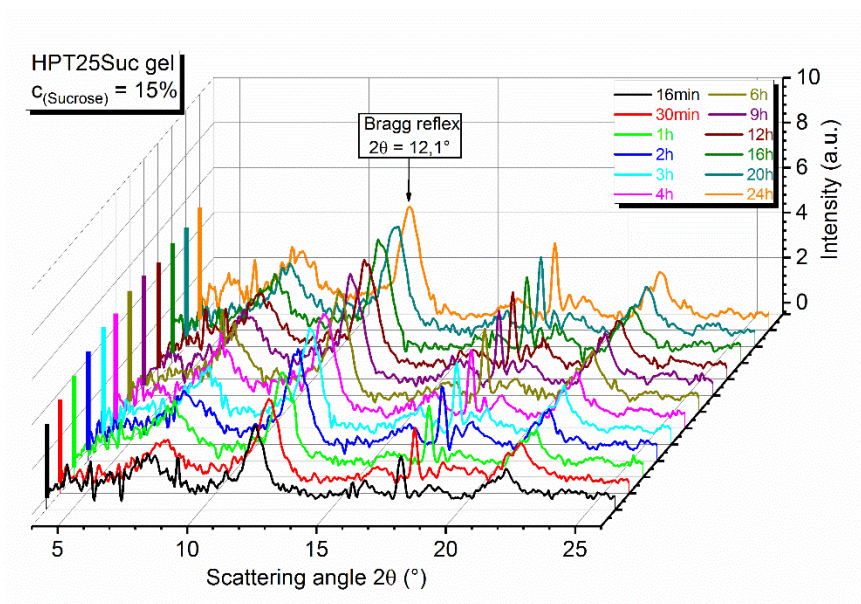


Fig. 142: XRD during gelation of an HP gel, prepared at 25 °C, with 15% (w/w) of sucrose in the solvent and 600 rpm shear rate.

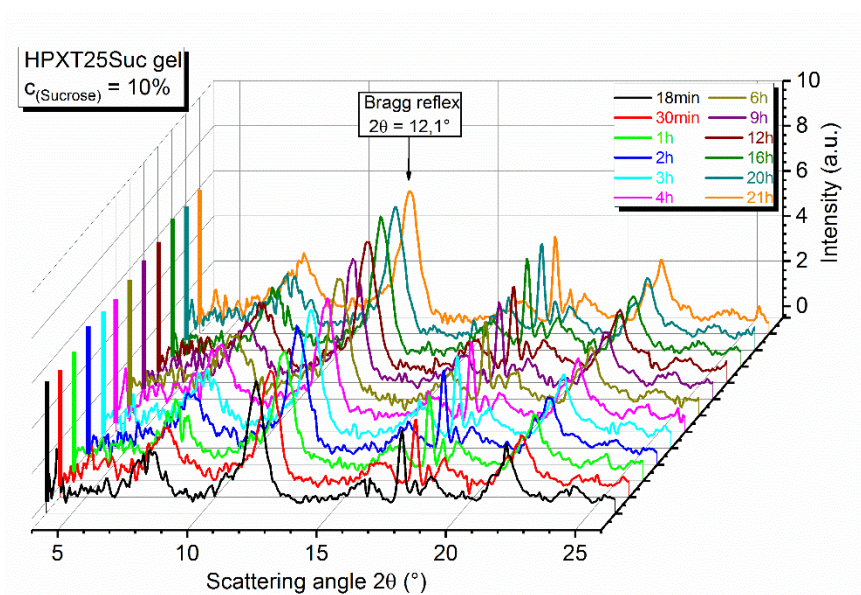


Fig. 143: XRD during gelation of an HPX gel, prepared at 25 °C, with 10% (w/w) of sucrose in the solvent and 600 rpm shear rate.

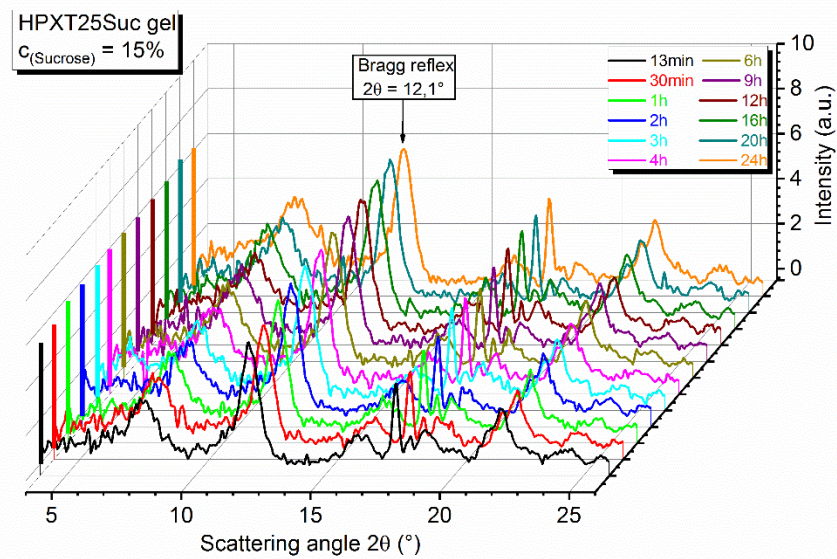


Fig. 144: XRD during gelation of an HPX gel, prepared at 25 °C, with 15% (w/w) of sucrose in the solvent and 600 rpm shear rate.

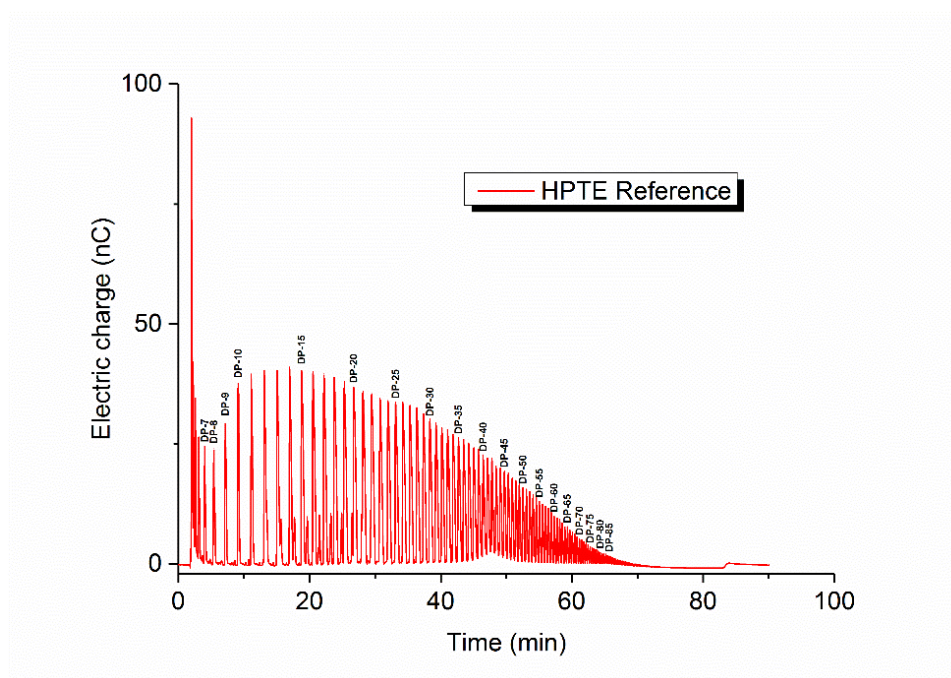


Fig. 145: HP separated according to DP, used as reference for the HPAEC measurements with ethanol-water mixtures acting as solvent.

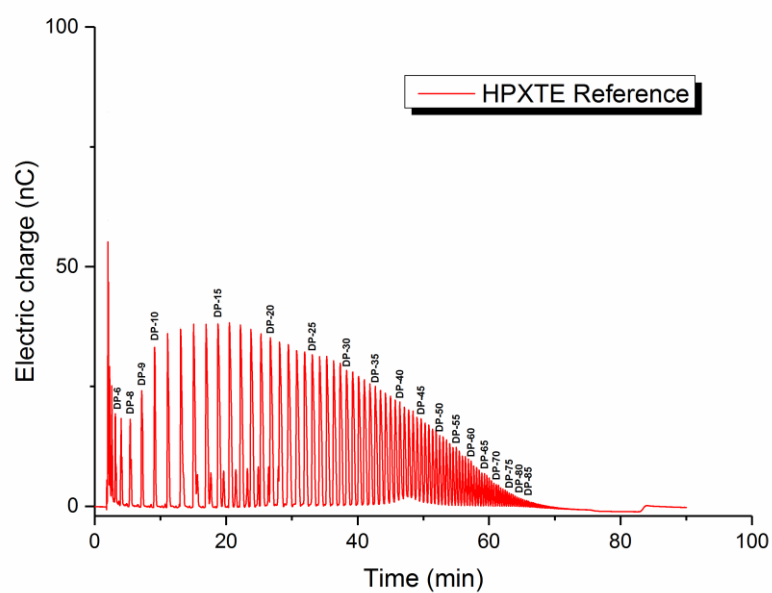


Fig. 146: HPX separated according to DP, used as reference for the HPAEC measurements with ethanol-water mixtures acting as solvent.

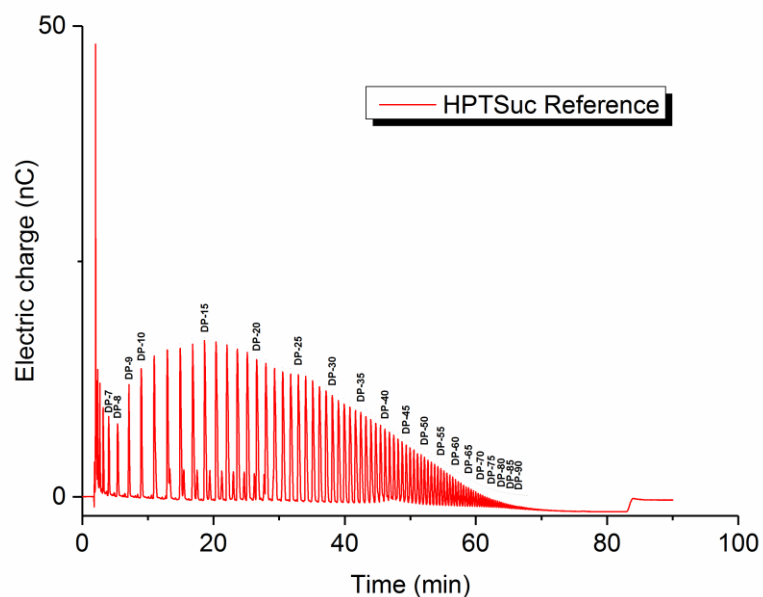


Fig. 147: HP separated according to DP, used as reference for the HPAEC measurements with sucrose-water mixtures acting as solvent.

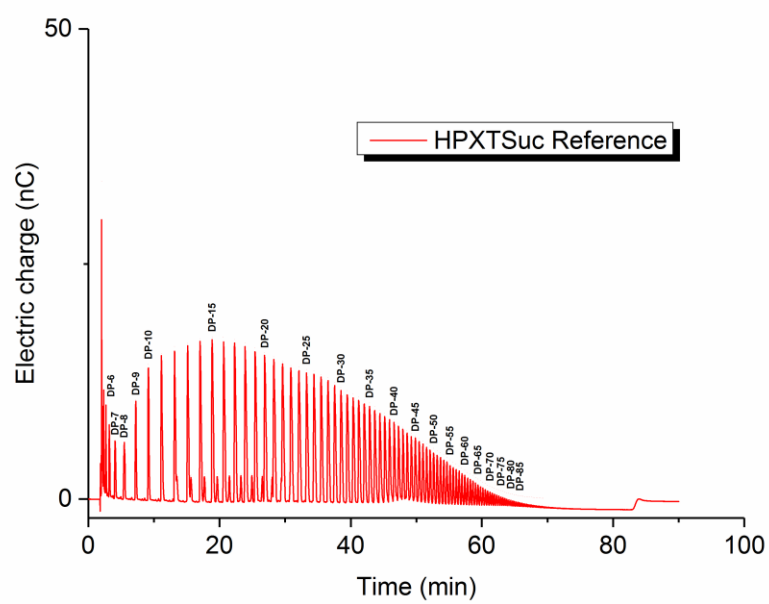


Fig. 148: HPX separated according to DP, used as reference for the HPAEC measurements with sucrose-water mixtures acting as solvent.